Constant Rate of Momentum Change Ejector: Simulation, Experiments and Flow Visualisation

A thesis submitted by

Mohamed Alsafi, M Eng

For the award of

Doctor of Philosophy

2017

Abstract

An ejector is a momentum-transfer device that requires no external mechanical input or moving parts. However, ejectors have low performance due to irreversibilities such as viscous losses and shocks in the primary stream and diffuser. It has previously been argued that by maintaining a constant rate of momentum change along the ejector duct, shock losses could be eliminated or at least minimised, and so the Constant Rate of Momentum Change (CRMC) ejector was introduced. The CRMC configuration appears to have significant potential, but the CRMC design prescription relies on: (1) an arbitrary choice for the constant rate of momentum change along the length of the duct; and (2) complete mixing between primary and secondary streams at the entrance to the duct. This thesis investigates the themes of shock losses and mixing within a CRMC ejector using physical experiments and computational simulation.

The CRMC ejector duct and the primary nozzle were manufactured using 3D printing technology and then an experimental test bench using air as the working fluid was assembled and successfully tested. The primary nozzle had a throat diameter of 3.2 mm and an exit diameter of 13.6 mm; the CRMC duct had a throat diameter of 25.48 mm. Extensive experimental tests were carried out for primary pressure between 200 kPa and 270 kPa, and secondary pressure between 0.6 kPa and 5 kPa. The results demonstrate the primary nozzle exit position within the entrainment region has a limited effect on the ejector performance in terms of the entrainment ratio and critical back pressures. A gas dynamic model was used to compare the performance of the present CRMC ejector with different ejector profiles (both conventional and CRMC) working with different fluids. The CRMC ejector showed a slightly better performance in terms of entrainment ratio and compression ratio. When CFD simulations of the present CRMC ejector were compared with a conventional ejector at a similar operating condition, the total pressure of the CRMC ejector remained 15 % larger than the conventional ejector but this higher performance was due to different primary flow shock structures, not due to improvements in the compression process within the diffuser. Differences in the primary flow structure are thought to be caused by the different contraction angle of the secondary flow area. Higher entrainment ratio and compression ratio were simulated for the CRMC ejector relative to the conventional ejector but were not as high as expected from the CRMC design.

To investigate the mixing of the flow within the CRMC ejector, a laser-based visualisation technique was developed. A transparent CRMC ejector test section was designed, fabricated, and operated in the ejector system using air as the working fluid. The laser-based flow visualisation used a laser light beam of diameter of 1 mm to illuminate the seeded secondary flow and thus, the unmixed primary flow was defined. The wall static pressure of the seeded flow agrees well with that of the unseeded flow which indicates that the seeding has a very small effect on the flow. Analysis of the images by digital image processing tools enabled identification of the jet core flow length which was found to lie between 65 mm and 95 mm from the nozzle exit at the selected operating conditions.

The primary and secondary flows entering the CRMC duct are certainly not fully mixed as assumed in the CRMC design prescription. Furthermore, enhancement of the distribution of the wall static pressure and centreline total pressure is not directly attributable to the CRMC prescription. The modest performance improvements associated with the present CRMC design relative to the performance of a conventional duct should be balanced against the added complexity associated with manufacturing a CRMC duct when considering the CRMC design for future applications.

Certification of Thesis

This thesis is entirely the work of Mohamed Al-Safi except where otherwise acknowledge. The work is original and has not previously been submitted for any other award, except where acknowledged.

Student and supervisors signatures of endorsement are held at USQ.

David Buttsworth

Principal Supervisor

Ray Malpress

Associated Supervisor

Acknowledgments

My deepest gratitude goes first and foremost to my supervisors Professor David Buttsworth and Dr Ray Malpress, for their constant encouragement and guidance. They have walked me through all the stages of the writing of this thesis. Without their consistent and illuminating instruction, this thesis could not have reached its present form. Their guidance is of great value to me for helping me so much in building the experimental apparatus and analysing the results.

My thanks also goes to Dr Ahmed Sharrifian for his support. I would like to thank Dr Khalid Saleh for his technical support. I would like to express my gratitude to all those who helped me during the development of this thesis, including the workshop staff and library staff. I would also like to express my gratitude to the fellow lab members who were of so much help in conducting the experiments and providing deep insights and a comfortable environment.

No words can express my gratitude to my family for their support from the time of inception of my dream to the day it was fulfilled. I would also like to acknowledge many who helped me with the thesis both academically and emotionally. I would like to state my deep appreciation for all my friends and colleagues: their friendship and advice were much appreciated. I would like to thank the Ministry of Higher Education in Iraq for this opportunity to accomplish the Doctor of Philosophy degree. Finally, I would also like to thank the Australian Commonwealth Government's contribution to the program fees and for the opportunity to complete my PhD research at USQ.

Mohamed Alsafi

University of Southern Queensland

June 2017

Contents

Abstract **i**

Acknowledgments **iv**

List of Figures **xiv**

List of Tables **xxviii**

Chapter 1 Introduction **1**

1.1 Ejector history and applications 1

1.2 Ejector operation 2

1.3 Constant rate momentum change design 4

1.4 Design optimisation 4

1.5 Scope of study 5

1.6 Overview of the Dissertation 6

Chapter 2 Literature Review **8**

2.1 Introduction 8

2.2 Ejector analytical models 8

2.3 Operating conditions 10

2.4 Nozzle design 12

2.5 Nozzle exit position 18

2.6 Variable geometry ejectors 22

2.7 CRMC Ejectors 25

2.8 Computational fluid dynamics simulations 31

2.9 Flow visualization studies 35

2.10 Chapter Summary 39

Chapter 3 CRMC Ejector theory and design 41

3.1 Introduction 41

3.2 Theory description 42

3.3 CRMC ejector profile 45

3.4 Analytical study 49

3.5 Chapter Summary 52

Chapter 4 Apparatus design 53

4.1 Introduction 53

4.2 Apparatus layout 54

4.3 Primary nozzle 56

4.4 Primary flow line 59

4.5 Secondary flow 61

4.6 Secondary inlet 63

4.7 CRMC ejector duct manufacturing 64

4.8 Measurement arrangement 66

4.8.1 Flow meters 66

4.8.2 Pressure transducers 67

4.8.3 Thermocouples 69

4.9 Data acquisition 70

4.10 Chapter summary 70

Chapter 5 Preliminary tests 72

5.1 Chapter Overview 72

5.2 Flow facility 72

5.3 Preliminary test 78

5.3.1 Setting operating conditions 78

5.3.2 Effect of the nozzle exit position on the ejector performance . . . 80

5.3.3 System stability 81

5.3.4 System repeatability 83

5.4 Uncertainty analysis 85

5.5 Critical back pressure 87

5.6 Chapter Summary 88

Chapter 6 Results, analysis and discussion 90

6.1 Introduction 90

6.2 Operating conditions 91

6.3 Primary pressure effect 93

6.4 Nozzle position effect 97

6.5 Secondary pressure effect 103

6.5.1 On entrainment ratio 103

6.5.2 On achievable back pressure 104

6.6 Wall static pressure 106

6.7 Comparison with previous work 109

6.7.1 Comparison with gas dynamic model 109

6.7.2 Assessment of the validity of the Gas Dynamic Model 112

6.7.3 Comparison of CRMC steam ejectors with the Gas Dynamic Model116

6.7.4 Comparison of CRMC air ejectors with gas Dynamic Model . . . 117

6.8 Chapter Summary 119

Chapter 7 Computational fluid dynamic analysis 122

7.1 Introduction 122

7.2 Turbulence model 123

7.2.1 Turbulence model k-epsilon 123

7.2.2 Turbulence model sst-k-omega 124

7.3 Dimensionless wall distance 125

7.4 Computational simulation 126

7.4.1 Solution convergence 127

7.4.2 Ejector geometry 127

7.4.3 Boundary conditions 128

7.5 Validation of simulation 129

7.5.1 Static pressure: variation with grid density 129

7.5.2 Static pressure: variation with turbulence model 131

7.5.3 Entrainment ratio: variation with grid density 132

7.5.4 Entrainment ratio: variation with turbulence model 133

7.5.5 Summary 135

7.6 Experimental-theoretical-CFD comparison 136

7.6.1 Variation of entrainment ratio 136

7.6.2 Variation of wall static pressure 138

7.6.3 Variation of Mach number 141

7.6.4 Variation of primary pressure 142

7.6.5 Ejector flow modes 146

7.7 Comparison with conventional ejector 150

7.7.1 Arrangement of conventional ejector 150

7.7.2 Total pressure 152

7.7.3 Critical back pressure comparison 154

7.8 Chapter Summary 156

Chapter 8 Flow Visualisation 159

8.1 Introduction 159

8.2 System main components 160

8.2.1 Transparent duct 160

8.2.2 High speed camera 163

8.2.3 Seeding system 164

8.3 Experimental set up 167

8.4 Operating procedures 170

8.5 Experimental results 171

8.6 Core flow length 183

8.7 Chapter Summary 187

Chapter 9 Conclusion and recommendation 189

9.1 Conclusions 189

9.1.1 CRMC ejector 189

9.1.2 Computational simulation 191

9.1.3 Flow visualization 191

9.2 Summary and future work 192

References 194

Appendix A 203

A.1 Primary nozzle 203

A.2 Primary nozzle holder 204

A.3 Spider 205

A.4 Secondary flow pipe 206

A.5 Orifice plate 207

A.6 Entrainment section 209

A.7 Connection section 210

A.8 Condenser pipe 211

A.9 CRMC ejector part 1 212

A.10 CRMC ejector part 2 213

A.11 CRMC ejector part 3 214

A.12 CRMC ejector part 4 215

A.13 CRMC ejector part 5 216

A.14 CRMC ejector part 6 217

Appendix B Instrument calibration 218

B.1 Pressure transducer calibration 218

B.2 Flow meter calibration 221

Appendix C Tables of experimental data 224

List of Figures

1.1 Flow characteristics in a conventional gas or vapour ejector. 3

2.1 Schematic illustration of operation modes and variation of entrainment ratio with the condenser pressure from the work of Pridasawas (2006). . 11

2.2 Variation of system COP with the condensing temperature at different generator temperatures from the work of Dong, Chen, Wang, Kang & Ma (2017). 12

2.3 Conical and petal nozzles geometry from the work of Chang & Chen (2000). 13

2.4 Effective area and expansion angle in the mixing chamber from the work of Chunnanond & Aphornratana (2004). 14

2.5 Lobed nozzle geometry from the work of Opgenorth, Sederstrom, McDermott & Lengsfeld (2012). 15

2.6 Different nozzle shapes computationally tested by Yang, Long & Yao (2012). 16

2.7 Conventional and chevron nozzle used by Kong, Jin, Setoguchi & Kim (2013) 17

2.8 Variation of entrainment ratio with ratio of outlet diameter to the nozzle throat, γ_d, from the work of Fu, Li, Liu, Wu & Wu (2016). 18

2.9 Adjustable nozzle exit position in the conventional ejector from work of Aphornratana & Eames (1997). 19

2.10 Effect of the nozzle exit position on conventional steam ejector performance for primary pressure of 270 kPa and temperature of 130 °C and range of evaporator temperatures from the work of Al-Doori (2013). . . 20

2.11 Effect of nozzle exit position on the conventional steam ejector performance from the work of Dong, Ma & Guo (2013). 21

2.12 Schematic of a variable area ejector from the work of Kim, Lee, Setoguchi & Matsuo (2006). 23

2.13 Configuration of steam ejector with spindle (Ma, Zhang, Omer & Riffat 2010). 24

2.14 Profile of the CRMC ejector duct from the work of Eames (2002). . . . 26

2.15 Pressure and Mach number variation for CRMC ejector from the work of Eames (2002). 27

2.16 Profile of the convergent-divergent throat jet-pump from the work of Worall (2001). 28

2.17 Velocity profile along the CRMC and CPM ejector axis from the work of Seehanam, Pianthong, Behnia, Chunnanond & Aphornratana (2007). 28

2.18 Performance comparison of conventional and CRMC ejectors at different boiler temperatures from work of Chandra & Ahmed (2014). 29

2.19 Ejector geometry and movable primary nozzle from the work of Milazzo, Rocchetti & Eames (2014). 30

2.20 Improved CRMC ejector geometry and its movable primary nozzle from the work of Mazzelli & Milazzo (2015). 30

2.21 Filled contour of Mach number: effect of the condenser pressure on the ejector performance from the work of Sriveerakul, Aphornratana & Chunnanond (2007). 32

2.22 Variation of entrainment ratio with compression ratio for two CFD turbulence models with comparison to experimental data from the work of Hemidi, Henry, Leclaire, Seynhaeve & Bartosiewicz (2009). 33

2.23 Effect of converging duct angle on the contours of Mach number for primary pressure of 2.66 bar and secondary pressure of 0.16 bar from the work of Ji, Utomo, Woo, Lee, Jeong & Chung (2010). 34

2.24 Schlieren image of air flowing from the nozzle into the mixing section at stagnation conditions of 380 kPa and 25 °C from the work of Al-Doori (2013). 36

2.25 Optical device, TSI atomizer and acquisition system used by Desevaux (2001). 37

2.26 Phase averaged PIV flow visualization images showing vortex ring time evolution by Choutapalli (2006). 37

2.27 PIV experimental system used by Bouhanguel, Desevaux, Bailly & Girardot (2012). 38

2.28 Schlieren photographs of shock structures in the mixing chamber. (a) P_p=0.3 MPa, P_s=0.06 MPa; (b) P_p=0.3 MPa, P_s=0.08 MPa; (c) P_p=0.35 MPa, P_s=0.06 MPa; (d) P_p=0.35 MPa, P_s=0.08 MPa from the work of Zhu & Jiang (2014). 38

2.29 Images of shock wave acquired by Nishijimi, Tsuchii & Nakagawa (2016). 39

3.1 Illustration of the CRMC ejector duct and associated features. 45

3.2 Profile of the CRMC ejector duct. 47

3.3 Pressure profile along the CRMC ejector duct at the design point. . . . 49

3.4 Velocity profile along the CRMC ejector duct at the design point, the nozzle exit is at the start of the ejector duct. 50

3.5 Mach number profile along the CRMC ejector duct at the design point, the nozzle exit is at the start of the ejector duct. 51

3.6 Flow characteristic into the CRMC ejector. 52

4.1 Schematic diagram of the CRMC ejector plumbing and instrumentation. 54

4.2 CRMC ejector arrangement with main parts illustrated using solid modelling. 55

4.3 Schematic diagram of the CRMC ejector with main parts illustrated. . . 55

4.4 Profile of the primary nozzle with overall dimensions (all dimensions in mm). 57

4.5 Photograph of the primary nozzle produced by the 3D printer. 58

4.6 Holder of the primary nozzle with main dimensions (all dimensions in mm). 59

4.7 Profile of front view and section of side view of the hub with integral spokes with overall dimensions (all dimensions in mm). 60

4.8 Photograph of the centralising hub with integral spokes. 61

4.9 Secondary flow pipe, part 2 (all dimension in mm). 62

4.10 Secondary flow pipe (part 1) profile of the secondary flow line (all dimension in mm). 63

4.11 Profile of front view and section of side view of the entrainment section with main dimensions (all dimensions in mm). 64

4.12 Model of CRMC ejector part 1. 65

4.13 Photograph of the assembled CRMC ejector. 66

4.14 Correlation between primary stream mass flow rate and primary pressure. 68

4.15 Photograph of assembly of CRMC duct with pressure transducers connected. 69

5.1 Photograph of the experimental apparatus with supporting components: (A) primary supply line, (B) secondary flow control lever, (C) secondary supply line, (D) pressure transducers, (E) data acquisition (F) ejector duct, (G) outlet line connected to vacuum tank (H) outlet connected to secondary vacuum, (I) secondary pressure tappings, (VT) vacuum tank. 73

5.2 Pneumatic dead weight tester in the sub-atmospheric testing arrangement. 74

5.3 Secondary flow temperature recorded from flow meter and thermocouple positioned at the inlet of the secondary line. 76

5.4 Test running time over a range of secondary pressure at primary pressure of 200 kPa. 77

5.5 Test running time over a range of primary pressure at secondary pressure of 2.5 kPa. 77

5.6 Example of stability of the primary pressure during the test time for a nominal primary pressure of 200 kPa. 82

5.7 Example of stability of the secondary pressure during test time for nominal primary pressure of 200 kPa, and nominal secondary pressure of 2 kPa. 83

5.8 Wall pressure distribution for three experimental test results for the same nominal operating conditions of 200 kPa and 1.6 kPa for the primary and secondary pressure respectively. 84

5.9 Entrainment ratio variation with exit pressure for three experimental tests with the same nominal operating conditions of 200 kPa and 1.6 kPa for primary and secondary pressure respectively. 85

5.10 Exit pressure variation during test time at primary pressure of 200 kPa and secondary pressure of 2 kPa. 87

5.11 Secondary pressure variation during test time at primary pressure of 200 kPa. 88

6.1 Nozzle exit position and throat section profile for conventional and CRMC ejectors. 91

6.2 Experimental results for entrainment ratio over a range of exit pressures at 200 kPa primary and secondary pressure of 1.6 kPa. The nozzle exit position is 40 mm. 92

6.3 Variation of entrainment ratio with back pressure at a primary pressure of 200 kPa and a range of secondary pressures, P_s. The nozzle exit position is 40 mm. 93

6.4 Variation of entrainment ratio with back pressure at a primary pressure of 250 kPa and a range of secondary pressure, P_s. The nozzle exit position is 40 mm. 94

6.5 Secondary flow rate variation over a range of primary pressure and secondary pressure. The nozzle exit position is 40 mm. 95

6.6 Entrainment ratio variation over a range of primary pressure and secondary pressure. The nozzle exit position is 40 mm. 95

6.7 Experimental results of entrainment ratio over a range of NXP at primary pressure of 200 kPa and a range of secondary pressure. 98

6.8 Experimental results for entrainment ratio over a range of secondary pressures at primary pressures of 200 kPa, 225 kPa and 250 kPa. 103

6.9 Variation of the back pressure over a range of secondary pressure at primary pressure of 200 kPa and 250 kPa (1): Critical conditions (2): Breakdown conditions. 104

6.10 Entrainment ratio as a function of compression ratio over a range primary pressures. 105

6.11 Variation of entrainment ratio and critical back pressure at different operating conditions. The nozzle exit position is at 40 mm. 106

6.12 Experimental results of wall pressure along the ejector over a range of secondary pressure at primary pressure of 200 kPa. 107

6.13 Experimental results of wall pressure along the ejector over a range of secondary pressure at primary pressure of 225 kPa. 108

6.14 Maximum entrainment ratio variation with expansion ratio for the CRMC ejector performance at different operating conditions compared with the gas dynamic, GD model. 110

6.15 Critical compression ratio variation with expansion ratio for CRMC ejector performance at different operating conditions compared with the gas dynamic model. 112

6.16 Air ejector performance data with comparisons to the gas dynamic modelling for various conventional ejectors: maximum entrainment ratio variation with expansion ratio. 113

6.17 Air ejector performance data with comparisons to the gas dynamic modelling for various conventional ejectors: maximum compression ratio variation with expansion ratio. 114

6.18 CRMC steam ejector performance data with comparisons to the gas dynamic modelling: maximum entrainment ratio variation with expansion ratio. 116

6.19 CRMC steam ejector performance data with comparisons to the gas dynamic modelling: maximum compression ratio variation with expansion ratio. 117

6.20 CRMC air ejector performance data with comparisons to the gas dynamic modelling: maximum entrainment ratio variation with expansion ratio. 118

6.21 CRMC air ejector performance data with comparisons to the gas dynamic modelling: maximum compression ratio variation with expansion ratio. 118

7.1 Primary nozzle profile, all dimensions in mm. 127

7.2 Primary nozzle and CRMC ejector profile, all dimensions in mm. Numbers 1, 2, and 3 refer to primary, secondary, and exit flows respectively. 128

7.3 Comparison of simulated static pressure and experimental data for the three grid resolutions and for operating conditions of primary, secondary, and exit pressure of 200 kPa, 1.6 kPa, and 4.6 kPa respectively. 130

7.4 Meshing of the primary nozzle and a portion of the secondary flow duct. 130

7.5 Comparison between experimental data and CFD simulations of static pressure along the ejector wall for two turbulence models and for operating conditions of primary, secondary, and exit pressure of 200 kPa, 1.6 kPa, and 4.6 kPa respectively. 131

7.6 Comparison of simulated entrainment ratio of three grid resolutions and for primary pressure of 200 kPa, secondary pressure of 1.6 kPa and different back pressure. 133

7.7 Comparison between experimental data and CFD simulations of the entrainment ratio for two turbulence models and for primary pressure of 200 kPa, secondary pressure of 1.6 kPa and different back pressure. . . 134

7.8 Comparison between experimental data and CFD simulations of the entrainment ratio for two turbulence models and for primary pressure of 200 kPa, secondary pressure of 2.5 kPa and different back pressure. . . 135

7.9 Comparison of the entrainment ratio from CFD simulations and experimental data for cases (a) and (b) of Table 7.4. 137

7.10 Comparison of the entrainment ratio from CFD simulations and experimental data for cases (c) and (d) of Table 7.4. 137

7.11 Experimental and CFD results for pressure along the ejector wall at operating conditions of case 1 and case 2. 139

7.12 Theoretical and CFD results for pressure along the ejector axis for case 1.140

7.13 Theoretical and CFD results for pressure along the ejector axis for case 2.140

7.14 Theoretical and CFD results for Mach number along the ejector axis for case 2. 141

7.15 Contours of Mach number in the CRMC ejector showing shocks in the primary stream. 142

7.16 Static pressure distribution along the ejector axis for a range of primary pressure, 1.6 kPa as the secondary pressure, and 4.8 kPa as the back pressure. 143

7.17 Illustration of parameters used to define the sonic surface dimensions. Case illustrated is for the primary pressure of 200 kPa, secondary pressure of 1.6 kPa and exit pressure of 4.8 kPa. 144

7.18 Sonic surface at the primary pressure of (a) 200 kPa, (b) 220 kPa, (c) 230 kPa, (d) 240 kPa, (e) 250 kPa, secondary pressure of 1.6 kPa and exit pressure of 4.8 kPa. 145

7.19 CRMC ejector pressure map and pressure distribution along the axis for 200 kPa, 1.6 kPa, and 4.8 kPa as the primary, secondary, and back pressure respectively. 146

7.20 Velocity vector at primary pressure of 200 kPa and secondary pressure of 1.6 kPa, and 4.8 kPa as exit pressure. 147

7.21 Velocity stream lines of primary flow at operating conditions of 200 kPa as a primary pressure and secondary pressure of (a) 1.6 kPa, (b) 2.5 kPa, (c) 4 kPa, (d) 5 kPa. 148

7.22 Velocity map at primary pressure of 200 kPa, secondary pressure of 1.6 kPa, and 5.2 kPa as back pressure. 149

7.23 Velocity map at primary pressure of 200 kPa and secondary pressure of 1.6 kPa,and 5.5 kPa as exit pressure. 150

7.24 Conventional ejector geometry (all dimensions in mm), numbers 1, 2, 3, refer to primary, secondary, and exit flows respectively. 151

7.25 Conventional ejector pressure map and pressure distribution along the axis for 200 kPa, 1.6 kPa, and 4.8 kPa as the primary, secondary, and exit pressure respectively. 152

7.26 Total pressure distribution for the CRMC and a conventional ejector along the axis at primary pressure of 200 kPa, secondary pressure of 1.6 kPa, and back pressure of 4.8 kPa. 153

7.27 Ejector profiles for the conventional and CRMC ejectors (all dimensions in mm). 154

7.28 Pitot pressure and total pressure distribution in the CRMC and conventional ejectors at distance of 60 mm downstream of the primary nozzle. 155

8.1 Photograph of the parts used to create the mould to cast the transparent duct: a. inner parts b. outer parts. 160

8.2 Photograph of the assembled parts used to create the mould to cast the transparent duct: a. inner part b. outer part. 161

8.3 Photograph of a. mould b. mould inside encasing shield. 162

8.4 Photograph of the transparent ejector duct. 163

8.5 Micrograph of talc powder as loaded into the seeding system. 165

8.6 Micrograph of talc powder as delivered from the seeding system. 166

8.7 3D solid model of the seeding system. 167

8.8 Ejector apparatus schematic diagram for flow visualization. 168

8.9 3D sketch of the transparent ejector and flow visualization system. . . . 169

8.10 Photograph of the transparent ejector and flow visualization system. . . 169

8.11 Photo of the first section of the ejector during flow (the axial and radial distances are in pixel, 1 mm=17 pixel). 170

8.12 Static pressure plots along the ejector for seeded and unseeded flow at 200 kPa, 1.6 kPa and 4.8 kPa as the primary, secondary and back pressures respectively. 172

8.13 Photo of the first section of the ejector prior to testing. 173

8.14 Intensity variation within the ejector duct at locations between 2 and 75 mm from the nozzle exit at 190 kPa, 1.6 kPa and 4.5 kPa as a primary pressure, secondary pressure and back pressure respectively. 175

8.15 Intensity variation within the ejector duct at locations between 80 and 155 mm from the nozzle exit at 190 kPa, 1.6 kPa and 4.5 kPa as a primary pressure, secondary pressure and back pressure respectively. 176

8.16 Intensity variation within the ejector duct at locations between 2 and 75 mm from the nozzle exit at 200 kPa, 1.6 kPa, 4.8 kPa as a primary, secondary pressure and back pressure respectively. 177

8.17 Intensity variation within the ejector duct at locations between 80 and 155 mm from the nozzle exit at 200 kPa, 1.6 kPa and 4.8 kPa as a primary, secondary pressure and back pressure respectively. 178

8.18 Intensity variation within the ejector duct at locations between 2 and 75 mm from the nozzle exit at 210 kPa, 1.6 kPa and 5.2 kPa as a primary pressure, secondary pressure and back pressure respectively. 179

8.19 Intensity variation within the ejector duct at locations between 80 and 155 mm from the nozzle exit at 210 kPa, 1.6 kPa and 5.2 kPa as a primary pressure, secondary pressure and back pressure respectively. 180

8.20 Intensity variation within the ejector duct at locations between 2 and 75 mm from the nozzle exit at 220 kPa, 1.6 kPa and 5.7 kPa as a primary pressure, secondary pressure and back pressure respectively. 181

8.21 Intensity variation within the ejector duct at locations between 80 and 155 mm from the nozzle exit at 220 kPa, 1.6 kPa and 5.7 kPa as a primary pressure, secondary pressure and back pressure respectively. 182

8.22 Composite image of the flow at 200 kPa and 1.6 kPa as a primary and secondary pressure respectively (dimensions in mm). 183

8.23 Visualisation intensity data of flow for operating conditions of 200 kPa, 1.6 kPa and 4.8 kPa as a primary, secondary and back pressures respectively. . . . 184

8.24 Jet flow core diameter at different locations from the nozzle exit for range of primary and back pressures and 1.6 kPa as a secondary pressure. 185

8.25 Simulation of the turbulent kinetic energy along the ejector centreline for operating condition of 190 kPa, 1.6 kPa as primary and secondary pressures respectively. . . . 186

8.26 Jet core length for a range of primary pressure. . . . 187

A.1 Profile of the primary nozzle with overall dimensions, all dimensions in mm. . . . 203

A.2 Profile of the primary nozzle holder with overall dimensions, all dimensions in mm. . . . 204

A.3 Profile of the hub with integral spokes with overall dimensions, all dimensions in mm. . . . 205

A.4 Profile of the secondary flow pipe part 1 with overall dimensions, all dimensions in mm. . . . 206

A.5 Profile of the secondary flow pipe part 2 with main dimensions, all dimensions in mm. . . . 207

A.6 Profile of the orifice plate with main dimensions, all dimensions in mm. 208

A.7 Profile of the entrainment section with main dimensions, all dimensions in mm. . . . 209

A.8 Profile of the connection section with main dimensions, all dimensions in mm. . . . 210

A.9 Profile of the exit section with main dimensions, all dimensions in mm. . 211

A.10 Profile of the part 1 of CRMC ejector with main dimensions, all dimensions in mm. 212

A.11 Profile of the part 2 of CRMC ejector with main dimensions, all dimensions in mm. 213

A.12 Profile of the part 3 of CRMC ejector with main dimensions, all dimensions in mm. 214

A.13 Profile of the part 4 of CRMC ejector with main dimensions, all dimensions in mm. 215

A.14 Profile of the part 5 of CRMC ejector with main dimensions, all dimensions in mm. 216

A.15 Profile of the part 6 of CRMC ejector with main dimensions, all dimensions in mm. 217

B.1 Photograph of the pneumatic dead-weight tester model 550 series (Budenberg). 219

B.2 Photograph of the hydraulic dead-weight tester model 580 series (Budenberg). 219

B.3 Calibration of the Wika high pressure transducer-representative results. 220

B.4 Calibration of the Wika low pressure transducer-representative results. . 220

B.5 Calibration of the Omega flow meter-representative results. 222

B.6 Correlation of the flow rate and the pressure in the primary stream-representative results. 223

List of Tables

3.1 Ejector design parameters with the working fluid being air. 46

3.2 Flow conditions and dimensions of the designed CRMC duct. 48

4.1 Main specifications of 3D printer Type ProJet$^{\mathrm{TM}}$HD 3500. 57

4.2 VisiJet material specifications 58

4.3 Flow meter FMA-2600A-OMEGA specifications 67

4.4 Major specifications of three types of pressure transducers 69

5.1 Calibration of Wika and Sensortechnics GmbH pressure transducers. V_{meas}= measured voltage. Voltage in Volt, and pressure in kPa. 75

5.2 Results for nominal primary pressure of 200 kPa and nominal secondary pressure of 1.6 kPa. 80

5.3 Uncertainty analysis for the ejector experimental work. 86

6.1 calculated static pressure values at the primary nozzle exit. 97

6.2 Data from experiments with different nozzle positions and a nominal primary pressure of 200 kPa for a range of secondary and back pressures conditions. Primary mass flow rate was 3.58 g/s for the nominal primary pressure of 200 kPa. 100

6.3 Data of experimental with different nozzle positions and a nominal primary pressure of 225 kPa for a rage of secondary and back pressures conditions. Primary mass flow rate was 3.89 g/s for the nominal primary pressure of 225 kPa. 101

6.4 Data of experimental with different nozzle positions and a nominal primary pressure of 250 kPa for a range of secondary and back pressures conditions. Primary mass flow rate was 4.25 g/s for the nominal primary pressure of 250 kPa 102

6.5 Isentropic Mach number at the location of lowest measured wall static pressure for primary pressure of 200 kPa and 225 kPa and range of secondary pressure. 109

6.6 Entrainment ratio, expansion ratio, pressure lift ratio and breakdown pressure for various conventional ejectors working with air. 115

6.7 Entrainment ratio, expansion ratio, pressure lift ratio and breakdown pressure for various CRMC ejectors working with steam and air. 119

7.1 Different mesh resolutions used in the simulations. 126

7.2 Average error in simulation of the static pressure: comparison of different turbulence models. 132

7.3 average error for entrainment ratio simulations for different turbulence models from Figure 7.8. 135

7.4 Ejector operating conditions in the 4 cases presented in Figures 7.9 and 7.10. 138

7.5 Ejector operating conditions for experimental-analytical-CFD comparison. 138

7.6 Sonic surface dimensions at different primary pressures, a secondary pressure of 1.6 kPa and an exit pressure of 4.8 kPa. 145

7.7 Calculated values for the pitot and total pressure. 156

8.1 OLYMPUS® $i - SPEED\,3$ high speed camera specification. 164

8.2 Powder consumption during the experiments for a range of primary pressures and a secondary pressure of 1.6 kPa. P_p, $\dot{m}_s$, t, m, $\dot{m}$ refer to primary pressure, secondary mass flow rate, test time, powder consumption and powder mass flow rate respectively. 172

B.1 Calibration of Wika low pressure transducers. V_{meas}= measured voltage. Voltage in Volt, and pressure in kPa. 221

C.1 Data from experiments with different nozzle positions and a nominal primary pressure of 200 kPa for a range of secondary and back pressures conditions. Primary mass flow rate was 3.58 g/s for the nominal primary pressure of 200 kPa. 225

C.2 Data of experimental with different nozzle positions and a nominal primary pressure of 225 kPa for a rage of secondary and back pressures conditions. Primary mass flow rate was 3.89 g/s for the nominal primary pressure of 225 kPa. 226

C.3 Data of experimental with different nozzle positions and a nominal primary pressure of 250 kPa for a range of secondary and back pressures conditions. Primary mass flow rate was 4.25 g/s for the nominal primary pressure of 250 kPa. 227

C.4 Data of experimental with different nozzle positions and a nominal primary pressure of 270 kPa for a range of secondary and back pressures conditions. Primary mass flow rate was 4.55 g/s for the nominal primary pressure of 270 kPa. 228

Chapter 1

Introduction

1.1 Ejector history and applications

Ejectors are known as vacuum jets, jet pumps or thermo-compressors for different applications, and the working fluid may be a liquid or gas. These devices have been used extensively in the power generation and chemical processing industries for nearly a century. Ejectors also have applications in nuclear, distillation, vacuum evaporation and drying processes and the ability to handle highly corrosive vapours and fluids. The first wave of popularity of ejector refrigeration systems came in the early 1930s for the air conditioning of large buildings. However, mechanical vapour compression refrigeration systems were ultimately favoured due to their higher COP, smaller volume and reliable operation.

Recently, cooling technology interests have begun to realign with the ejector refrigeration system due to the rising cost of energy and the decreasing availability of energy resources. In addition, as incentives to protect the environment have grown, ejectors are becoming more popular in industrial fields because of associated energy savings and emission reduction (Sun & Eames 1995) and thus, the system has again become an attractive subject.

Ejectors have no moving or complicated parts, and so are easy to maintain and ejectors operate reliably with low capital and maintenance cost compared with conventional pumps or compressors. In addition, as an environmentally friendly alternative to traditional refrigerants, water vapour can be used as a working fluid in ejector refrigeration systems, providing an environmental protection factor. Ejectors have promising applications in energy savings due to their ability to utilize waste or low grade thermal energy.

1.2 Ejector operation

Figure 1.1 illustrates a conventional gas or vapour ejector and its flow characteristics. The ejector system is made up of the primary nozzle and mixing section, the secondary throat or constant area section and the subsonic diffuser. The high pressure primary flow (PF) enters the nozzle at (plane P) and starts to accelerate as it enters the nozzle convergent section and reaches the sonic condition at the nozzle throat (plane 1). While expanding through the nozzle divergent section, the velocity of primary flow increases. Due to the velocity increase, a low pressure region at the nozzle exit plane (plane 2) is created.

The motive flow (primary flow) draws the secondary fluid into the mixing section (plane 2) through the action of the mixing between the high speed primary flow and the initially lower speed secondary flow. The secondary flow is accelerated and matches the primary flow pressure at some point downstream (nominally the nozzle exit at plane 2), and the two streams mix as they move downstream. A compression effect occurs in a series of shocks induced at the ejector throat or constant area section (between plane 3 and plane 4), this effect is illustrated at the very end of the constant area section. When the mixed stream passes through the subsonic diffuser, and possibly due to the action of additional shock waves, the velocity of the mixture decreases and reaches a subsonic level and further compression is achieved. Finally, the mixed flow leaves the ejector at position (E) at which point it is pressurised close to the exit pressure.

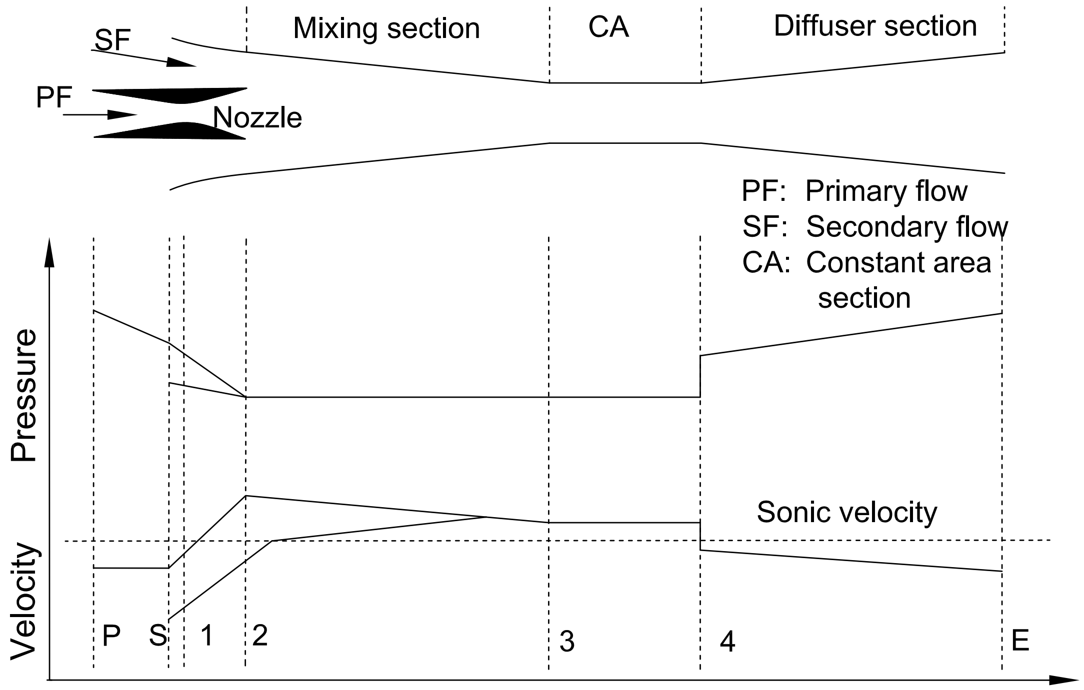

Figure 1.1: Flow characteristics in a conventional gas or vapour ejector.

The most significant parameter in ejector design is the entrainment ratio, ER which is defined as:

$$ER = \frac{\dot{m}_s}{\dot{m}_p} \tag{1.1}$$

where $\dot{m}_s$ is defined as the mass flow rate of the secondary stream, and $\dot{m}_p$ is the mass flow rate of the primary stream. In an ejector refrigeration cycle, an approximation for the coefficient of performance (COP) is sometimes used (Ruangtrakoon et al. 2012) is

$$COP \approx ER \tag{1.2}$$

The ratio of the exit pressure to the secondary pressure, which is called the pressure lift ratio (PLR) or compression ratio (CR), is the second key parameter used to evaluate the ejector performance

$$CR = \frac{P_c}{P_s} \tag{1.3}$$

where P_c is the ejector exit flow pressure, and P_s is the secondary flow pressure. In addition, the stagnation pressure ratio (SPR) which represents the ratio of the primary flow stagnation pressure to the secondary flow stagnation pressure also plays a significant role in ejector performance.

1.3 Constant rate momentum change design

The geometric configuration of a supersonic ejector has a significant effect on the ejector performance (Sun 1996, Chunnanond & Aphornratana 2004, Ruangtrakoon et al. 2012). A number of researchers have investigated the effect of ejector geometry on ejector performance. For example, they have investigated the effect of convergence and divergence angles, length and diameter of the constant area section, nozzle position and entrained flow entrance geometry. Varying degrees of success in augmentation of ejector performance have been achieved through many previous studies. However, significant improvement in ejector performance is yet to be obtained.

Performance improvements might be possible through improved designs that reduce pressure losses associated with the mixing process (Sun 1996) and methods to reduce pressure losses in the diffuser are also important. The constant rate of momentum change (CRMC) duct profile was proposed by Eames (2002) in an attempt to eliminate the shock-induced pressure losses that occur in a conventional ejector. In this design, it is assumed that the mixed flow undergoes a shock-less diffusion as it moves through a non-uniform cross sectional area ejector duct that causes its momentum to vary at a constant rate. Several authors have subsequently investigated the CRMC design and varying degrees of performance improvements relative to conventional ejector design have been reported (Worall (2001), Kumar, Singhal & Subbarao (2013), Mazzelli & Milazzo (2015)). The conditions under which performance improvements can be expected from the CRMC design are yet not clear.

1.4 Design optimisation

For many years computational fluid dynamics (CFD) has provided valuable information to assist in defining the optimum operating conditions for supersonic ejectors

(Riffat & Everitt 1999). CFD can be used to study the effects of compressibility and turbulence of the flow structure inside the proposed ejector and to examine the effects of operating conditions and nozzle exit position on the performance of the ejector. CFD can also be used for visualisation of ejector characteristics in a cost and time effective way. Although the quality and accuracy of CFD simulations of ejector performance varies from study to study, it is generally agreed that CFD can make an important contribution to ejector design optimisation (Little & Garimella 2016).

Flow visualisation inside the ejector has been used in a limited number of applications to validate existing CFD and provide qualitative information related to ejector flow. Capturing some effects of the ejector flow may not be possible with available computational, analytical and experimental tools. The mixing process inside the ejector is the area of highest uncertainty that impacts the entrainment ratio and compression ratio and a full understanding has not been achieved due to difficulties associated with the measurement of this complex flow behaviour. Non-intrusive visualisation techniques could provide visualisation of the mixing flow behaviour inside the proposed ejector enabling improved understanding of the mixing process, and therefore could ultimately improve the design of ejectors (Little & Garimella 2016).

1.5 Scope of study

Methods of CFD and flow visualisation are applied to an ejector design using the CRMC prescription to assess its performance and enhance the understanding of the CRMC design within the context of conventional ejector duct performance. The following tasks have been completed.

- Design, fabricate and commission an open system air ejector based on CRMC theory, suitable for flow visualisation studies.
- Develop flow seeding and laser-based visualisation methods suitable for the CRMC ejector.
- Acquire new data which provides additional insight into the ejector mixing and compression process within the CRMC ejector.

- Compare the performance of a conventional ejector geometry with the proposed CRMC geometry and determine if changes to the characteristics of the shocks are a contributor to performance changes.

- Evaluate the CRMC ejector relative to different types of ejectors using different working fluids.

Although the work seeks to make contributions to the understanding of CRMC and other ejectors for the purpose of improving their performance, the chosen operating conditions for the air ejector reflect the pressure ratios encountered by steam ejectors used in refrigeration applications.

1.6 Overview of the Dissertation

This dissertation is arranged in the following chapters:

Chapter 1 Introduction to the supersonic ejector, and scope of the present study.

Chapter 2 This chapter presents a review of previous studies that focused on conventional and variable area ejector design and operation, experimental, computational, and flow visualization studies.

Chapter 3 This chapter describes how the CRMC theory is employed in this work. An analysis of the design is also presented in this chapter.

Chapter 4 An overview of the apparatus design and fabrication of the CRMC ejector duct is presented in this chapter. Pressure, temperature, and flow measuring devices are also introduced in this chapter.

Chapter 5 Preliminary experimental work which includes the system stability, system repeatability and uncertainty of measuring tools is presented in this chapter. The effect of the variation of the nozzle exit position on the ejector performance is also presented.

Chapter 6 The experimental data is presented and discussed in this chapter. Results illustrate the effect of operating conditions such as primary, secondary, and exit pressures on the ejector performance. Results for the entrainment ratio and pressure distribution along the ejector wall are presented.

Chapter 7 Computational analysis including the simulation of the ejector using CFD and comparison with experimental data is presented in this chapter.

Chapter 8 This chapter presents the flow visualisation technique and the design and fabrication of the transparent duct and particle seeding system. Image processing and data analysis which presents the flow behaviour inside the ejector, are also presented in this chapter.

Chapter 9 This chapter includes the overall conclusion and presents recommendations for future work.

Chapter 2

Literature Review

2.1 Introduction

Many theoretical and experimental studies have been completed in efforts to understand the fundamentals of ejector operation and to understand the effect of various parameters on performance. Ejectors were first applied in 1901 (ASHRAE 1986) for removing air from a steam engine's condenser. Since then, researchers have focused their efforts to improve the performance of the ejector utilised in a variety of application such as refrigeration, pumping and evacuation systems.

The review describes and evaluates the development of the different aspect of design, fabrication, and operation of the ejector up to the present. Previous analytical, computational, experimental, and flow visualization studies are included.

2.2 Ejector analytical models

Application of ejectors in the first attempt to develop the ejector-driven refrigeration system by Le Blank and Parsons occurred in 1901 (ASHRAE 1986). It was quickly realised that the performance of the ejector played a crucial role in the performance of the refrigeration system, promoting research into ejector characteristics.

Keenan (1950) performed a theoretical study of ejectors and classified them into two categories according to the position of the nozzle: (1) Constant-Area Mixing (CAM) method which means that the nozzle exit is located within the ejector constant-area section and the mixing of the primary and the secondary flows occurs inside the constant-area section; (2) Constant-Pressure Mixing (CPM) method which means that the nozzle exit is located within the suction chamber which is in front of the constant-area section and the mixing process occurs at constant pressure. The results from the Keenan (1950) investigation was that CPM gives a better performance than the CAM ejector and is thus widely used. In Keenan (1950) paper, one-dimensional continuity, momentum, and energy equations were used for the first time to analyse the ejector operation. The author is considered as the founder of ejector analysis theory. However, this theory is unable to predict the phenomenon that produces the well known constant capacity characteristics of ejector flow, in which the entrainment ratio remains constant until the condenser pressure increases to a point (the critical operation point) at which the secondary flow is no longer choked.

Munday & Bagster (1977) proposed a theory to describe stream choking effects. The authors assumed the presence of an effective area (annulus area formed between the primary jet core and the ejector walls) for the secondary flow to account for this phenomenon. This area according to their theory, remains constant and independent of the ejector exit pressure downstream.

Eames, Aphornratana & Haider (1995) presented theoretical and experimental studies of a small-scale steam-jet refrigerator and introduced a theoretical model including irreversibility associated with the primary nozzle, the mixing chamber and the diffuser. This model was based on a constant-pressure mixing process, but without considering the choking of the secondary flow.

Huang et al. (1999) analysed the operation of 11 different ejectors working with R141b and further developed Keenan's model by assuming:

- A hypothetical throat occurs inside the constant area section to allow the secondary flow to pass and reach a choked condition.
- A mixing process between primary and secondary flow starts at the hypothetical

throat and continues with constant pressure.

- A shock will occur at the end of the constant area section leading to a sudden pressure rise.

The results attained by Huang et al. (1999) demonstrated good agreement with experiments. However, the ejector modelling assumption would not be applicable to all ejector configurations.

2.3 Operating conditions

Sun (1997) investigated the performance characteristics of an open steam jet refrigeration system. The operating conditions of the system were between 95 ^{o}C and 135 ^{o}C for the generator temperatures and between 5 ^{o}C and 15 ^{o}C as the evaporator temperatures. The results illustrate that increasing generator temperature initially causes an increase in the entrainment ratio, but further generator temperature rise causes entrainment ratio to decrease. In addition, the results show that increasing the evaporator temperature leads to improving system performance. It was concluded that the evaporator temperature has a significant impact on the ejector performance.

A closed steam ejector refrigeration system was experimentally studied by Chunnanond & Aphornratana (2004). Three primary nozzle throat diameters, 0.5 mm, 1.75 mm, and 2 mm were used in this work. The boiler temperature ranged between 120 ^{o}C and 140 ^{o}C, while the evaporator temperature ranged between 5 ^{o}C to 15 ^{o}C. The author concluded that super heating of the primary flow does not have a significant effect on the system performance or the critical condenser pressure. Furthermore, the study showed the system performance declines as the primary pressure increases for a given secondary pressure.

Pridasawas (2006) studied the influence of the exit pressure on the entrainment ratio as in Figure 2.1 which shows three ejector operation modes: double choked, single choked, and unchoked mode.

- When the condenser pressure is lower than the critical pressure and both primary and secondary flows are choked, highest ejector performance can be obtained. This region is called the "critical mode" and "double-choking" occurs.

- The ejector performance dropped when the exit pressure increased beyond the critical pressure value and only the primary flow is choked. Thus, the entrainment ratio decreases as the back pressure increases. This region is called the "subcritical mode" and "single-choking" occurs.

- The ejector stops working when the back pressure exceeds a specific value. As the back pressure continues to increase, back-flow occurs through the secondary flow line. This region is referred to as the "back-flow mode" and ejector "malfunction" occurs.

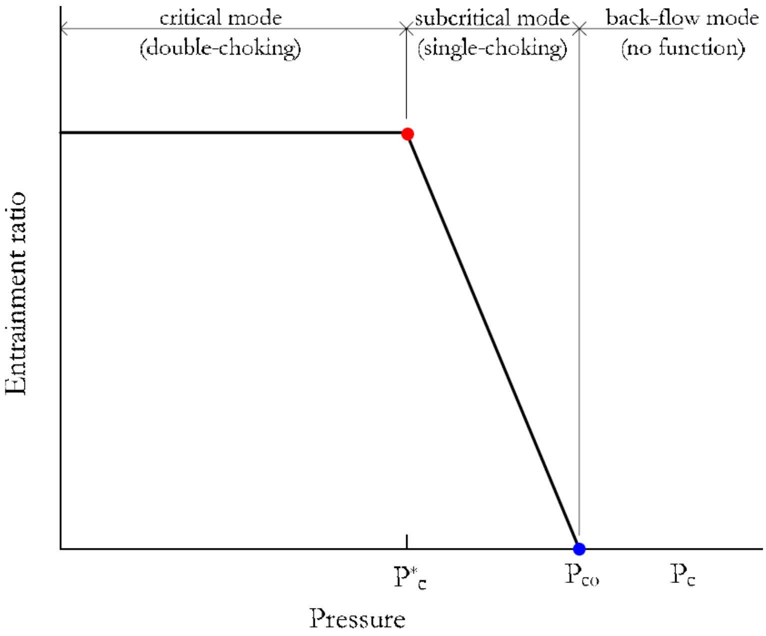

Figure 2.1: Schematic illustration of operation modes and variation of entrainment ratio with the condenser pressure from the work of Pridasawas (2006).

Meyer, Harms & Dobson (2009) tested a 2.5, 3, and 3.5 mm primary nozzle throat diameter in an open system ejector configuration using steam and operated with a temperature range of 85 ^oC to 140 ^oC as the primary flow stagnation temperature, 5 ^oC to 10 ^oC as a secondary flow stagnation temperature, and 5.63 kPa as an exit pressure. The study illustrated that the ejector works well at primary flow temperatures below

100 ^{o}C and concluded that the primary flow temperature, secondary flow temperature, exit pressure, and the primary nozzle exit position have a significant effect on the ejector performance.

Dong et al. (2017) developed and tested a steam ejector refrigeration system in order to assess its ability to function properly in refrigeration applications with extra low-temperature heat sources below 40 ^{o}C. The working performance of the steam ejector at generating temperatures ranging from 40 ^{o}C to 70 ^{o}C was also investigated. The study concluded that the configuration can operate successfully at this range of low temperatures as illustrated in Figure 2.2

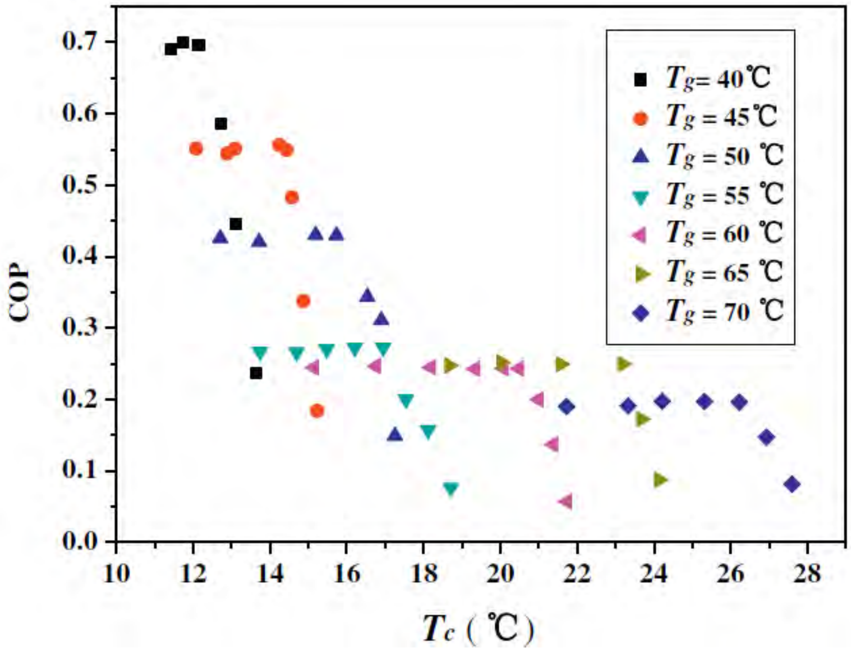

Figure 2.2: Variation of system COP with the condensing temperature at different generator temperatures from the work of Dong et al. (2017).

2.4 Nozzle design

Chang & Chen (2000) proposed a novel petal nozzle as illustrated in Figure 2.3 to enhance the performance of a steam jet refrigeration system. Experimental results from this study show that the entrainment ratio and the COP of the system with a petal nozzle are better than that with a conical nozzle used in typical ejector refrigeration cycle when operated at larger area ratios (constant area section to nozzle throat area). In addition, the author experimentally demonstrated that more efficient mixing can be achieved by using this kind of nozzle and that more kinetic energy can be recovered to enhance the back pressure. The suggested nozzle is similar in many characteristics to that of a conical nozzle but could operate with higher pressure ratio. Its complicated shape adds complexity to fabrication which detracts from any positive characteristics of performance.

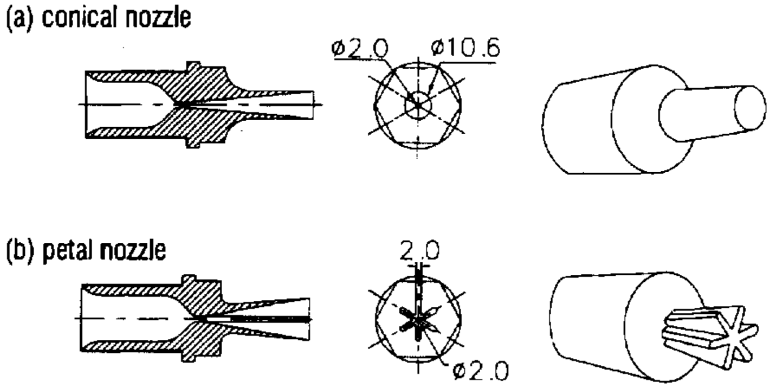

Figure 2.3: Conical and petal nozzles geometry from the work of Chang & Chen (2000).

Chunnanond & Aphornratana (2004) investigated the effect of nozzle geometry and position on the performance of steam ejector refrigeration. In this study, the authors indicated that using either a smaller nozzle or moving the nozzle away from the mixing chamber could increase the ejector entrainment ratio. They assert this may occur because withdrawing the nozzle provides a larger effective area allowing a larger entrained secondary flow as in Figure 2.4. In addition, the study illustrated that the presence of super heated steam has no effect on the system performance other than to avoid ejector erosion damage by wet motive steam.

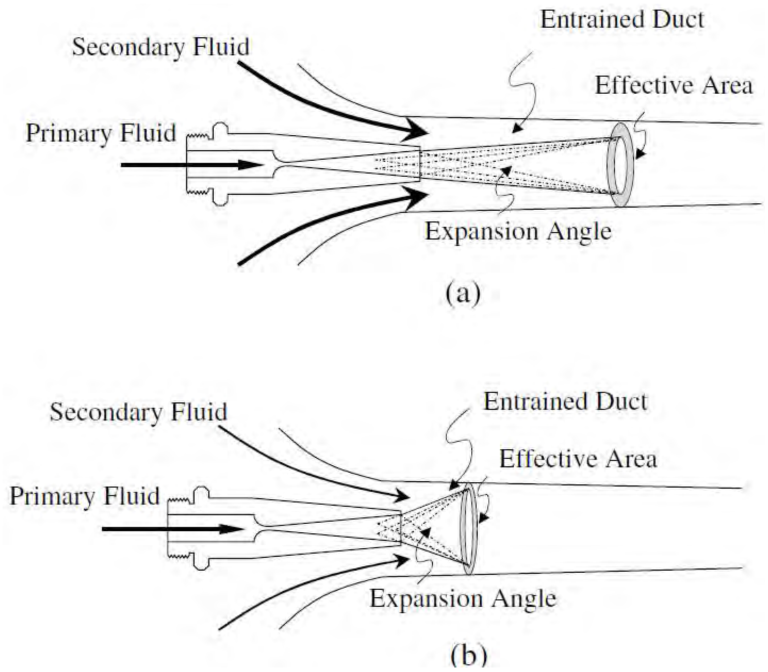

Figure 2.4: Effective area and expansion angle in the mixing chamber from the work of Chunnanond & Aphornratana (2004).

Chaiwongsa & Wongwises (2008) used R134a as a working fluid to study the influence of the nozzle outlet diameter on ejector efficiency. The study analysed various nozzle outlet diameter (2 mm, 2.5 mm, 3 mm) and concluded that using nozzles with different outlet diameter has little effect on system performance and the 2 mm nozzle diameter produces the best performance.

Park (2009) introduced a swirled motive flow thermal vapour compressor as a new attempt to enhance its entrainment performance by letting the motive steam flow into the primary nozzle with a swirl component. The author used various swirl angles to investigate the influence of the swirl motion on the ejector entraining performance. The study concluded that the swirled motive flow increased the entrainment ratio by 2% compared with the no swirl ejector.

Opgenorth et al. (2012) focused on the reduction of the primary fluid flow rate required to obtain higher entrainment ratio at a given secondary flow and increasing the total pressure recovery. Designs for supersonic ejectors in refrigeration applications aiming to improve the performance by enhancing mixing process were introduced. Flow instability and vortices for mixing were created by adding lobes to the circular nozzle design as in Figure 2.5. The study demonstrated that an optimum number of lobes exists to achieve an effective way to improve the mixing process between the entrained flow and the motive flow. The best compression ratio achieved by this study was 6.25 compared to 4 for the circular nozzle. However, the complex design of the lobed nozzle is considered the main limitation of this configuration.

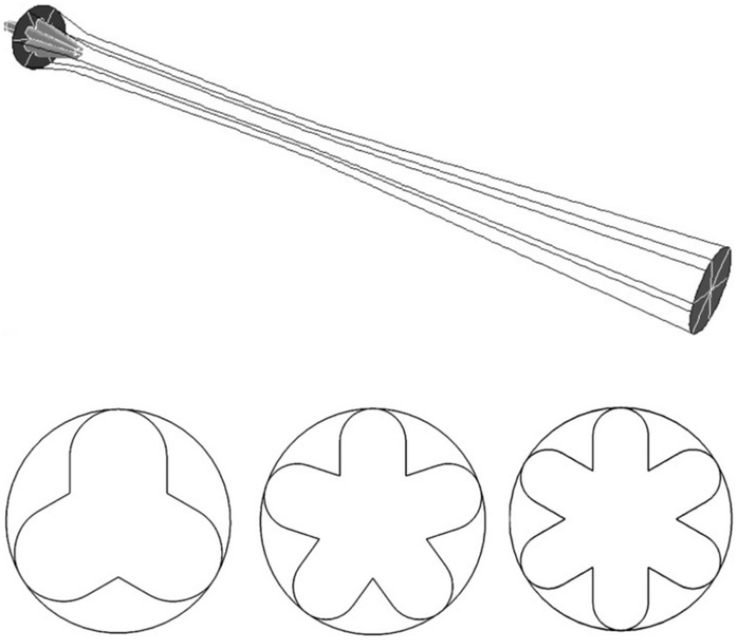

Figure 2.5: Lobed nozzle geometry from the work of Opgenorth et al. (2012).

Yang et al. (2012) numerically studied the effects of different nozzle structures on the performance of steam ejectors using a computational fluid dynamics (CFD) technique which revealed the stream-wise vortex and span-wise vortex distributions in the mixing chamber in lobed jet mixing flow. The study investigated the performance of five different nozzle structures, namely, conical, elliptical, square, rectangular and cross-shaped nozzles under similar operating conditions as in Figure 2.6. It was found that the entrainment ratio of the ejector equipped with the conical nozzle was better than the other nozzles but the conical nozzle achieved a lower critical back pressure than the square and the cross-shaped nozzles.

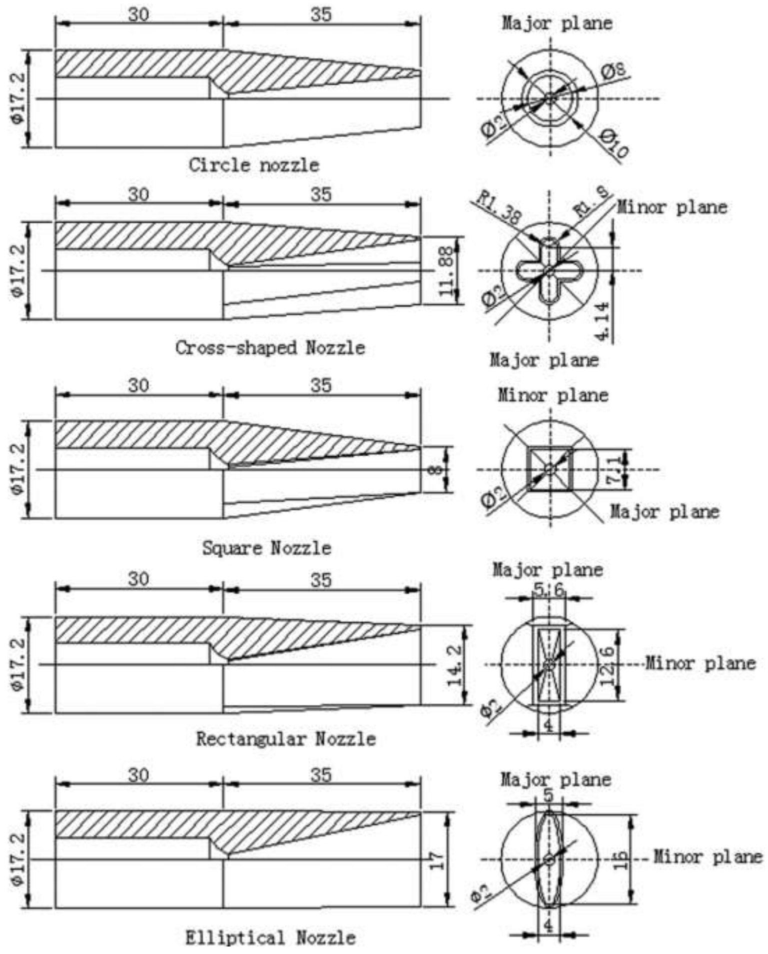

Figure 2.6: Different nozzle shapes computationally tested by Yang et al. (2012).

The study pointed out that a higher entrainment ratio can be achieved by efficient mixing due to the interactions between the stream wise vortex and the span wise vortex. In addition, when the vortices contact the inner wall of the mixing chamber, the effective area (the area between the primary nozzle jet core and the ejector inner wall which the secondary flow passes through) reduces and energy losses increase. Consequently, significant decrease in both the entrainment ratio and critical back pressure occurs. Lin et al. (2013) used a CFD technique to investigate the optimum geometry of the adjustable ejector. Several important geometrical parameters including primary nozzle diverging angle, constant pressure mixing section length, primary nozzle exit position, and converging angle of the constant pressure mixing chamber were modelled using CFD and experimentally validated. The study concluded that the primary nozzle diverging angle and the length of the constant pressure mixing section parameters are most sensitive to the variations in the flow conditions and the pressure recovery properties than other parameters.

A comparison between a chevron nozzle and conventional nozzle as illustrated in Figure 2.7 and an assessment of their effect on the ejector performance was numerically performed by Kong et al. (2013). The Chevron nozzle shows the better results: entrainment ratio was improved 14.8 % on average, and the maximum improvement was 21.8 %. At the same time, pressure recovery was increased 8.5 % on average. The study concluded that the chevron nozzle shows better results in both the entrainment ratio and compression ratio, even with a smaller primary stream mass flow rate.

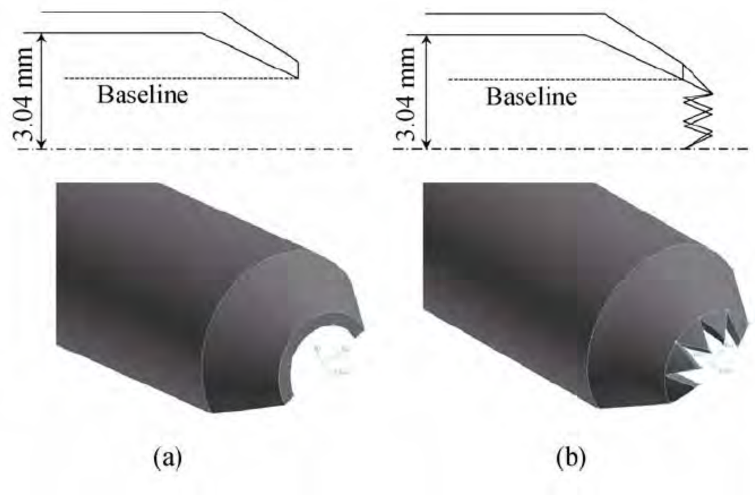

Figure 2.7: Conventional and chevron nozzle used by Kong et al. (2013)

.

Using different nozzle shapes could improve the mixing process in the ejector and therefore enhance the ejector performance. However, using these configurations in ejector system is limited by their complicated construction and high manufacturing costs.

Fu et al. (2016) investigated numerically the influences of primary nozzle characteristic on a steam ejector's performance. The effects of the primary nozzle outlet diameter as well as the divergent section length under different secondary pressures on a steam ejector were reported. The study revealed that for given operation conditions with other geometry parameters of the steam ejector unchanged, the ratio of the nozzle outlet diameter, γ_d to the nozzle throat has a very strong influence on the entrainment ratio of the ejector as in Figure 2.8.

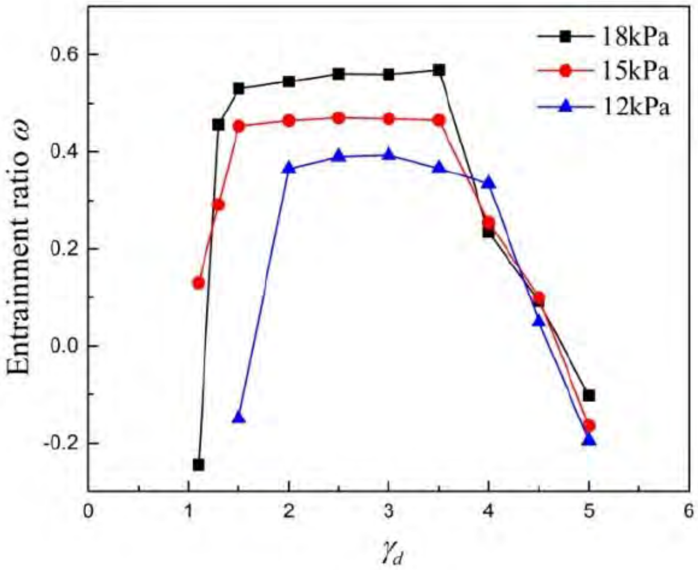

Figure 2.8: Variation of entrainment ratio with ratio of outlet diameter to the nozzle throat, γ_d, from the work of Fu et al. (2016).

2.5 Nozzle exit position

Watanabe (1972) experimentally studied the effect of the nozzle exit position on the constant area ejector performance. The study demonstrated that a maximum entrainment ratio could be achieved by positioning the primary nozzle at the optimum position within the mixing section. Vyas & Kar (1975) conducted a limited study to examine the effect of the nozzle exit position on the ejector efficiency. The study concluded that moving the nozzle exit position away from the mixing section entrance could actually cause a significant reduction in entrainment ratio.

The ESDU (1986) design guide suggests that the nozzle should be placed at a distance of 0.5 to 1.0 times length of the mixing chamber's throat diameter upstream of the mixing chamber inlet. However, because of the complex nature of the flow structure, it is difficult to give precise recommendations for the optimum nozzle position.

To provide more flexible operation than a totally fixed geometry ejector, Aphornratana

& Eames (1997) introduced a configuration with a manually adjustable primary nozzle to investigate the influence of changing the nozzle exit position on the ejector performance. The COP of the system and the cooling capacity decreased by moving the primary nozzle downstream, into the mixing section, positive values on NXP as illustrated in Figure 2.9. On the other hand, when the nozzle was retracted from the mixing chamber, the COP and cooling capacity increased, but at expense of critical back pressure. The study showed that a single optimum primary nozzle exit position cannot be achieved to meet all operating conditions and each operating condition requires a particular optimum nozzle position.

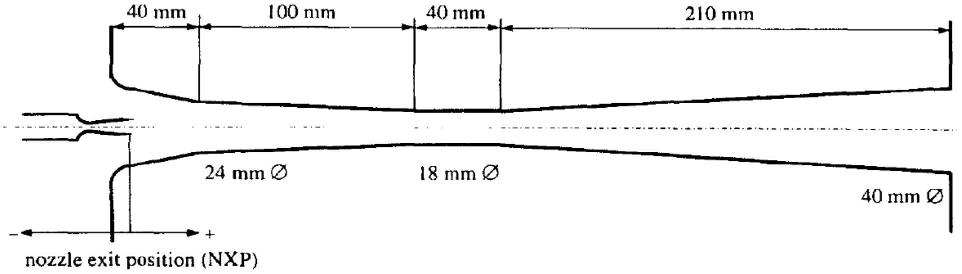

Figure 2.9: Adjustable nozzle exit position in the conventional ejector from work of Aphornratana & Eames (1997).

Al-Doori (2013) tested experimentally four nozzle positions to investigate the effect on performance in a constant pressure steam ejector. The selected positions of the nozzle lip relative to the commencement of the mixing section were 6, -4, -18, and -32 mm. The tests were carried out with steam as a working fluid at primary pressure of 270 kPa and temperature of 130 °C and evaporator temperature of 6, 10, and 14 °C. The highest value of COP was obtained at NXP = -32 mm as shown in Figure 2.10. The tests revealed that the ejector entrainment ratio improves when the primary nozzle moves upstream. This result was attributed to the increase of the area available for the secondary flow to pass through, and therefore more secondary flow would be entrained into the mixing section.

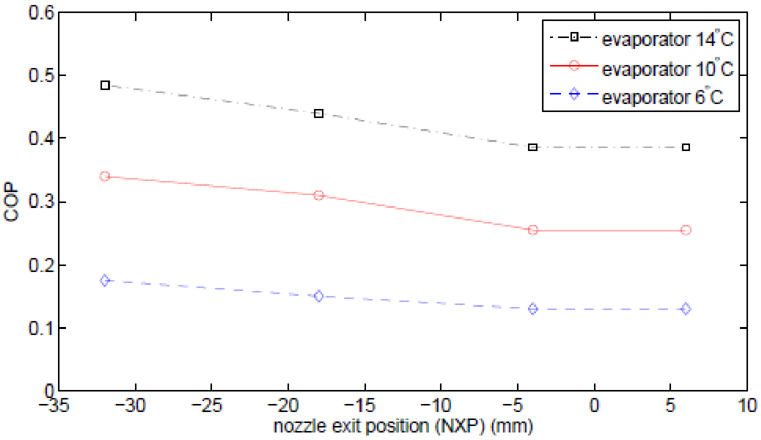

Figure 2.10: Effect of the nozzle exit position on conventional steam ejector performance for primary pressure of 270 kPa and temperature of 130 °C and range of evaporator temperatures from the work of Al-Doori (2013).

Dong et al. (2013) used three different movable nozzle geometries to study the effect of the nozzle exit position on steam ejector performance at different operating conditions. The study illustrated that the optimum nozzle exit position was located between 56 mm to 96 mm as illustrated in Figure 2.11. In addition, the authors claimed that the nozzle throat diameter does not affect the optimum nozzle exit position and the optimum position is not related to the operating conditions, nozzle dimensions, and ejector diffuser size.

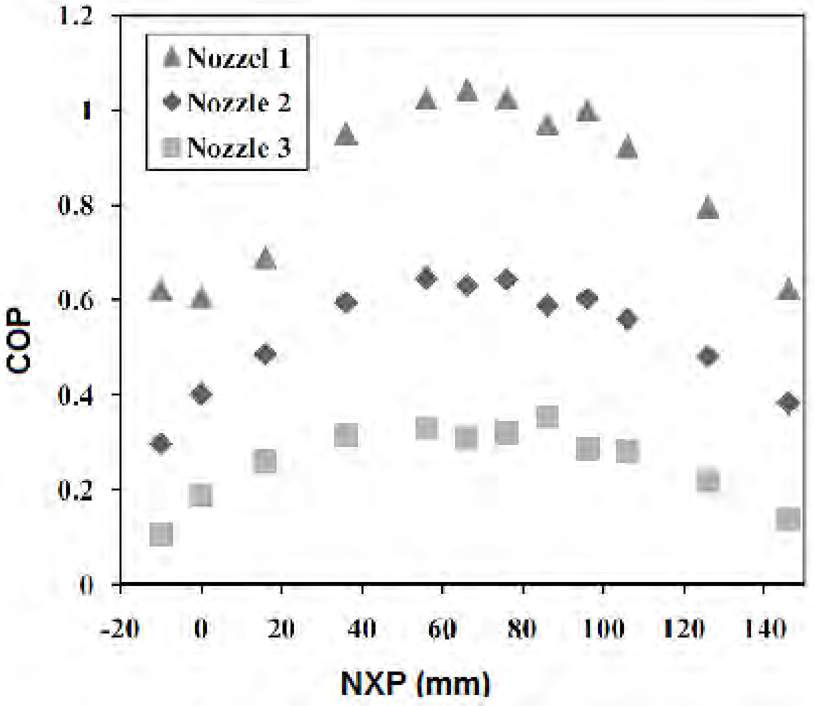

Figure 2.11: Effect of nozzle exit position on the conventional steam ejector performance from the work of Dong et al. (2013).

Chong et al. (2014) presented experimental and numerical studies to examine the influence of the nozzle exit position on supersonic air ejector performance. The results indicated that there is an optimal nozzle exit position corresponding to maximum entrainment ratio, but the exit pressure critical value is not affected by the nozzle exit position.

It can be concluded that the primary nozzle geometry has some effect on the ejector working performance. The nozzle exit position significantly affects ejector performance and nozzle position can be adjusted to start up and to fine tune ejector performance. An optimum nozzle position covering all ejector operating conditions is not possible and each operating condition requires a particular nozzle position. However, the main advantage of ejector having no moving parts would be removed.

From published information, it seems that conventional ejector performance is still relatively poor. This leaves a large margin available for improvement, potentially justifying efforts to explore unconventional approaches.

2.6 Variable geometry ejectors

Conventional supersonic ejectors are designed according to the assumption of constant area mixing (CAM) or constant pressure mixing (CPM). Occurrence of shock series in the constant area and diffuser regions is a common problem in both these conventional designs. The occurrence of a series of shocks in these regions causes a loss of total pressure. To produce a high efficiency supersonic ejector, the shocks should be eliminated or at least minimized. In literature, a number of authors have reported that the performance of the ejector cycles could be improved by using ejectors that do not have any constant area region.

Ejector-related work often illustrates that the variation of the operating conditions can cause a significant change in the constant area ejector performance. The optimum ejector performance can be achieved over a very limited range of operating conditions; slight changes in the operating conditions can cause a significant deterioration in ejector performance.

Eames et al. (1995) carried out experimental and theoretical studies into fixed geometry ejectors. The study showed that the cooling capacity and thus, the ejector performance at off design operation is limited by the condenser pressure, which would itself be governed by the ambient conditions in an application. The study also suggested that the system cooling capacity is independent of the operating conditions in a given range. The study concluded that if the ejector was designed with variable geometry such as cross-section areas or nozzle exit position, the cooling capacity could be made independent of the operating temperatures in a given range.

Sun (1996) carried out experimental and theoretical studies to investigate the influence of the ejector geometry on its performance. The study indicated that fixed geometry ejectors can not perform well unless they operate exactly at their designed operating conditions. The study suggested that the geometry of an ejector in the refrigeration cycle should be variable in order to cope with variations of working conditions and maintain optimum performance and constant cooling capacity of the system. The study concluded that if a variable geometry ejector was available there would be no critical pressure value as increasing the ejector back pressure causes a gradual reduction in entrainment ratio rather than a sudden drop that occurs in the fixed-geometry ejector.

Kim et al. (2006) performed CFD analysis on a variable area ejector using air as a working fluid. The ejector throat area ratio was varied by a moveable cone-cylinder which was inserted into a conventional ejector to provide such variable area ejector as in Figure 2.12. However, pressure losses due to flow disruption is considered a significant drawback of this arrangement.

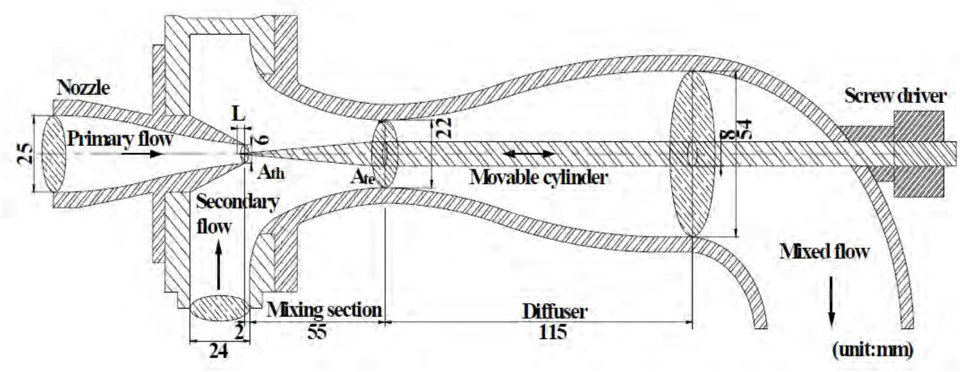

Figure 2.12: Schematic of a variable area ejector from the work of Kim et al. (2006).

Ma et al. (2010) introduced a steam ejector refrigeration system with a spindle placed in front of the primary nozzle inlet to control flow rate into the nozzle, as shown in Figure 2.13. The spindle changes the primary nozzle throat area and therefore changes the area ratio (the ratio of the constant area throat section to primary nozzle throat area) of the ejector. The primary flow can be adjusted using the spindle in order to provide a higher entrainment ratio and COP as well as more flexible operation. The study showed that when the spindle position was moved towards the nozzle, the cooling capacity decreased due to the decreased primary flow while the critical back pressure increases significantly which allows the ejector to operate at higher condenser pressure.

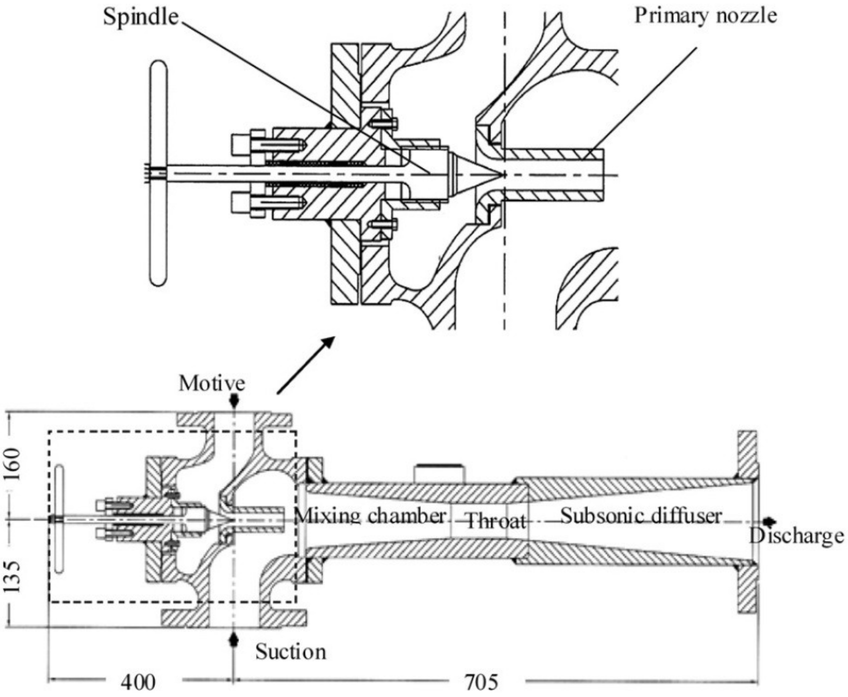

Figure 2.13: Configuration of steam ejector with spindle (Ma et al. 2010).

Dennis (2009) presented a performance comparison between fixed and variable geometry ejectors. In this comparison, a performance map for fixed and variable geometry ejector was suggested. The comparison indicated that the critical point of the back pressure was removed from the variable geometry ejector performance. The study noted that a range of mixing duct diameters from 8 mm to 22 mm would be sufficient for a proposed ejector to operate satisfactorily over the required range of temperature.

More recently, Dennis & Garzoli (2011) used software modelling to examine the use of variable geometry ejectors in cold stores to improve the ejector system performance using a solar collector as a power source. The results showed that a hypothetical variable geometry ejector provides 8-13 % higher solar fraction over a fixed geometry ejector and thus, the area of the solar collector could be decreased by 80 % when using a variable geometry ejector rather than the fixed geometry ejector.

Pereira et al. (2014) studied two geometrical factors, the area ratio and the nozzle exit position using R600a as a working fluid. A movable spindle was installed in the primary nozzle to control the area ratio. The influence of the nozzle exit position and condenser pressure on ejector performance were studied. The benefit of applying the variable geometry design over a fixed geometry configuration was assessed. An 80 % increase in the COP was obtained when compared to the performance of a fixed geometry ejector for a condenser pressure of 3 bar with identical operating conditions.

Gutiérrez & León (2014) studied an ejector that used variable geometry mechanisms and evaluated it using CFD simulations. The design used a primary nozzle with interchangeable outlets and these outlets were designed to enhance the mixing process between the motive and the secondary fluids by increasing the exit perimeter of the nozzle and producing flow instability. An increased entrainment ratio of the ejector was achieved. An improvement of 8.23 % over the base line ejector entrainment ratio was determined with CFD.

Although several researchers have examined the variable area ejector, so far academic literature does not report a practical application of such an ejector concept.

2.7 CRMC Ejectors

Eames (2002) proposed a new ejector design with a continuous variation of cross sectional area based on a Constant Rate Momentum Change (CRMC) theory as shown in Figure 2.14. The new theory was proposed to replace the conventional ejector design used in both constant area mixing and constant pressure mixing with CRMC ejector. Theory proposes that to eliminate the pressure losses associated with the shock compression of the mixed flow, the flow momentum is compelled to change at constant rate as it moves downstream. By this means, shock wave occurrence could be eliminated and thus, more total pressure would be conserved and converted to actual static pressure gain, which will allow the ejector to operate more effectively.

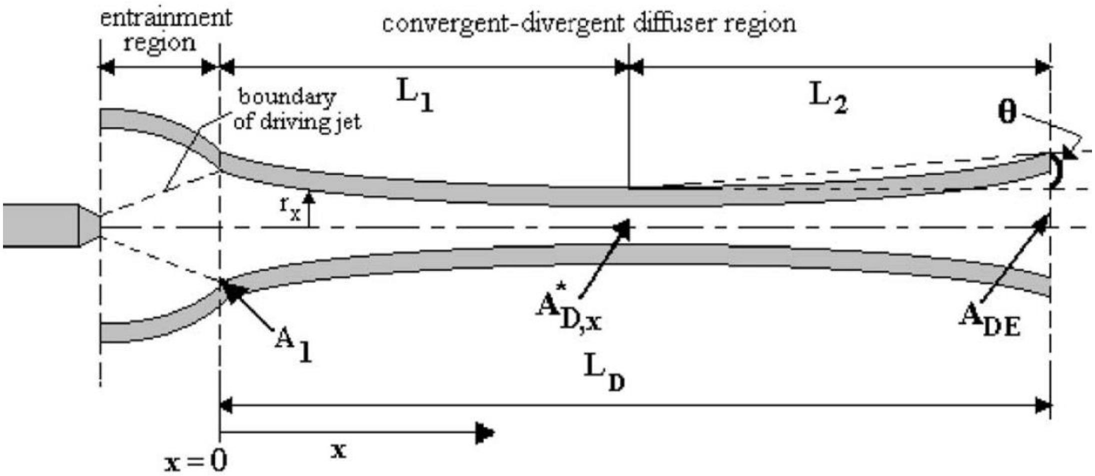

Figure 2.14: Profile of the CRMC ejector duct from the work of Eames (2002).

In this design it is supposed that there is a gradual increase in static pressure and decrease in Mach number and velocity of flow because the shock in the ejector diffuser is eliminated as sketched in Figure 2.15. An apparent reduction in the total pressure losses associated with the shock formation in constant area ejectors is removed in this new configuration.

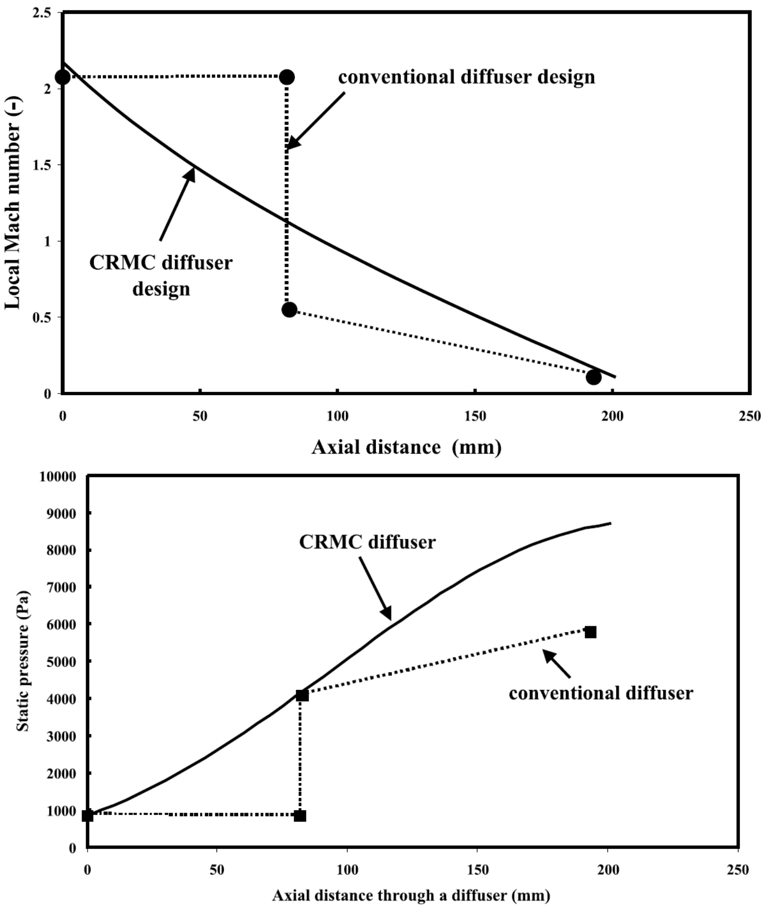

Figure 2.15: Pressure and Mach number variation for CRMC ejector from the work of Eames (2002).

Theoretical results presented by Eames (2002) show that both the entrainment ratio and pressure lift ratio could be significantly enhanced above those achieved from constant area ejectors. Eames (2002) drew on the experimental work by Worall (2001) in an effort to experimentally validate the theoretical simulations.

Worall (2001) performed experiments on a CRMC steam ejector as illustrated in Figure 2.16. Experimental data obtained by Worall (2001) showed that a small variation in pressure lift ratio (ratio of exit pressure to secondary pressure) causes large changes in entrainment ratio. However, the entrainment ratio varied over a range in a series of peaks and troughs which could make the performance of such a system unpredictable over its operational range.

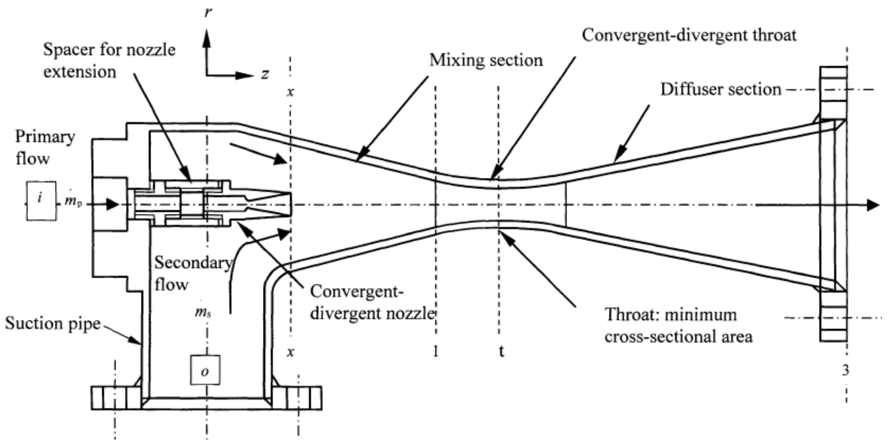

Figure 2.16: Profile of the convergent-divergent throat jet-pump from the work of Worall (2001).

As an assessment of Eames (2002) theory, Seehanam et al. (2007) presented a numerical study to describe the flow behaviour and ejector performance using CRMC theory and compared the CRMC ejector with the constant pressure mixing ejector (CPM). The study showed that CRMC provides a constant velocity for a longer distance along the ejector centreline as shown in Figure 2.17. Furthermore, velocity change on the ejector axis is actually more gradual in the CPM ejector case than it is in the CRMC ejector case. The CRMC theory specifies a constant velocity gradient along the ejector. Hence the Seehanam et al. (2007) indicates significant departure of the CRMC ejector from the CRMC theory, as originally proposed.

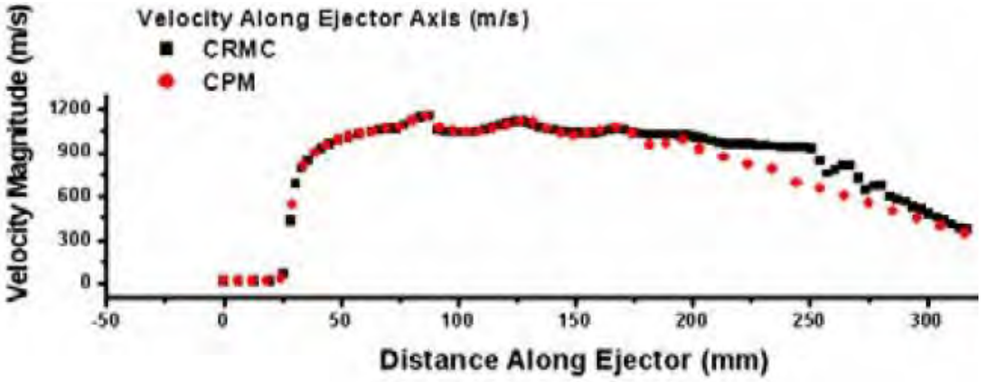

Figure 2.17: Velocity profile along the CRMC and CPM ejector axis from the work of Seehanam et al. (2007).

Eames, Ablwaifa & Petrenko (2007) used a CRMC ejector a refrigeration system using

R245fa as the working fluid. The effect of the primary nozzle geometry and its position within the ejector at different operating conditions was evaluated. It was concluded that these parameters have a significant effect on the ejector performance. However, the performance of the ejector designed according to the CRMC prescription was not evaluated relative to a more conventional design.

A performance comparison between a conventional CPM ejector and a CRMC ejector was performed by Chandra & Ahmed (2014). The two ejectors were experimentally tested for boiler temperatures below 120 °C and evaporator temperatures below 15 °C. It was found that the steam jet refrigeration system would operate stably at low boiler temperatures of around 90 °C and that the CRMC ejector enhanced the performance of the refrigeration system which the authors claim was achieved by eliminating the shock from the ejector although no actual evidence of shock elimination was provided. It was noted in this study that by using the CRMC ejector, the pressure lift ratio increased up to 40 % as illustrated in Figure 2.18.

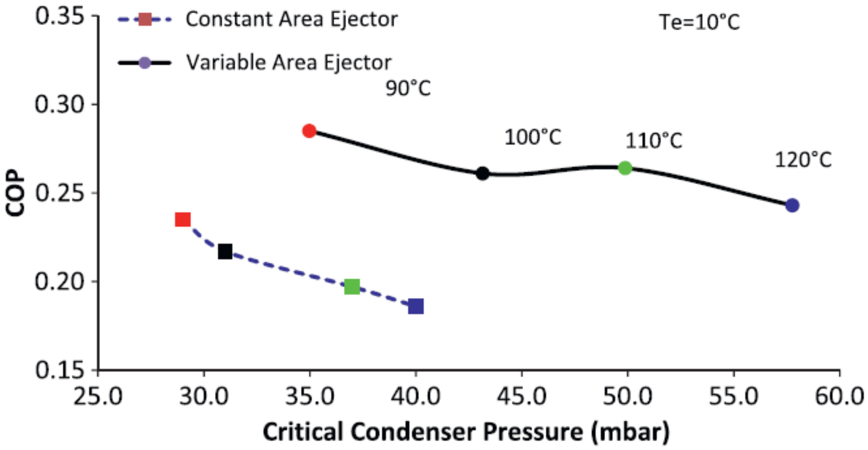

Figure 2.18: Performance comparison of conventional and CRMC ejectors at different boiler temperatures from work of Chandra & Ahmed (2014).

Kumar et al. (2013) investigated numerically and experimentally the effect of the CRMC method taking into account frictional effects inside the variable cross section of supersonic ejector on ejector design. The numerical results were in good agreement with the experimental data at double choked conditions. However, for single choked conditions, the disagreement was significant.

Milazzo et al. (2014) used a CRMC based ejector with a moveable primary nozzle in a two-stage prototype cooling system using R245fa as a refrigerant as presented in Figure 2.20. However, the COP was lower relative to an absorption refrigeration system and hence required substantial improvement through detailed thermodynamic and CFD design optimization. Mazzelli & Milazzo (2015) than improved the CRMC ejector design by increasing the ejector length as presented in Figure 2.20. The study also modelled the friction losses inside the ejector and according to this study, such losses have a minor influence on the entrainment ratio in the double choked mode, but do have a significant influence on the entrainment ratio at the single choked mode. However, the extra length could introduce packaging complexity and in any case, this design needs further improvement in terms of entrainment ratio, mixing and compression ratio.

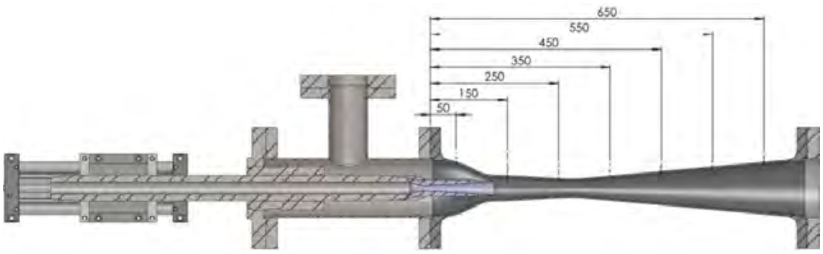

Figure 2.19: Ejector geometry and movable primary nozzle from the work of Milazzo et al. (2014).

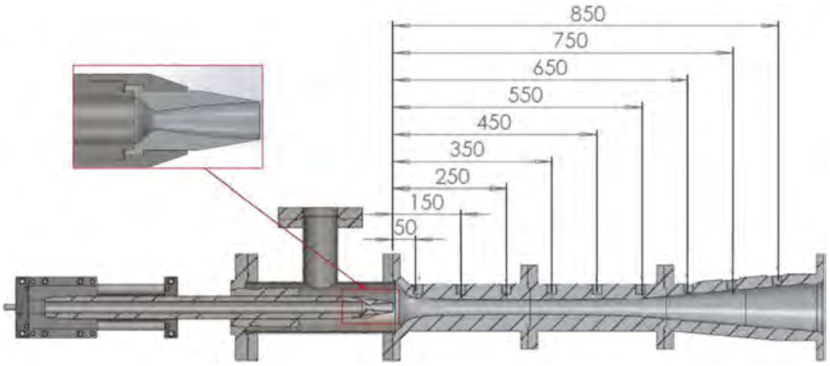

Figure 2.20: Improved CRMC ejector geometry and its movable primary nozzle from the work of Mazzelli & Milazzo (2015).

2.8 Computational fluid dynamics simulations

Prototype testing of ejectors is generally accepted as the conclusive way to determine the performance. However, high cost associated with such work raises a need for alternative methods to determine ejector performance. With the rapid development of Computational Fluid Dynamics (CFD) capability, numerical simulation has became a viable method to refine ejector performance. It is an effective tool to study the influence of geometry and operating conditions. Recently, researchers have demonstrated the ability of CFD to reveal the flow phenomena and mixing process in different parts of the ejector which are not accessible through experimental work.

Hedges & Hill (1974) developed a finite-difference scheme for simulation of ejector flow, and this effect was at the forefront of the application of CFD techniques to the simulation of flow inside ejectors. Riffat & Everitt (1999) used CFD to simulate an air conditioned vehicle ejector refrigeration system with a compressible flow model. The CFD results show no signs of shocks and a little reversed flow close to the entrance of the mixing chamber whereas the experimental results indicated the presence of shocks.

An ejector working with R141b as a refrigerant was designed and simulated using CFD by Rusly (2004). Three different flow fields related to operating conditions and entrainment ratio were simulated. The best ejector performance was obtained when the entrained flow was choked and the flow was over an expanded state. The simulation showed a weak oblique shock wave, particularly in the secondary nozzle section filling the centre part of the section slightly off the wall. Bartosiewicz et al. (2005) used CFD to simulate six turbulent, supersonic air ejector models. This study focused on the shock location and the average compression effect. The results were compared with the experimental results obtained by Desevaux & Aeschbacher (2002). Among all other turbulence models used in this study, the $\kappa - \omega - sst$ demonstrated the best simulation of the mixing process inside the ejector. In addition, the computational models were able to correctly simulate the different operational modes of the ejector, ranging from the on-design mode, with maximum secondary flow rate, to the off-design mode, in which the secondary flow rate and entrainment ratio drops to zero.

Sriveerakul et al. (2007) used CFD to evaluate the effect of the ejector geometry and operating conditions on the working performance of the ejector. The obtained results were validated through comparison with experimental results and provide a credible insight into the flow phenomena inside the ejector as illustrated in Figure 2.21. The study concluded that the CFD method is a proficient tool in simulating ejector performance and providing a better understanding of the flow within the ejector. Therefore, CFD can be considered as an effective tool to improve the design of the ejector.

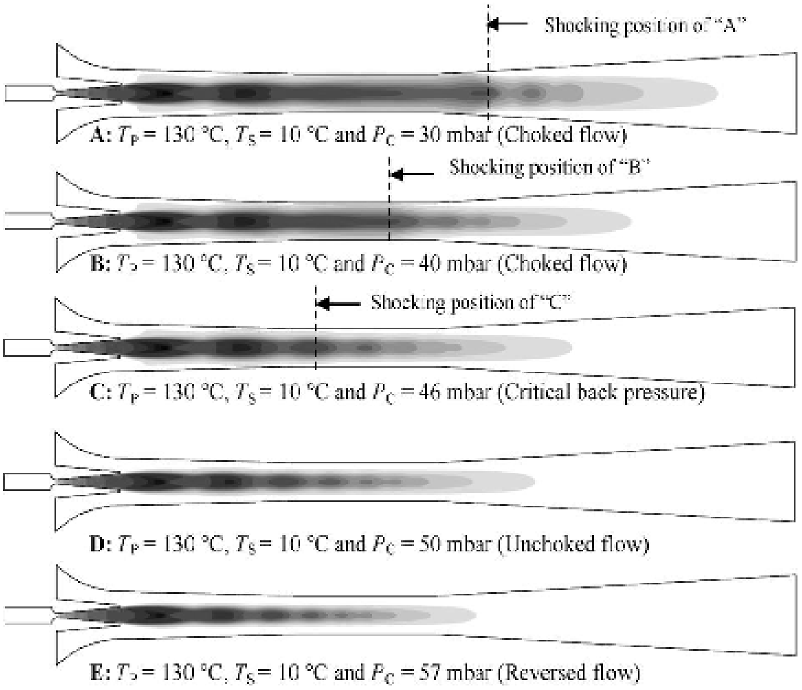

Figure 2.21: Filled contour of Mach number: effect of the condenser pressure on the ejector performance from the work of Sriveerakul et al. (2007).

Hemidi et al. (2009) introduced a comparison between CFD and experimental results for ejectors operating over a range of conditions. This study focused on the behaviour of two turbulence models: $\kappa - \epsilon$ and $\kappa - \omega - sst$. Over the whole range of operating conditions, the overall deviation from experimental result was below 10 % for the $\kappa - \epsilon$ model, while the results for the $\kappa - \omega - sst$ model are in less agreement. However, the difference between the two models diminishes when the ejector operates in the double chocked mode as illustrated in Figure 2.22.

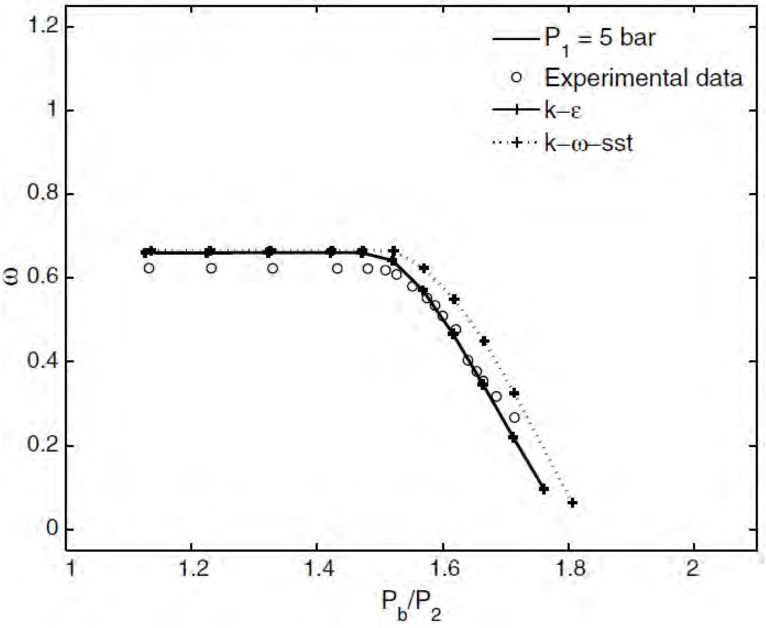

Figure 2.22: Variation of entrainment ratio with compression ratio for two CFD turbulence models with comparison to experimental data from the work of Hemidi et al. (2009).

Varga, Oliveira & Diaconu (2009*a*) used the $\kappa - \epsilon$ model to simulate a steam ejector and investigate the efficiencies of an ejector's main parts (primary nozzle, suction area, mixing area and diffuser section). The results illustrate that the nozzle efficiency is independent of the operating conditions and the nozzle throat diameter can slightly affect this efficiency. Suction efficiency is constant before the back pressure reaches the critical value and drops significantly beyond this point. Other efficiencies increase as back pressure increases until the critical value is reached.

Ji et al. (2010) conducted a computational fluid dynamics (CFD) investigation into the flow structure inside a steam ejector. The study focused on the effects of operating pressure and ejector geometry on the flow structure and performance of the steam ejector. The CFD results were verified with available experimental data. The angle of the converging duct was considered as the geometrical parameter in this study and values used were 0, 0.5, 1, 2, 3.5 and 4.5° as illustrated in Figure 2.23. The ejector with a converging duct angle of $\alpha = 1°$ has the best performance. The study concluded that the CFD results were in good agreement with the experimental results and the CFD visualisation was claimed to be of great benefit to the study as it revealed phenomena inside the ejector in detail.

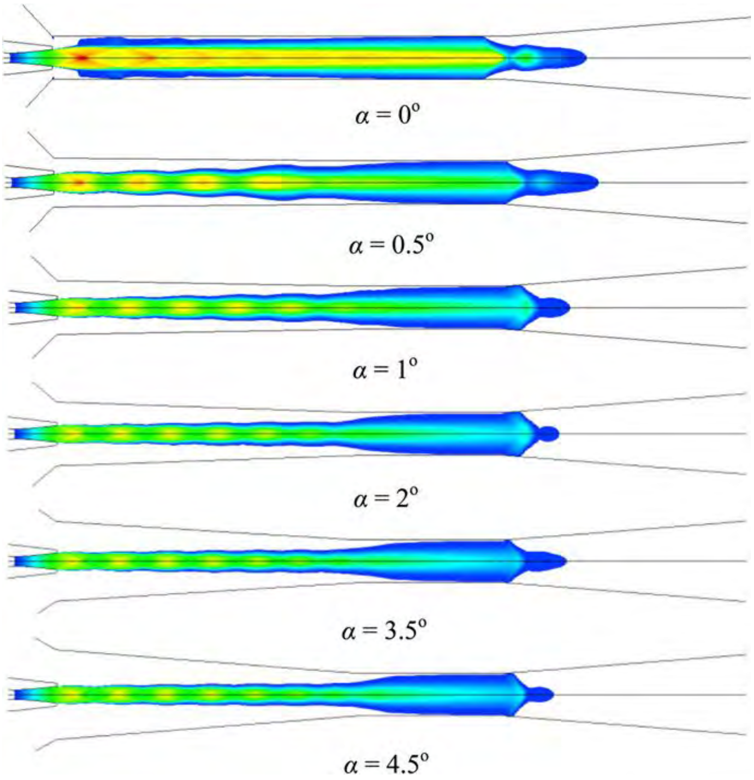

Figure 2.23: Effect of converging duct angle on the contours of Mach number for primary pressure of 2.66 bar and secondary pressure of 0.16 bar from the work of Ji et al. (2010).

More recently, Varga, Oliveira & Ma (2011) simulated a steam ejector with a primary nozzle with a movable spindle to provide a variable primary nozzle geometry. A comparison between the CFD results and experimental results was carried out. The average relative error of the secondary flow rate was 7.7 %. The study found that the simulation deviation from experimental data increased as the generator temperature decreased to reach around 22 % for 120 °C. However, only 70 % of the cases were within acceptable accuracy.

Scott, Aidoun & Ouzzane (2011) experimentally investigated a supersonic ejector using R245fa as the working fluid to validate numerical models of ejectors used in refrigeration applications. The CFD results predicted the ejector global performance properties with good agreement. The maximum critical pressure difference between the CFD and experimental results was 15.8 % at a primary flow temperature of 80 °C and a secondary flow temperature of 10 °C and 5.1 % when the primary flow temperature was 100 °C and the secondary flow temperature was 0 °C.

Al-Doori (2013) used CFD with $\kappa - \omega$ turbulence model and an ideal gas to simulate a supersonic steam ejector. The results were in good agreement compared with the experimental work. The differences between numerical and experimental results in terms of entrainment ratio were 2.6 % and 2.9 % for primary pressures of 200 kPa and 270 kPa respectively with an evaporator temperature of 14 °C. Whereas, in terms of critical back pressure, the differences were 15.4 % and 8.8 % respectively at the same operating conditions. In addition, local ejector flow features such as flow recirculation inside the diffuser and mixing section, reversed flow in the secondary inlet, and shock waves were simulated reasonably.

2.9 Flow visualization studies

Experimental flow visualization has been an important research instrument in the area of fluid dynamics and it remains an effective tool to investigate compressible, supersonic, and turbulent flow phenomena and to validate proposed models. Previous studies have applied visualisation techniques to ejectors. Fabri & Siestrunck (1958) used schlieren methods to visualize different flow patterns in supersonic air ejectors and to propose a categorisation of the ejector's flow regimes. The authors investigated the flow in six different nozzles in supersonic air ejectors working at different operating conditions. A number of flow regimes were categorised by comparing experimental results with theoretical work. The schlieren visualisation method has also been utilized by Matsuo et al. (1985) for analysing the performance of a supersonic air ejector operating with and without secondary flow through a rectangular ejector duct. Hong et al. (2004) used a schlieren system and high speed camera to investigate a new method to improve ejector performance. The researchers reduced the primary flow velocity by allowing it to expand through rotor-vanes. Schlieren visualization was used to capture unsteady phenomena in the mixing chamber entrance. The method showed high sensitivity to changes of density at a normal direction to the flow than in any other direction.

More recently, Al-Doori (2013) used a schlieren technique to visualize air flowing from the primary nozzle. Two types of shock waves were observed in this study: oblique shock waves through over-expanded supersonic flow and shock waves created by a pitot tube as shown in Figure 2.24. However, the schlieren method is a primarily qualitative techniques and does not allow an effective visual distinction between the two interacting flows in ejectors (Bouhanguel et al. 2012).

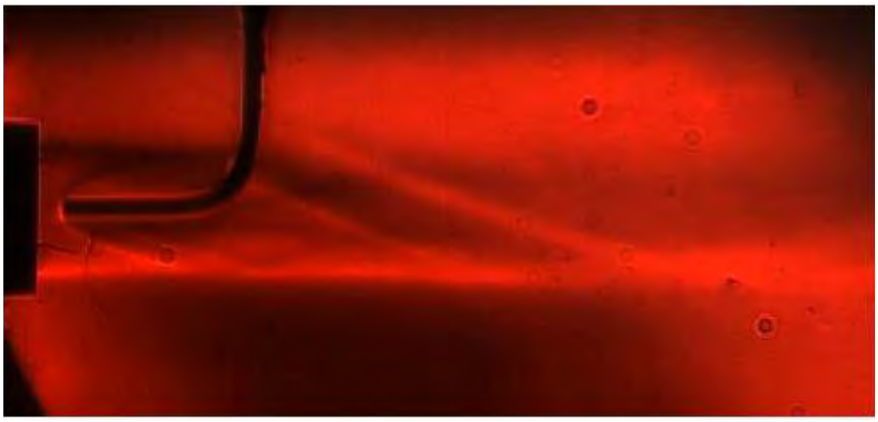

Figure 2.24: Schlieren image of air flowing from the nozzle into the mixing section at stagnation conditions of 380 kPa and 25 °C from the work of Al-Doori (2013).

Porcar & Prenel (1976) used Rayleigh and Mie scattering techniques (imaging techniques based on light scattering by small particles) to visualize shock waves in no-secondary flow supersonic air ejectors with diffused water droplets as particles.

To discriminate visually between the primary and secondary flows before they are fully mixed, Desevaux (2001) used a laser sheet method. This method was successful when the entrainment ratio was below 0.3 and gave poor results for higher entrainment ratio values. The water nano-droplets occurred when the induced air was moist. A TSI atomiser (model 9306A) was used to produce fluorescent doped droplets of diameter 0.1 to 2 μm. However, this method does not permit visualisation of the entire mixing zone but only the mixing region which has marked differentiation of the nano water droplets. Figure 2.25 shows the experimental apparatus including a TSI atomiser and the data acquisition system used by Desevaux (2001).

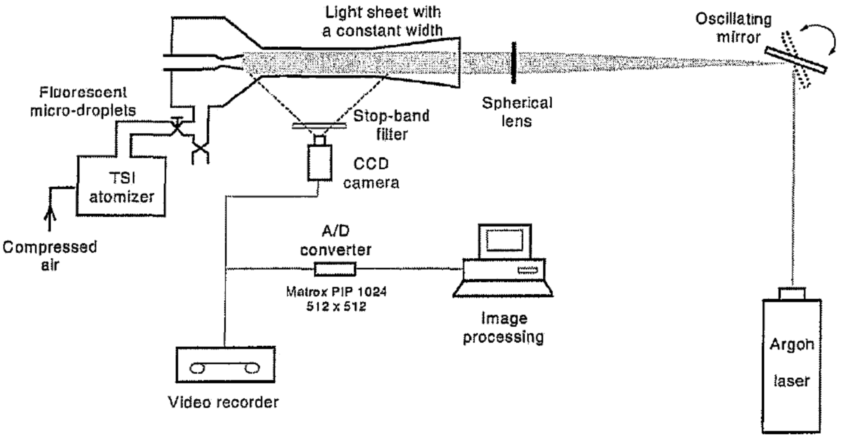

Figure 2.25: Optical device, TSI atomizer and acquisition system used by Desevaux (2001).

Unfortunately, such visualisation methods in ejectors are primarily qualitative techniques (Bouhanguel et al. 2012).

Choutapalli (2006) investigated the flow field characteristics of the pulsed jet ejector using Particle Image Velocimetry (PIV) as illustrated in Figure 2.26. Experiments were carried out at three different area ratios that help to define the conditions for maximum thrust augmentation. The results show that in the presence of the ejector duct, the pulsed jet primary vortex induces a secondary vortex on the wall and the strength of the induced vortex depended strongly on the proximity of the ejector wall. In addition, for the optimal condition where maximum thrust augmentation was observed, the strength of the induced vortex was found to be highest.

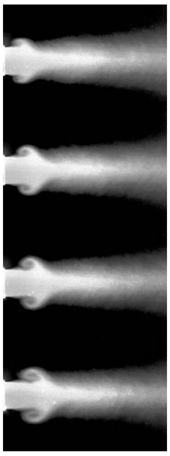

Figure 2.26: Phase averaged PIV flow visualization images showing vortex ring time evolution by Choutapalli (2006).

Bouhanguel et al. (2012) presented velocity measurements using Particle Image Velocimetry with two flow seeding methods (natural and artificial scattering tracers) on a supersonic air ejector as shown in Figure 2.27. The PIV technique provided more information than conventional laser tomography visualizations and thus, proved to be a very interesting tool for the validation of CFD simulations in supersonic ejectors.

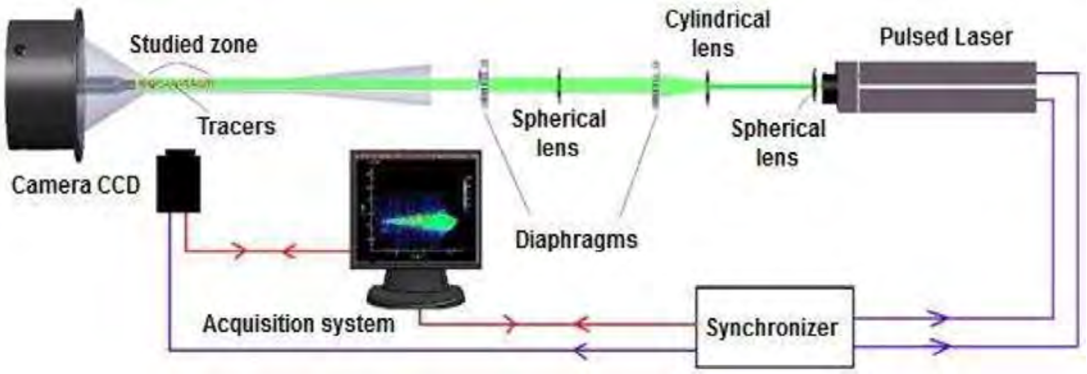

Figure 2.27: PIV experimental system used by Bouhanguel et al. (2012).

Zhu & Jiang (2014) investigated the shock wave structures in an ejector mixing chamber by Schlieren flow visualization as shown in Figure 2.28. The results show that the waves generated in the nozzle flow do not reach the mixing chamber wall when the ejector is working at the sub-critical mode. The study demonstrated a correlation between wavelength of the waves structures and the ejector performance.

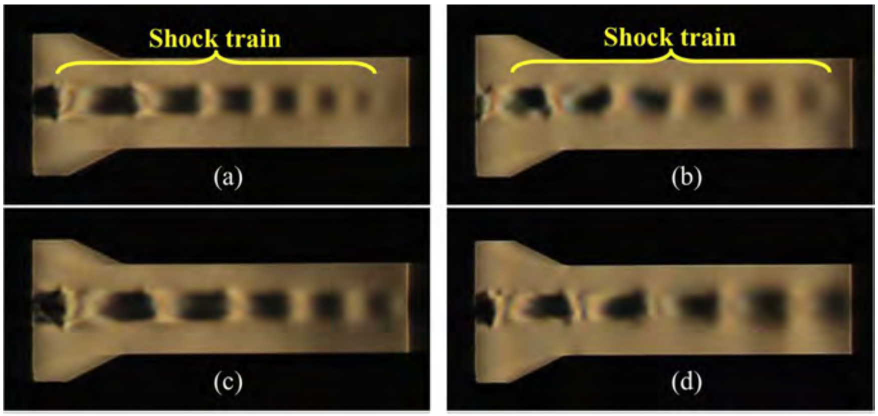

Figure 2.28: Schlieren photographs of shock structures in the mixing chamber. (a) P_p=0.3 MPa, P_s=0.06 MPa; (b) P_p=0.3 MPa, P_s=0.08 MPa; (c) P_p=0.35 MPa, P_s=0.06 MPa; (d) P_p=0.35 MPa, P_s=0.08 MPa from the work of Zhu & Jiang (2014).

Rao & Jagadeesh (2014) used time resolved schlieren and laser scattering flow visualization to measure the non-mixed length of the two flows inside a rectangular ejector duct. It was observed that the length lies within 4.5 to 5.2 times the height of the mixing duct and shrinks by 46.7 % when the primary flow is over-expanded.

Nishijimi et al. (2016) visualised the structure of a two-phase-flow shock wave in an ejector nozzle using a transmitted optical beam and a high-speed camera with representative results shown in Figure 2.29. The study concluded that as the pressure rises in the ejector outlet, the shock wave moves from the outlet to the nozzle throat and changes from an oblique shock wave to a normal shock wave.

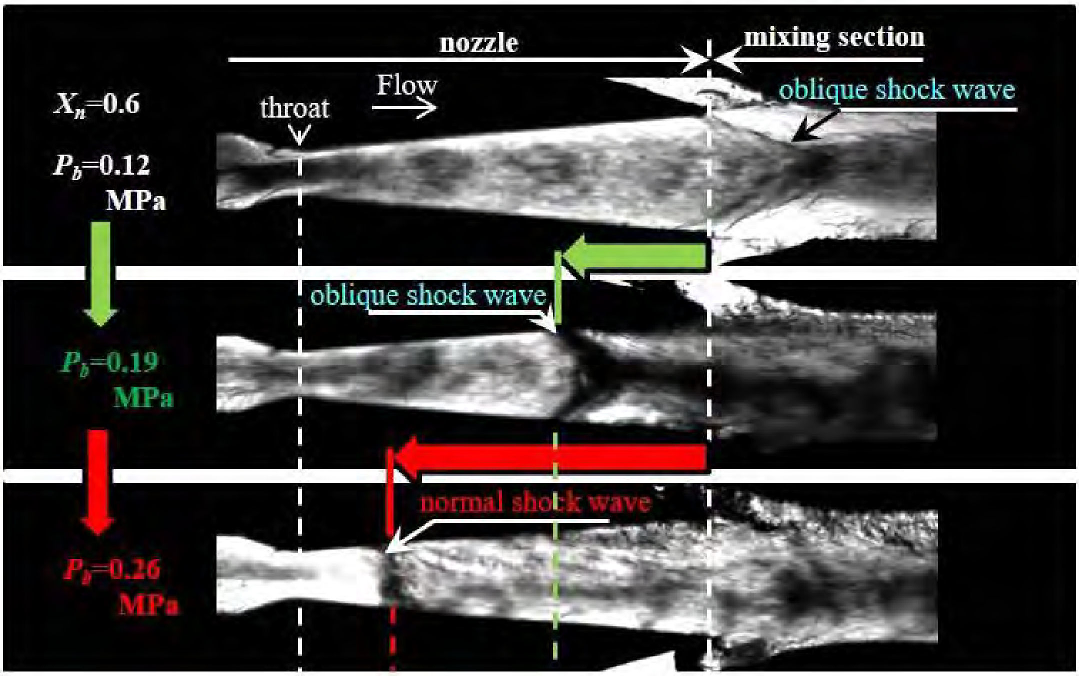

Figure 2.29: Images of shock wave acquired by Nishijimi et al. (2016).

2.10 Chapter Summary

This chapter has catalogued previous work related to the design, fabrication, simulation and analysis of the ejector and its component parts such as the primary nozzle, mixing section, secondary throat, and diffuser.

Researchers have performed analytical, numerical, and experimental studies with both open and close ejector cycles to determine ejector performance. A number of studies have focused on the primary nozzle design and have achieved some progress. Other studies have focused on the ejector geometry and the sensitivity of the ejector performance to any minor change in this geometry. In addition, flow behaviour inside these parts has been thoroughly analysed to identify the main causes impeding ejector improvements. The most promising concept appears to be variable geometry, but application of such concepts is difficult due to design complexity and manufacturing difficulties.

In spite of this extensive research, ejector design has changed little over time. However, in recent years, a new approach described as the CRMC ejector has been introduced. Several studies have adopted this approach for ejector design with varying degrees of success. The configuration appears to have significant potential, but the strengths and weaknesses of the approach have not been defined with any clarity.

Despite some shortcomings, CFD techniques have proved to be an effective tool to provide further insight into ejector design and analysis. Researchers have also successfully visualised the mixing flows inside ejectors. The application of CFD and flow visualisation to the CRMC ejector has significant potential to enhance understanding of CRMC ejectors.

Chapter 3

CRMC Ejector theory and design

3.1 Introduction

Conventional supersonic ejectors are designed for either constant area mixing (CAM) or constant pressure mixing (CPM). The CPM arrangement theoretically provides better performance than CAM (Keenan 1950) making it more desirable in industrial applications. However, these designs have relatively low efficiency overall and an inability to work over a broad range of operating conditions.

The occurrence of a series of shocks in CAM and CPM designs causes a loss of total pressure. If these total pressure loss effects could be minimised, systems using ejectors could be more widely used for applications such as refrigeration and vacuum systems. To produce a high efficiency supersonic ejector, the shock series associated with the compression process can be eliminated or at least minimized by changing the flow momentum at a constant rate along the ejector duct, at least according to the CRMC theory, Eames (2002).

In the program of analysis for the CRMC duct, air is chosen as the working fluid to avoid complications due to the potential presence of two phase flow that can arise using other working fluids. Air also allows convenient work in various aspects of ejector flow experiments such as flow visualisation to investigate flow behaviour inside the ejector as the system can be open.

3.2 Theory description

Eames (2002) suggested that the performance of the ejector refrigeration cycle could be improved by using ejectors that do not have any constant area region. The argument is that if the momentum of the combined primary and secondary flows changes at a constant rate within an appropriately designed variable area ejector duct, total pressure losses caused by the shock wave compression associated with other ejectors could be eliminated.

The prescription of the required area variation of the constant rate of momentum change (CRMC) ejector geometry was described by Eames (2002) using,

$$\frac{d\dot{M}}{dx} = \dot{m}_p(1+ER)\frac{dV}{dx} = \beta \tag{3.1}$$

where:

$\dot{M}$: Momentum of the flow

x: Axial position along the ejector duct

$\dot{m}_p$: Mass flow rate through the primary flow inlet

ER: Entrainment ratio $(\frac{\dot{m}_s}{\dot{m}_p})$

$\dot{m}_s$: Mass flow rate through the secondary flow inlet

V: Velocity at x

β: Constant rate of momentum change

In obtaining the above equation and applying it to the specification of an ejector area variation, the following assumptions are necessary:

1. Primary and secondary streams are the same gas.
2. The primary and secondary stagnation pressures and temperatures and flow rates are known.
3. Pressures of primary and secondary flows at the Nozzle Exit Position (NXP) plane are the same.
4. The Mach number and velocity of the primary and secondary flows at the nozzle exit position are known.

From equation 3.1 it is observed that a linear variation of flow speed V_{Dx} with axial distance will generate a constant rate of momentum change. The velocities at the beginning and end of the CRMC duct can be specified as $V_{Dx} = V_1$ at $x = 0$ and $V_{Dx} = V_{DE}$ at $x = L_D$ and thus, to calculate the flow velocity at each point in the ejector, the following equation is used

$$V_{Dx} = V_1 - \frac{(V_1 - V_{DE})x}{L_D} \qquad \text{for} \qquad 0 \leq x \leq L_D \tag{3.2}$$

where V_{Dx} is the flow velocity along the ejector duct, V_1 is the flow velocity at the ejector duct start, V_{DE} is the flow velocity at the ejector duct exit and L_D is the ejector duct length. Assuming that the mixing process occurs at constant static pressure from the primary nozzle exit (NE) up to the start of the CRMC duct, the conservation of momentum principle will give

$$V_1 = \frac{V_{NE} + ER(V_s)}{1 + ER} \tag{3.3}$$

where V_s is the secondary stream velocity at the nozzle exit position. To complete the specification of flow velocity at any point along the duct, the length of the duct L_D, and the velocity at this position V_D both need to be defined. So that losses are small after the flow leaves the CRMC duct, a low value for V_{DE} should be specified. The duct length is specified empirically based on experience with similar ejectors.

To obtain the total temperature at the start of the CRMC duct, the following equation from the conservation of energy principle can be used

$$T_{o,1} = \frac{T_{o,p} + ER(T_{o,s})}{1 + ER} \tag{3.4}$$

while the static temperature at the same point can be obtained as

$$T_1 = T_{o,1} - \frac{V_1^2}{2C_p} \tag{3.5}$$

and the total pressure $P_{o,1}$ at this point will be

$$P_{o,1} = P_{NE}(\frac{T_{o,1}}{T_1})^{(\frac{\gamma}{\gamma - 1})} \tag{3.6}$$

The secondary flow at the entry of the mixing section is assumed to be subsonic, so that the static pressure at the nozzle exit can be calculated as

$$P_{NE} = P_{o,s} - \frac{\rho_s V_s^2}{2} \tag{3.7}$$

To determine the duct diameter at any location along the ejector axis (x), the static pressure and temperature at this point are needed and these can be calculated as

$$T_x = T_{o,1} - \frac{V_{Dx}^2}{2C_p} \tag{3.8}$$

$$P_x = P_{o,1}(\frac{T_x}{T_{o,1}})^{\frac{\gamma}{\gamma - 1}} \tag{3.9}$$

The fluid density can be obtained from the ideal gas law

$$\rho_x = \frac{P_x}{RT_x} \tag{3.10}$$

The Mach number is given by

$$M_x = \frac{V_{Dx}}{\sqrt{\gamma RT_x}} \tag{3.11}$$

The diffuser diameter at point x can be obtain by applying mass flow continuity as

$$D_{Dx} = 2\sqrt{\frac{\dot{m}_p(1 + ER)RT_x}{\pi P_x V_{Dx}}} \tag{3.12}$$

where

R is the specific gas constant, C_p is the specific heat of gas at constant pressure, γ is the ratio of specific heat values, $P_{o,p}$ and $T_{o,p}$ are the stagnation pressure and temperature of the vapour or gas supplied to the primary nozzle, $T_{o,s}$ and $P_{o,s}$ are the stagnation pressure and temperature of the gas supplied at the secondary stream.

3.3 CRMC ejector profile

The equations presented in Section 3.2 can be used to calculate the ejector duct diameter at each point along the ejector axis from the starting point at $x = 0$ to the exit point at $x = L$ as illustrated in Figure 3.1.

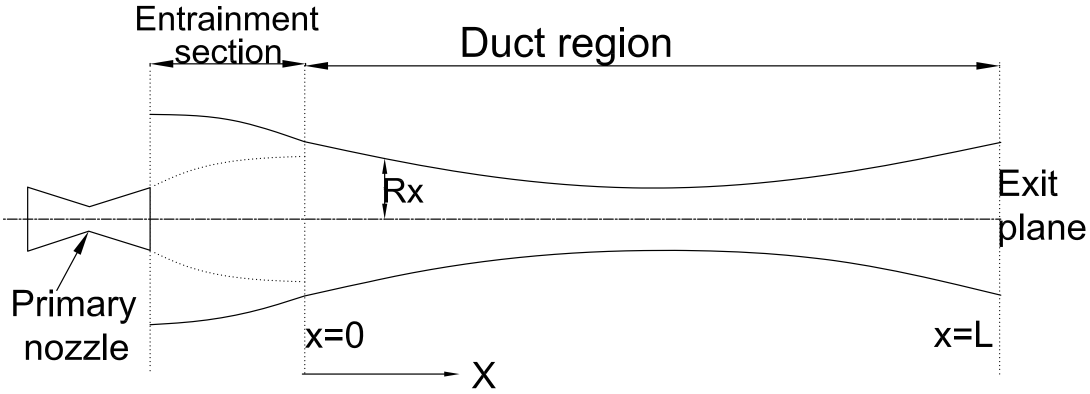

Figure 3.1: Illustration of the CRMC ejector duct and associated features.

The values of the key parameters which represent the design point of the CRMC ejector are listed in Table 3.1. The working fluid for the experimental ejector was air, so this dictated the values of R and γ. The air was available in the laboratory in an unheated state, so that the stagnation temperature was specified as approximately the ambient value for both primary and secondary streams. Primary pressure $P_{o,p}$, primary mass flow rate $\dot{m}_p$, secondary pressure $P_{o,s}$, entrainment ratio ER and CRMC duct length L_D were chosen to match approximately previous studies of a conventional supersonic ejector by Al-Doori (2013) and were considered as the design point of the present configuration.

Table 3.1: Ejector design parameters with the working fluid being air.

Parameter	Symbol	Value	Unit	Source
Primary pressure	$P_{o,p}$	200	kPa	design point
Primary temperature	$T_{o,p}$	298	K	ambient temperature
Primary mass flow	$\dot{m}_p$	0.00329	kg/s	design point
Secondary pressure	$P_{o,s}$	1.6	kPa	design point
Secondary temperature	$T_{o,s}$	298	K	ambient air
Entrainment ratio	ER	0.38	-	design point
Duct length	L_D	0.45	m	design point
Secondary flow inlet velocity	V_s	50	m/s	specified
Flow exit velocity	V_{DE}	50	m/s	specified
Specific heat ratio	γ	1.4	-	air working gas
Gas constant	R	287	J/kg K	air working gas

Solving the equations at the specified operating conditions listed in Table 3.1 resulted in the ejector parameters as listed in Table 3.2 with the profile duct shown in Figure 3.2.

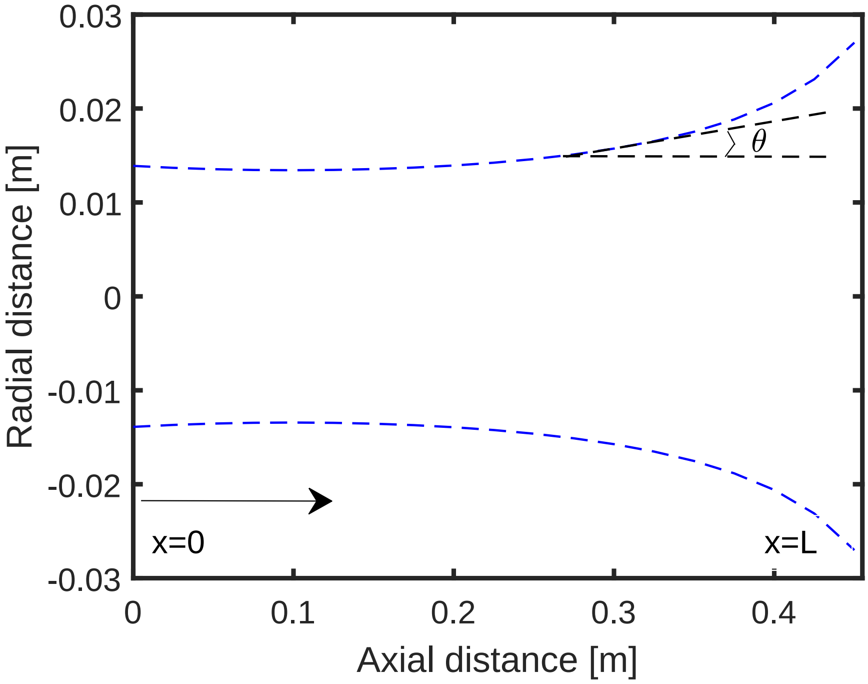

Figure 3.2: Profile of the CRMC ejector duct.

Table 3.2: Flow conditions and dimensions of the designed CRMC duct.

x (m)	P (kPa)	V (m/s)	T (K)	Mach	D (m)	$\theta°$
0.0	1.52	403.92	216.5	2.67	0.02768	1.034
0.025	1.73	384.2578	224.2	2.5	0.02688	0.796
0.05	1.93	364.5956	231.5	2.33	0.02626	0.585
0.075	2.14	344.9334	238.4	2.17	0.02584	0.440
0.1	2.415	325.2711	245	2.026	0.02556	0.226
0.125	2.6293	305.6	251	1.88	0.02548	0.048
0.15	2.842	285.94	258	1.74	0.02548	0.131
0.175	3.0514	266.28	263	1.6	0.02568	0.324
0.2	3.2556	246.6	268	1.48	0.02604	0.536
0.225	3.4527	226.96	272.4	1.35	0.02662	0.777
0.25	3.6409	207.297	276.6	1.23	0.02742	1.054
0.275	3.8183	187.63	280	1.11	0.0285	1.436
0.3	3.9833	167.97	283.7	0.984	0.02994	1.883
0.325	4.1343	148.3	287	0.87	0.03074	2.469
0.35	4.27	128.648	289.4	0.75	0.03182	3.360
0.375	4.3889	108.98	291.7	0.634	0.0324	5.718
0.4	4.49	98.2	89.32	0.52	0.04394	7.351
0.425	4.5725	69.66	295	0.41	0.054	14.935
0.45	4.6	50	296	0.3	0.0772	29.263

As prescribed, the CRMC duct diameter varies gradually to provide a gradual change in flow area from the start to the end of the ejector. From the inlet diameter of 27.68 mm, the diameter decreases until the throat diameter of 25.48 mm is reached, after which the duct diameter increases to reach 77.2 mm at the outlet. However, the increase in the duct diameter is accompanied by an increase in the angle of the divergent part of the duct (θ) as Table 3.2 shows. Such an increase in the divergence angle of the diffuser could lead to flow separation, particularly at the end of the duct due to a dramatic increase in the divergence angle in this region. Quick calculation could provide a primitive impression of such claim. Calculation of the dynamic pressure at the downstream of the diffused for typical operating conditions indicate that it is on the order of 1 % of the static pressure, so losses due to flow separation in this region should be small.

3.4 Analytical study

Figure 3.3 illustrates that according to design equations, the static pressure along the CRMC ejector duct gradually increases. The removal of shock compression has the potential to improve the ejector performance in terms of pressure lift ratio (P_{DE}/P_s) by more than 50 % relative to that of the conventional ejector (Eames 2002). However, it is not certain that the actual CRMC duct eliminates such shock series. Obviously, the absence of any shock compression in Figure 3.3 is due to the inherent assumptions of the theoretical model. The significance of eliminating shock waves from the CRMC duct is examined in the upcoming chapters.

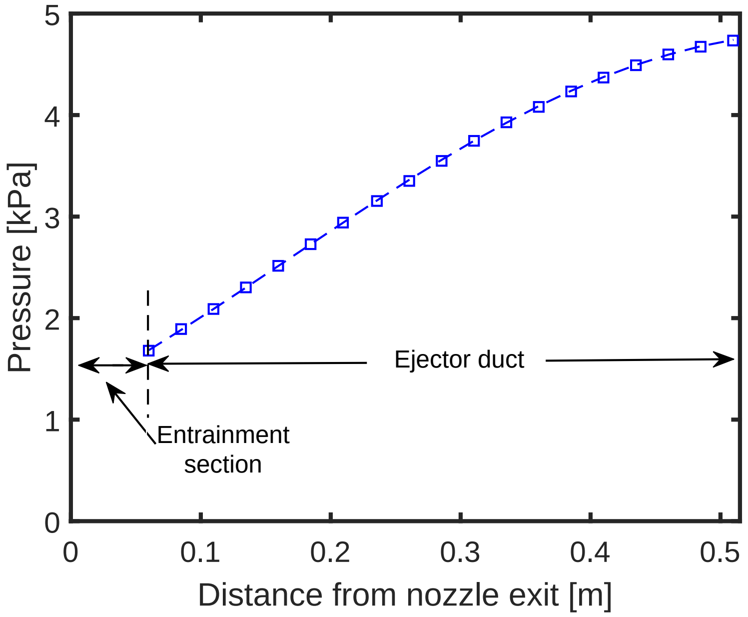

Figure 3.3: Pressure profile along the CRMC ejector duct at the design point.

Figures 3.4 and 3.5 depict the theoretical Mach number and velocity along the ejector duct. It is clear that both velocity and Mach number profiles have the same trend. The flow starts as a supersonic flow at the highest velocity of 403 m/s and Mach number of 2.67 at the nozzle exit plane. The flow then decelerates to sonic flow with velocity of 178 m/s and Mach number of unity at 290 mm downstream of the start of the ejector as the static pressure increases. The flow deceleration is maintained as the pressure rise continues to reach its highest value matching the back pressure at the exit plane.

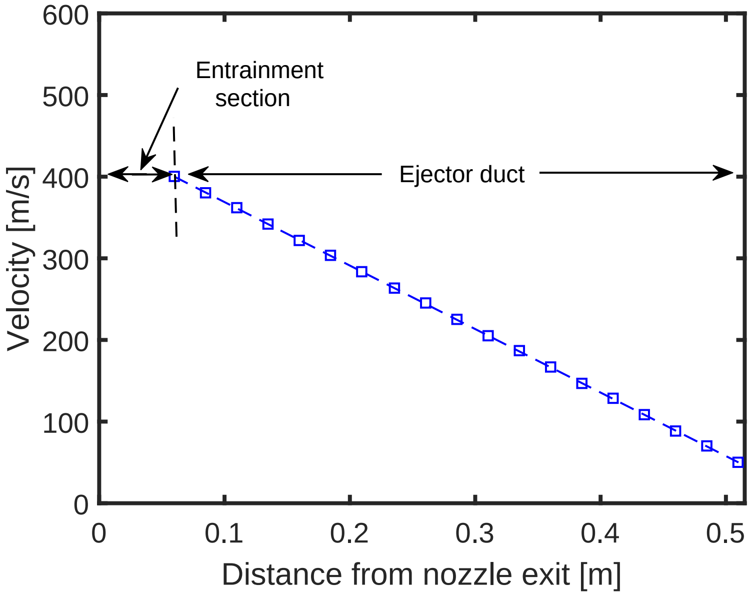

Figure 3.4: Velocity profile along the CRMC ejector duct at the design point, the nozzle exit is at the start of the ejector duct.

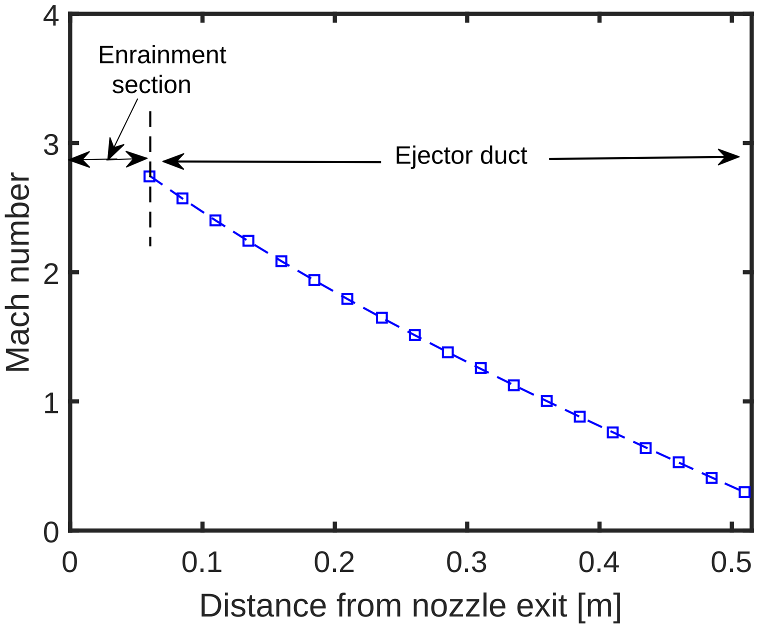

Figure 3.5: Mach number profile along the CRMC ejector duct at the design point, the nozzle exit is at the start of the ejector duct.

Figure 3.6 presents the CRMC ejector and its expected flow characteristics. Relative to the conventional ejector characteristic (as illustrated in Figure 1.1), it is anticipated that upstream of the nozzle exit position, both ejectors will behave in a similar way. Downstream of the nozzle exit position, the pressure and velocity changes of the proposed configuration are gradual, rather than sudden changes as shown for a conventional ejector in Figure 1.1. The sudden increase in static pressure and sudden decrease in velocity between planes 3 and 4 in Figure 1.1 is expected to be a gradual in CRMC flow behaviour.

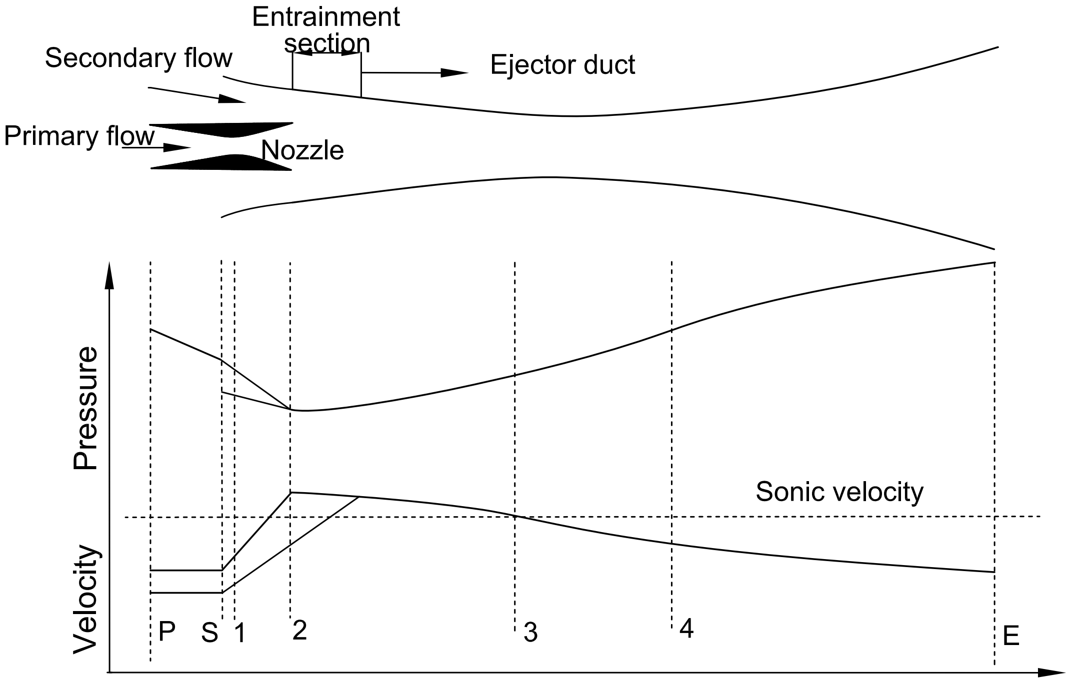

Figure 3.6: Flow characteristic into the CRMC ejector.

3.5 Chapter Summary

A supersonic ejector duct based on CRMC theory was designed. Assumptions were made and gas dynamic equations were used based on work by Eames (2002). Air was specified as the working fluid. The design point was chosen to match previous studies of a conventional supersonic ejector by Al-Doori (2013). The ability of the theoretical model to predict accurately the global and local parameters is under investigation.

Chapter 4

Apparatus design

4.1 Introduction

A new experimental facility was built at the University of Southern Queensland to investigate the applicability of the CRMC theory and to understand the flow behaviour inside the ejector and evaluate its performance. The aim was to establish an apparatus which could be used in the present work, and in future programs to support researchers to further investigate the parameters of the primary and secondary streams and mixing behaviour within the ejector duct. The apparatus is an assembly of four subsystems: the ejector and it accessories, the compressed air system, and vacuum system and the supporting measurement devices, controls and data acquisition system.

This chapter focuses on the design of the apparatus of the ejector, based on Constant Rate Momentum Change (CRMC) theory and the measurement methods used to characterise its performance. The apparatus was developed to evaluate the ejector performance using air at various operating conditions. A schematic diagram of the apparatus is given in Figure 4.1 showing the arrangement of the plumbing and instrumentation.

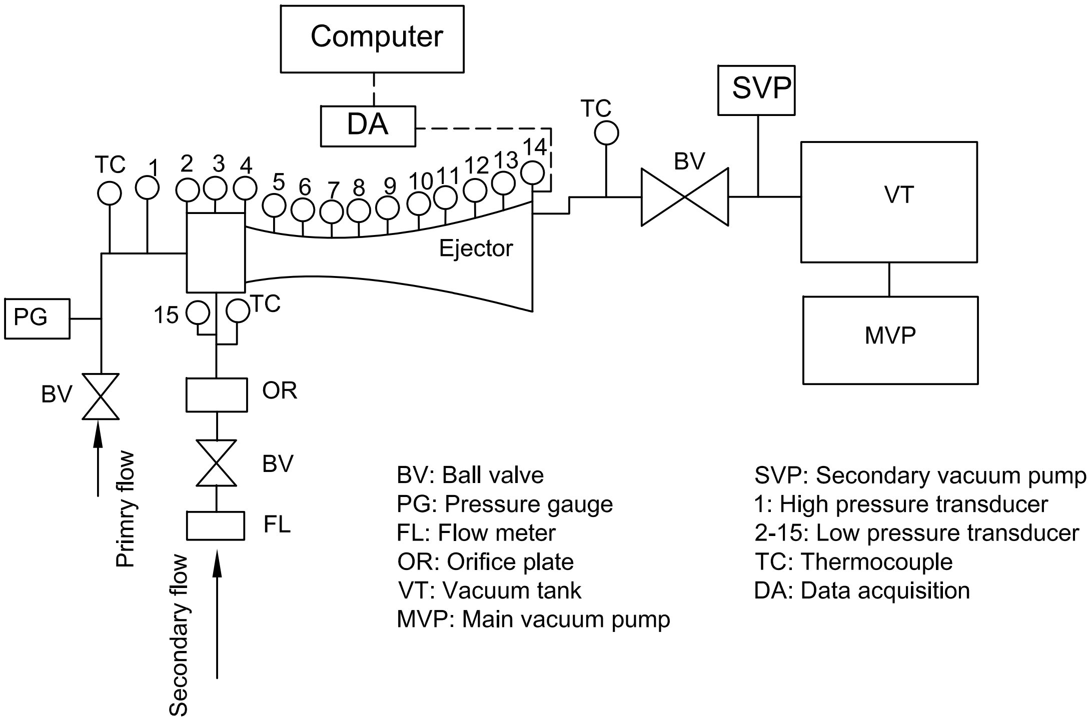

Figure 4.1: Schematic diagram of the CRMC ejector plumbing and instrumentation.

4.2 Apparatus layout

Figure 4.2 represents an assembly of the experimental rig taken from solid modelling software and in more details, Figure 4.3 represents an assembly of the experimental rig. A moveable primary nozzle (part 7) was included in the CRMC ejector system design. The nozzle exit position (NXP) can be varied in the longitudinal direction by moving the primary flow pipe (part 4). The NXP is defined as zero when the nozzle exit plane coincides with the commencement of the entrainment section (part 8) and is positive as the NXP moves downstream into the ejector to reach its limit position of 60 mm at the commencement of the CRMC duct section (parts 9-14).

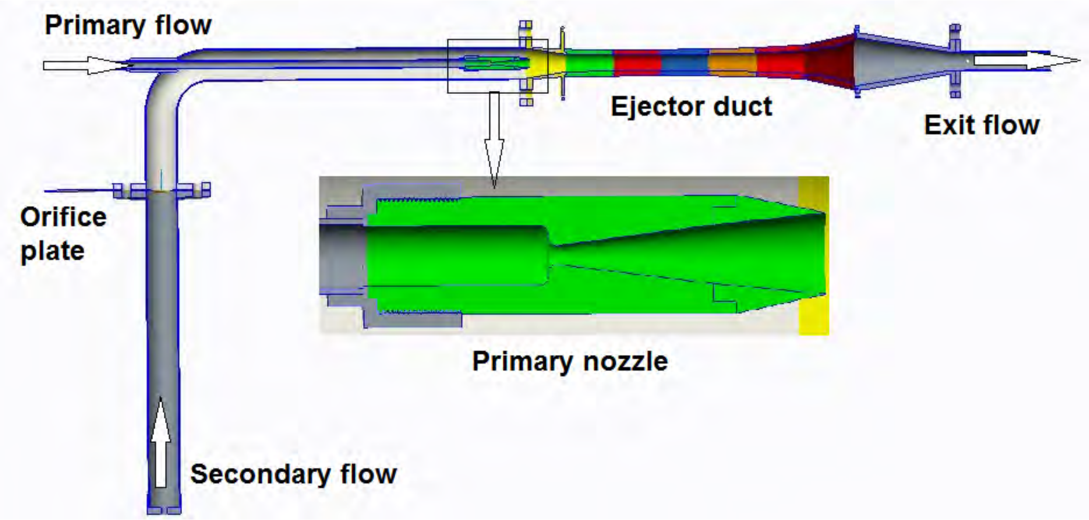

Figure 4.2: CRMC ejector arrangement with main parts illustrated using solid modelling.

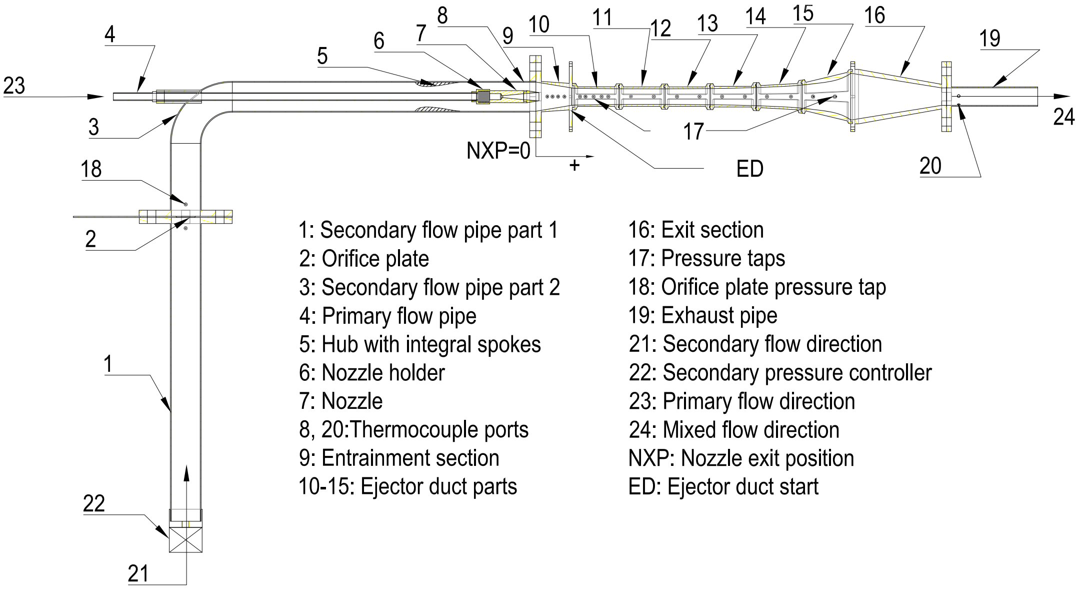

Figure 4.3: Schematic diagram of the CRMC ejector with main parts illustrated.

It should be noted that, for this experimental investigation, the apparatus was developed as an open-loop system with air as the working fluid. The primary air flow is controlled by a ball valve and pressure regulator to provide the desired pressure and flow rate. Initially the air flow rate was measured by a variable area flow meter type FMA-2600A-OMEGA with an accuracy of 2 % (OMEGA User's Guide). The temperature of the working fluid at various points in the ejector was measured by K-type thermocouples.

The primary temperature was essentially constant over the experimental program so a correlation between primary pressure and primary mass flow was established to replace the need for a dedicated flow meter on the primary flow line. Details of this correlation development are explained in Section 4.8.2. The entrained air is drawn from room conditions. The ejector is connected to the vacuum system through a ball valve. The minimum possible pressure was maintained at the ejector outlet with the addition of a secondary vacuum pump as shown in Figure 4.1. A ball valve at the ejector exit allows control of the exit flow pressure. The temperature of the mixture exiting the ejector is measured by a K-type thermocouple located on the line upstream of the ball valve. The data is collected through a National Instruments Compact data acquisition (cDAQ) system. The data acquisition system is presented in more detail in Section 4.9.

4.3 Primary nozzle

The performance of the ejector is governed by the mixing process between primary and secondary flows. Boosting the mixing process requires a well-designed nozzle geometry. Al-Doori (2013) designed a convergent-divergent primary nozzle to deliver high pressure steam to an ejector in a refrigeration system. That primary nozzle was designed according to the ESDU (1986) recommendations with the target of delivering 12.75 kg/hr of steam at a stagnation pressure and temperature of 200 kPa and 298 K. In the present study air was used as a working fluid but the same nozzle shape was used as in Al-Doori (2013)'s work.

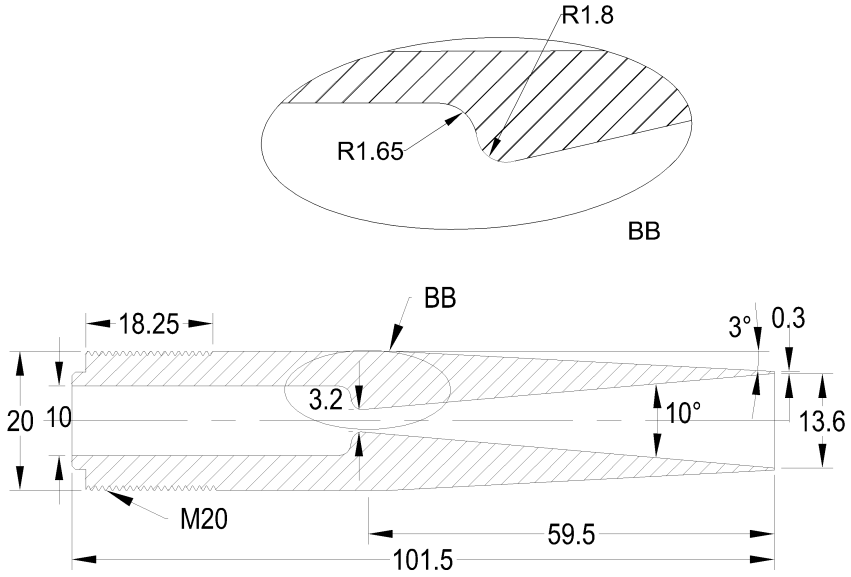

Figure 4.4: Profile of the primary nozzle with overall dimensions (all dimensions in mm).

Part 7 in Figure 4.3 refers to the primary nozzle which was fabricated from VisiJet Crystal material and was manufactured in the USQ workshop using the Multi-Jet-Modelling (MJM) Technology, 3D printers type ProJet^{TM}HD 3500. Table 4.1 presents the specifications of the 3D printer machine.

Table 4.1: Main specifications of 3D printer Type ProJet^{TM}HD 3500.

Feature	Definition
Printing mode	High Definition
Net build volume (xyz)	298 x 185 x 203 mm
Resolution	375 x 375 x 790 DPI (xyz); 32μ layer
Accuracy	0.001-0.002 mm
Build material	VisiJet®Crystal
Support material	VisiJet®S300
Operating temperature range	18-28 °C
Input data file formats	STL and SLC

The chosen 3D printer technology produces high definition parts and smooth surface finish which minimize the friction losses in the flow. Creo parametric 2.0 software was used to produce the file used by the 3D printer. Dimensioned drawings of the nozzle are presented in Figure 4.4 and in Appendix A. A photograph of the nozzle is shown in Figure 4.5. Table 4.2 presents the properties of the material used in producing the nozzle.

Figure 4.5: Photograph of the primary nozzle produced by the 3D printer.

Table 4.2: VisiJet material specifications

Properties	Specification
Density @ 80 ^oC (liquid), g/cm^3	1.02
Tensile strength, MPa	42.4
Tensile modulus, MPa	1463
Elongation at break point, %	6.83
Flexural strength, MPa	49
Heat distortion temp @ 66 psi, ^oC	56

4.4 Primary flow line

The convergent-divergent primary nozzle was mounted in the threaded holder as shown in Figure 4.3, part 6, which is shown in greater detail in Figure 4.6 and in Appendix A.

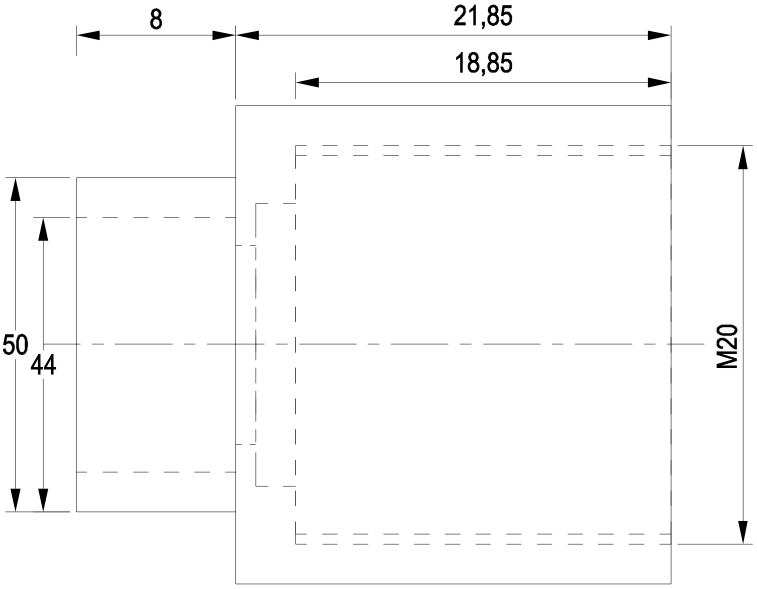

Figure 4.6: Holder of the primary nozzle with main dimensions (all dimensions in mm).

The primary nozzle holder as illustrated in Figure 4.6 was fabricated in the USQ workshop using a brass alloy material. The primary nozzle holder was connected to the movable 10.5 mm inside diameter, copper primary flow pipe (part 4 Figure 4.3) allowing the axial adjustment of the nozzle relative to the CRMC ejector duct.

A scale was placed on the primary flow pipe to provide a reference for the locations of the primary nozzle exit position from the end of the secondary flow pipe, part 3 in Figure 4.3. It is important to ensure that the nozzle is centred along the ejector duct axis by the primary nozzle and the primary flow pipe being concentric and coaxial. The primary flow pipe is connected to a shop air source via a ball valve and pressure regulator as shown in Figure 4.1.

To centralise the primary pipe, a 3D printed part referred to as a “hub with integral spokes” as shown in Figure 4.7 and in Appendix A was used. The hub with integral spokes is part 5 in Figure 4.3 and allows for the external movement required to alter the position of the nozzle. The shape of the hub with integral spokes minimizes the disruption to the secondary flow. A photograph of the device is presented in Figure 4.8.

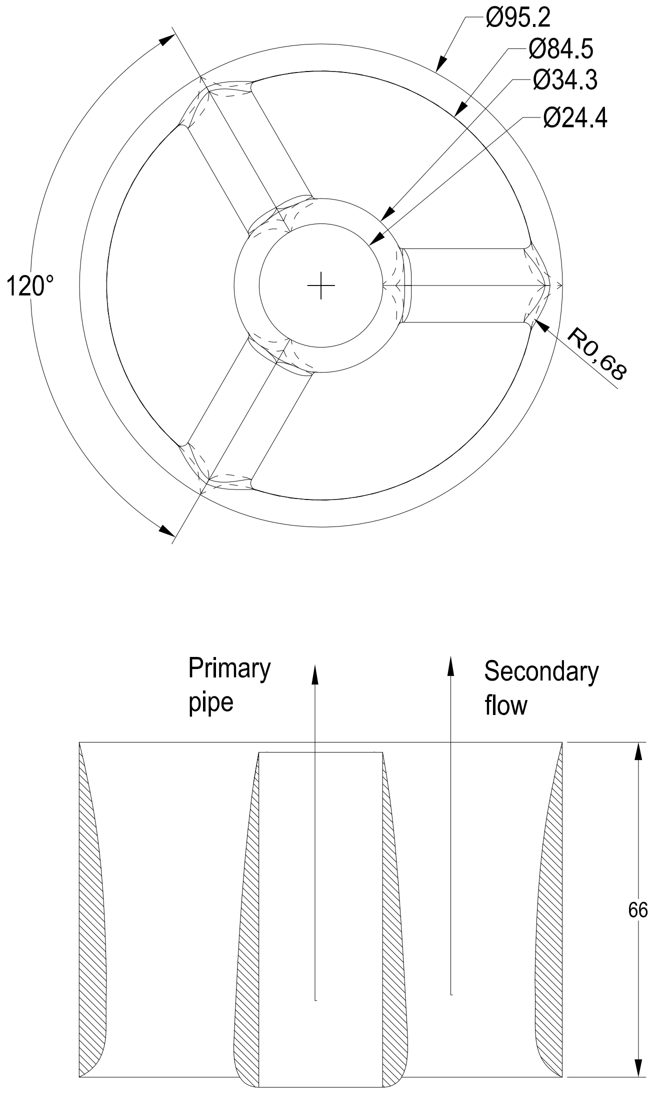

Figure 4.7: Profile of front view and section of side view of the hub with integral spokes with overall dimensions (all dimensions in mm).

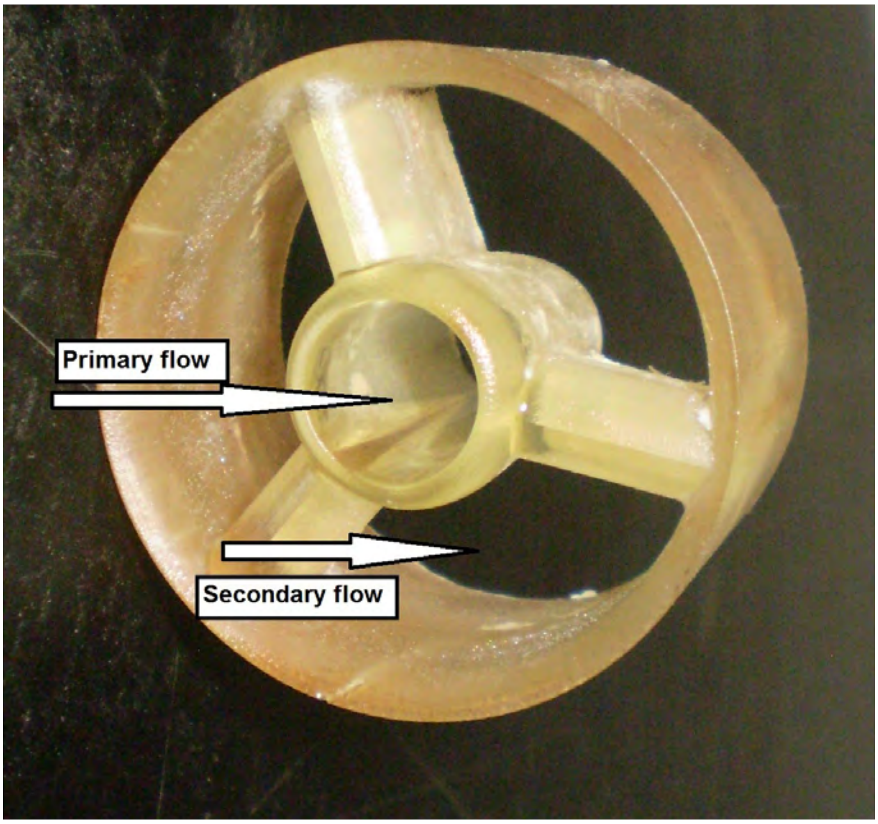

Figure 4.8: Photograph of the centralising hub with integral spokes.

4.5 Secondary flow

The primary flow pipe passes through a 800 mm long and 48 mm diameter bent secondary pipe as shown in Figure 4.9 and in Appendix A. This results in an annular volume between the outer surface of the primary flow pipe and the inner surface of the secondary flow pipe. The area of the annular section is 1676 mm^2. The secondary flow enters this pipe via a ball valve and flow meter in order to monitor and control the secondary mass flow rate entering the ejector duct. To minimize the pressure losses due to friction forces between flow stream and conduit walls, attention has been paid to the conduit manufacturing process to avoid any obstacles that could cause a flow disturbance to the secondary flow and, therefore affected the ejector performance.

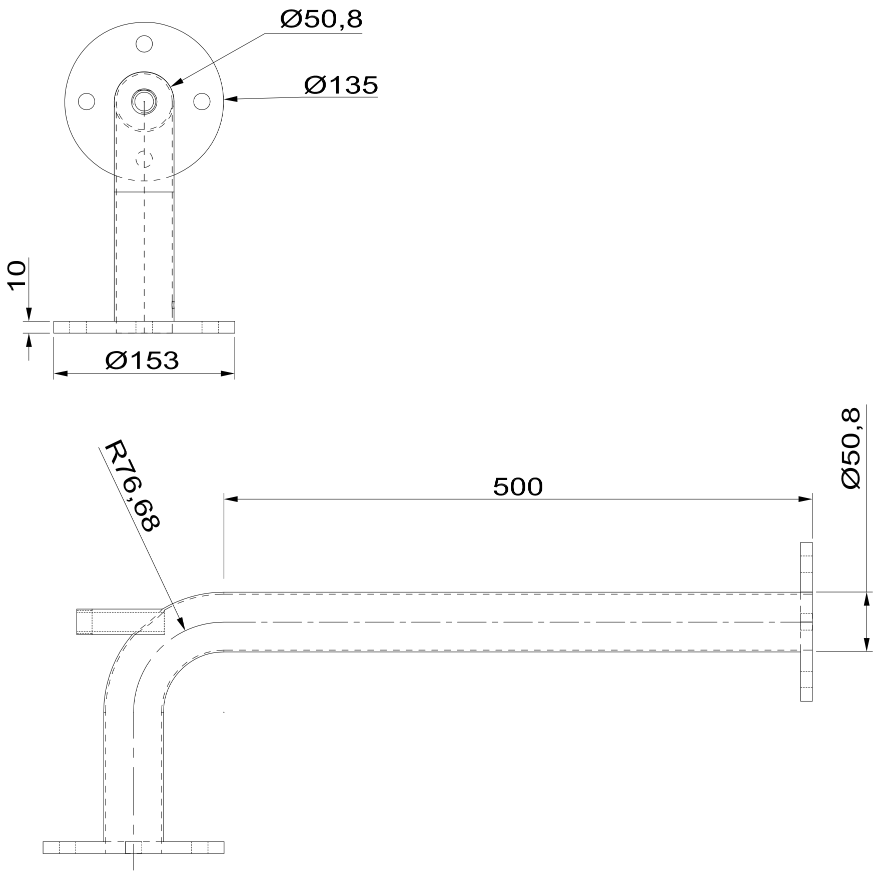

Figure 4.9: Secondary flow pipe, part 2 (all dimension in mm).

The secondary flow conduit consists of two flanged parts: the upper part which is referred to by number 3 in Figure 4.3 and is shown in more details in Figure 4.9 and the lower part which is referred to by number 1 in Figure 4.3 and is shown in greater detail in Figure 4.10 and in Appendix A. The orifice plate was positioned between the flanges of the upper and lower parts for the measurement of the secondary flow rate accessing the ejector duct through the secondary flow line. To control secondary flow pressure, a $\frac{1}{4}$ inch ball valve was used. A 40 cm long extension handle was used on the ball valve to improve the precision in maintaining the secondary pressure at its set point, which was achieved through manual adjustment.

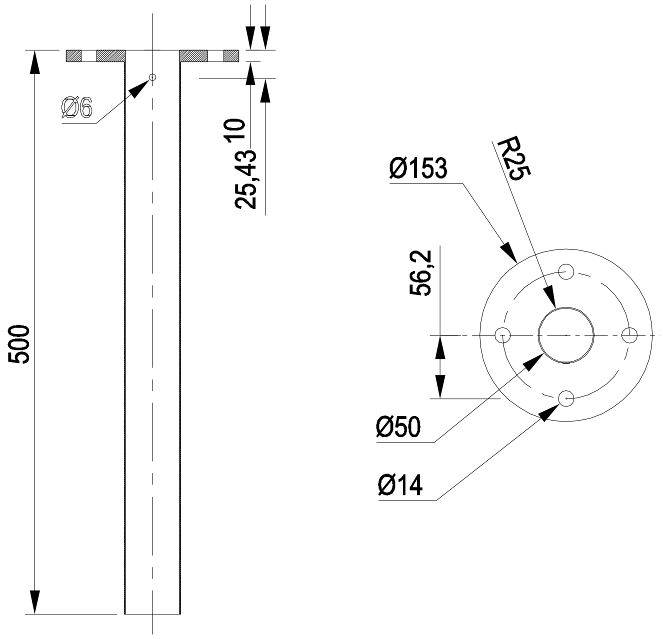

Figure 4.10: Secondary flow pipe (part 1) profile of the secondary flow line (all dimension in mm).

4.6 Secondary inlet

To enhance the ejector performance, minimizing the pressure losses of the secondary flow entering the entrained section is important. The secondary flow enters the entrained section through an annular gap between the primary nozzle and the ejector body. This region is usually referred to as the secondary inlet. Yadav & Patwardhan (2008) have shown that the geometry of the secondary inlet section has a significant effect on the ejector performance. The secondary flow inlet should be very smooth and sharp constrictions or expansions should be avoided. ESDU (1986) indicates that the secondary inlet can have a conical shape and the best cone full angle lies between 20° and 40°. High friction losses, however, are associated with a long conical shape which could cause undesirable pressure losses in this section. To enhance the ejector performance it is necessary to minimize these losses. As a result, the secondary inlet should be as short as possible (Kastner & Spooner 1950). A conical contraction full angle of 20° has been selected.

To investigate the flow behaviour inside the area upstream of the ejector duct and to obtain the required static pressure data, 4 pressure tappings were made in the secondary inlet section wall as shown in Figure 4.3, parts 17. The diameter of the pressure taps was 1 mm and these were connected to the low pressure transducers. The inlet section was connected to the secondary flow line using two bolted flanges. A 60 mm diameter O-ring was used to seal the joint flanges to ensure that there is no air leakage through the gap between the two flanges. Figure 4.11 shows the main dimensions of the entrainment section.

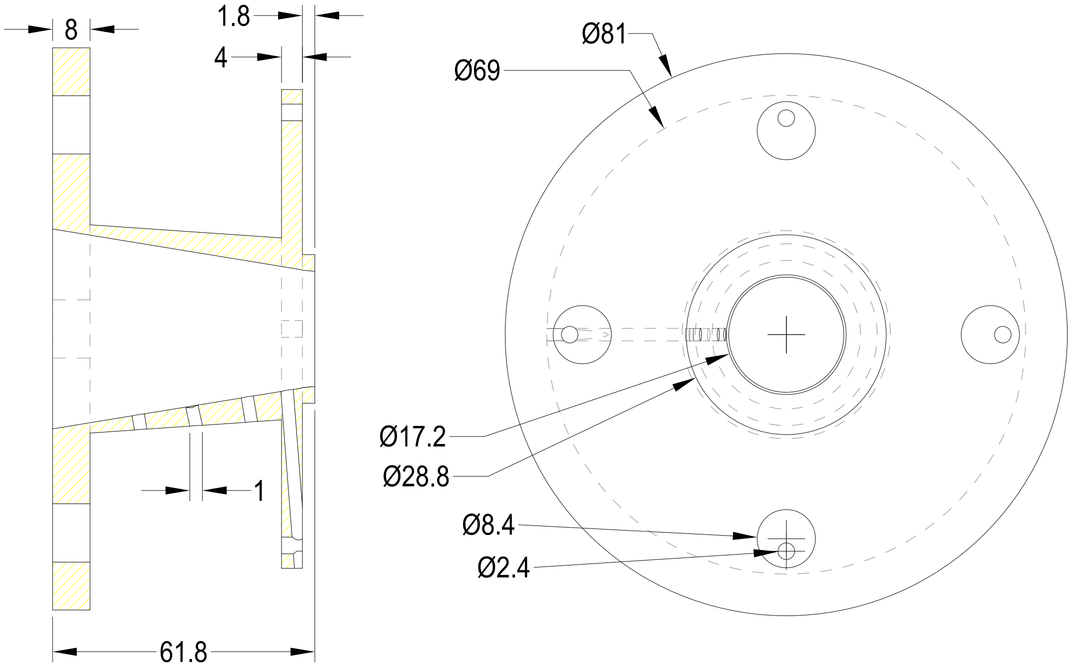

Figure 4.11: Profile of front view and section of side view of the entrainment section with main dimensions (all dimensions in mm).

4.7 CRMC ejector duct manufacturing

The CRMC duct was designed in an effort to reduce the pressure losses due to shocks with the flow compression in the ejector duct. VisiJet®Crystal material was used to fabricate the CRMC duct using a 3D printer Type ProJet™HD 3500. The main specifications of this printer are given in Table 4.1. The CRMC design was reported in Chapter 3, identifying the geometry of the new configuration.

The CRMC duct was modelled using PTC Creo parametric 2.0 solid modelling software. Material was trimmed from the ejector duct parts to reduce the cost of manufacture but the required overall strength of the design at the ejector operating conditions was also a consideration. Figure 4.12 shows the Creo model for the part 1 of the ejector duct.

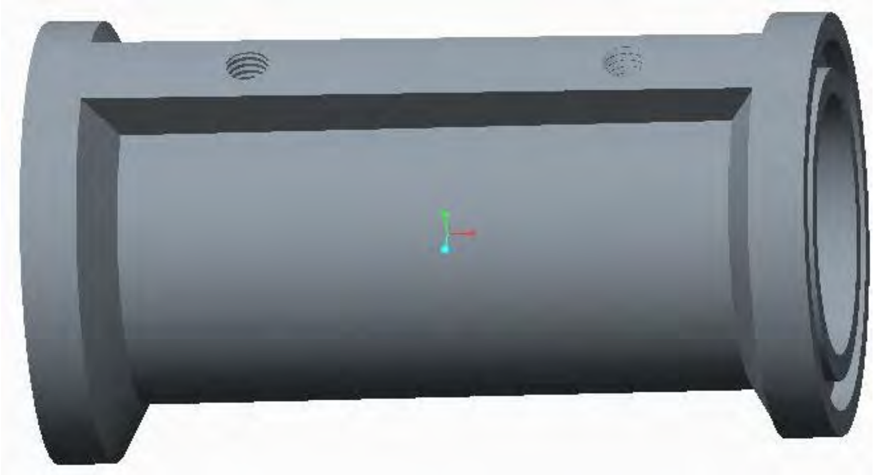

Figure 4.12: Model of CRMC ejector part 1.

The total length of the CRMC ejector duct design is 455 mm. The duct was built in several sections because of the limited print-size available on the printer and to reduce the cost and time to print.

The ejector duct was built in six parts, the first five parts at 75 mm long each, and part 6 at 80 mm long. Dividing the ejector into many parts also makes it easy to change and re-fabricate each part separately if needed. In order to measure the static pressure along the ejector duct wall, 16 pressure tappings of 1 mm diameter were made in the ejector wall as part of the print process. Parts 9 to 15 in Figure 4.3 refer to the ejector duct parts.

The first pressure tap was positioned at 25.6 mm, then the distance between pressure taps was set to 37.5 mm, placing the last tap at 36 mm up stream of the ejector exit edge. Figure 4.13 shows the assembly of ejector duct and pressure tappings. Three additional pressure tappings were positioned in the first part of the ejector duct (part 10) and three pressure tappings were placed in the entrainment section (part 9). More details can be found in Appendix A.

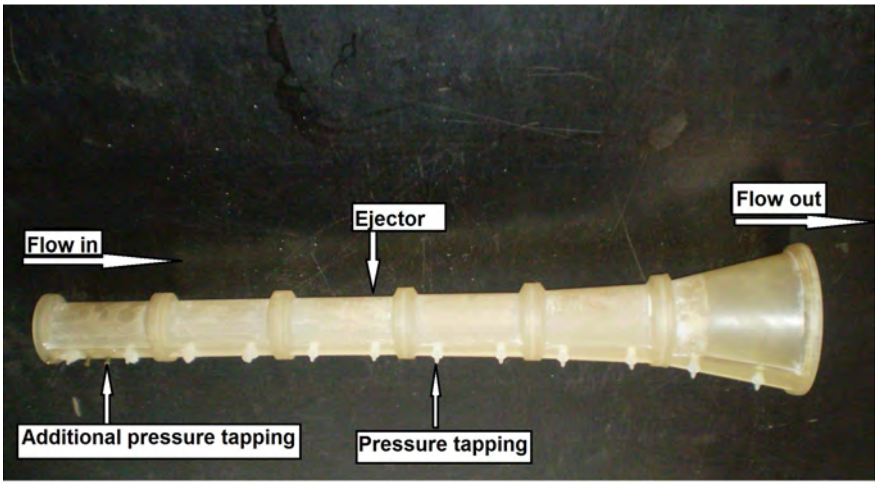

Figure 4.13: Photograph of the assembled CRMC ejector.

4.8 Measurement arrangement

The instrumentation in this apparatus consists of flow meters, pressure transducers and thermocouples.

4.8.1 Flow meters

The two key parameters in the ejector performance are the entrainment ratio and the compression ratio. The entrainment ratio represents the ratio of secondary mass flow rate to the primary mass flow rate as given in Equation 1.1. To measure the primary mass flow rate, a laminar flow mass flow meter (FMA-2600A-OMEGA) with a maximum operating line pressure of 1 MPa was used. The voltage output of the flow meter was usually around 0.01 Vdc for zero flow and 5 Vdc for full-scale flow. The output voltage is linear over the entire operating range of the meter. To ensure that the best possible device accuracy was obtained, a 50 micron filter on a pressure regulator was installed upstream of the flow meter to eliminate/minimize any debris and/or water droplets in the air flow which may affect the device accuracy. However, because the primary flow was always choked at the nozzle throat, the flow meter was replaced by a correlation between the pressure and mass flow rate in the primary stream line as it will be explained in Section 4.8.2. Using this correlation allowed the flow meter to be used on the secondary flow line. Table 4.3 shows the main specifications of the flow meter used in the present work and Figure 4.1 shows its position in the experimental rig.

Table 4.3: Flow meter FMA-2600A-OMEGA specifications

Type	Specification	Description
Accuracy	±(1 %)	of reading
Operating temperature	-10 ~ 50	°C
Maximum pressure	1	MPa
Typical response time	100	Millisecond
Humidity range	0 ~ 100 %	Non-condensing
Standard conditions (STP)	25°C & 14.696 PSIA	Mass reference conditions
Input/Output signal	Mass flow	0 ~ 5 Vdc

4.8.2 Pressure transducers

The second major part of the measurement system is the pressure transducers. Two types of pressure transducers were used in the present work, high and low-pressure range transducers. The high-pressure range transducers were type Wika 10-A series and these were used to measure the primary static pressure. Further, due to limited availability of flow meters, pressure readings were used to indicate the flow rate in the primary stream. A linear correlation between pressure and mass flow rate in the primary flow line using the flow meter was developed and is shown in Figure 4.14. This allowed the one available flow meter to be used on the secondary flow line.

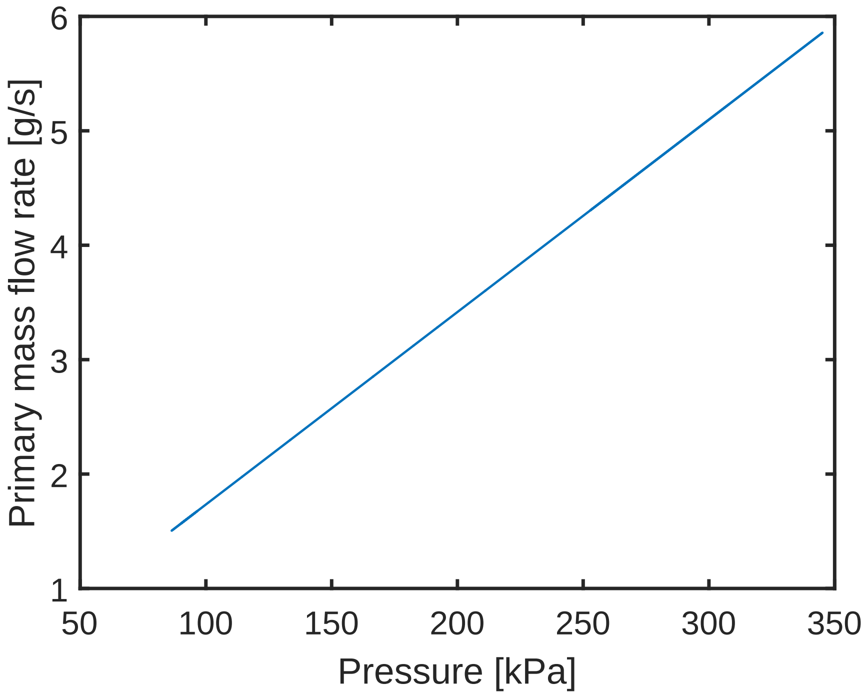

Figure 4.14: Correlation between primary stream mass flow rate and primary pressure.

Six low-pressure transducers type BSDX series (Manufacturer: Sensortechnics GmbH) were used in the present work. Three pressure transducers were placed in the entrainment section (part 8) and three others were placed in the first part of the ejector duct (part 9). The BSDX series pressure transducers were used due to their high frequency response as reported in Manufacturer Data Sheet. The BSDX series pressure transducers are highly sensitive to the input power as reported in Manufacturer Data Sheet, thus the supplied voltage for the BSDX transducers was set at 5.00 V while, for the Wika series which, are not sensitive to the precise supply voltage, a value of 15 V was used.

The pressure transducers were connected to the ejector stream line via 1 mm diameter plastic hose as illustrated in Figure 4.15. The connection technique only provided accurate readings of the static pressure distribution along the ejector wall for quasi steady state operation. More details can be found in Appendix B.

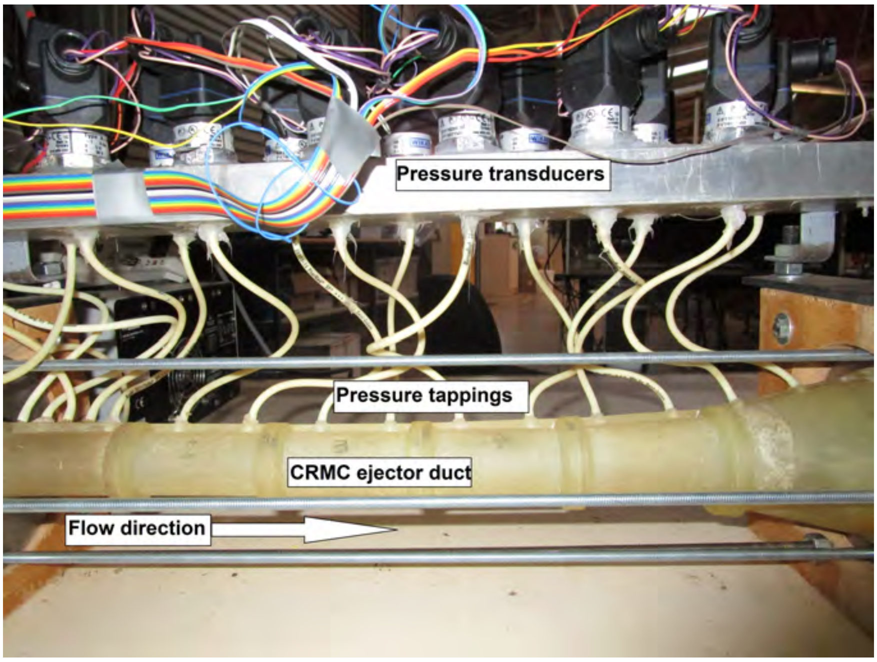

Figure 4.15: Photograph of assembly of CRMC duct with pressure transducers connected.

Table 4.4 shows the major specifications of the three types of pressure transducers and Figure 4.1 illustrates their positions in the ejector system.

Table 4.4: Major specifications of three types of pressure transducers

Type	Pressure bar	Voltage V	Temperature $^{\circ}C$	Accuracy %
Wika A-10 H.P.	$0 \sim 7$	$14 \sim 30$	$-30 \sim 80$	0.5
Wika A-10 L.P.	$0 \sim -1$	$14 \sim 30$	$-30 \sim 80$	0.5
BSDX L.P.	$0 \sim -1$	5.00	$-20 \sim 105$	$0.5 \sim 1$

4.8.3 Thermocouples

Nickel-chromium/nickel-aluminium (type K) thermocouples were used to measure the temperature at two locations, first at the inlet of the secondary flow which represents the static temperature of the secondary stream and secondly, at the ejector exit position which represents the mixed flow stagnation temperature at the ejector duct exit. Room-temperature air was used as the working fluid so temperature variations were minimal. The positions of the thermocouples within the ejector system is illustrated in Figure 4.1. More details can be found in Appendix B.

4.9 Data acquisition

All pressure transducers and thermocouples were wired to a National Instruments Compact Data Acquisition (cDAQ) system. A program was written using National Instruments LabView which interfaces via the NI-DAQ drivers and USB. The system consists of chassis NI 9178 with a number of signal conditioning amplifiers and analogue to digital conversion modules. The first group of two NI 9223 4-Channel ($\pm$ 10 V, 16Bit simultaneous analogue input) modules was connected to the Wika pressure transducers and sampled at a frequency of 100Hz. The second group of modules included one NI 9205 32-Channel ($\pm 10\,\text{V} \sim \pm\ 200\,\text{mV}$, 16-Bit analogue input) module which was used for the BSDX pressure transducers and two sets of NI 9219 4-Channel universal analogue inputs, both of them operating at 100Hz to convert thermocouple readings to digital values representing degrees Celsius and volts. Output voltage signals were converted to required pressure data using correlations from calibration data presented in Chapter 5.

4.10 Chapter summary

A new apparatus for supersonic ejector experiments based on the CRMC theory has been developed for research at the University of Southern Queensland. A combination of software and hardware tools were used to model and fabricate the convergent-divergent nozzle, CRMC ejector, primary flow line, secondary flow line, discharged flow line, and other parts.

High pressure transducers and two types of low pressure transducer were used in the experimental rig. Measuring devices for mass flow rate, high pressure, low pressure, and temperature with a data acquisition system were connected to the apparatus. All these devices were calibrated prior to use. As air is the working fluid, the system facilitates future work in various aspects of ejector flow analysis including flow visualisation to investigate the flow behaviour inside the ejector.

Chapter 5

Preliminary tests

5.1 Chapter Overview

This chapter describes initial experiments and results for the basic performance of the CRMC ejector duct. Preliminary tests reported in this chapter, were carried out prior to the main tests reported in Chapter 6. Multiple tests of the set up were completed to confirm function, control options, and data acquisition capabilities. System reliability and stability in operation at varying operating conditions were confirmed. Tests were conducted three times at each operating condition to confirm if reliable results were being obtained. All the experiments were conducted using air as the working fluid.

5.2 Flow facility

Figure 5.1 shows a photograph of the experimental installation in its operating conditions. Descriptions of individual components of the apparatus and their specifications with an explanation of their roles in the system were given in detail in Chapter 4.

A pressurized air source from the laboratory's shop-air supply was used as the regulated pressure supply for the primary flow to the experimental rig. This allowed a continuous operation of the ejector at given operating conditions for a limited, but sufficient time.

The pressurized primary air was filtered to remove impurities such as debris, dust and oil droplets by using a pressure regulator with integral filter in series with the primary supply regulator.

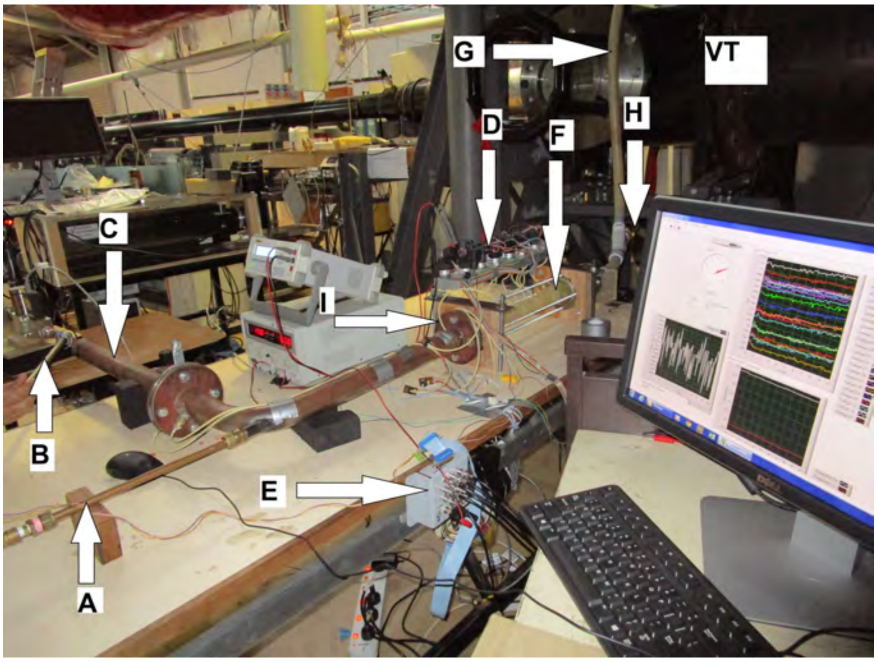

Figure 5.1: Photograph of the experimental apparatus with supporting components: (A) primary supply line, (B) secondary flow control lever, (C) secondary supply line, (D) pressure transducers, (E) data acquisition (F) ejector duct, (G) outlet line connected to vacuum tank (H) outlet connected to secondary vacuum, (I) secondary pressure tappings, (VT) vacuum tank.

The pressurized air is directed to the primary nozzle via the primary supply line. Primary pressure, P_p was controlled by the experiment's pressure regulator. The supply pressure regulator, upstream from the experiment's regulator, was set at approximately 100 kPa above the experiment's regulator pressure. Primary mass flow rate $\dot{m}_p$ was measured using a correlation to primary pressure that was produced experimentally as previously explained in Chapter 4.

The primary flow is accelerated in the convergent-divergent nozzle before entering the mixing chamber. Due to the primary flow expansion, a low pressure region is created near the nozzle exit plane and thus, the secondary flow is induced. The secondary flow is air taken from surrounding atmosphere through a ball valve located at the entry of the secondary flow pipe to regulate the secondary pressure.

A flow meter Omega-FMA-2600A was used to measure the secondary mass flow rate $\dot{m}_s$ with specification as reported in Chapter 4. In the entrainment section, primary flow and secondary flow mix together and within the CRMC duct, a gradual pressure increase occurs. Finally, the mixed flow leaves the ejector system with an elevated pressure at the ejector exit.

Sixteen Wika pressure transducers model 10-A and seven Sensortechnics GmbH pressure transducers model BSDX were connected to the pressure taps located along of the ejector wall to provide static pressure data. The output voltage signals from the pressure transducers were converted to a pressure value using correlations produced experimentally by calibrating the transducers individually. Calibration was completed using a Budenberg dead-weight tester model 550 as shown in Figure 5.2. Table 5.1 shows the correlations resulting from the calibrations.

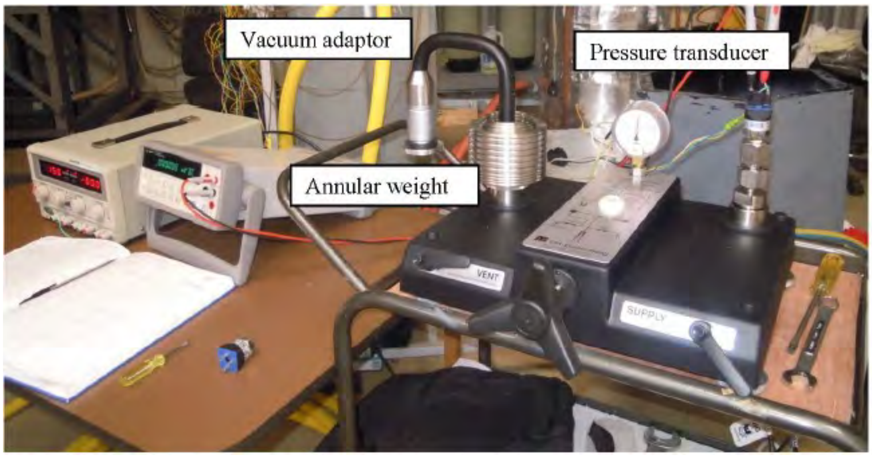

Figure 5.2: Pneumatic dead weight tester in the sub-atmospheric testing arrangement.

Table 5.1: Calibration of Wika and Sensortechnics GmbH pressure transducers. V_{meas}= measured voltage. Voltage in Volt, and pressure in kPa.

	Serial number	Pressure	Equation
1	110263XV	H.P	Pa=120.59V_{meas}-1.5289+Patm
2	1102HF3P	L.P	Pa=20.132V_{meas}-101.15+Patm
3	1102HF3L	L.P	Pa=20.113V_{meas}-100.92+Patm
4	1102HF3B	L.P	Pa=20.087V_{meas}-100.4+Patm
5	1102HF3C	L.P	Pa=20.087V_{meas}-100.91+Patm
6	1102HF3I	L.P	Pa=20.092V_{meas}-101.18+Patm
7	1102HF3M	L.P	Pa=20.13V_{meas}-101.297+Patm
8	1102HF3N	L.P	Pa=20.076V_{meas}-100.67+Patm
9	1102HF3O	L.P	Pa=20.07V_{meas}-101.19+Patm
10	1102GF3E	L.P	Pa=20.066V_{meas}-100.2+Patm
11	1102HF3D	L.P	Pa=20.024V_{meas}-101.3+Patm
12	1102HF3F	L.P	Pa=20.038V_{meas}-101.23+Patm
13	1102HF3J	L.P	Pa=20.071V_{meas}-101.1+Patm
14	1102HF3K	L.P	Pa=20.102V_{meas}-101.1+Patm
15	1102HF3G	L.P	Pa=20.089V_{meas}-101.05+Patm
16	1102HF3H	L.P	Pa=20.107V_{meas}-101.1+Patm
17	BSDX1	L.P	Pa=21V_{meas}-105.2+Patm
18	BSDX2	L.P	Pa=21.2V_{meas}-103.3+Patm
19	BSDX3	L.P	Pa=21V_{meas}-105.1+Patm
20	BSDX4	L.P	Pa=21V_{meas}-105.2+Patm
21	BSDX5	L.P	Pa=21V_{meas}-105.1+Patm
22	BSDX6	L.P	Pa=21V_{meas}-105.27+Patm
23	BSDX7	L.P	Pa=21V_{meas}-103.91+Patm

Two Type-K thermocouples were used during testing. One was positioned at the inlet of the secondary line to measure the temperature of the secondary flow entering the ejector. To ensure that the recorded flow conditions are consistent, this thermocouple was positioned on the same plane of the secondary flow pressure transducer. The other thermocouple was positioned at the exit of the ejector flow. The flow meter also measured temperature and Figure 5.3 shows the comparison of the flow meter temperature reading and thermocouple over several tests. The readings of flow meter matches that of lab view very well which indicates essentially adiabatic flow conditions in the secondary inlet.

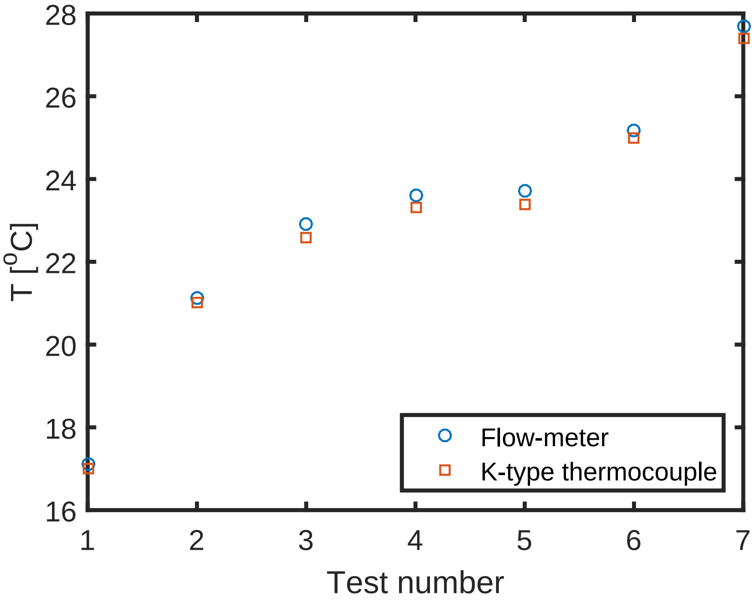

Figure 5.3: Secondary flow temperature recorded from flow meter and thermocouple positioned at the inlet of the secondary line.

A large dump tank (total volume of approximately $9\,m^3$) was available in the laboratory. The dump tank was evacuated to an absolute pressure of 0.5 kPa. The vacuum system provided enough vacuum volume to maintain test running times of between 200 and 300 seconds which was sufficient to collect the required data. The test running time was terminated by back flow in the ejector. In the present work, test running time depends on three parameters: (1) initial vacuum section pressure, (2) primary pressure, (3) and secondary pressure. The test running time varied directly with the secondary flow pressure, and inversely with the primary flow pressure and initial pressure in the vacuum tanks. Figure 5.4 shows test running time over a range of secondary pressure and primary pressure of 200 kPa, and Figure 5.5 shows test running time over a range of primary pressure at secondary pressure of 2.5 kPa.

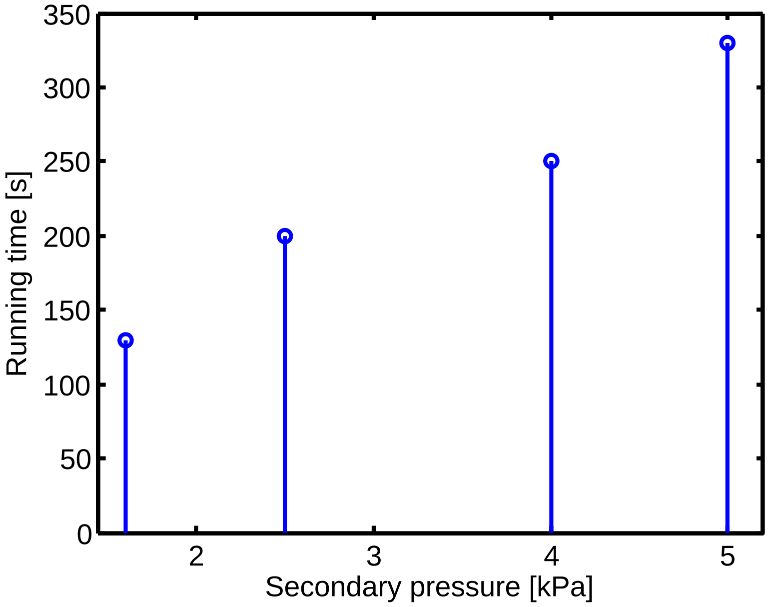

Figure 5.4: Test running time over a range of secondary pressure at primary pressure of 200 kPa.

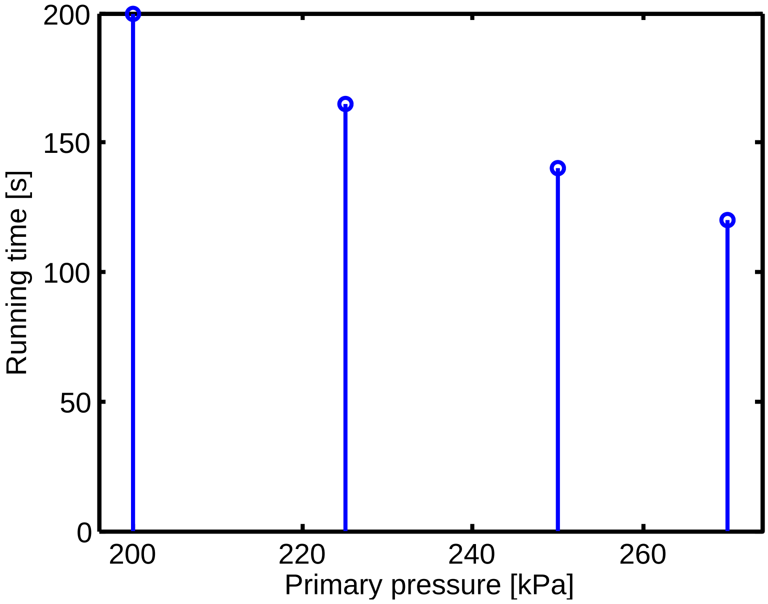

Figure 5.5: Test running time over a range of primary pressure at secondary pressure of 2.5 kPa.

The ejector exit was connected to the vacuum system via a $1\frac{1}{4}$ inch diameter and 1.2 m long flexible hose. The flexible hose was maintained as short as possible and the apparatus was positioned close to the test section to reduce the pressure losses within the ejector exit flow (see Figure 4.15) providing the maximum usable run time before ejector back flow resulted.

5.3 Preliminary test

Key fluid flow parameters at all inlet and outlet critical points of the ejector system at various operating conditions were measured experimentally. These parameters include primary stagnation pressure and temperature, secondary stagnation pressure and temperature, primary and secondary flow rates, entrainment ratio, and back pressure. In addition, it is beneficial to evaluate the influence of the nozzle exit position on the ejector performance as will be described in the following sections. The experiment's operation, reliability and reproducibility is established through comparison of multiple runs. To ensure that all the measuring devices were operating as required, preliminary tests were conducted prior to the main tests for each operating condition.

5.3.1 Setting operating conditions

The secondary pressure was measured with a transducer, part D in Figure 5.1. The secondary pressure was set by controlling the flow rate through the secondary flow controllable valve, part B. Changing the secondary flow rate was achieved by adjusting the secondary flow valve position.

Atmospheric pressure and temperature in the laboratory were obtained from a precision barometer and thermometer.

At a given atmospheric pressure, the output voltage of the secondary pressure transducer, which was displayed on the voltmeter, varied with the secondary pressure value at this point according to

$$V_s = \frac{P_s + 100.97 - P_{atm}}{20.102} \tag{5.1}$$

where:

V_s: output signal (Voltage) from pressure transducer [V]

P_s: targeted secondary pressure [kPa]

P_{atm}: atmospheric pressure [kPa].

This voltage value (and hence the pressure) was maintained constant by adjusting the position of the ball valve during the experiment as the back pressure increased with time due to mass accumulation in the dump tank.

The experimental system is evacuated by two different capacity vacuum pumps, a high capacity pump (MVT) which is connected to the vacuum section (VT), and a low capacity pump (SVP) which is connected directly to the ejector system. The evacuation process is carried on until the pressure reaches the required value which is typically around 0.5 kPa absolute pressure inside the section test. However, a pressure higher than this value is also acceptable, but the test running time would be reduced.

Once the vacuum pressure reaches the required value, pressurized primary air is supplied by opening the ball valve (BV). The primary pressure is controlled by a regulator (PGR). The secondary flow valve is then opened. All the key parameters such as the primary, secondary, wall and mixed flow pressures were recorded simultaneously by the LabView data acquisition system. Temperatures of primary, secondary and mixed flow in the most important locations along the ejector system were recorded as well. In addition, primary and secondary mass flow rates were recorded in the same way.

Each test was continued until the secondary flow rate was zero as it was displayed on the digital flow meter. The tests were terminated when the secondary flow ceased. The flow meter used in the present work is one-direction flow device which required that there is no reverse flow recorded during these tests.

The data acquisition system was set to record data 10 times per second. On average, the time required to complete each test was approximately 5 minutes, however, with no unexpected operational challenges, the turn around time could exceed 2 hours because of the time required to pump down the main vacuum tanks. Finally, at the end of the test, all valves were shut off simultaneously to protect the system and measuring devices from excessive high and low pressures.

5.3.2 Effect of the nozzle exit position on the ejector performance

The primary nozzle position in the ejector duct has a significant impact on the ejector performance. Small movements could cause a remarkable change in the performance (ESDU 1986). As the CRMC is a relatively new configuration, the optimal position of the nozzle in the CRMC ejector is not defined by ESDU. To determine the optimal position of the nozzle in the ejector system, seven locations of the nozzle exit were tested in the present study: 0, 10, 20, 30, 40, 50, and 60 mm. These dimensions refer to the quantity NXP which is defined as the distance from the upstream edge of the entrainment region to the primary nozzle exit. Table 5.2 shows results of different nozzle positions.

Table 5.2: Results for nominal primary pressure of 200 kPa and nominal secondary pressure of 1.6 kPa.

NXP (mm)	0	10	20	30	40	50	60
P_a (kPa)	94.78	94	93.8	94.18	94.13	94.3	94.25
T_p (°C)	25.5	24.4	23.6	25.56	23.6	22.58	22.5
T_s (°C)	25.2	24	23.2	25.1	23.2	22.1	22
T_o (°C)	24	22.12	21.5	23.5	21.19	20.4	20.26
P_p (kPa)	198.67	208	201	202.6	204.3	200.77	200.75
P_s (kPa)	1.59	1.65	1.64	1.62	1.57	1.51	1.65
P_c (kPa)	4.5	4.5	4.5	4.48	4.42	4.45	4.6
$\dot{m}_s$ (g/s)	1.18	1.26	1.22	1.28	1.212	1.16	1.12
ER	0.35	0.35	0.35	0.37	0.347	0.34	0.33

Atmospheric pressure variations affected the voltage readings from the transducers so it was necessary to record barometric pressure P_{atm} for each test. In addition, working fluid temperature also changes due to ambient temperature variations. The temperature of the primary flow is higher than that of the secondary flow in all tests which can be attributed to the slightly higher temperature of the pressurised primary flow rather than room temperature of the secondary flow. However such a slight temperature difference has no significant effect on the flow behaviour inside the ejector duct. From Table 5.2 it can also be seen that the critical exit pressure remains almost constant for different nozzle positions.

The targeted primary pressure for the tests included in Table 5.2 was 200 kPa and for the secondary pressure it was 1.6 kPa. Similar deviations can be observed in secondary pressure measured values. The maximum value of ± 4 % deviation in both primary and secondary pressures was obtained. Such deviations are associated with manually-setting the pressure regulator and control valve of the primary pressure and the secondary pressure respectively.

5.3.3 System stability

To correctly evaluate the ejector performance, the temporal stability of the primary pressure and secondary pressure needs to be high. Figure 5.6 represents the primary stream pressure during tests for nominal primary flow pressure of 200 kPa. The reading of the high pressure transducer at the condition of 200 kPa started with a pressure of 200.5 kPa and a ended with 199 kPa, indicating about 0.7 % reduction from its original value during the test time. Such a slight pressure reduction has no significant influence on the outcomes of the ejector testing. In addition, Table 5.2 shows that the variations in the primary inlet temperature are very minor, indicating that the pressurized air supplied to the system is relatively steady.

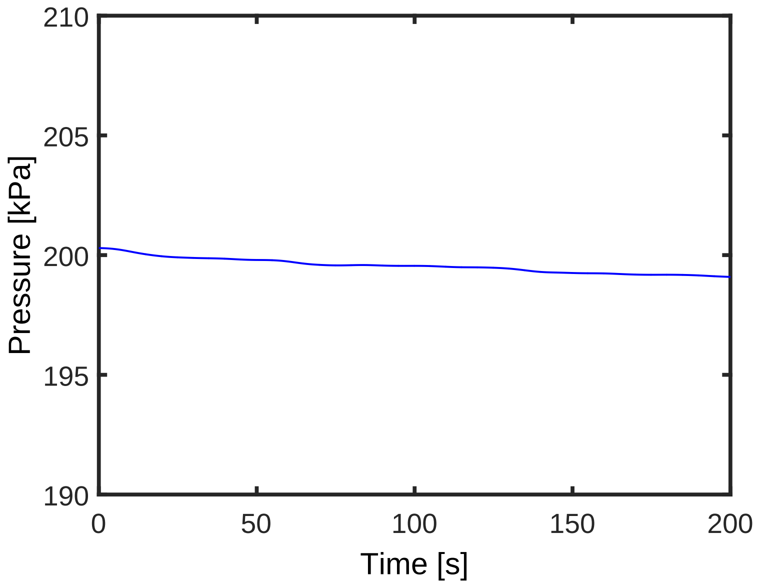

Figure 5.6: Example of stability of the primary pressure during the test time for a nominal primary pressure of 200 kPa.

Figure 5.7 represents the secondary stream pressure during tests for a nominal secondary flow pressure of 2 kPa. It can be seen that the secondary pressure is stable for ejector operation within the double-choking region. Beyond this time, the secondary pressure is less stable. As the ejector starts to operate at the unchoked region, the secondary pressure starts to increase, so to maintain the secondary pressure value approximately constant, the secondary flow is regulated manually by the control valve (part B in Figure 5.1).

The manually-regulated secondary flow valve is the major cause of the pressure fluctuations in the secondary pressure as observed in Figure 5.7. Some procedures have been implemented to minimize the pressure fluctuations during the test time such as using two pressure regulators on the high pressure line. In addition, on the low pressure line, fine tune adjusting of the control valve was an effective way to minimize the pressure fluctuation. Under these condition, the observed variations are within an acceptable range, and do not have a significant effect on the ejector performance that is deduced from the experiments.

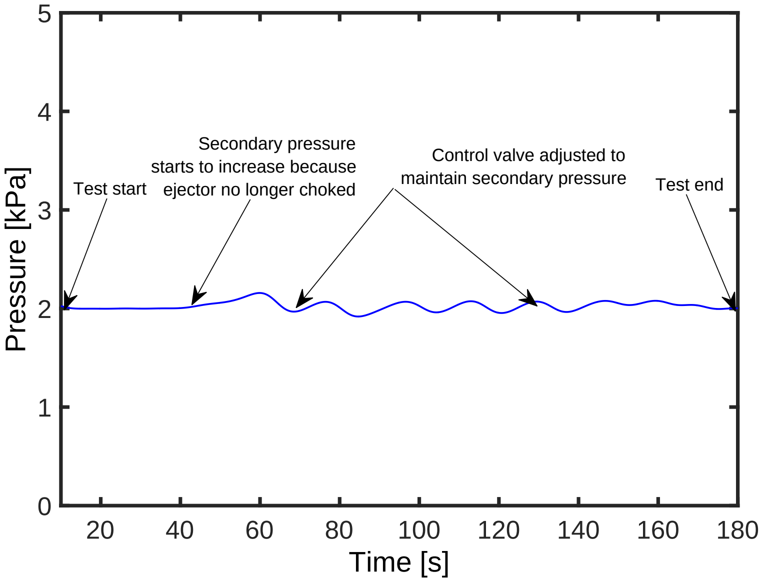

Figure 5.7: Example of stability of the secondary pressure during test time for nominal primary pressure of 200 kPa, and nominal secondary pressure of 2 kPa.

5.3.4 System repeatability

To ensure that the obtained experimental results were repeatable, each test was conducted three times for each single operating condition. Figure 5.8 shows static pressure distribution along the ejector wall at a choked operation mode for three tests with the same operating conditions. The results of the three tests are very close to each other, demonstrating test reliability.

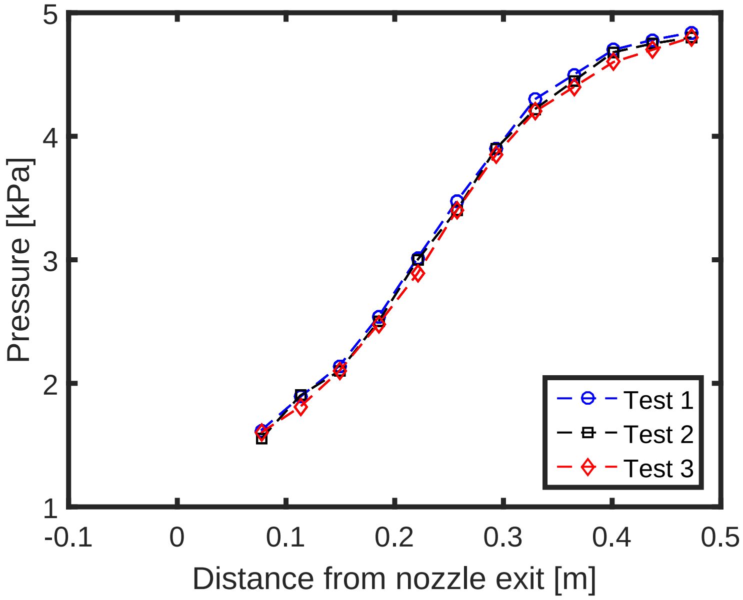

Figure 5.8: Wall pressure distribution for three experimental test results for the same nominal operating conditions of 200 kPa and 1.6 kPa for the primary and secondary pressure respectively.

Figure 5.9 shows that for the three repeated tests there is no measurable difference in the entrainment ratio in the choked flow region however, the difference in the unchoked flow entrainment ratio is around ± 4.5 %. The variability in terms of the critical back pressure amounts to approximately ± 5 %. These values are considered to indicate acceptably consistent operation of the ejector.

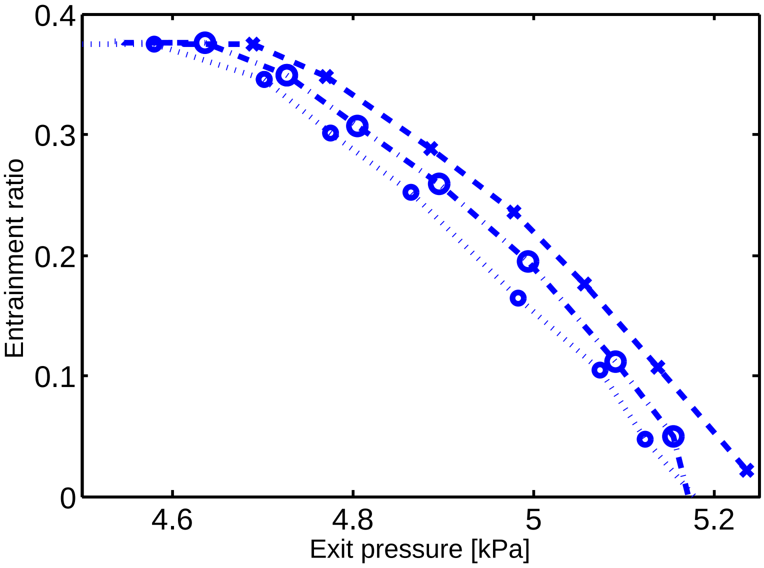

Figure 5.9: Entrainment ratio variation with exit pressure for three experimental tests with the same nominal operating conditions of 200 kPa and 1.6 kPa for primary and secondary pressure respectively.

To maintain the secondary flow rate constant, the valve is controlled manually and thus, it is hard to obtain a consistent secondary flow value for each test and this is considered the main contributor to the variability in the unchoked flow region. The uncertainty in the mass flow meter and the pressure transducers are less significant contributors to the observed variability.

5.4 Uncertainty analysis

Typical uncertainty values for the ejector parameters measured in the present experimental work are presented in Table 5.3. The mass flow rate of the primary stream is measured using a pressure-flow rate correlation as explained in Section 4.8.2. The pressure in this correlation was measured using a Wika 10-A pressure transducer. According to specifications, the accuracy of this type of pressure transducer is 0.5 %. The entrained flow rate is measured using a FMA-2600A-OMEGA flow meter with 1 % accuracy. Two types of pressure transducers are used to measure the pressures along the wall of the ejector flows, and the back pressure.

Laboratory temperature is considered as the primary flow temperature and is measured by the laboratory thermometer. The uncertainty of the barometer is 0.01 %. The temperature at the suction port and the exit port of the ejector are measured by K-type thermocouples with an uncertainty of 0.7 % for temperature expressed in degree centigrade. The mass flow rate through the nozzle of the ejector can also be calculated from the choked flow gas-dynamics relationship using the measured inlet temperature and pressure, and the properties of air. It was found that the calculated value of the mass flow rate through the nozzle coincides with the measured one to within about 3 %. The uncertainty in the measurements from each device was taken from the user's guide of that device. The total uncertainty for each parameter is taken as the square root of the sum of the squares uncertainty of each contributor. For example, the total uncertainty of the primary mass flow rate is $\sqrt{(0.5)^2 + (0.01)^2 + (1)^2} = 1.2\,\%$ and from Table 5.3, it can be seen that the measurement uncertainty of the primary air mass flow rate is the largest contributor to the uncertainty in the entrainment ratio.

Table 5.3: Uncertainty analysis for the ejector experimental work.

Measured parameter	Sensor	Uncertainty %	Total Uncertainty %
P_p	Υ Φ	0.5 0.01	0.5
$\dot{m}_p$	Υ Φ Ψ	0.5 0.01 1	1.2
P_s	Υ Φ	0.5 0.01	0.5
$\dot{m}_s$	Ψ	1	1
P_c	Υ Φ	0.5 0.01	0.5
ER	Υ Ψ, Ψ Φ	0.5 1,1 0.01	1.5
T	Θ	0.7	0.7

The symbols Υ, Φ, Ψ, Θ, refer to pressure transducer, barometer, mass flow meter, thermocouple respectively.

5.5 Critical back pressure

Figures 5.10 shows the variation of the back pressure during the test time. It is observed that as the test run starts, the back pressure starts to increase. In the present work, the last pressure tapping on the ejector duct (part 17 in Figure 4.3) represents the back pressure. This pressure is very close to the pressure of the main vacuum tank (VT in Figure 4.15). As long as the secondary flow is choked, the back pressure steadily increases with no influence on the upstream flow conditions. When the back pressure reaches a certain value at which the secondary flow rate starts to decline, the ejector is no longer functioning in the double-choked condition. The point in the exit pressure history at which the variation of downstream pressure starts to disturb the flow field and the secondary flow rate starts to decrease is referred to as the "critical back pressure".

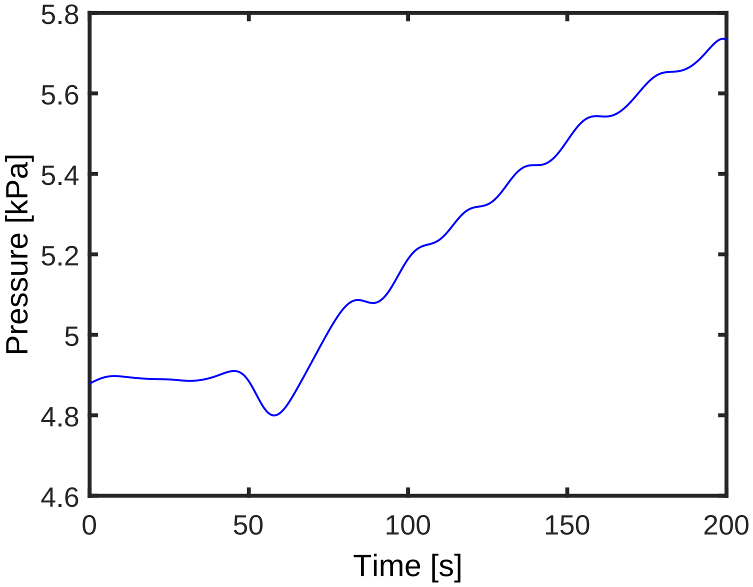

Figure 5.10: Exit pressure variation during test time at primary pressure of 200 kPa and secondary pressure of 2 kPa.

Figure 5.11 shows effects of the two operating regions of the ejector, the choked flow and the unchoked flow region. At operating conditions of 200 kPa as primary pressure and 2 kPa as secondary pressure, the ejector operates at choked conditions for around 50 s of the test time. In this region, the downstream conditions have no effect on the ejector performance. Beyond this time, the secondary flow rate starts to decrease gradually, identifying that the ejector has entered the unchoked operation region. In this region, the ejector performance is highly dependent on the downstream operating conditions and its performance declines gradually for the remaining 130 s of the test time until it reaches the malfunction point at zero secondary flow. Any further increase in exit pressure causes the flow to attempt to move in the opposite direction through the secondary flow conduit. The primary flow remains choked during the test time due to the high pressure difference between the primary pressure and back pressure.

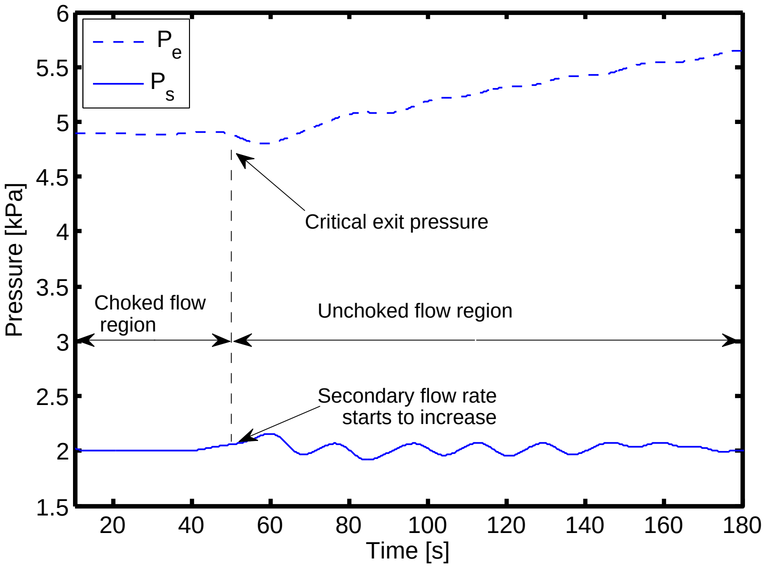

Figure 5.11: Secondary pressure variation during test time at primary pressure of 200 kPa.

5.6 Chapter Summary

Preliminary tests were performed at each operating condition to confirm functionality of the CRMC ejector system. The following is a summary of the results obtained in this chapter

- The experiments can be performed as planned, with the instrumentation and measurement systems operating reliably. Measurement uncertainties, systematic errors, and system stability were all within an acceptable range. Results were consistent with expectations based on prior simulations.

- To ensure that the experimental test results are consistent and accurate, each test was repeated three times for each operating conditions.
- The ejector functions properly and the differences in static pressure distribution along the ejector wall were around 1 % across the repeated experiments.
- In terms of repeatability of entrainment ratio measurements across the repeated tests, deviations of around 5 % were registered in the unchoked operating mode, but there was essentially no deviation between the repeated tests when the ejector was operated in the choked mode.
- In terms of repeatability of critical back pressure (or exit pressure at a specified entrainment ratio), deviations of around 5 % were also registered in the unchoked operating mode. Such differences are considered acceptable and encourages further experiments in the present work.

Chapter 6

Results, analysis and discussion

6.1 Introduction

This chapter provides experimental results for the CRMC ejector using air as the working fluid. The effect of varying operating conditions such as primary pressure, secondary pressure and exit pressure on the ejector performance was examined. The position of the nozzle within the ejector was also investigated to evaluate its influence on the ejector performance and to identify the optimum nozzle position for peak ejector performance.

The static pressure along the ejector wall and entrainment ratio were investigated for several nozzle positions at different operating conditions. The ability of the new configuration to cope with varying operating conditions, to enhance the entrainment ratio and to pump the secondary pressure to a higher exit pressure relative to conventional ejectors was investigated. Comparisons of present results with a gas dynamic model and previous experimental work on ejectors using the same and different working fluids are also presented. This establishes where the CRMC concept is placed relative to accepted ejector configurations.

6.2 Operating conditions

Experimental work was based on four primary pressures: 200, 225, 250, and 270 kPa. Each test was carried out with the secondary pressure ranging from 0.9 kPa to 5 kPa, and the back pressure ranging from 4.5 kPa to 8 kPa. Nozzle exit positions of 0, 10, 20, 30, 40, 50, and 60 mm downstream from the start of the entrainment region were evaluated. The 60 mm nozzle position corresponds to the nozzle exit being in the same plane as the commencement of the ejector duct. The definition of the nozzle exit position is illustrated in Figure 6.1. For further details of the arrangement and apparatus, see Chapter 4. Figure 6.2 presents the CRMC ejector performance at operating conditions of 200 kPa primary pressure and secondary pressure of 1.6 kPa with the nozzle exit position at 40 mm.

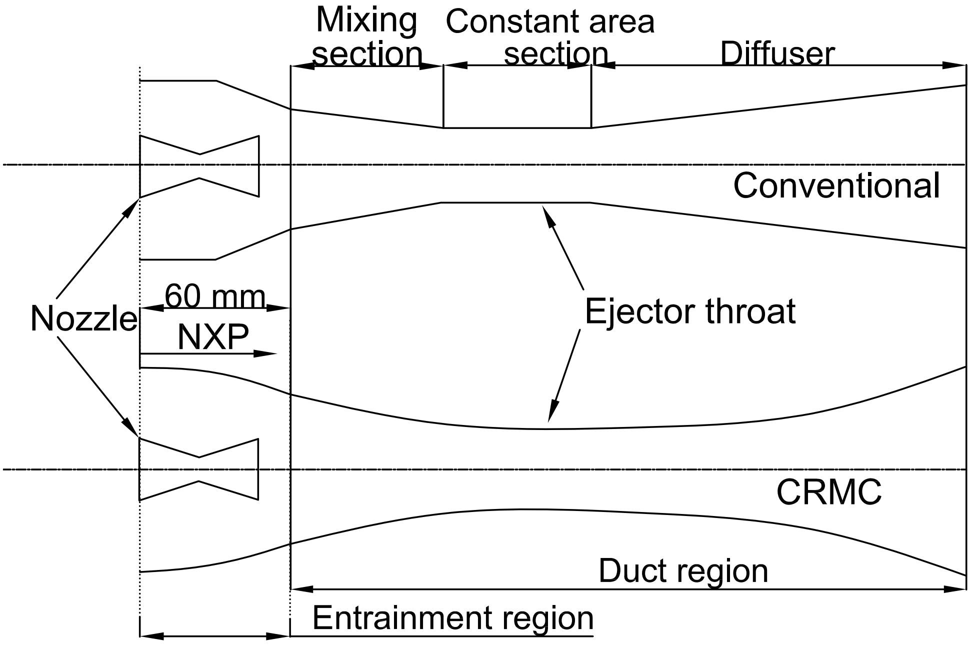

Figure 6.1: Nozzle exit position and throat section profile for conventional and CRMC ejectors.

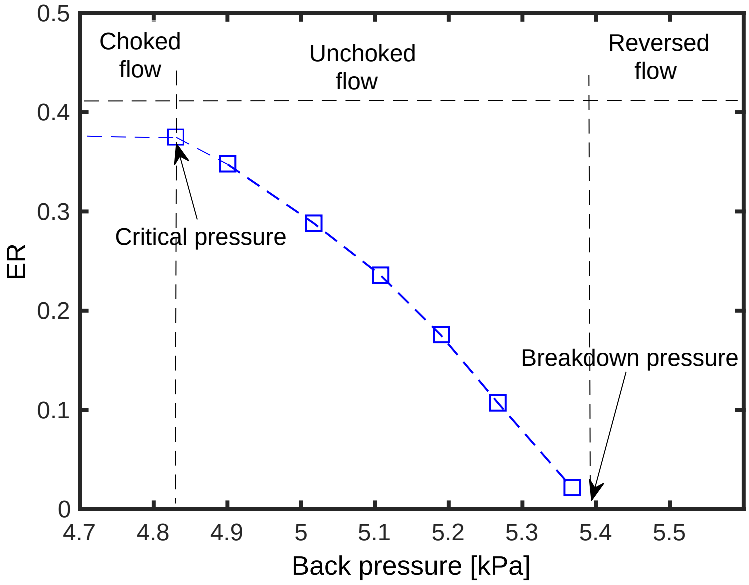

Figure 6.2: Experimental results for entrainment ratio over a range of exit pressures at 200 kPa primary and secondary pressure of 1.6 kPa. The nozzle exit position is 40 mm.

When using the entrainment ratio as an index, three operating regimes can be identified as shown in Figure 6.2.

- Choked flow. The entrainment ratio is constant and independent of ejector downstream conditions which means the primary and secondary flows are choked.
- Unchoked flow. The entrainment ratio starts to decline due to the decrease in secondary flow rate as the back pressure increases. This indicates the secondary flow is unchoked whereas the primary flow remains choked.
- Reversed flow. The primary flow remains choked, but back pressure increases enough to produce a reversed flow through the secondary flow passage and the ejector is no longer functioning.

The point where the back pressure is at its maximum value while the entrainment ratio remains at its highest value is defined as the “critical point” or “critical pressure”. For any given inlet conditions in a specific ejector configuration, the critical point is of considerable importance because at this point, the highest entrainment ratio and highest back pressure can be simultaneously achieved. However, the ejector is still able to function within the unchoked flow region, but with lower a entrainment ratio.

Figure 6.2 also shows that the entrainment ratio remains constant as the back pressure increases within the choked region. The maximum value of the entrainment ratio in choked operation in this case was 0.38. The entrainment ratio is independent of the exit pressure up to 4.83 kPa. For back pressures higher than the critical pressure, the entrainment ratio becomes dependent on the back pressure and decreases as the back pressure increases and no secondary flow is entrained at a back pressure of 5.4 kPa which is referred to as the "break down pressure". Beyond the break down pressure point, an increase of the back pressure results in a reversed flow through the secondary flow conduit.

6.3 Primary pressure effect

When the primary flow pressure is held constant at 200 kPa, Figure 6.3 illustrates the ejector performance for secondary pressures of 1.6, 2.5, 4 and 5 kPa.

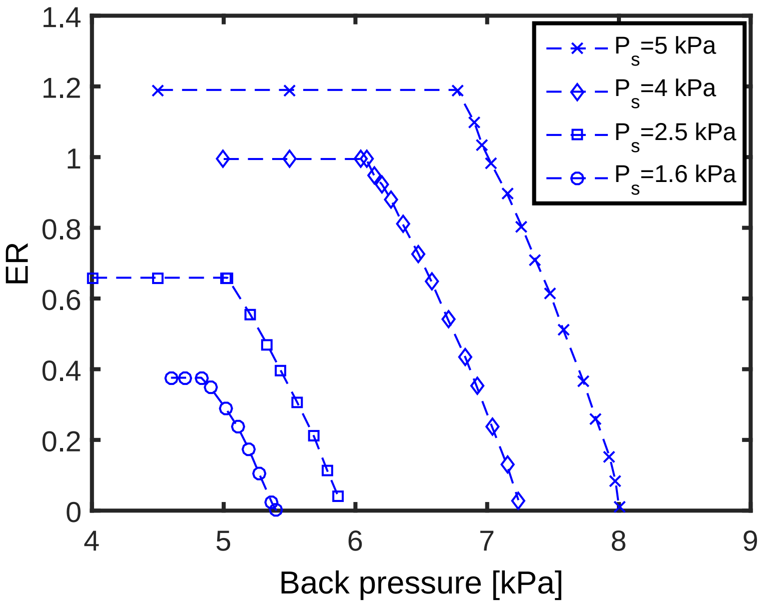

Figure 6.3: Variation of entrainment ratio with back pressure at a primary pressure of 200 kPa and a range of secondary pressures, P_s. The nozzle exit position is 40 mm.

In Figure 6.4 the primary pressure was increased to 250 kPa while the same range of secondary pressure was used. The curves at other primary pressures show similar trends.

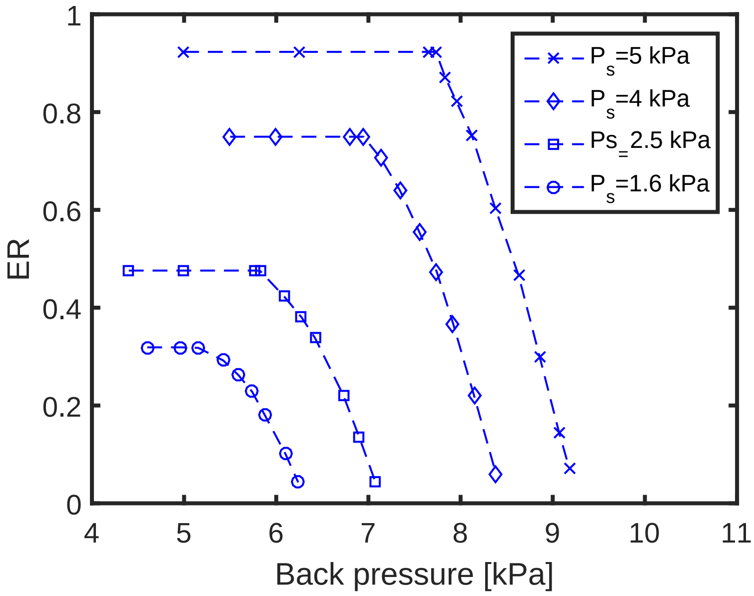

Figure 6.4: Variation of entrainment ratio with back pressure at a primary pressure of 250 kPa and a range of secondary pressure, P_s. The nozzle exit position is 40 mm.

Figure 6.5 shows the variation in the secondary flow rate over a range of primary pressures. As the primary pressure increases, the secondary flow rate gradually increases to reach its optimum value at a primary pressure of 225 kPa. Increasing the primary mass flow rate by increasing the primary pressure causes the entrainment of more secondary flow as long as the primary jet lateral expansion is relatively small and the effective area remaining in the duct is sufficient for such secondary flow to pass. Beyond the optimum point, the secondary flow starts to decline as the primary pressure increases.

Such behaviour could be attributed to two sources. Firstly, as the primary pressure increases, the primary flow expands further which leads to a decrease of the effective area that is available to the secondary flow to pass through and therefore decreases the secondary flow rate which consequently, decreases the entrainment ratio. Secondly, the primary mass flow increases as the primary pressure increases and thus for a given secondary flow rate, and according to its definition, the entrainment ratio decreases as the primary flow rate increases, thus the entrainment ratio as presented in Figure 6.6 and the secondary mass flow rate as presented in Figure 6.5 have very similar trends.

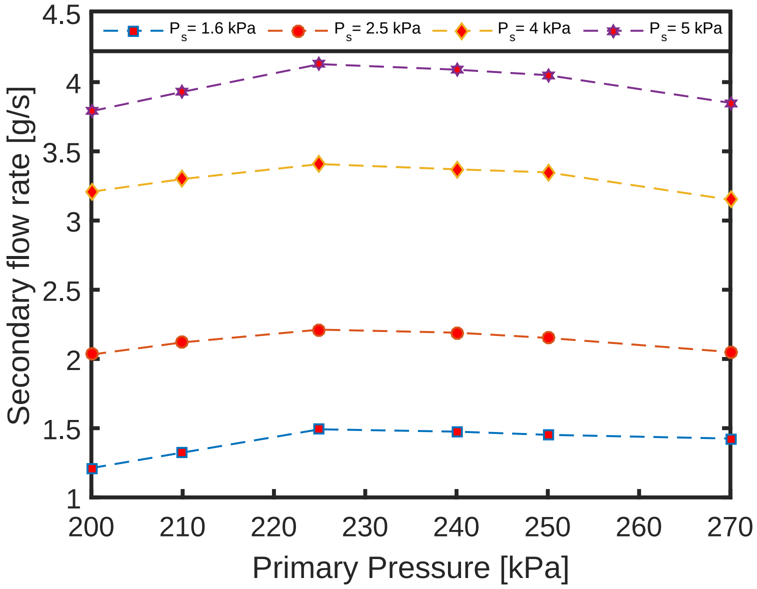

Figure 6.5: Secondary flow rate variation over a range of primary pressure and secondary pressure. The nozzle exit position is 40 mm.

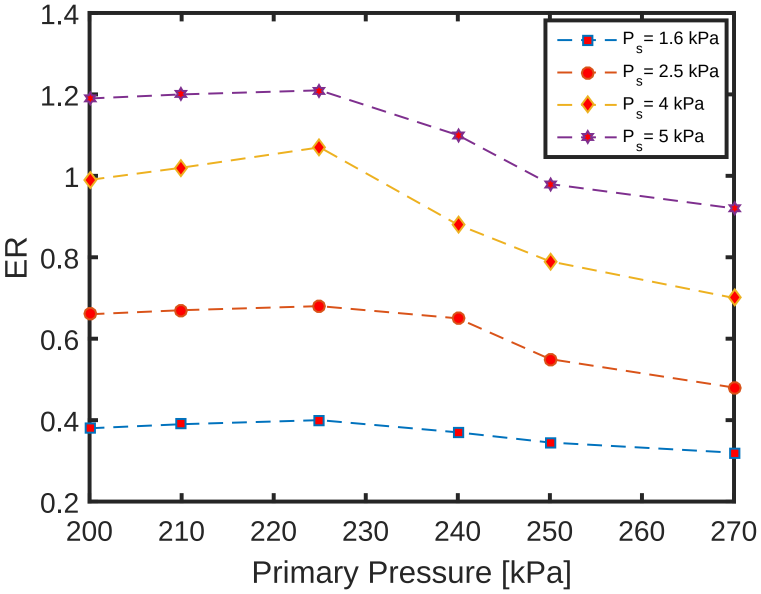

Figure 6.6: Entrainment ratio variation over a range of primary pressure and secondary pressure. The nozzle exit position is 40 mm.

It is evident that increasing the primary flow pressure will not always improve the system performance in terms of entrainment ratio in the present work. It is likely that the same would apply for cooling capacity in ejector refrigeration systems. Increases in the primary pressure could provide significant advantages in other ways such as improved pressure lift ratio which could allow the ejector to operate well in a wider range of operating conditions.

The primary jet leaving the nozzle can be classified as under-expanded, correctly expanded, or over-expanded flow. In the case of an under-expanded flow, the primary stream will expand further after leaving the primary nozzle. This case occurs when the static pressure at the primary nozzle exit plane is higher than that in the surrounding flow. In the case of an over-expanded flow, the primary stream will get compressed after leaving the primary nozzle and this case occurs when the static pressure at the primary nozzle exit plane is lower than that in the surrounding flow. The level of expansion of the primary jet may significantly affect the ejector performance. The level of expansion of the primary jet of the present work can be determined approximately using gas dynamic relationships. The Mach number at the primary nozzle exit can be calculated from the equation

$$\left(\frac{A_n}{A_t}\right)^2 = \frac{1}{(M_n)^2}\left[\frac{2}{\gamma+1}\left(1+\frac{\gamma-1}{2}(M_n)^2\right)\right]^{(\gamma+1)/(\gamma-1)} \tag{6.1}$$

where:

A_n: Nozzle exit area

A_t: Nozzle throat area

M_n: Mach number at the nozzle exit

γ: Specific heat ratio

The nozzle used in this work had throat and exit diameters of 3.2 mm and 13.6 mm respectively, and produced an exit Mach number of 4.

The static pressure at the nozzle exit can be calculated using the equation

$$\frac{P_p}{P_n} = \left(1+\frac{\gamma-1}{2}(M_n)^2\right)^{\frac{\gamma}{\gamma-1}} \tag{6.2}$$

where:

P_p: Primary pressure

P_n: Static pressure at the nozzle exit

The values of the static pressure at the nozzle exit for the range of the primary pressure operating conditions that are used in the present work are represented in Table 6.1.

Table 6.1: calculated static pressure values at the primary nozzle exit.

P_p (kPa)	200	210	225	240	250	270
P_n (kPa)	0.607	0.637	0.683	0.728	0.760	0.820

The nozzle exit static pressure values in Table 6.1 are substantially larger than the static pressure values in the secondary stream (see Section 6.6), except in the case of $P_p = 200\,\text{kPa}$ and $P_s = 0.6\,\text{kPa}$. Therefore, it can be concluded that the primary flow in majority of these cases is over-expanded. This point is discussed in more detail in Chapter 7, Section 7.6.4.

6.4 Nozzle position effect

The effect on the entrainment ratio is reported for given nozzle locations. All the following experiments are in the ejector choked flow conditions. Figure 6.7 shows the entrainment ratio for different nozzle exit positions for a primary pressure of 200 kPa and a range of secondary pressures. The optimum nozzle position is the point where the maximum entrainment ratio is achieved. In the present work, the maximum entrainment ratios achieved for the choked mode of operation were 0.38, 0.66, 0.99, 1.19 for secondary pressure of 1.6, 2.5, 4, 5 kPa, respectively.

Figure 6.7 shows that at all secondary pressure values, the entrainment ratio increases gradually as the nozzle moves downstream from NXP=0 mm and reaches its highest value for a NXP between 30 mm and 50 mm which corresponds to locations between 10 mm and 30 mm upstream of the start of the ejector duct. From Figure 6.7, it can be seen that for secondary pressures of 1.6 kPa and 5 kPa the entrainment ratio sensitivity to NXP is not as high as for secondary pressures of 2.5 kPa and 4 kPa.

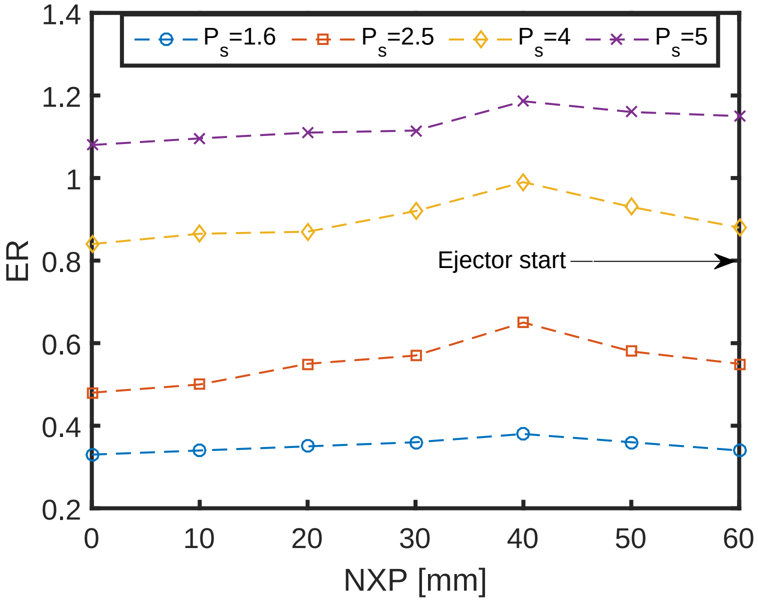

Figure 6.7: Experimental results of entrainment ratio over a range of NXP at primary pressure of 200 kPa and a range of secondary pressure.

For conventional ejector ducts, ESDU (1986) recommended that the optimum nozzle exit location is upstream of the mixing section by distance of between 0.5 and 1 times the ejector throat diameter. The ejector throat diameter is the minimum diameter along the ejector duct which in the present (CRMC) work is 25.48 mm. In this case, according to the ESDU (1986) recommendations, the optimum nozzle exit location is between 12 and 26 mm upstream of the start of the ejector duct corresponding to NXP values between 34 mm and 48 mm which agrees well with present experimental results presented in Figure 6.7.

In literature however, there is no recommendations for the optimum position of the NXP within the CRMC ejector. It was found that the NXP for optimum entrainment ratio does not alter the critical back pressure significantly. This suggests the CRMC optimum NXP is independent of the operating conditions. In practice, this means that there is no need to relocate the NXP as the back pressure increases as was suggested for the conventional ejector studied by Eames, Wu, Worall & Aphornratana (1999) and Aphornratana & Eames (1997). These authors suggested that each operating condition required a particular nozzle position. Similar results were obtained by Rusly, Aye, Charters & Ooi (2005) and Pianthong, Seehanam, Behnia, Sriveerakul & Aphornratana (2007) in which their analysis showed that NXP has only a small influence on entrainment ratio of the conventional ejector. Dong et al. (2013) showed that the critical pressure value of their conventional ejector was not affected by the nozzle exit position. As shown in Tables 5.2 and 6.2, the critical pressure remains independent of nozzle position which means that, in this case, the CRMC ejector and the conventional ejector are very similar. Data from experimental tests for nozzle position is presented in Tables 6.2, 6.3, and 6.4 where subscripts p, s, c refer to primary, secondary, and exit conditions respectively. Additional data from the experimental tests is presented in Appendix C.

Table 6.2: Data from experiments with different nozzle positions and a nominal primary pressure of 200 kPa for a range of secondary and back pressures conditions. Primary mass flow rate was 3.58 g/s for the nominal primary pressure of 200 kPa.

NXP (mm)	P_{atm} (kPa)	T_s (°C)	T_c (°C)	P_s (kPa)	P_p (kPa)	P_c (kPa)	$\dot{m}_s$ (g/s)	ER
0	94.78	25.5	24.0	1.59	198.67	5.40	1.18	0.33
	94.20	17.1	15.0	2.57	202.00	5.90	2.26	0.48
	93.90	21.1	18.2	4.00	200.00	7.30	3.38	0.84
	94.05	23.5	20.3	5.00	196.50	7.80	3.96	1.08
10	94.00	24.40	22.1	1.65	208.00	5.40	1.258	0.34
	93.93	24.1	21.7	2.44	202.50	5.98	1.866	0.50
	93.90	23.7	20.8	4.00	216.00	7.30	3.1	0.87
	94.00	22.9	19.7	5.00	200.00	7.80	3.954	1.10
20	93.80	23.6	21.5	1.63	201.00	5.40	1.22	0.35
	94.00	24.3	21.8	2.45	200.00	5.90	1.88	0.55
	93.80	25.19	23.2	4.00	201.00	7.30	3	0.87
	93.80	25.1	22.0	5.00	202.20	7.77	3.752	1.08
30	94.18	25.6	23.50	1.62	202.60	5.48	1.278	0.36
	94.15	26.6	24.2	2.56	202.50	5.88	1.984	0.57
	94.13	27.3	24.5	4.00	202.85	7.20	2.996	0.92
	94.10	27.3	24.2	5.00	202.33	7.94	3.79	1.15
40	94.13	23.6	21.9	1.6	204.30	5.42	1.212	0.38
	94.13	22.5	20.4	2.50	204.77	5.95	2.032	0.66
	94.18	21.5	19.0	4.00	203.40	7.26	3.208	0.99
	94.20	20.8	18.0	4.87	201.27	8.0	3.79	1.19
50	94.30	22.6	20.4	1.51	200.77	5.45	1.282	0.36
	94.25	24.5	22.2	2.40	205.50	5.92	1.764	0.58
	94.20	25.4	22.6	4.00	206.40	7.22	3.092	0.93
	94.20	25.0	22.2	5.00	200.36	7.90	3.89	1.16
60	94.25	22.5	20.3	1.65	200.75	5.60	1.12	0.34
	94.25	21.5	19.2	2.43	200.77	6.00	1.896	0.55
	94.25	19.8	17.3	4.00	201.32	7.08	3.2	0.88
	94.28	19.0	16.3	4.88	201.18	7.98	3.994	1.15

Table 6.3: Data of experimental with different nozzle positions and a nominal primary pressure of 225 kPa for a rage of secondary and back pressures conditions. Primary mass flow rate was 3.89 g/s for the nominal primary pressure of 225 kPa.

NXP (mm)	P_{atm} (kPa)	T_s (°C)	T_c (°C)	P_s (kPa)	P_p (kPa)	P_c (kPa)	$\dot{m}_s$ (g/s)	ER
0	94.2	22.5	19.4	1.58	225.3	5.75	1.4	0.36
	94.0	24.0	21.5	2.5	225.00	6.35	2.1	0.51
	94.4	23.5	21.7	4.00	225.4	7.80	3.304	0.88
	94.1	24.5	22.3	5.00	226.0	8.30	4.036	1.14
10	94.20	24.70	22.7	1.65	225.00	5.77	1.148	0.365
	93.95	24.5	21.5	2.48	225.3	6.48	2.106	0.52
	94.60	23.7	20.5	4.00	225.00	7.65	3.26	0.89
	94.50	23.9	20.7	5.00	225.30	8.4	4.014	1.16
20	93.60	23.5	21.5	1.6	225.40	5.82	1.44	0.38
	94.20	24.5	21.6	2.5	225.00	7.0	2.12	0.59
	94.40	25.0	23.0	4.00	225.60	7.75	3.3	0.91
	94.50	25.50	22.40	5.00	225.5	8.44	4.032	1.18
30	94.4	24.6	23.0	1.6	225.6	5.88	1.458	0.38
	94.2	26.3	24.5	2.51	225.50	7.08	2.144	0.67
	94.3	25.5	23.0	4.00	225.85	7.76	3.376	1.1
	94.3	25.3	23.2	5.00	225.0	8.55	4.05	1.22
40	94.3	23.3	22.5	1.6	225.4	5.97	1.492	0.39
	94.5	23.5	21.4	2.50	226.0	7.2	2.212	0.68
	94.2	21.5	20.0	4.00	225.40	7.61	3.408	1.11
	94.20	21.5	19.2	5.0	225.0	8.4	4.13	1.21
50	94.20	22.1	20.2	1.61	226.0	5.8	1.442	0.38
	94.6	24.0	22.0	2.50	225.0	6.46	2.124	0.59
	94.4	24.3	22.5	4.00	224.40	7.72	3.332	0.96
	94.4	24.4	22.4	5.00	224.36	8.45	4.11	1.19
60	94.0	19.8	17.8	1.58	225.0	5.9	1.42	0.37
	94.5	21.3	19.5	2.5	226.0	6.55	2.08	0.57
	94.2	22.9	20.4	4.00	225.4	7.74	3.28	0.91
	94.4	23.4	21.7	5.0	225.7	8.59	3.99	1.18

Table 6.4: Data of experimental with different nozzle positions and a nominal primary pressure of 250 kPa for a range of secondary and back pressures conditions. Primary mass flow rate was 4.25 g/s for the nominal primary pressure of 250 kPa

NXP (mm)	P_{atm} (kPa)	T_s (°C)	T_c (°C)	P_s (kPa)	P_p (kPa)	P_c (kPa)	$\dot{m}_s$ (g/s)	ER
0	94.2	22.5	19.4	1.58	253	6.1	1.36	0.32
	94.1	23.0	21.0	2.5	254.00	6.80	2.06	0.49
	94.0	23.1	21.2	4.00	254.00	8.30	3.244	0.74
	94.05	23.5	20.3	5.00	254.50	8.80	3.976	0.92
10	94.00	24.40	22.1	1.65	254.00	6.140	1.378	0.33
	93.9	24.0	21.3	2.48	253.00	6.98	2.046	0.49
	94.0	23.7	20.8	4.00	254.00	8.0	3.2	0.75
	94.00	22.9	19.7	5.00	253.00	9.0	3.954	0.93
20	93.80	23.4	21.0	1.6	254.00	6.2	1.4	0.33
	94.00	24.0	21.6	2.5	254.00	8.10	2.08	0.50
	93.80	25.2	23.2	4.00	254.00	8.2	3.24	0.77
	93.90	25.0	22.0	5.00	253.5	9.1	3.952	0.94
30	94.8	24.6	23.50	1.6	253.6	6.28	1.418	0.35
	94.5	26.8	24.8	2.51	253.50	8.28	2.104	0.52
	94.1	25.3	23.5	4.00	253.85	8.32	3.316	0.79
	94.10	27.3	24.2	5.00	254.0	9.15	3.99	0.95
40	94.1	23.7	22.0	1.6	254.0	6.32	1.452	0.36
	94.1	22.5	20.4	2.50	254.0	7.3	2.152	0.52
	94.18	21.5	19.0	4.00	253.40	8.5	3.348	0.79
	94.20	20.5	18.2	5.0	254.0	9.2	4.05	0.94
50	94.20	22.1	20.2	1.61	254.0	6.15	1.402	0.33
	94.5	24.4	22.4	2.50	254.0	7.0	2.084	0.50
	94.20	24.4	22.6	4.00	253.40	8.22	3.272	0.76
	94.1	24.0	22.2	5.00	254.36	9.0	4.01	0.93
60	94.3	19.7	17.8	1.58	254.0	6.2	1.38	0.318
	94.25	21.5	19.4	2.5	253.0	7.10	2.04	0.475
	94.2	22.9	20.4	4.00	253.4	8.4	3.22	0.74
	94.2	23.4	20.7	5.0	253.7	9.2	3.99	0.92

6.5 Secondary pressure effect

6.5.1 On entrainment ratio

Figure 6.8 shows the impact of the variation of the secondary pressure on the entrainment ratio of the ejector when the primary pressure was maintained at 200 kPa, 225 kPa and 250 kPa. In all three cases it can be seen that the entrainment ratio increases as the secondary pressure increases for a fixed nozzle position of NXP=40 mm. This position was chosen based on the optimal entrainment ratio. Changes in the effective secondary flow area resulting from the relative pressure between the primary and secondary streams which was used to explain the primary pressure effect on entrainment ratio, can also be used to explain the effect of changing secondary pressure.

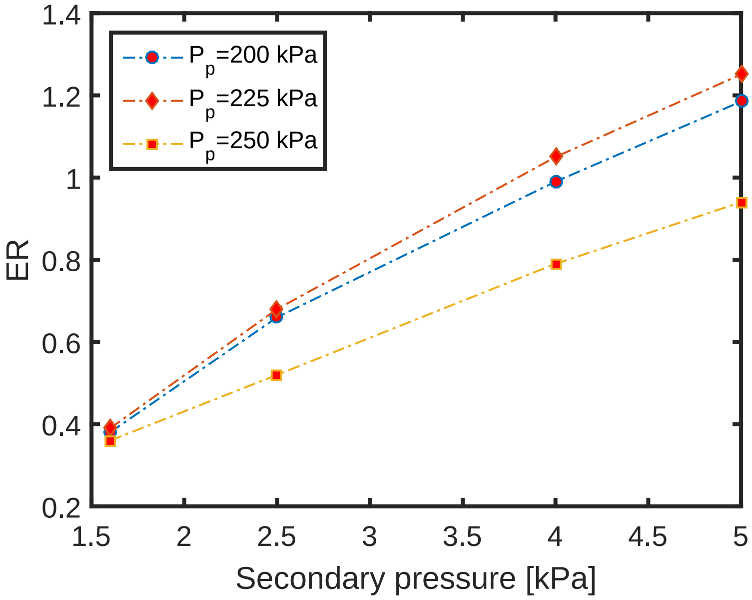

Figure 6.8: Experimental results for entrainment ratio over a range of secondary pressures at primary pressures of 200 kPa, 225 kPa and 250 kPa.

For the secondary pressure at the lowest value tested of 1.6 kPa, the entrainment ratio is 0.38, 0.39 and 0.36 at primary pressure of 200 kPa, 225 kPa, and 250 kPa respectively. With increasing secondary pressure, the entrainment ratios increases in an approximately linear manner and reaches highest value for all cases when the secondary pressure reaches 5 kPa, the maximum value tested. With increasing secondary pressure, the relative pressure difference between the secondary stagnation pressure and the mixing chamber at the nozzle exit increases and causes more secondary flow to be entrained.

6.5.2 On achievable back pressure

Figure 6.9 represents the effect of secondary pressure on the ejector back pressure at two primary pressures: 200 kPa and 250 kPa. The curves labelled (1) and formed by the solid lines, refer to the critical operating pressure, and those labelled (2) and formed by the broken line, refer to the breakdown condition. All the curves have the same trend. Achievable back pressure increases with increasing secondary pressure.

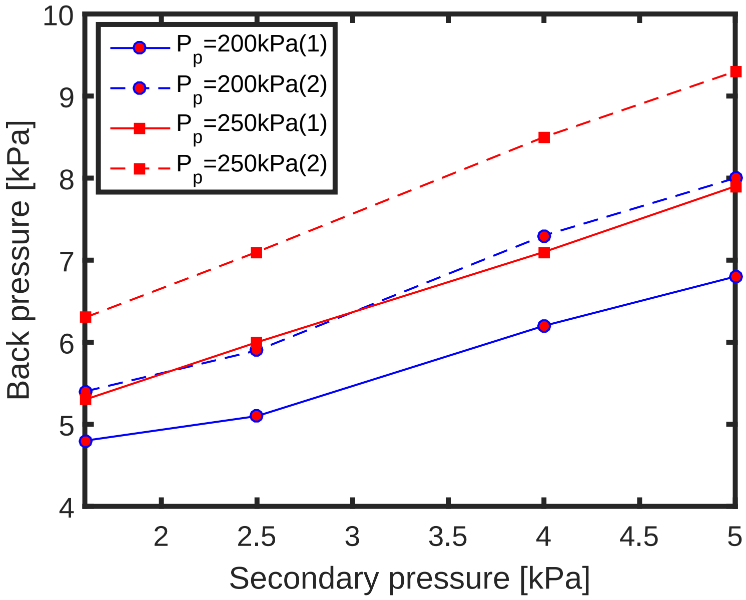

Figure 6.9: Variation of the back pressure over a range of secondary pressure at primary pressure of 200 kPa and 250 kPa (1): Critical conditions (2): Breakdown conditions.

The achievable back pressure rises as the secondary pressure rises at all primary pressure conditions. The back pressure varies approximately proportionally with the secondary pressure. The achievable back pressure results from the momentum and pressure of the mixed flow. At a given primary pressure, as the secondary pressure increases, the momentum of the mixed flow increases and thus, additional momentum would be recovered as a pressure at the end of the diffuser. It can be seen that a

50 % increase in the secondary pressure raises the back pressure and the break down pressure by 7.5 %.

The ratio of critical back pressure to secondary pressure represents a key non dimensional parameter for ejector performance. This ratio is referred to as the compression ratio or pressure lift ratio. Figure 6.10 shows the entrainment ratio as a function of the compression ratio. At all primary pressure values, the entrainment ratio decreases as the compression ratio increases. At a primary pressure of 225 kPa, the highest entrainment ratio (1.22) was achieved when the compression ratio was at its lowest value (1.68). The highest compression ratio of 3.95 was achieved when the entrainment ratio was 0.35 at the primary pressure of 250 kPa.

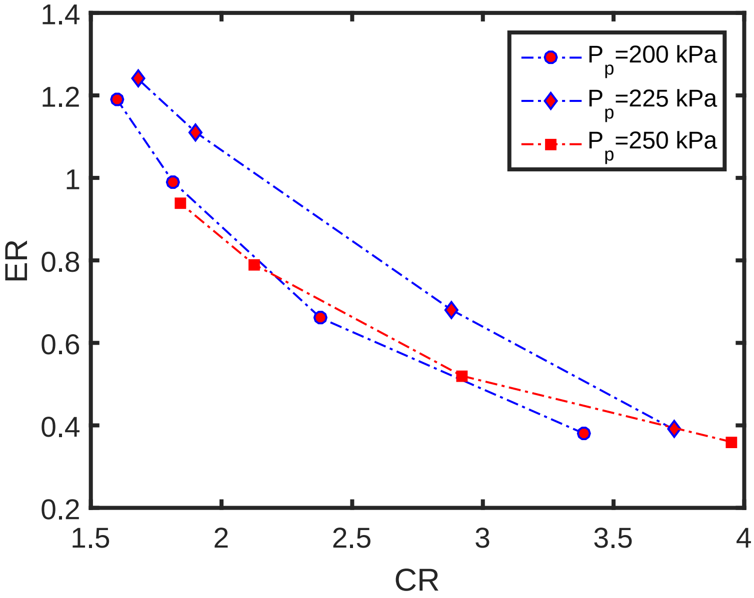

Figure 6.10: Entrainment ratio as a function of compression ratio over a range primary pressures.

Figure 6.11 shows the performance map of the CRMC ejector. This figure combines the information reported in the present section.

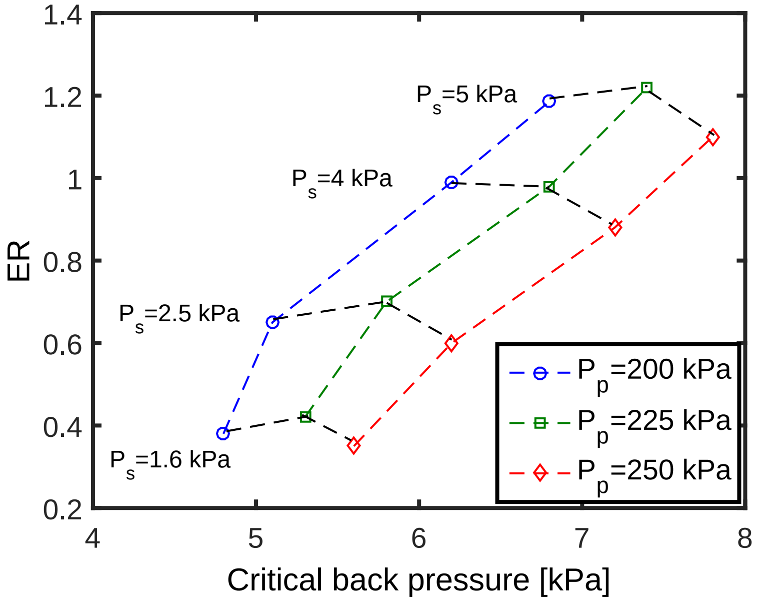

Figure 6.11: Variation of entrainment ratio and critical back pressure at different operating conditions. The nozzle exit position is at 40 mm.

6.6 Wall static pressure

Experiments were carried out to determine the variation in the static pressure along the ejector wall. The curves in Figure 6.12 show the static pressure distribution along the ejector wall over a range of secondary pressures with a primary pressure of 200 kPa and the nozzle exit position of 0 mm, which corresponds to the nozzle exit positioned at the start of the entrainment section 9 in Figure 4.3. It can be seen that all the static pressure curves have the same general trend. It is clear that the static pressure increases more or less gradually along the ejector wall as expected from the CRMC-designed ejector. However, rate of rise of the wall static pressure observed in Figure 6.12 is not especially gradual relative to the pressure rise that can be observed in conventional ejectors.

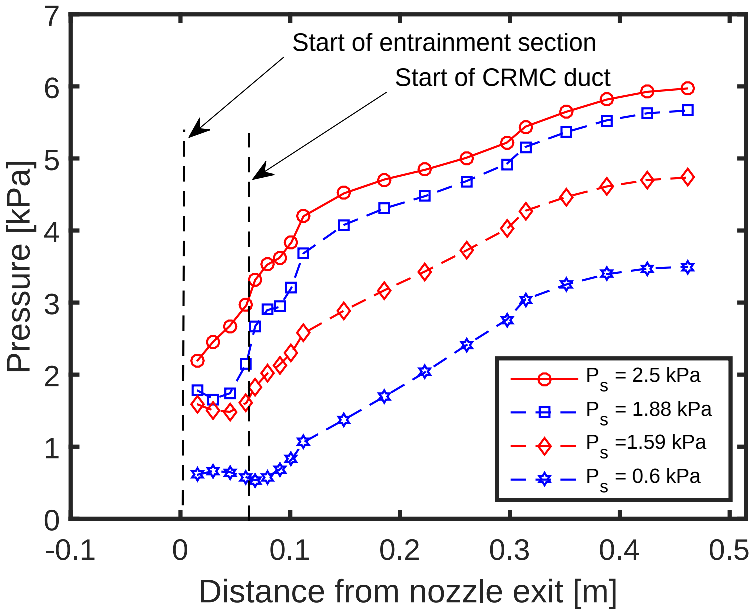

Figure 6.12: Experimental results of wall pressure along the ejector over a range of secondary pressure at primary pressure of 200 kPa.

To improve the resolution of wall pressure data, an extra seven low pressure transducers tappings were added to the entrainment region and the first part of the ejector duct. This provided more information about wall static pressure in these important regions. A comparison between Figure 6.12 and Figure 5.8 shows the additional detail obtained from the extra pressure transducers. At a secondary pressure of 0.6 kPa, the lowest pressure point was at 68 mm downstream of the nozzle exit, whereas it occurs at a distance of 45 mm downstream of the nozzle exit for a secondary pressure of 1.59 kPa. When the secondary pressure was increased to 1.88 kPa the lowest pressure point was located at 30 mm downstream of the nozzle exit. Increasing the secondary pressure to 2.5 kPa moved the lowest pressure point further upstream, but because the static pressure measurement locations did not extend upstream of the nozzle exit location, it is not possible to precisely define what the global minimum pressure was, or where it occurred in this particular case.

Figure 6.13 shows the static pressure on the wall of the ejector for primary pressure of 225 kPa and a range of secondary pressure. Pressure variations similar to those observed in Figure 6.12 can be seen in the higher primary pressure case of Figure 6.13, but a more rapid pressure rise near the start of the CRMC duct occurs in the Figure

6.13.

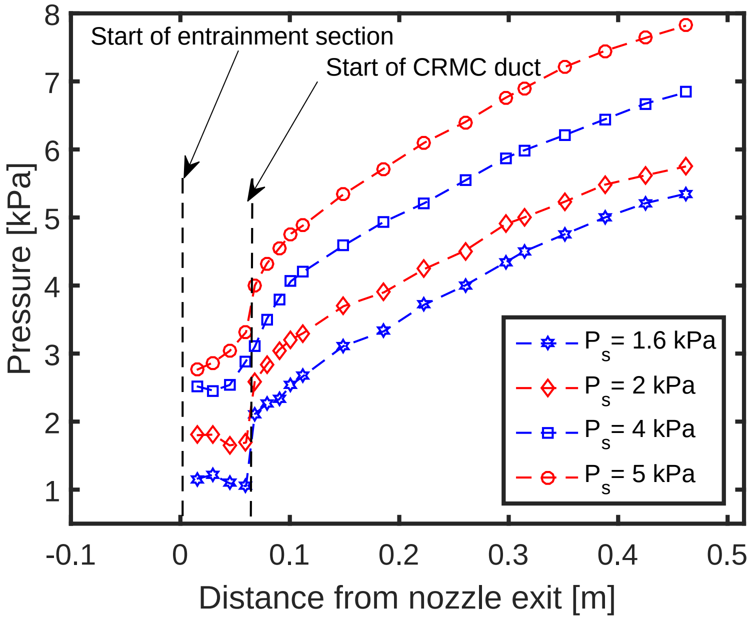

Figure 6.13: Experimental results of wall pressure along the ejector over a range of secondary pressure at primary pressure of 225 kPa.

Isentropic choking of the secondary stream is sometimes assumed in gas dynamic ejector models. If such choking occurs, the static pressure in the secondary stream is expected to fall to a sonic value corresponding to isentropic acceleration from the secondary inlet stagnation pressure. From experimental data such as that presented in Figures 5.8 and 6.13, the minimum value of static pressure P_{min} on the ejector wall for each condition can be defined and the location where the P_{min} occurs within the ejector duct also can be defined. Thus, a representative isentropic Mach number in the secondary stream at this location can be calculated using

$$\frac{P_s}{P_{min}} = (1 + \frac{\gamma - 1}{2} M^2)^{\frac{\gamma}{\gamma-1}} \tag{6.3}$$

The values of P_{min}, the location of the P_{min} within the ejector duct and the calculated isentropic Mach number for a range of operating conditions are listed in Table 6.5. Values in parentheses in this table indicate values associated with the lowest measured pressure, but these may not be the lowest actual pressures, because the pressure measurement location did not extend far enough upstream at these operating conditions.

Table 6.5: Isentropic Mach number at the location of lowest measured wall static pressure for primary pressure of 200 kPa and 225 kPa and range of secondary pressure.

P_p (kPa)	P_s (kPa)	P_{min} (kPa)	Location from nozzle exit (mm)	M
200	0.6	0.353	68	0.4
	1.59	1.484	45	0.316
	1.88	1.66	30	0.422
	2.5	(2.187)	(15)	(0.44)
225	1.6	1.05	60	0.8
	2	1.65	45	0.78
	4	2.456	38	0.865
	5	(2.76)	(15)	(0.962)

The Mach number values in Table 6.5 demonstrate that isentropic-choked conditions were not generated for all secondary pressures and primary pressure of 200 kPa. For the primary pressure of 225 kPa, the isentropic Mach number for all secondary pressures values also showed that isentropic-choked flow conditions were not generated, although higher Mach numbers in the secondary stream were achieved.

6.7 Comparison with previous work

6.7.1 Comparison with gas dynamic model

In an attempt to establish a consistent means to compare the performance of different kinds of ejectors, Buttsworth (2017) introduced a gas dynamic model to simulate the entrainment ratio and the compression ratio of ejectors. This model enables identification of justifiable calibration factors that are applicable across a range of ejectors. This model provides an inviscid reference which is then used in the evaluation of experimental data from different geometry ejectors. The simulation of the maximum entrainment ratio of the gas dynamic model is not affected by whether the mixing process takes place under constant area or constant pressure condition, but the critical back pressure is affected by the mixing process which gives this model the necessary validity to be applicable on the CRMC ejector. However, the viscous flow losses have not been included in this model. Results of the CRMC ejector from Table 6.6 and gas dynamic model results (referred to as the GD model) are graphically represented in Figures 6.14 and 6.15.

Figure 6.14 presents the maximum entrainment ratio (choked secondary flow conditions) as a function of expansion ratio (ratio of primary pressure to secondary pressure, $\frac{P_p}{P_s}$) of the CRMC ejector at primary pressures of 200 kPa, 225 kPa and 250 kPa. It can be seen that the simulated maximum entrainment ratio slightly overestimates the experimental data of the CRMC ejector when the primary pressure is 200 kPa and 250 kPa. At a primary pressure of 225 kPa, the pressure at which the optimum entrainment ratio was achieved for the configuration used in the present work, the experimental data points fall on the simulation line. In all cases, the primary nozzle exit positions within the ejector was tuned to obtain the maximum entrainment ratio.

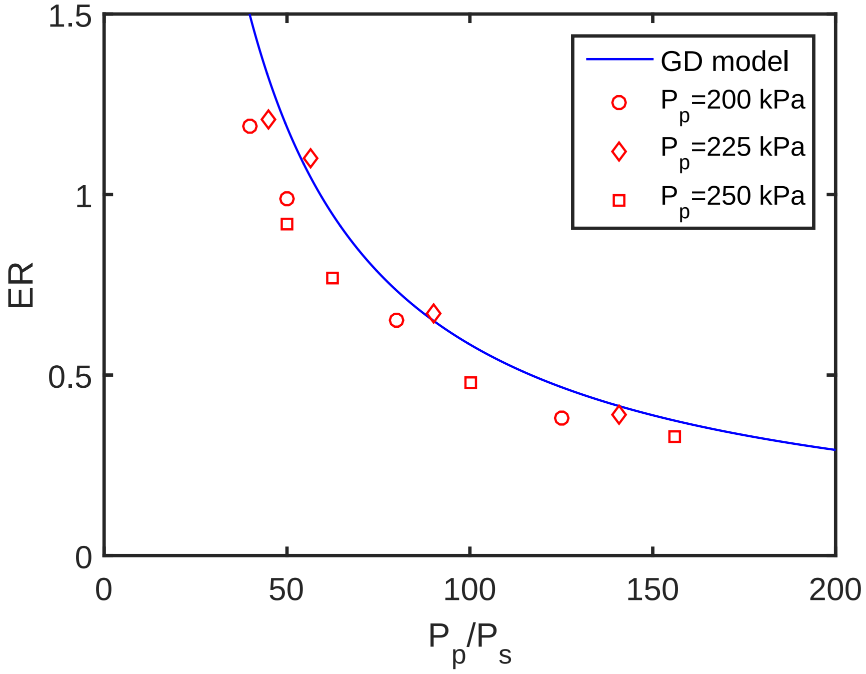

Figure 6.14: Maximum entrainment ratio variation with expansion ratio for the CRMC ejector performance at different operating conditions compared with the gas dynamic, GD model.

Figure 6.15 presents the critical compression ratio (ratio of critical back pressure to secondary pressure $\frac{P_{b,crit}}{P_s}$) of the CRMC ejector at primary pressures of 200 kPa, 225 kPa, and 250 kPa. In the case of the compression ratio simulation, the gas dynamic model has been tuned to give agreement with previous experimental results from a range of ejectors (Buttsworth 2017). For almost all cases, the experimental compression ratio exceeds the values from the gas dynamic model which, by virtue of the empirical calibration, is representative of the performance of conventional ejectors. In the case of the primary pressure of 200 kPa, all data points fall above the simulated line by a small margin. The margin generally becomes larger for the case of the primary pressure of 225 kPa. For the case of 250 kPa, the data points follow a similar trend, exceeding the simulations by a modest margin, except at the highest expansion ratio P_p/P_s. While experimental uncertainty is a possible explanation for this behaviour, several test runs were repeated at different times with excellent repeatability of results. This suggests that the likely cause of the different behaviour at the highest expansion ratios is the fluid mechanics inside the ejector.

It can be seen that the compression ratio of the CRMC ejector data points for the primary pressure of 225 kPa provides the largest margin over the simulated performance from the gas dynamic model. The high performance of the CRMC ejector in the case of primary pressure of 225 kPa represents the optimum ejector performance which achieved by the position of the primary nozzle exit plane relative the start of the ejector duct.

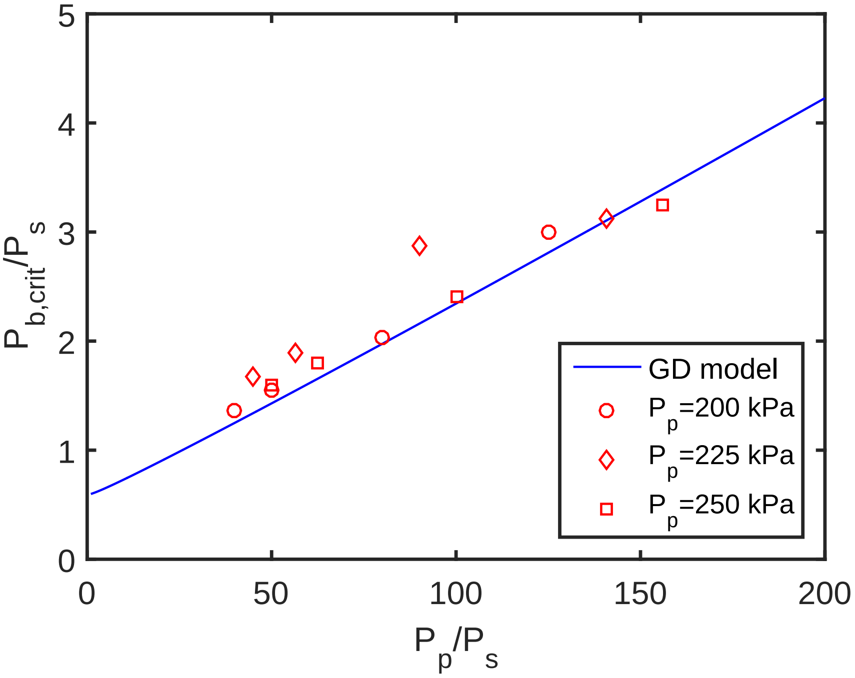

Figure 6.15: Critical compression ratio variation with expansion ratio for CRMC ejector performance at different operating conditions compared with the gas dynamic model.

6.7.2 Assessment of the validity of the Gas Dynamic Model

Data on the maximum entrainment ratio and critical compression ratio in Table 6.6 for several conventional ejectors using air as a working fluid are presented in Figures 6.16 and 6.17 respectively. In Table 6.6 $d_{ej,th}, A_{ej,th}, d_{n,th}, A_{n,th}$ refer to the ejector throat diameter, ejector throat area, nozzle throat diameter and nozzle throat area respectively. Results from the gas dynamic model described in Section 6.7.1 is also presented in these figures. Figure 6.16 shows that the simulated entrainment ratio overestimates the experimental data of Hemidi et al. (2009) and Mazzelli, Little, Garimella & Bartosiewicz (2015). The experimental data of Chong, Hu, Chen, Wang, Liu & Yan (2014) overestimates the simulated results with four out of the five data points.

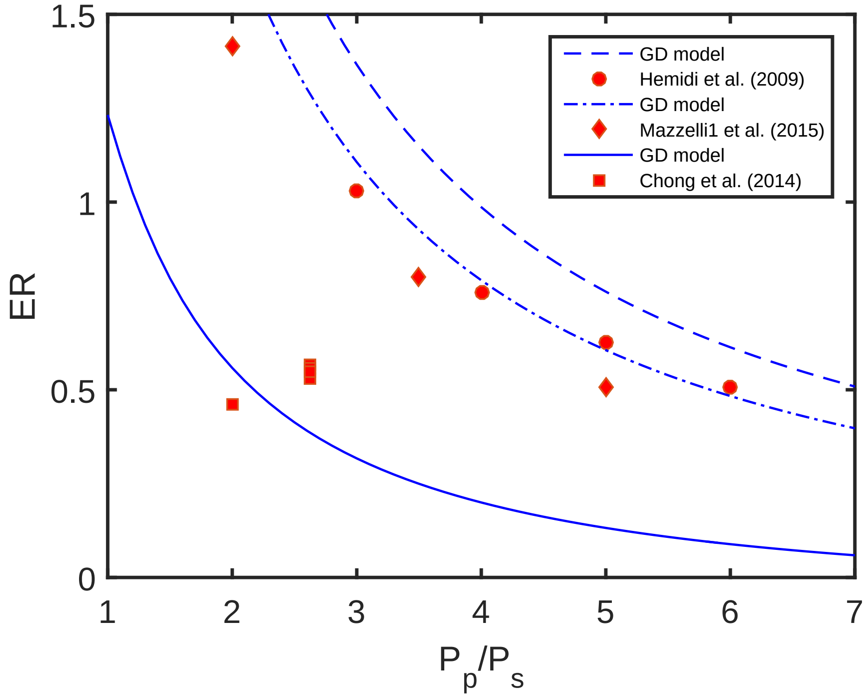

Figure 6.16: Air ejector performance data with comparisons to the gas dynamic modelling for various conventional ejectors: maximum entrainment ratio variation with expansion ratio.

Figure 6.17 shows the simulated results and the experimental data of critical compression ratio of those ejectors. The critical compression ratio of all ejectors exceeds the simulated results by a substantial margin for Hemidi et al. (2009) and Mazzelli et al. (2015) while, for Chong et al. (2014) the margin is insignificant.

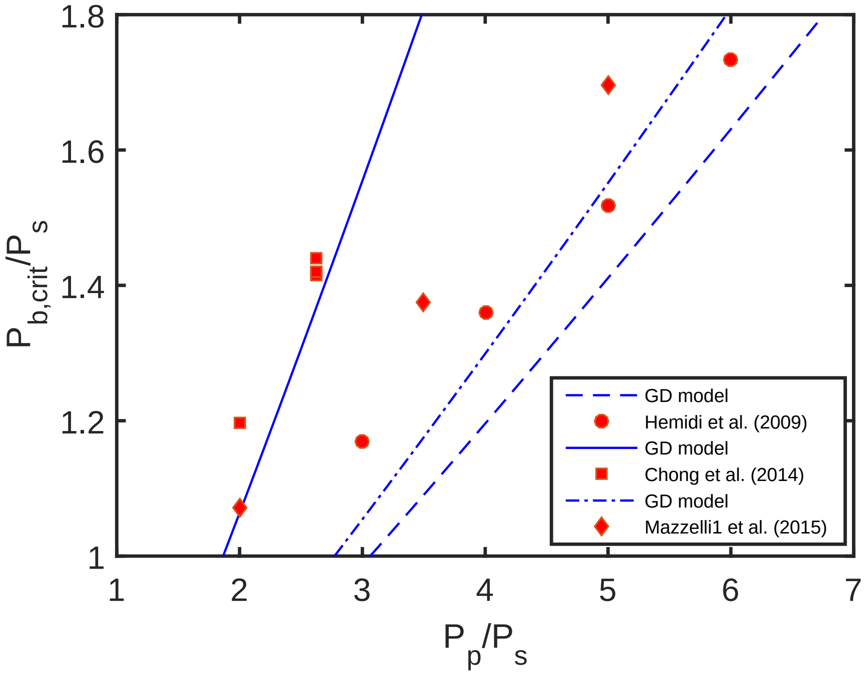

Figure 6.17: Air ejector performance data with comparisons to the gas dynamic modelling for various conventional ejectors: maximum compression ratio variation with expansion ratio.

A direct comparison between the CRMC ejector data and the data from the referenced ejectors is not possible because of the very different expansion ratio values. The general trends of comparison between the gas dynamic model and the referenced ejectors of various configurations and operating conditions suggest that the CRMC ejector is operating with a similar behaviour to the conventional ejectors as can be seen through the comparisons with the GD model in Figures 6.14, 6.15, 6.16, and 6.17.

An important non-dimensional factor affecting ejector performance is the area ratio which is defined as the area ratio between the constant area throat diameter and the primary nozzle throat diameter. When the primary flow emerges from the primary nozzle and maintains its definition as primary fluid for some distance, the secondary fluid is entrained into the mixing region between the primary fluid and the ejector wall. For an ejector at given primary pressure, secondary pressure and nozzle geometry, increasing the mixing section area will result in a greater flow area for the secondary stream. The entrainment ratio will increase but since the momentum available from the primary flow is same, the ejector is unable to compress the mixture to as high a discharge pressure.

In a conventional ejector, according to Varga, Oliveira & Diaconu (2009*b*), increasing area ratio increases entrainment ratio and decreases the critical back pressure. Therefore, for each operating condition, an optimal area ratio should exist. From the performance of the CRMC ejector relative to the performance of conventional ejectors using the gas dynamic model, it is reasonable to predict that the CRMC ejectors are also subject to this rule. So, the area ratio must be designed properly to obtain the best performance for both kinds of ejectors.

Table 6.6: Entrainment ratio, expansion ratio, pressure lift ratio and breakdown pressure for various conventional ejectors working with air.

Source	$d_{ej,th}$ (mm)	$d_{n,th}$ (mm)	$\frac{A_{ej,th}}{A_{n,th}}$	ER	$\frac{P_p}{P_s}$	$\frac{P_b}{P_s}$	$\frac{P_{bd}}{P_s}$
Hemidi et al. (2009)	6.7	3.3	5.304	1.03	2.472	3.00	1.32
				0.353	10.0	2.574	1.61
				0.326	11.45	2.781	1.86
				0.155	15.1	3.56	2.10
Chong et al. (2014)	9.4	6.3	2.157	0.462	2.0	1.198	1.53
				0.528	2.625	1.42	1.89
				0.566	2.625	1.415	1.91
				0.56	2.625	1.42	1.89
				0.546	2.625	1.44	1.89
Mazzelli et al. (2015)	27.06	5.98	4.525	1.414	1.5	1.016	1.16
				1.35	2.0	1.087	1.28
				1.088	2.5	1.178	1.4
				0.886	3.0	1.287	1.52
				0.753	3.5	1.402	1.64
				0.63	4.0	1.51	1.76
				0.54	4.5	1.623	1.88

6.7.3 Comparison of CRMC steam ejectors with the Gas Dynamic Model

Figures 6.18 and 6.19 represent the maximum entrainment ratio and the critical compression ratio as a function of expansion ratio from CRMC steam ejectors and the gas dynamic model. The experimental data was taken from work of Worall (2001) and Chandra & Ahmed (2014) as reported in Table 6.7 and plotted relative to the data for the gas dynamic model (Buttsworth 2017). The gas dynamic model treats the steam as an ideal gas with $\gamma = 1.32$. Stagnation temperature ratios closely approximating the actual experimental conditions have been used for the simulation. For the data of Worall (2001) and Chandra & Ahmed (2014), the experimental values of entrainment ratio are above the simulated values by a considerable margin.

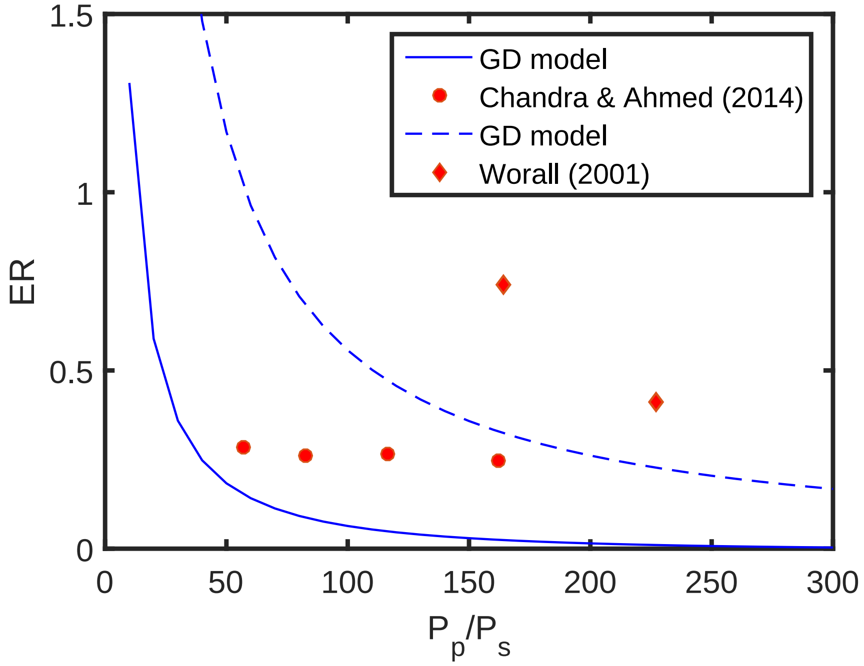

Figure 6.18: CRMC steam ejector performance data with comparisons to the gas dynamic modelling: maximum entrainment ratio variation with expansion ratio.

In contrast, Figure 6.19 shows that the compression ratio data of Chandra & Ahmed (2014) falls well below the simulated result and in the case of Worall (2001), one data point is slightly higher than the simulated values while the other point is well below the simulated result.

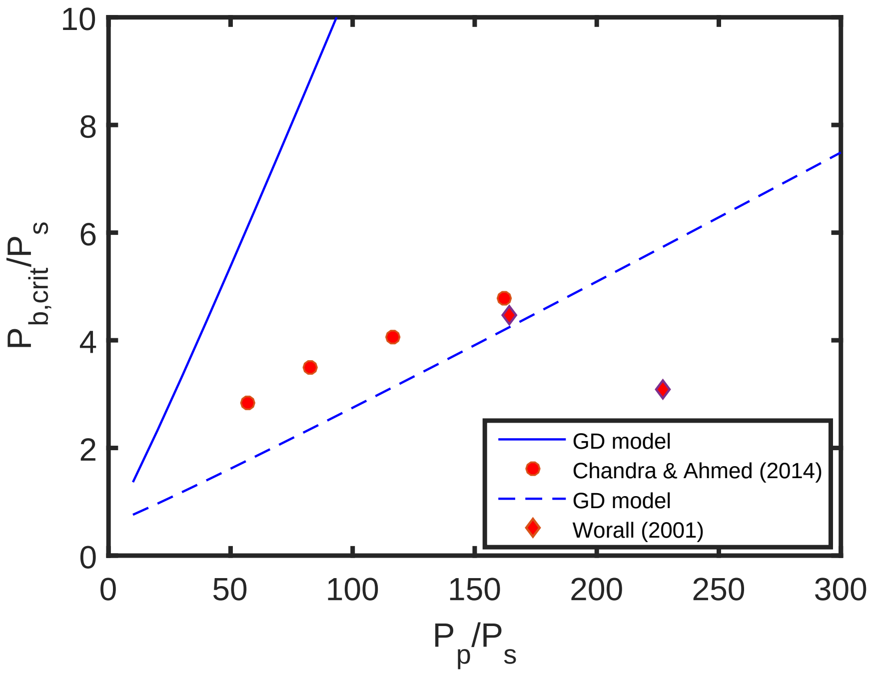

Figure 6.19: CRMC steam ejector performance data with comparisons to the gas dynamic modelling: maximum compression ratio variation with expansion ratio.

6.7.4 Comparison of CRMC air ejectors with gas Dynamic Model

Figures 6.20 and 6.21 represent data on the entrainment ratio for the choked secondary flow conditions and the critical compression ratio for maintaining choked secondary flow as a function of the expansion ratio for the present work and from a publication on an air CRMC ejector as described in Table 6.7.

Unfortunately, the available data is very limited for CRMC ejectors working with air. Figure 6.20 shows the data of the present work and the work of Kumar et al. (2013) are very consistent with the simulations from the gas dynamic model.

Figure 6.21 shows the data of critical compression ratio as a function of expansion ratio of the present work relative to work of Kumar et al. (2013) and the gas dynamic model. In this case, the present work exhibits better performance than the work of Kumar et al. (2013) relative to the gas dynamic model line.

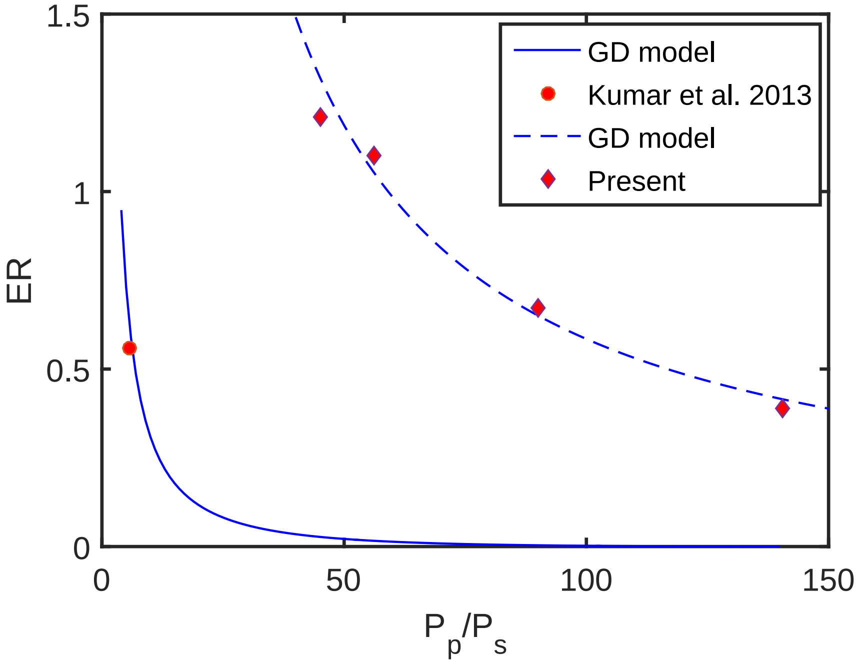

Figure 6.20: CRMC air ejector performance data with comparisons to the gas dynamic modelling: maximum entrainment ratio variation with expansion ratio.

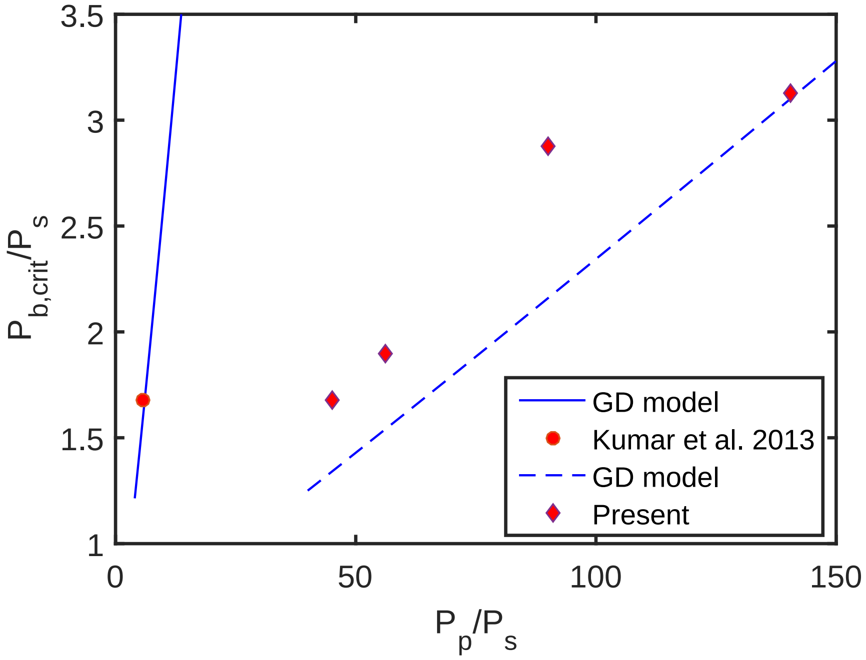

Figure 6.21: CRMC air ejector performance data with comparisons to the gas dynamic modelling: maximum compression ratio variation with expansion ratio.

It can be seen that both entrainment ratio and critical back pressure can be varied simultaneously by adjusting primary flow pressure, secondary flow pressure and area ratio. However, the only adjustment which can increase both parameters simultaneously, is an increase of secondary pressure. It can be concluded that as the geometrical parameters play a significant role in determining the performance of the conventional ejectors, they play the same role in the determining the performance of the CRMC ejector. Given that the higher the critical pressure and entrainment ratio are, the better the ejector performance, the trade-off between entrainment ratio and the compression ratio of conventional and CRMC ejectors is predominant regardless of working fluid and operating conditions.

Table 6.7: Entrainment ratio, expansion ratio, pressure lift ratio and breakdown pressure for various CRMC ejectors working with steam and air.

Source	$d_{ej,th}$ (mm)	$d_{n,th}$ (mm)	$\frac{A_{ej,th}}{A_{n,th}}$	ER	$\frac{P_p}{P_s}$	$\frac{P_b}{P_s}$	$\frac{P_{bd}}{P_s}$
Worall (2001) working fluid: steam	14.48	2	55	0.41	164	4.47	-
				0.74	227.64	3.1	-
Chandra & Ahmed (2014) working fluid: steam	12.81	3.5	13.4	0.245	161.78	4.77	-
				0.265	116.75	4.075	-
				0.26	82.58	3.5	-
				0.285	57.144	2.85	-
Kumar et al. (2013) working fluid: air	9.78	4.31	5.15	0.55	56.25	1.38	1.678
Present work working fluid: air	25.48	3.2	63.4	0.38	140.625	3.125	3.75
				0.68	90.0	2.88	3
				1.11	56.25	1.9	1.975
				1.21	45	1.68	1.75

6.8 Chapter Summary

Extensive experimental work with a CRMC ejector using air as a working fluid was performed. Analysis of the flow in the CRMC ejector including entrainment ratio, back pressure, and static pressure along the ejector duct was undertaken. The following is a summary of the results obtained in this chapter.

- The present apparatus, when operated at primary pressure of 200 kPa, can produce an entrainment ratio of 0.38, 0.66, 0.99, and 1.19 at secondary pressure of 1.6, 2.5, 4, and 5 kPa respectively, when the back pressure is sufficiently low.
- At same operating conditions, the ejector produces back pressures of 4.8, 5.1, 6.2, and 6.8 kPa respectively when the flow is at the critical conditions and the nozzle exit position is at 40 mm downstream of the start of the entrainment region.
- At the same operating conditions, the ejector is unable to entrain any secondary flow at back pressures exceeding 5.4, 5.9, 7.3, and 7.8 kPa, respectively.
- The optimum ejector performance was achieved when the NXP was between 30 and 50 mm downstream of the entrainment section start, which corresponds to 10 to 30 mm upstream of the ejector duct start.
- NXP does not influence significantly the ejector performance and the optimum possible is not affected strongly by the operating conditions. This result agrees well with other literature.
- The optimum primary pressure that the ejector worked with was 225 kPa; the achieved entrainment ratio was 0.4, 0.68, 1.11, 1.21 at secondary pressures of 1.6 kPa, 2.5 kPa, 4 kPa, and 5 kPa respectively.
- As the secondary pressure increases, the entrainment ratio increases and the relationship between these two parameters is nearly linear.
- Critical back pressure increases linearly as the secondary pressure increases when the primary pressure is held constant.
- The maximum isentropic Mach number values at the minimum static pressure value demonstrate that isentropic-choked conditions are not generated for all secondary pressures and primary pressure of 200 kPa. For the primary pressure of 225 kPa, the isentropic Mach number for all secondary pressures values was higher, but still showed isentropic-choked flow conditions were not generated.

- Geometrical parameters play the same role in the establishing of performance of the CRMC ejector as they do in a conventional ejector. The trade-off between entrainment ratio and the compression ratio of conventional and CRMC ejectors is predominant.

- The CRMC static pressure measurements on the ejector wall were not especially gradual relative to conventional ejectors. There is no strong evidence of eliminating the shocks associated with the compression process inside a conventional ejector. To assess the CRMC compression process, an extensive numerical study is carried out by employing CFD in Chapter 7.

The experimental results from this study can be used to validate the results obtained from both analytical and computational methods (CFD). Employing CFD techniques can provide an improved understanding in flow characteristics through an ejector which may lead to further enhancement of ejector performance. In addition, in the experiment, it is very difficult to detect or visualise flow phenomenon. CFD visualization is pursued for this purpose.

Chapter 7

Computational fluid dynamic analysis

7.1 Introduction

Experimental work is essential to understand and optimise the flow behaviour inside an ejector. Key parameters of the flow such as static pressure, mass flow rate, and flow velocity provide a substantial view into the ejector performance. However, the experimental data are relatively costly when complete details such as the mixing process which involves compressible flow, shock interactions and turbulent mixing of two streams inside the ejector are required. Computational Fluid Dynamic (CFD) modelling has become a reliable design tool for improving ejector performance and it provides an alternative approach to experimentation (He, Li & Wang 2009). The flow behaviour inside the ejector is characterised by differential equations. The CFD method solves discretized versions of these equations numerically to simulate the behaviour of the flow.

In the present work, the commercial CFD package ANSYS FLUENT v14.5, based on a finite volume approach, was used to simulate the fluid flow within the axisymetric ejector geometry. The high speed flow processes that occur in ejectors produce a highly turbulent flow. Therefore, accurate flow modelling requires the use of a proven turbulence model. There are many turbulence models in the literature which have been applied to ejector flows.

In this chapter, simulations from the two most commonly used turbulence models in literature, $k - \epsilon$ and the $sst - k\omega$, were compared with the experimental data of the present work which was presented in Chapter 6 to identify the most suitable turbulence model for examining the details of the flow behaviour inside the ejector duct. Once the turbulence model was selected, an analysis of the complicated flow behaviour inside the CRMC ejector was performed. Further, the numerical study was compared with not only the experimental results, but also with the theoretical results for the CRMC design that were obtained in Chapter 3.

7.2 Turbulence model

Since there are no clear recommendations for selecting the turbulence model, modelling of the supersonic ejectors is still an open problem. Therefore, to achieve reasonable simulation of the ejector operation, the trial of more than one turbulence model seems a reasonable approach. Two turbulence models: the realizable $k - \varepsilon$ model (Rusly et al. 2005), and the $sst - k\omega$ (Riffat & Omer 2001) which are both available in Fluent, are considered in the present work. As the $k - \epsilon$ and $sst - k\omega$ models have a relatively low computational cost, both appear suitable approaches for ejector analysis (Bartosiewicz, Aidoun, Desevaux & Mercadier 2005, Bartosiewicz, Aidoun & Mercadier 2006). However, the assumption that the turbulence is isotropic is a significant assumption in both of these approaches.

7.2.1 Turbulence model k-epsilon

The standard $k - \epsilon$ model is a semi-empirical turbulence model based on the transport equations for the turbulence kinetic energy (k) and the turbulence dissipation rate (ϵ). Those two parameters can be mathematically expressed as:

$$k = \frac{1}{2}\overline{u_i' u_j'} \tag{7.1}$$

$$\epsilon = 2v\overline{e'_{ij}e'_{ij}} \tag{7.2}$$

where, $e_{ij} = \dfrac{\partial u_i}{\partial x_j}$

Formulation of the $k - \epsilon$ model requires writing transport equations for the turbulence kinetic energy, k, and the turbulence dissipation rate, ϵ, as can be done for any scalar quantity. However, these equations have a number of complicated terms that need to be modelled.

$$\frac{\partial(\rho k)}{\partial t} + \frac{\partial(\rho k u_i)}{\partial x_i} = \frac{\partial\Big((\mu + \frac{\mu_t}{\sigma_k})\frac{\partial k}{\partial x_j}\Big)}{\partial xj} + G_k - \rho\epsilon - 2\rho\epsilon M_t^2 \tag{7.3}$$

$$\frac{\partial(\rho\epsilon)}{\partial t} + \frac{\partial(\rho\epsilon u_i)}{\partial x_i} = \frac{\partial\Big((\mu + \frac{\mu_t}{\sigma_\epsilon})\frac{\partial \epsilon}{\partial x_j}\Big)}{\partial xj} + C_{1\epsilon}\frac{\epsilon}{k}G_k - C_{2\epsilon}\rho\epsilon\frac{\epsilon^2}{k} \tag{7.4}$$

where, G_k represents the generation of turbulence kinetic energy due to the mean velocity gradient and it is given by:

$$G_k = -\rho\overline{u'_i u'_j}\frac{\partial u_j}{\partial x_i} \tag{7.5}$$

and $M_t = \sqrt{\dfrac{k}{a^2}}$, $C_{1\epsilon}$ and $C_{2\epsilon}$ are constants and σ_k, σ_ϵ are the turbulent Prandtl numbers for k and ϵ, respectively.

7.2.2 Turbulence model sst-k-omega

Mass equation:

$$\frac{\partial\bar{\rho}}{\partial t} + \frac{\partial}{\partial x_i}(\bar{\rho}\bar{u}_i) = 0 \tag{7.6}$$

Momentum equation:

$$\frac{\partial}{\partial t}(\bar{\rho}\bar{u}_i) + \frac{\partial}{\partial x_i}(\bar{\rho}\bar{u}_j\bar{u}_i) = -\frac{\partial P}{\partial x_i} + \frac{\partial}{\partial x_j}(\bar{t}_{ji} + \rho\bar{\tau}_{ji}) \tag{7.7}$$

Energy equation:

$$\begin{gathered}\frac{\partial}{\partial t}\Big[\bar{\rho}(\tilde{e} + \frac{\tilde{u}_i\tilde{u}_i}{2} + k)\Big] + \frac{\partial}{\partial x_i}\Big[\bar{\rho}\tilde{u}_j(\tilde{h} + \frac{\tilde{u}_i\tilde{u}_i}{2} + k)\Big] = \\ \frac{\partial}{\partial x_j}\Big[(\frac{\mu}{Pr_L} + \frac{\mu_T}{Pr_T})\frac{\partial\tilde{h}}{\partial x_j} + (\mu + \frac{\sigma^*\rho k}{\omega})\frac{\partial k}{\partial x_j}\Big] + \frac{\partial}{\partial x_i}\Big[\tilde{u_i}(t_{ij} +\tilde{}\rho\bar{\tau}_{ij})\Big]\end{gathered} \tag{7.8}$$

Molecular and Reynolds-Stress tensors:

$$\bar{\tau}_{ij} = 2\mu\bar{S}_{ij}, \qquad \bar{\rho}\tau_{ij} = 2\mu T\bar{S}ij - \frac{2}{3}\bar{\rho}k\delta_{ij}, \qquad \bar{S}_{ij} = S_{ij} - \frac{1}{3}\frac{\partial\tilde{u}k}{\partial\tilde{x}k}\delta_{ij} \tag{7.9}$$

Eddy viscosity:

$$\mu T = \frac{\rho k}{\tilde{\omega}}, \quad \tilde{\omega} = max\Big[w, C_{lim}\sqrt{\frac{2\bar{S}_{ij}\bar{S}ij}{\beta^*}}\Big], \quad C_{lim} = \frac{7}{8} \tag{7.10}$$

Turbulence kinetic energy:

$$\frac{\partial}{\partial t}(\bar{\rho}k) + \frac{\partial}{\partial x_j}(\bar{\rho}\tilde{u}_j k) = \bar{\rho}\tau_{ij}\frac{\partial\tilde{u}_i}{\partial x_i} - \beta^*\bar{\rho}k\omega + \frac{\partial}{\partial x_j}\Big[\Big(\mu + \sigma^*\frac{\bar{\rho}k}{\omega}\Big)\frac{\partial k}{\partial x_i}\Big] \tag{7.11}$$

Specific dissipation rate:

$$\begin{aligned}\frac{\partial}{\partial t}(\bar{\rho}\omega) + \frac{\partial}{\partial x_j}(\bar{\rho}\tilde{u}_j\omega) = \alpha\frac{\omega}{k}\rho\tau_{ij}\frac{\partial\tilde{u}_i}{\partial x_i} - \beta\bar{\rho}\omega^2 + \sigma_d\frac{\bar{\rho}}{\omega}\frac{\partial k}{\partial x_j}\frac{\partial\omega}{\partial x_j} \\ +\frac{\partial}{\partial x_j}\Big[\Big(\mu_\sigma\frac{\bar{\rho}k}{\omega}\Big)\frac{\partial\omega}{\partial x_j}\Big]\end{aligned} \tag{7.12}$$

Closure coefficients:

$$\alpha = 0.52, \quad \beta = \beta_o f_\beta, \quad \beta^* = 0.09, \quad \sigma = 0.5, \quad \sigma^* = 0.6, \quad \sigma_{do} = 0.125 \tag{7.13}$$

$$\beta_o = 0.0708, \quad Pr_T = 0.8888, \quad \sigma_d = \begin{cases} 0 & \frac{\partial k}{\partial x_j}\frac{\partial\omega}{\partial x_j} \leq \\ \sigma_{do} & \frac{\partial k}{\partial x_j}\frac{\partial\omega}{\partial x_j} > 0 \end{cases} \tag{7.14}$$

$$\frac{1 + 85\chi_\omega}{1 + 100\chi_\omega}, \quad \chi = \mid \frac{\Omega_{ij}\Omega_{jk}\hat{S}_{ki}}{(\beta^*\omega)^3} \mid, \quad \hat{S}_{ki} = S_{ki} - 0.5\frac{\partial\tilde{u}_m}{\partial x_m}\delta_{ki} \tag{7.15}$$

7.3 Dimensionless wall distance

The dimensionless wall distance (y^+) is a non-dimensional normal distance from the ejector wall and is a relevant parameter for the wall bounded flow simulation and expressed as (Wilcox 1998)

$$y^+ = \frac{yv^*\rho_{wall}}{\mu_{wall}}, \qquad v^* = \sqrt{\frac{\tau_{wall}}{\rho_{wall}}}, \qquad \tau_{wall} \approx \mu_{wall}\Big(\frac{\partial u}{\partial y}\Big)_{y=0} \tag{7.16}$$

Within the CFD context, the first cell size adjacent to the wall has a y value and is represented by y^+. For the $sst - \kappa\omega$ turbulence model, $y^+ < 1$ for the first cell is recommended and different turbulence models may require different y^+ values (Roy &

Blottner 2003). In the present work, y^+ has a different value for the different mesh densities. For example, the y^+ value of 0.24 is a representative for the fine mesh and Table 7.1 shows the y^+ values, the number of cells, and the aspect ratio for the three mesh resolutions: coarse, medium, and fine. In each case, the reported value of y^+ was taken on the parallel section of the mixing chamber using a simulation with boundary conditions of 200 kPa, 1.6 kPa, 4.6 kPa for the primary, secondary, and back pressures respectively. The near wall treatment was left as the "standard wall function", which has been used successfully by others in the simulation of wall bounded flows with very high Reynolds number (Sriveerakul et al. 2007).

Table 7.1: Different mesh resolutions used in the simulations.

resolution	Number of cells	y^+	Maximum aspect ratio
Coarse	30000	2.4	1.92
Medium	40000	1.35	1.86
Fine	50000	0.24	1.67

7.4 Computational simulation

Computational fluid dynamic (CFD) simulations using ANSYS FLUENT v14.5 were performed to simulate the internal flows inside the CRMC ejector ejector. The advantages of this method are: (1) it is a time and cost effective way to estimate the performance of the ejector; (2) CFD is a reasonably convenient tool, and optimization analysis can be performed at moderate expense of time and cost; and (3) local parameters which are difficult to obtain by experimental means can be estimated using CFD (Meakhail & Teaima 2013). The axi-symmetric method was applied to model the ejector geometry in a 2D domain instead of attempting to solve a computationally-demanding 3D model.

The density-based coupled-implicit solver was used to calculate the flow field with a second order discretization for the momentum and energy equations. The near-wall treatment was left as the standard wall function, which has given reasonably accurate results for the wall bounded flows with very high Reynolds number in other studies (Ruangtrakoon et al. 2012).

7.4.1 Solution convergence

According to Al-Ansary & Jeter (2004), the numerical solution is considered to be converged if the mass balance is accurate with an error less than of 0.1% and the residuals of the continuity, velocity, energy, and turbulence parameters are less than 10^{-3} . However, in the present work, the residuals for each conservation equation are required to fall below 10^{-6}. In addition, at convergence, the global mass imbalance is checked for the boundaries and is required to be

$$\left| \frac{\sum \dot{m}_{in} - \sum \dot{m}_{out}}{\sum \dot{m}_{in}} \right| \leq 1 \times 10^{-6} \tag{7.17}$$

which can be typically achieved with around 100000 iterations for the fine mesh.

7.4.2 Ejector geometry

The geometry of the computational domain of the modelled nozzle and CRMC ejector duct were taken from the experimental configuration presented in Chapter 5. Figures 7.1 and 7.2 show respectively the nozzle and the CRMC ejector duct profiles that were used in the present numerical study. Dimensions for the CRMC duct were obtained theoretically in Chapter 3 and included in Table 3.2.

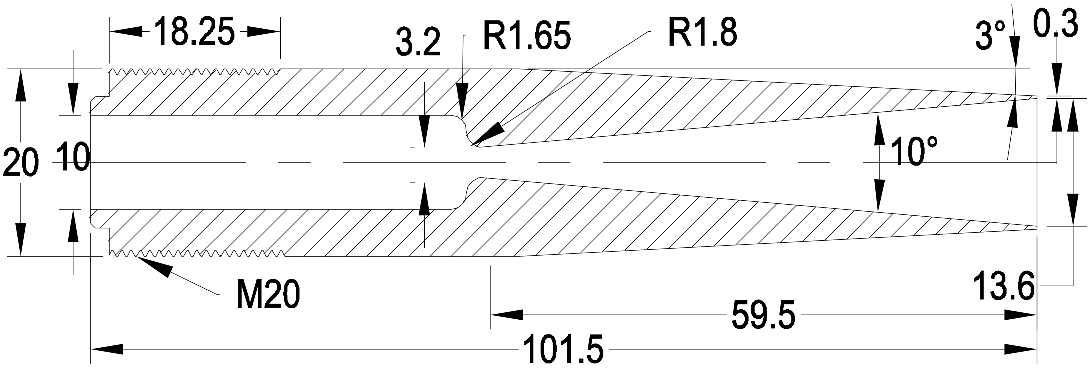

Figure 7.1: Primary nozzle profile, all dimensions in mm.

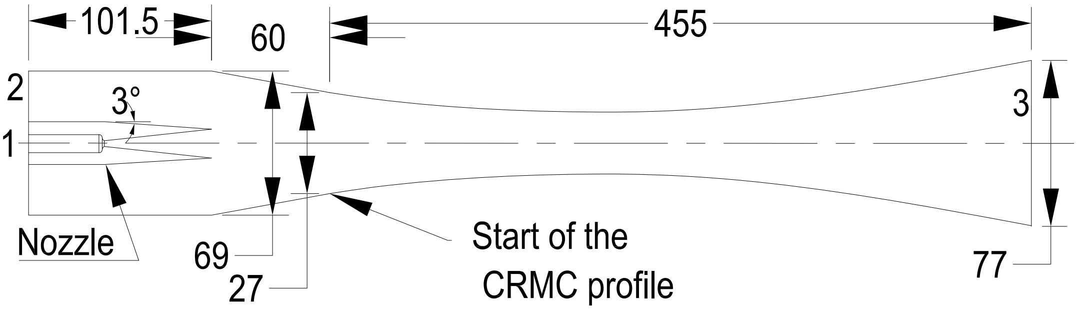

Figure 7.2: Primary nozzle and CRMC ejector profile, all dimensions in mm. Numbers 1, 2, and 3 refer to primary, secondary, and exit flows respectively.

7.4.3 Boundary conditions

Once the grid was finalized for the CRMC ejector system geometry, accurate boundary conditions were set to simulate actual operating conditions. Boundary conditions were applied to the two inlets and the one outlet of the ejector. High pressure primary flow conditions were set at the location where the primary flow enters the primary nozzle, location 1 as illustrated in Figure 7.2. Low pressure secondary flow conditions were set at the entrance of the entrainment section, location 2 in Figure 7.2. Both the primary and secondary pressures measured are static pressures; their values are measured experimentally and incorporated in the CFD model boundary conditions as total pressures. This is a reasonable approach since the respective velocities have been calculated to be a few meters per second resulting in static and total pressures effectively being equal at these locations. Outlet conditions of the discharged flow were set at the ejector exit, location 3 in Figure 7.2. As a result of using ambient temperature air as a working fluid, the temperature difference in these three locations is not significant. Parameters for the three boundary conditions were measured for each experimental test as reported in Chapter 5 and Chapter 6 and these values were used in the CFD model.

7.5 Validation of simulation

The experimental data were used to validate the CFD simulations. Two CFD turbulence models, $sst - k\omega$ and $k - \epsilon$ were selected for the initial ejector simulations. The working fluid used in the present study is air, and its density was defined by the ideal gas law.

7.5.1 Static pressure: variation with grid density

For successful CFD simulations, a suitable computational grid for the geometry being modelled is necessary. The following considerations were taken into account:

- The most common grids are those based on triangular and quadrilateral cells.
- Quadrilateral cells are most easily aligned with the overall ejector flow direction.

Strong gradients are expected in some ejector regions, such as the nozzle throat, nozzle walls, secondary flow duct and the ejector duct walls thus, the grid density is increased in these regions. The grid had primarily structured quadrilateral elements with about 3×10^4, 4×10^4, and 5×10^4 elements in the coarse, medium, and fine cases respectively. In order to test the sensitivity of the numerical results to the mesh density and to assess the level of mesh independence, results from the three mesh sizes were examined. Figure 7.3 shows a comparison between CFD results of the static pressure on the ejector wall for the three different grid resolutions and the experimental measurements of the present work. In the present experimental work, the static pressure distribution on the ejector wall was measured at different points. Figure 7.3 shows the results from the $sst - k\omega$ turbulence model.

The differences between the coarse mesh simulation and the experimental data is about 6.7 %, this percentage difference decreased to about 3 % for both the medium and fine meshes. The medium mesh was selected for the present simulation because of the demonstrated degree of mesh independence, and to reduce the running time of the simulation, which was found to be much shorter than that of the fine mesh. Figure 7.4

shows a fine mesh of the convergent-divergent primary nozzle and part of secondary flow duct.

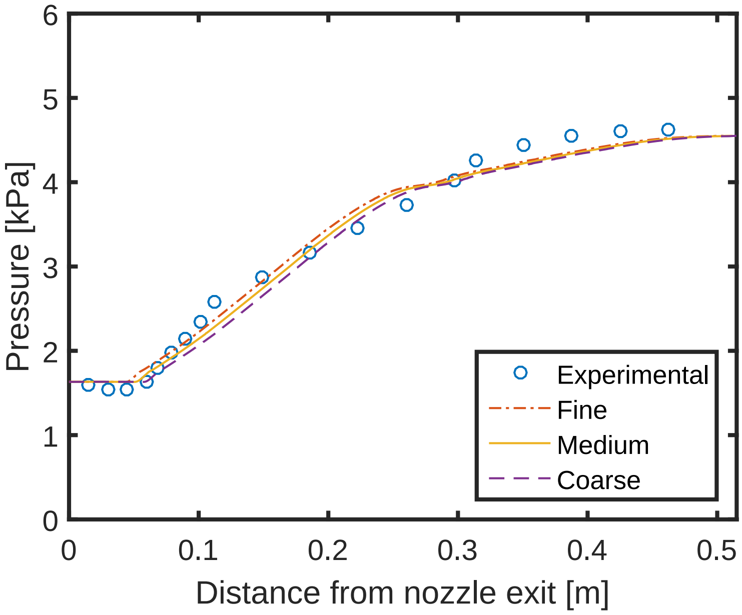

Figure 7.3: Comparison of simulated static pressure and experimental data for the three grid resolutions and for operating conditions of primary, secondary, and exit pressure of 200 kPa, 1.6 kPa, and 4.6 kPa respectively.

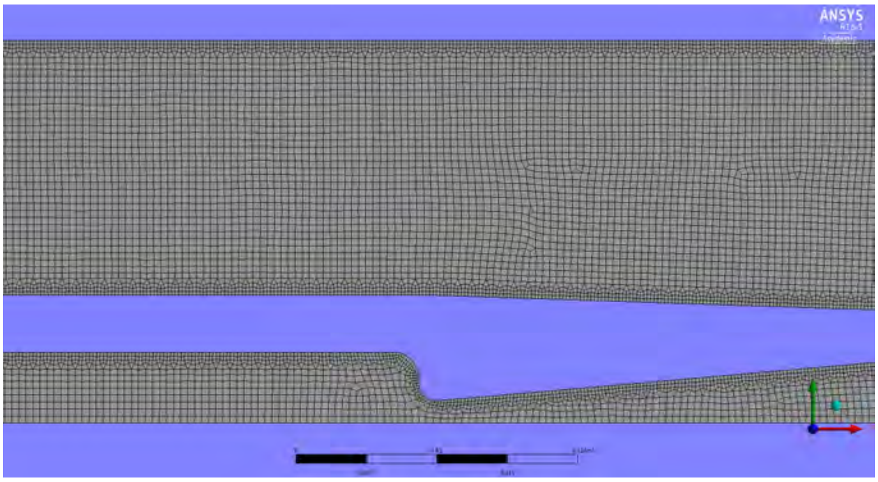

Figure 7.4: Meshing of the primary nozzle and a portion of the secondary flow duct.

7.5.2 Static pressure: variation with turbulence model

A comparison between numerical results from the two turbulence models and experimental data for the static pressure distribution along the ejector wall is presented in Figure 7.5 for the same operating conditions as used in Figure 7.3. The simulations using the two turbulence models $sst - k\omega$ and $k - \epsilon$ are reasonably consistent with each other as well as with the experimental results. However, the $k - \epsilon$ turbulence model demonstrates a higher discrepancy compared with the experimental data than the $sst - k\omega$ model at distance from the nozzle exit between 0.2 and 0.3 m.

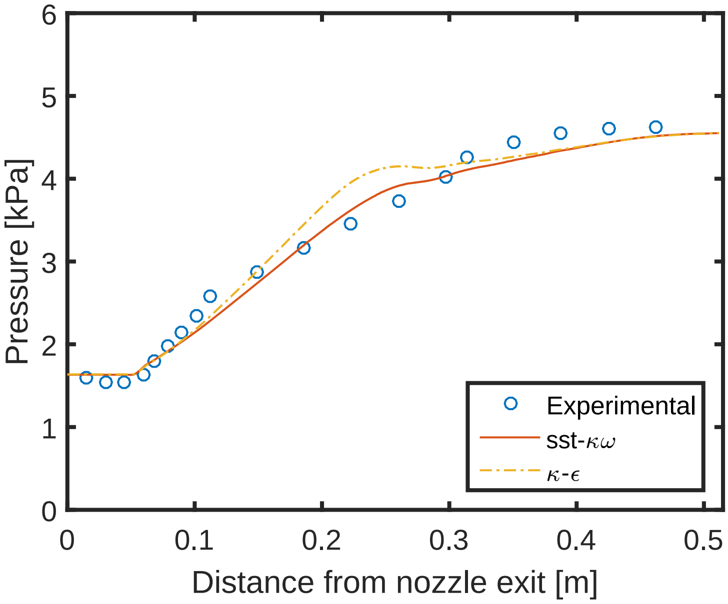

Figure 7.5: Comparison between experimental data and CFD simulations of static pressure along the ejector wall for two turbulence models and for operating conditions of primary, secondary, and exit pressure of 200 kPa, 1.6 kPa, and 4.6 kPa respectively.

A comparison between the errors in the static pressure distribution along the ejector wall simulated using the two turbulence models in this study and work in literature is presented in Table 7.2. Sriveerakul et al. (2007) compared their experimental data with commercial CFD software. Yang et al. (2012) compared their simulations to the experimental work of Sriveerakul et al. (2007) for three turbulence models and Al-Doori (2013) compared experimental data with a simulations using Eilmer3. The values of the error reported in Table 7.2 were obtained by calculating the average values of the errors for all pressure transducers along the ejector according to

$$\text{Error } \% = \frac{1}{n}\sum_{i=1}^{n} \frac{\text{CFD's static pressure - Experimental static pressure}}{\text{Experimental static pressure}} \times 100 \quad (7.18)$$

where n is the number of pressure measurement locations. The wall static pressure values from the two turbulence models were taken at the same nineteen locations of the experimental data from Chapter 6 and presented in Figure 7.5. The simulations consistently under-estimate the static pressures in the ejector duct in all cases considered in Table 7.2. The average errors in the simulated static pressures in the present work are relatively low compared to the majority of results presented in Table 7.2.

Table 7.2: Average error in simulation of the static pressure: comparison of different turbulence models.

Author	Turbulence model	Error (%)
Sriveerakul et al. (2007)	realizable $k-\epsilon$	-8
Yang et al. (2012)	realizable $k-\epsilon$	-6
Yang et al. (2012)	standard $k-\epsilon$	-12
Yang et al. (2012)	RNG $k-\epsilon$	-10
Al-Doori (2013)	$k-\omega$	-2
Present work	$sst-k\omega$	-6.3
Present work	realizable $k-\epsilon$	-6.8

7.5.3 Entrainment ratio: variation with grid density

Computations were performed using three different levels of discretization of the flow domain: coarse, medium, and fine resolutions using the $sst-k\omega$ turbulence model. Figure 7.6 illustrates a comparison between the simulated entrainment ratio results for the three different grid resolutions and the experimental data. The difference between the coarse mesh simulation and the experimental data is about 10.53 %. This percentage difference decreases to about 3 % for the medium mesh, and about 2.63 % for the fine mesh. Given the entrainment ratio results from the medium mesh differ from the experimental results by about the same amount as the fine mesh, the medium mesh has been used for further entrainment ratio simulations to minimise simulation time.

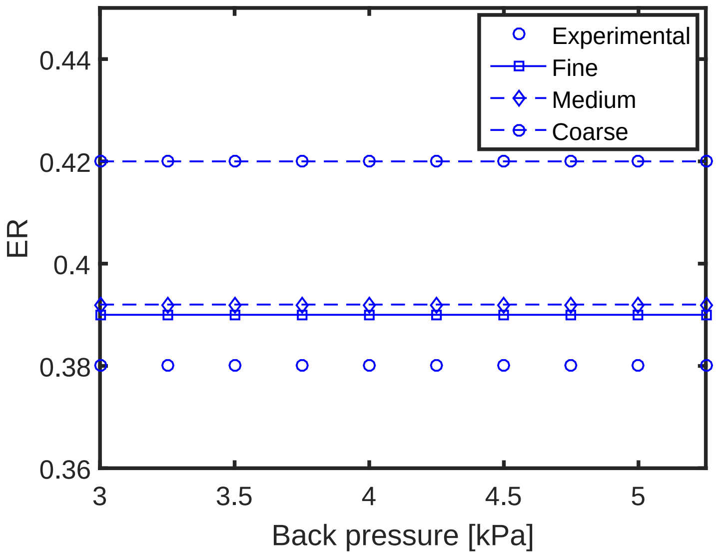

Figure 7.6: Comparison of simulated entrainment ratio of three grid resolutions and for primary pressure of 200 kPa, secondary pressure of 1.6 kPa and different back pressure.

7.5.4 Entrainment ratio: variation with turbulence model

Figure 7.7 and Figure 7.8 present the variation of the entrainment ratio at primary pressure of 200 kPa and range of ejector back pressures for secondary pressures of 1.6 kPa and 2.5 kPa. In both figures, the experimental results from Chapter 6 were used, and the numerical results obtained from the two different turbulence models are presented. In general, both turbulence models overestimate the entrainment ratio. For Figure 7.7, the ejector is operating in the double choked mode, while for Figure 7.8, the ejector operates in both the double choked and single choked modes. In Figure 7.7, the average discrepancy between the experimental data and the $sst - k\omega$ turbulence model was 3 % whereas, between the experimental data and the $k - \epsilon$ turbulence model it was 4.3 %.

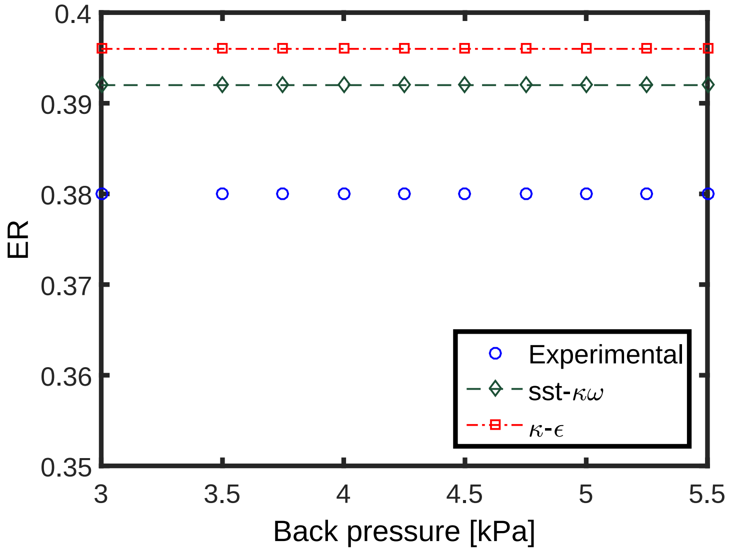

Figure 7.7: Comparison between experimental data and CFD simulations of the entrainment ratio for two turbulence models and for primary pressure of 200 kPa, secondary pressure of 1.6 kPa and different back pressure.

For the results in Figure 7.8, the discrepancies between experimental results and the two turbulence models are listed in Table 7.3. The discrepancy between the experimental data and either of the two turbulence models is quite small, but the $sst - k\omega$ model produces a lower error than the $\kappa - \epsilon$ model. However, for the single choked mode, the discrepancy is high. Figure 7.8 shows that in the double choked mode, the simulation overestimates the entrainment ratio while in the single choked mode, the simulation underestimates the entrainment ratio.

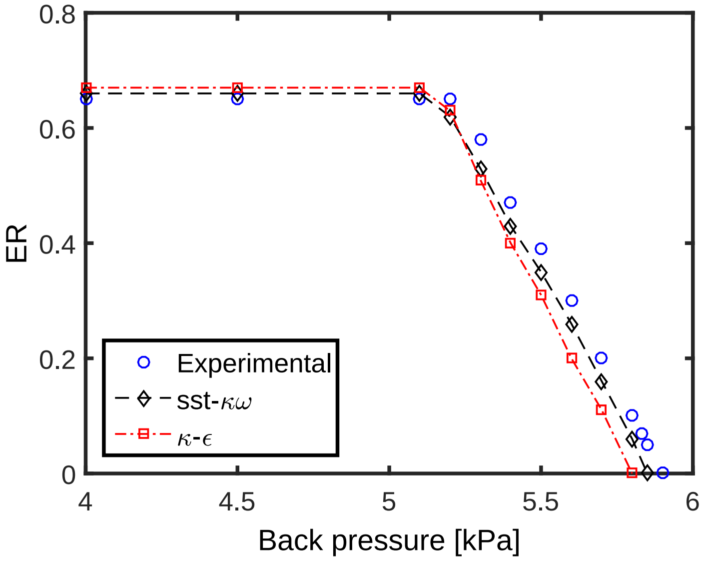

Figure 7.8: Comparison between experimental data and CFD simulations of the entrainment ratio for two turbulence models and for primary pressure of 200 kPa, secondary pressure of 2.5 kPa and different back pressure.

Table 7.3: average error for entrainment ratio simulations for different turbulence models from Figure 7.8.

Model	Double choke error	Single choke error
$sst - k\omega$	0.0154	0.02
$k - \epsilon$	0.031	0.1

7.5.5 Summary

The $sst - k\omega$ turbulence model simulates the ejector performance slightly more accurately than the $k - \epsilon$ turbulence model in terms of the static pressure and the entrainment ratio. This conclusion is consistent with other studies in which the limitations of the $k - \epsilon$ turbulence model in simulations of the ejector performance becomes more clear as the motive pressure increases (Dennis 2009), and the $sst - k\omega$ turbulence model has shown better performance in term of local parameters and stream mixing (Bartosiewicz et al. 2005). Therefore, the $sst - k\omega$ turbulence model is used in all future analysis in this thesis since it provides slightly better simulation of ejector performance relative to the $k-\epsilon$ turbulence model.

Given the CFD simulations are able to produce static pressures and entrainment ratios for double choked ejector operation with average errors in the vicinity of 5 %, it is anticipated that a similar level of agreement would be achieved in the simulation of other local features such as the static pressure distribution along the axis of the ejector, Mach number contour lines, and flow streamlines. Direct measurement inside the ejector duct may be the preferred method to obtain the required flow parameters. However, the flow nature and geometrical complexity of the ejector and its limited available area to insert such tools into the flow path with no disturbance makes it necessary to rely on the CFD technique for such analysis.

7.6 Experimental-theoretical-CFD comparison

A comparative analysis of present experimental data using the fabricated model as in Figure 4.13, theoretical simulations using the analytical model as in Figure 3.2, and CFD simulations for the CRMC ejector duct is presented in this section.

7.6.1 Variation of entrainment ratio

Over the range of operating conditions as listed Table 7.4, Figures 7.9 and 7.10 present a comparison between experimental results obtained in Chapter 6 and CFD simulations using the $sst-k\omega$ turbulence model. For all cases, the $sst-k\omega$ model over-estimates the value of entrainment ratio relative to the experimental data in the double choked flow region, but under-estimates the critical back pressure relative to the experimental data. The values of entrainment ratio in the double choked flow region were 0.38, 0.66, 0.99, 1.19 based on the experimental data for cases (a), (b), (c) and (d) respectively, while the corresponding values were 0.39, 0.68, 1.05, 1.21 for the $sst-k\omega$ model. The maximum difference between the experimental data and the $sst-k\omega$ model was about 3 % for case (b). The critical back pressures for those cases based on the experimental data were found to be 4.8 kPa, 5 kPa, 6.1 kPa, 6.7 kPa for cases (a), (b), (c) and (d) respectively, while based on the $sst-k\omega$ model, the corresponding values were 4.7 kPa, 4.85 kPa, 6 kPa, 6.55 kPa. The maximum difference was again found to be about 3 % for case (b). The origin of such differences might be attributed to the the turbulence model.

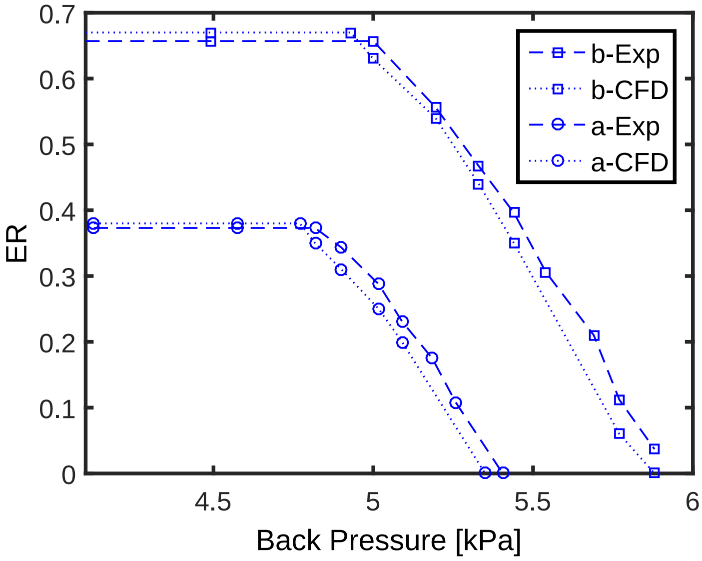

Figure 7.9: Comparison of the entrainment ratio from CFD simulations and experimental data for cases (a) and (b) of Table 7.4.

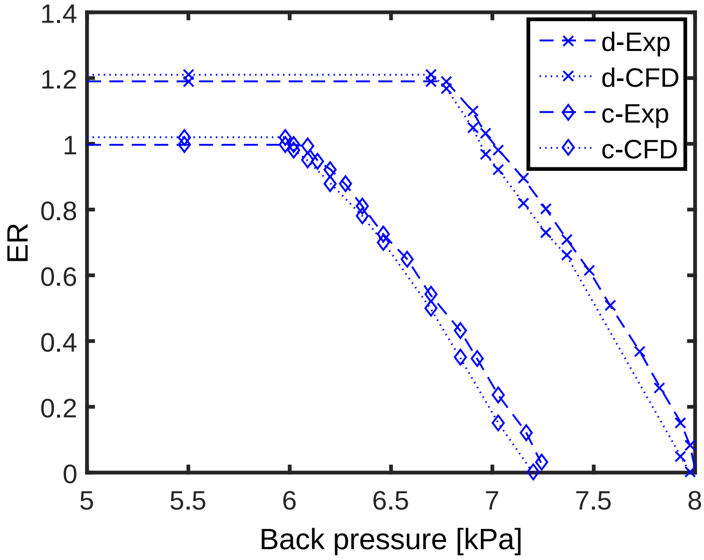

Figure 7.10: Comparison of the entrainment ratio from CFD simulations and experimental data for cases (c) and (d) of Table 7.4.

Table 7.4: Ejector operating conditions in the 4 cases presented in Figures 7.9 and 7.10.

Case	Primary pressure (kPa)	Secondary pressure (kPa)
a	200	1.6
b	200	2.5
c	200	4
d	200	5

7.6.2 Variation of wall static pressure

Two operating conditions from the experimental work in Chapter 6 were selected for CFD simulation as presented in Table 7.5. Figure 7.11 presents the experimental and numerical results of the static pressure distribution along the ejector wall. The average difference between the experimental and CFD results of case 1 is 2.8 % whereas it is 3.45 % in case 2.

Table 7.5: Ejector operating conditions for experimental-analytical-CFD comparison.

Case	Primary pressure (kPa)	Secondary pressure (kPa)	Back pressure (kPa)
1	200	1.4	4.5
2	200	1.8	5

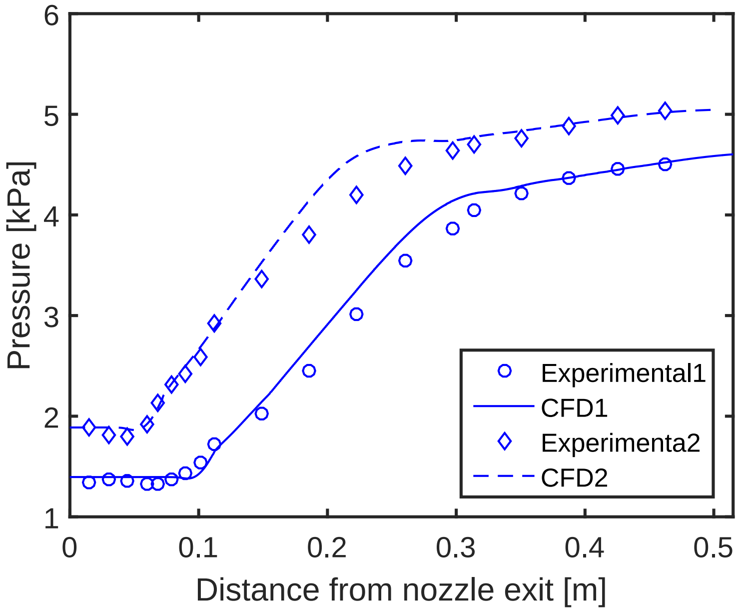

Figure 7.11: Experimental and CFD results for pressure along the ejector wall at operating conditions of case 1 and case 2.

Figure 7.12 presents a comparison between the static pressure along the ejector axis obtained analytically and numerically for case 1 conditions. The analytical result was obtained using the set of equations presented in Chapter 3. In this figure, the shock train stemming from the nozzle exit plane is not captured within the analytical model. The analytical model is not able to accurately predict flow conditions in this region of the ejector. The onset of the mixing between the primary and secondary flow also starts at the nozzle exit plane and the analytical model does not accurately treat the mixing process.

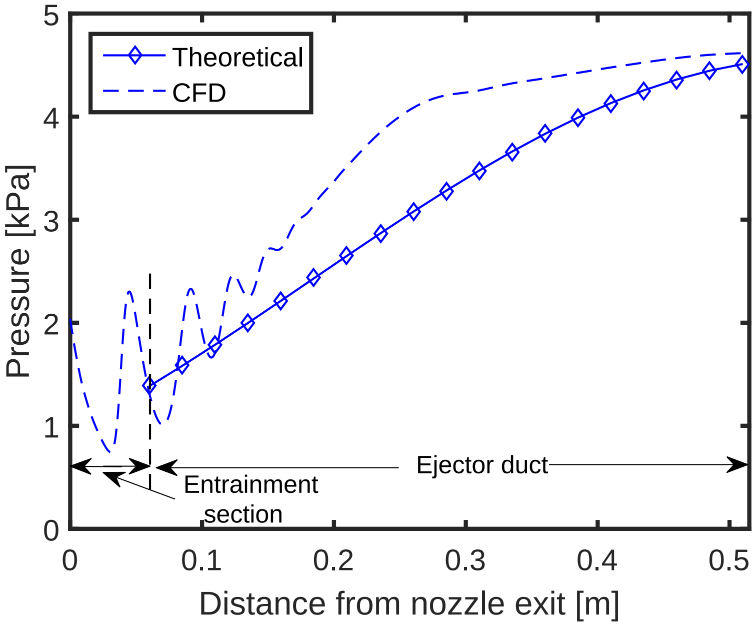

Figure 7.12: Theoretical and CFD results for pressure along the ejector axis for case 1.

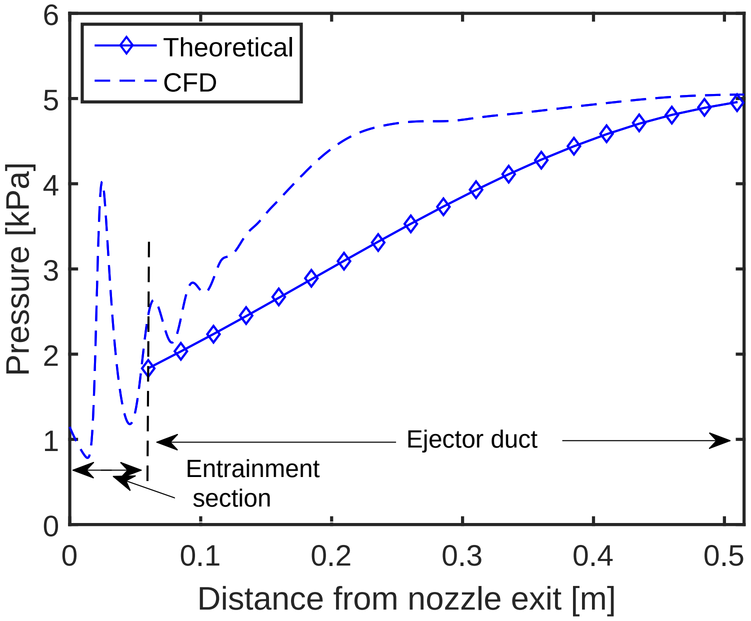

Figure 7.13: Theoretical and CFD results for pressure along the ejector axis for case 2.

Figure 7.13 presents a comparison between the static pressure along the ejector axis obtained theoretically and numerically for the case 2 conditions. The CFD results in Figure 7.13 show that the primary flow pressure on the ejector axis oscillates within the entrainment section. The secondary flow mixes with the primary flow due to the velocity difference between the two streams. The analytically specified static pressure value of 1.4 kPa in the operating conditions of Figure 7.12, and 1.8 kPa in the operating conditions of Figure 7.13 are not specially close to the value of the mean of the pressure fluctuations in the entrainment region for both cases.

7.6.3 Variation of Mach number

Figure 7.14 presents the other key aspect, the variation of Mach number along the ejector axis for case 2. According to the theoretical analysis, the Mach number of the primary flow at the entrance of the ejector is 2.66, which is not very close to the mean value of the oscillating Mach number that is simulated numerically.

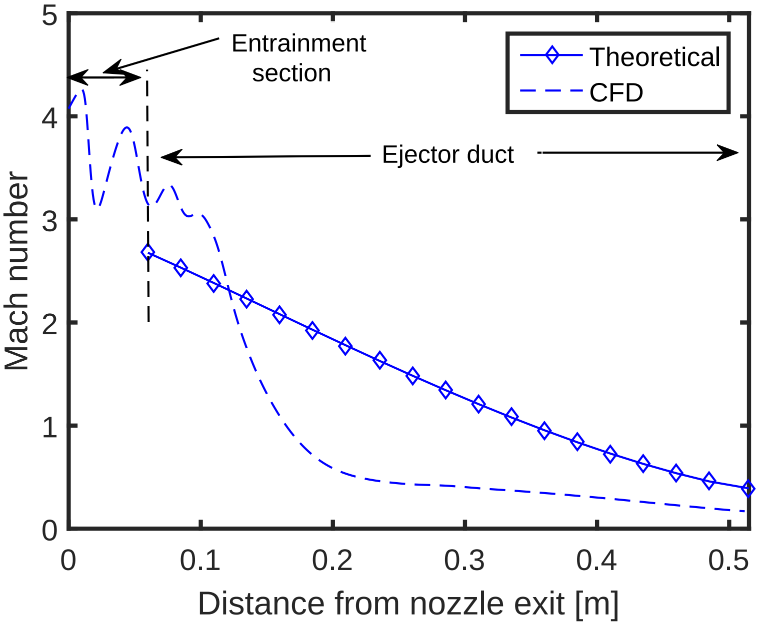

Figure 7.14: Theoretical and CFD results for Mach number along the ejector axis for case 2.

CFD results show that the Mach number remains largely supersonic and the flow experiences shock waves along the axis of the mixing region and a small portion of the ejector duct. Downstream of this shock wave region, the Mach number rapidly declines and the effects of the shock waves disappear and the flow reaches a sonic state at a distance of about 0.16 m downstream of the nozzle exit which coincides with a distance of 0.1 m downstream of the commencement of the ejector duct. Further decline in Mach number occurs as the flow moves downstream and reaches its lowest value at the ejector exit.

Results from the CFD study show the flow within the ejector to be significantly different from the analytical calculations. This can be explained by the one-dimensional nature of the analytical method, where it is assumed that the flow entering the ejector has a uniform Mach number. However as shown in Figure 7.15, this is not the case, rather the flow entering the ejector consists of a central supersonic jet surrounded by low velocity entrained flow. The effects of shock waves within the supersonic jet are not captured within the analytical method. Improvements in performance through the optimization of the geometry should be possible using a higher accuracy approach than that available from the one-dimensional model.

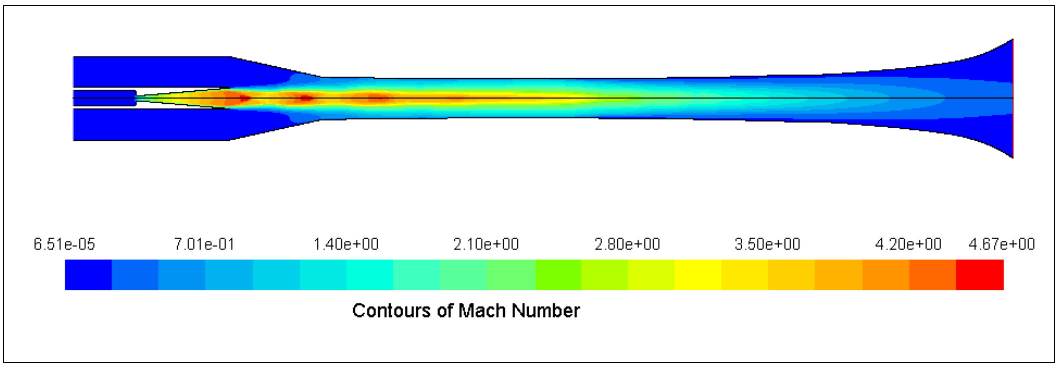

Figure 7.15: Contours of Mach number in the CRMC ejector showing shocks in the primary stream.

7.6.4 Variation of primary pressure

Figure 7.16 shows the static pressure distribution along the ejector centreline for a range of primary pressures, 1.6 kPa as the secondary pressure, and 4.8 kPa as the back pressure. For the lowest primary pressure of 200 kPa, the ejector exhibits a series of shocks downstream of the primary nozzle. These shocks extend about 100 mm downstream which includes, in addition to the entrainment section, a 30 mm part of the CRMC duct. Beyond this shock series, the static pressure increases in a more or less gradual manner as the CRMC theory suggests. A similar behaviour was observed for the slightly higher primary pressures of 220 kPa and 230 kPa. As the primary pressure increases further, a second shock series starts to appear, becoming particularly clear at a primary pressure of 250 kPa at a distance of 0.2 m downstream of the nozzle exit.

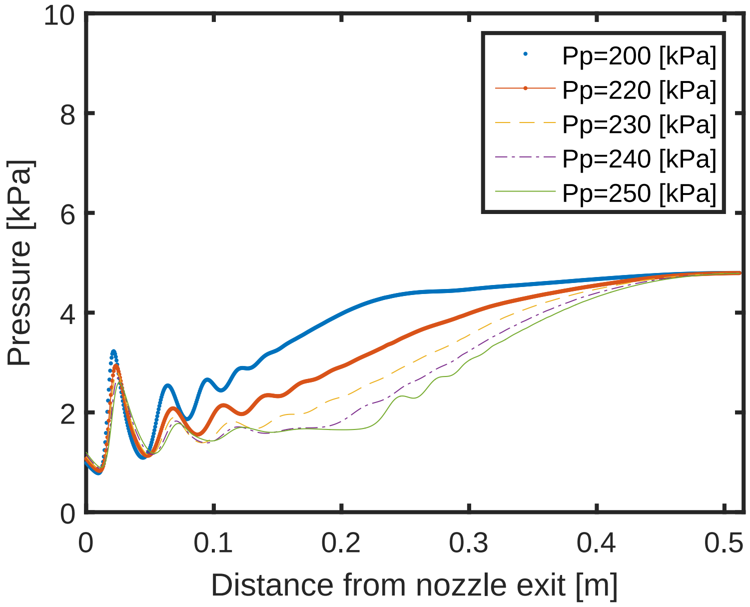

Figure 7.16: Static pressure distribution along the ejector axis for a range of primary pressure, 1.6 kPa as the secondary pressure, and 4.8 kPa as the back pressure.

The primary pressure of 250 kPa could be considered as a critical value for the present CRMC ejector model: for a primary pressure higher than this value, the CRMC ejector has variations in static pressure on the centreline that indicate the momentum is no longer changing at constant rate. From the experimental data, at the secondary pressure of 1.6 kPa, the entrainment ratio of the ejector reaches its highest value for a primary pressure 230 kPa (see Chapter 6), Section 6.3, Figure 6.6.

The primary pressure design point of the present ejector is 200 kPa, as stated in Chapter 3. From the present simulations, it is observed that apart from the primary nozzle flow region, the CRMC ejector includes a gradual and largely shock-free increase in static pressure until the primary pressure reaches value of 230 kPa. Thus, it appears this CRMC ejector can operate at higher primary pressure conditions by 25 % relative to the design point conditions. Beyond this primary pressure, the ejector performance declines relative to its performance at the design point. However, smooth variations in static pressure were observed in conventional ejector design of (Al-Doori 2013) thus, a strong evidence of elimination of the shock series in the CRMC ejector still needed.

Figure 7.16 indicates that increasing primary pressure causes a decrease in the shock wave strength within the flow downstream of the nozzle exit. This case is different to the flow behaviour observed in the conventional ejector when the shock waves strengthen as the primary pressure increases (Desevaux, Marynowski & Khan 2006). However, when the flow at the nozzle exit is over-expanded as it is in the present work, the magnitude of the shock compression reduces as the primary pressure increases. In the work of Desevaux et al. (2006), the flow at the nozzle exit was under-expanded.

Figures 7.17 and 7.18 illustrate the effect of primary pressure on the flow field in the ejector duct. The sonic line dimensions are listed in Table 7.6. In this table, L_{M1} refers to the length of the sonic surface measured from the nozzle exit to the ejector centreline, D_{M1} refers to the sonic surface maximum diameter, and L_{DM1} refers to the location of this maximum diameter relative to the nozzle exit. The Mach number in combination with the flow static pressure indicates the mixed flow ability to overcome the back pressure. It can be seen that the sonic surface (Mach 1) extends further down stream as the primary pressure increases which allows the ejector to operate successfully at higher back pressure. At a primary pressure of 200 kPa the sonic surface extends to 160 mm and increases to 380 mm at pressure of 250 kPa. The total distance between the nozzle exit and the ejector exit is 515 mm.

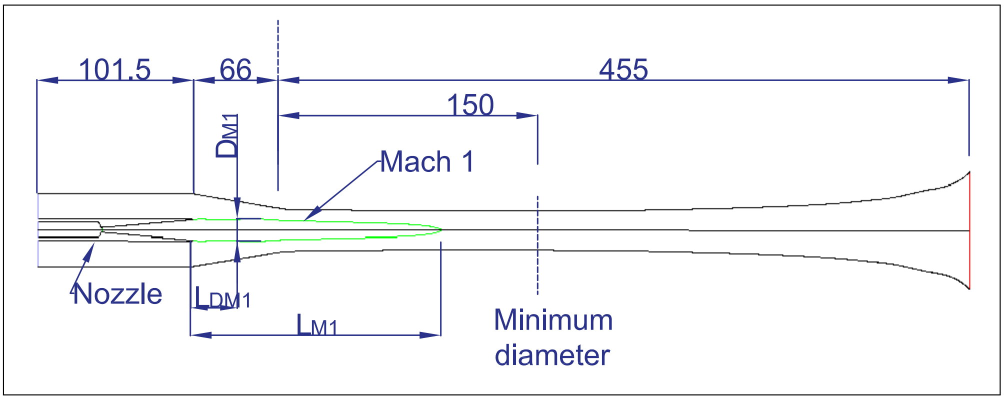

Figure 7.17: Illustration of parameters used to define the sonic surface dimensions. Case illustrated is for the primary pressure of 200 kPa, secondary pressure of 1.6 kPa and exit pressure of 4.8 kPa.

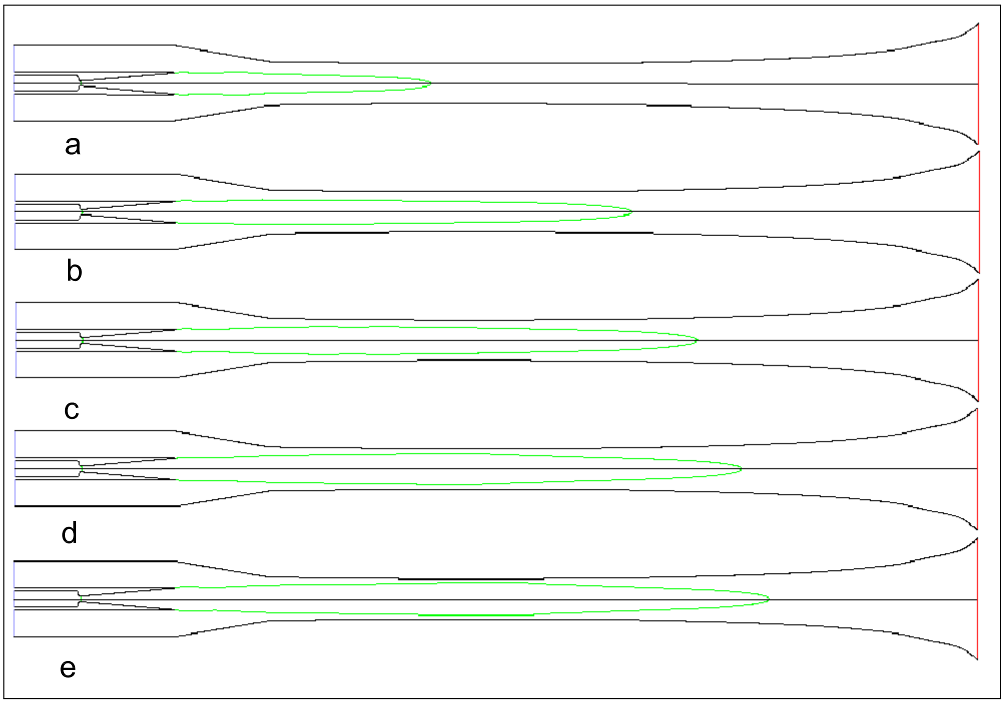

Figure 7.18: Sonic surface at the primary pressure of (a) 200 kPa, (b) 220 kPa, (c) 230 kPa, (d) 240 kPa, (e) 250 kPa, secondary pressure of 1.6 kPa and exit pressure of 4.8 kPa.

Table 7.6: Sonic surface dimensions at different primary pressures, a secondary pressure of 1.6 kPa and an exit pressure of 4.8 kPa.

case	Primary pressure (kPa)	ER	D_{M1}(mm)	L_{DM1}(mm)	L_{M1} (mm)
a	200	0.39	15	42	160
b	220	0.42	17	90	290
c	230	0.42	18	135.5	323
d	240	0.36	20	165	360
e	250	0.33	20.2	179	380

The sonic surface maximum diameter varies from 15 mm for case (a) to 20.2 mm for case (e). The area available to the secondary flow is governed by two parameters, the jet diameter and its position relative to ejector axis as the ejector diameter is varying along the axis. This diameter achieved at primary pressure 220 kPa where the maximum sonic surface diameter is 17 mm and is located at 90 mm downstream of the primary nozzle exit. As the primary pressure increases, the maximum sonic surface diameter increases and is located further downstream where the ejector diameter becomes smaller and reaches its minimum value at 216 mm downstream of the nozzle exit. However, the detrimental effect of such increase is reducing the available area to secondary flow to mix with the primary flow. Consequently, the entrainment ratio decreases with increasing primary pressure as illustrated in Figure 6.6.

7.6.5 Ejector flow modes

7.6.5.1 Choked flow mode

Figure 7.19 shows a map of the static pressure distribution along the ejector duct at a choked operating condition. The exit pressure is slightly less than the critical back pressure to ensure that the ejector operates in the double-choked mode. The entrainment ratio is 0.39 as long as the back pressure is lower than its critical value.

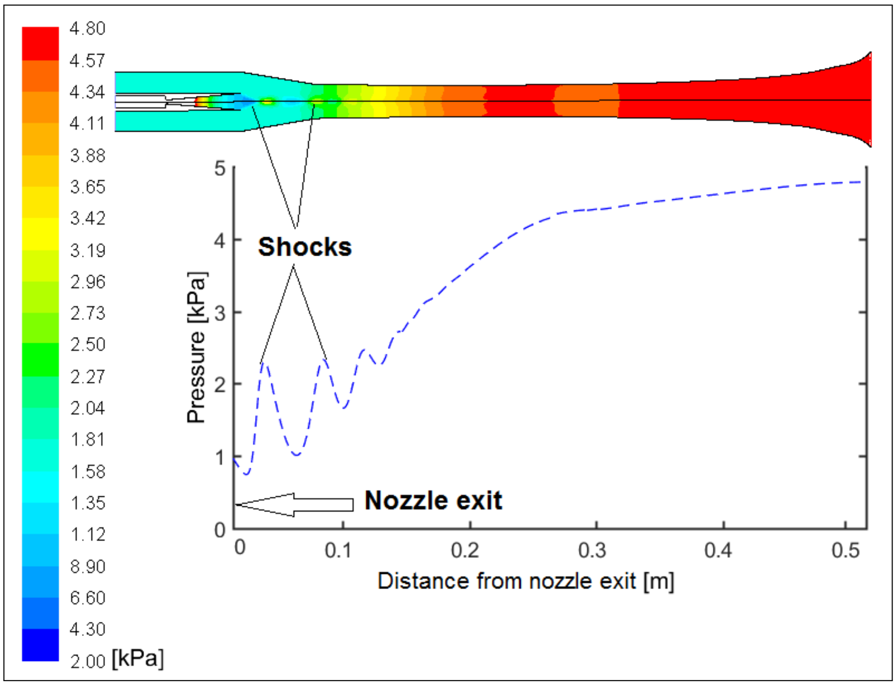

Figure 7.19: CRMC ejector pressure map and pressure distribution along the axis for 200 kPa, 1.6 kPa, and 4.8 kPa as the primary, secondary, and back pressure respectively.

The variation of the static pressure along the centreline of the ejector indicates the presence of shock waves as shown in Figure 7.19. The primary nozzle flow is fully supersonic, but conditions right downstream of its exit are over-expanded resulting in such shocks.

Additional simulations of ejector flow for a range of operating conditions were preformed. Figure 7.20 shows a CFD flow visualization inside the CRMC ejector showing the flow direction at operating conditions of 200 kPa as a primary pressure, 1.6 kPa as a secondary pressure, and 4.8 kPa as an exit pressure.

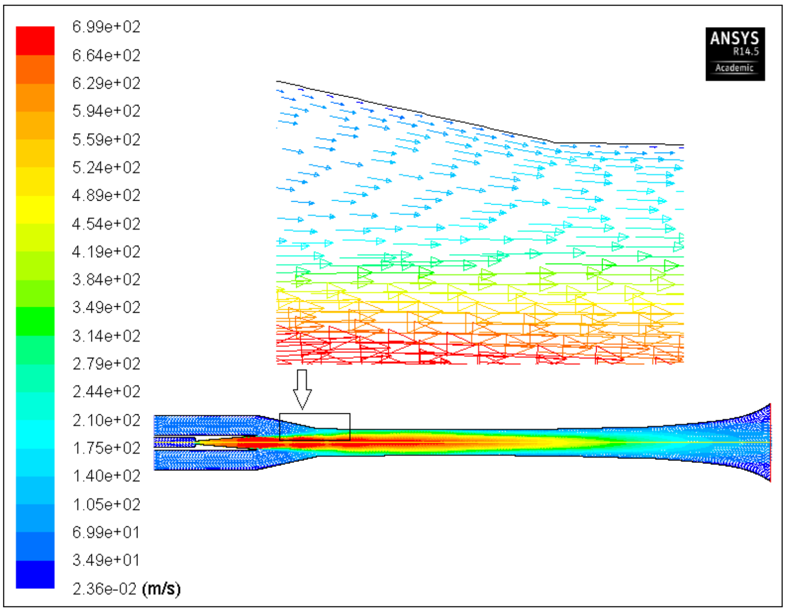

Figure 7.20: Velocity vector at primary pressure of 200 kPa and secondary pressure of 1.6 kPa, and 4.8 kPa as exit pressure.

Figures 7.20 shows there is no reversed flow or recirculated flow observed when ejector operates at such operating condition which means that the ejector can be operating in the double-choked mode. Reversed flow and/or recirculated flow reduces the amount of secondary flow entering the ejector duct. Within the choked flow regime, the entrainment ratio is constant and independent of the ejector downstream conditions as shown in Figure 7.8.

Figure 7.21 presents velocity maps of the primary nozzle flow at different operating conditions. Referring to Table 7.4, for the cases (a) and (b), the supersonic jet at the nozzle exit slightly converges toward the jet centre. For the higher secondary pressure cases (c) and (d), the primary flow is over-expanded and the flow tends to converge more strongly through the shock compression process at the nozzle exit. This convergence provides a bigger cross section area for the secondary flow to be entrained leading to higher mass flow rate in the secondary stream.

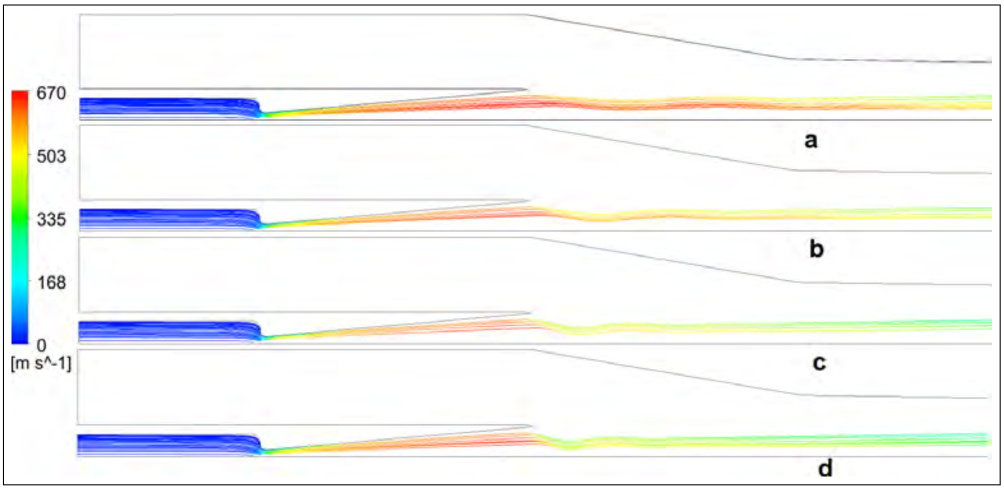

Figure 7.21: Velocity stream lines of primary flow at operating conditions of 200 kPa as a primary pressure and secondary pressure of (a) 1.6 kPa, (b) 2.5 kPa, (c) 4 kPa, (d) 5 kPa.

7.6.5.2 Un-choked flow mode

In the un-choked or single choked ejector flow regime, the primary flow is still choked but the secondary flow is un-choked. Any slight increase in the flow back pressure beyond the critical value results in a sharp decrease in the secondary mass flow rate. This mode can be recognized by the appearance of a circulation flow at the conical mixing chamber wall as shown in Figure 7.22 which represents flow inside the ejector at operating conditions of 200 kPa, 1.6 kPa, and 5.2 kPa as primary, secondary, and exit pressure respectively.

Figure 7.22 illustrates the position of the recirculation of the secondary flow. The recirculation blocks the secondary flow passage causing a reduction in the entrained secondary flow rate and thus, reducing in the ejector performance. As the back pressure increases, the extent of the recirculation zone increases and ultimately block all the area available to the secondary resulting in a zero entrainment ratio.

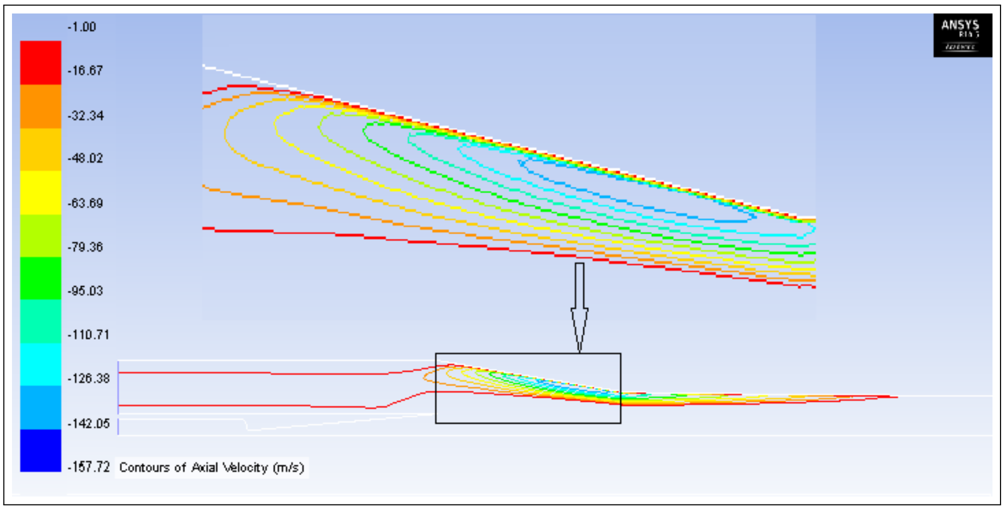

Figure 7.22: Velocity map at primary pressure of 200 kPa, secondary pressure of 1.6 kPa, and 5.2 kPa as back pressure.

7.6.5.3 Reversed flow mode

Any further back pressure increase beyond its value at zero entrainment ratio causes the primary stream to be forced back to the entrance of the secondary flow conduit. Simulation of the reverse flow mode in the ejector is shown in Figure 7.23 which shows flow inside the ejector at operating conditions of 200 kPa, 1.6 kPa, and 5.5 kPa as primary, secondary, and exit pressure respectively. As the back pressure is increased to values higher than its value at the zero secondary flow condition, the primary flow does not have enough momentum to overcome such back pressure and thus, the flow reverses its direction to the lower pressure area in the secondary flow conduit.

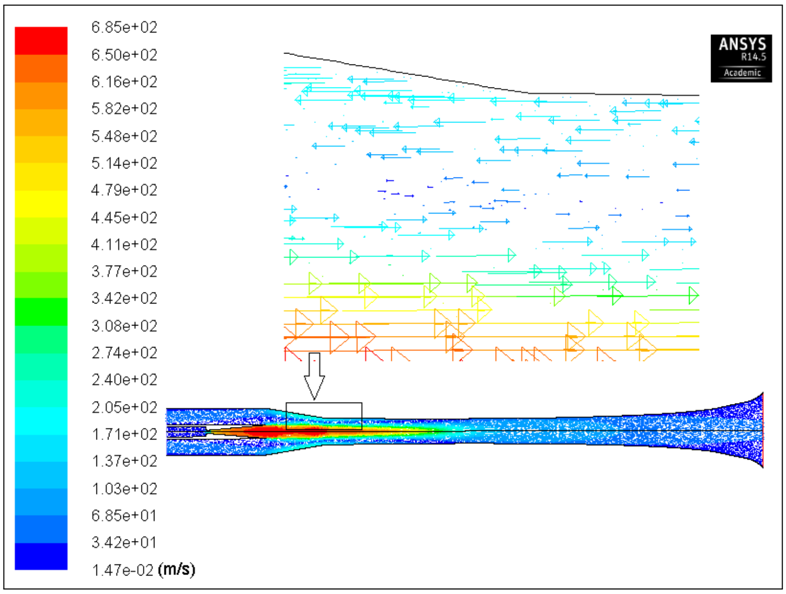

Figure 7.23: Velocity map at primary pressure of 200 kPa and secondary pressure of 1.6 kPa,and 5.5 kPa as exit pressure.

7.7 Comparison with conventional ejector

7.7.1 Arrangement of conventional ejector

A comparison of the CRMC duct with the conventional ejector of Al-Doori (2013) was performed. Figure 7.24 shows the geometry of the conventional ejector which consists of a mixing section, a constant area section, and a diffuser. The total length of the illustrated ejector is 556.5 mm. The minimum ejector diameter (throat) is 25.4 mm for both ejectors. Both ejectors used nominally identical primary nozzles as illustrated in Figure 7.1.

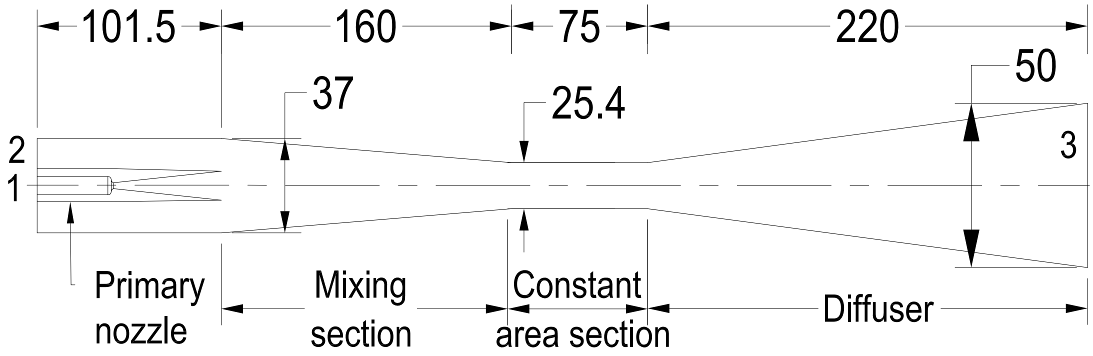

Figure 7.24: Conventional ejector geometry (all dimensions in mm), numbers 1, 2, 3, refer to primary, secondary, and exit flows respectively.

Simulation for both ejectors were performed with boundary conditions of 200 kPa, 1.8 kPa, 4.8 kPa as a primary, secondary and back pressures respectively.

The conventional ejector as introduced in Section 7.7 was operated at the same boundary conditions (200 kPa as a primary pressure, 1.6 kPa as a secondary pressure, and 4.8 kPa as a back pressure) and same working fluid. It can be seen that the first shock in the conventional ejector is stronger and the shock train extends to a larger distance than in the CRMC ejector as illustrated in Figure 7.25. For the present operating conditions, the entrainment ratio for the conventional ejector was 0.33, where as the entrainment ratio of the CRMC ejector was 0.39. The shocks associated with the ejector duct compression process have a distribution that coincides with the phase of the nozzle shock train. Such waves have also been observed previously by Matsuo, Sasaguchi, Kiyotoki & Mochizuki (1982), Dutton & Carroll (1988), and Ruangtrakoon, Thongtip, Aphornratana & Sriveerakul (2013). This kind of shock compression is not observed in the present work with the CRMC ejector.

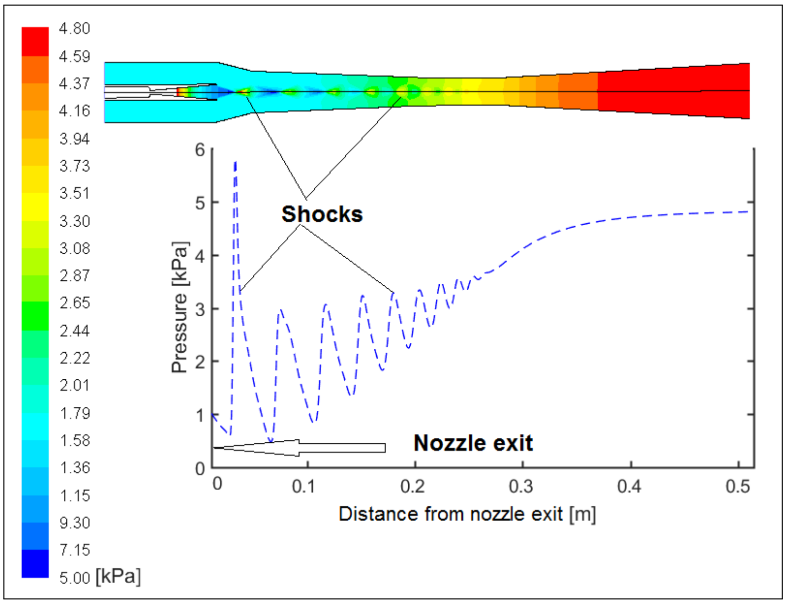

Figure 7.25: Conventional ejector pressure map and pressure distribution along the axis for 200 kPa, 1.6 kPa, and 4.8 kPa as the primary, secondary, and exit pressure respectively.

7.7.2 Total pressure

Figure 7.26 presents the total pressure for CRMC and conventional ejectors from the CFD simulations. Numerical results show a significant difference in the primary flow total pressure between CRMC and conventional ejector. The total pressure suddenly decreases as the flow exits the nozzle. The largest drop in the total pressure occurs at the first shock wave system and the observed difference implies that the first shock is weaker in the CRMC ejector than that in the conventional ejector.

The CRMC ejector flow retains more of the primary nozzle total pressure on entering the mixing region, and this is consistent with the observation that entrainment ratio for the CRMC is higher. The CFD simulated entrainment ratio for the CRMC was 0.42 and that for the conventional ejector was 0.33 in the present case.

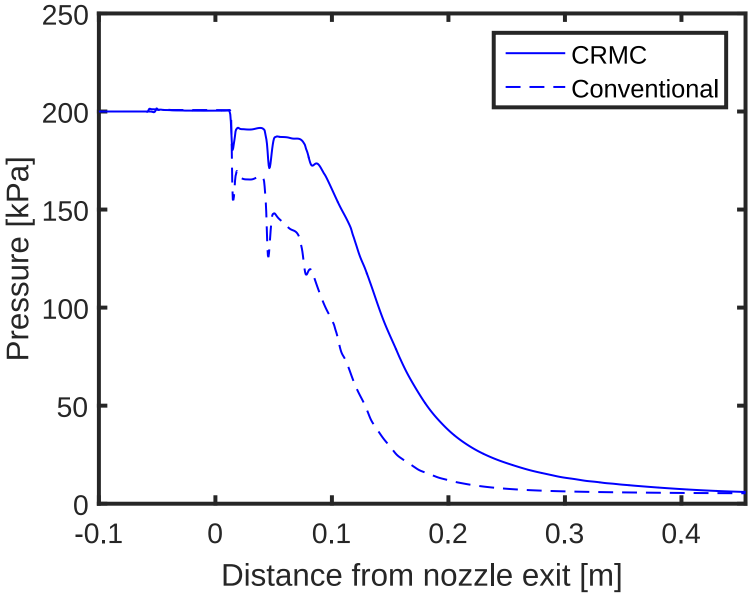

Figure 7.26: Total pressure distribution for the CRMC and a conventional ejector along the axis at primary pressure of 200 kPa, secondary pressure of 1.6 kPa, and back pressure of 4.8 kPa.

The fact that the pressure loss occurs in the area close to the nozzle exit might be attributed to the local design differences between the conventional and CRMC ejector ducts. Figure 7.27 shows the design of mixing area for the CRMC and the conventional ejectors. The secondary flow contraction angle for the conventional ejector is 2° whilst, for the CRMC ejector it is 0.42°. Such a difference can affect the secondary flow rate into the two ejectors. In addition, the interaction between the primary stream and the secondary stream would be affected by this geometric difference. Given primary nozzles are essentially identical, the difference in the total pressure along ejector axis at nozzle exit would arise from the local secondary flow adjacent to the primary nozzle, and in particular, the local value of secondary pressure adjacent to the primary nozzle exit.

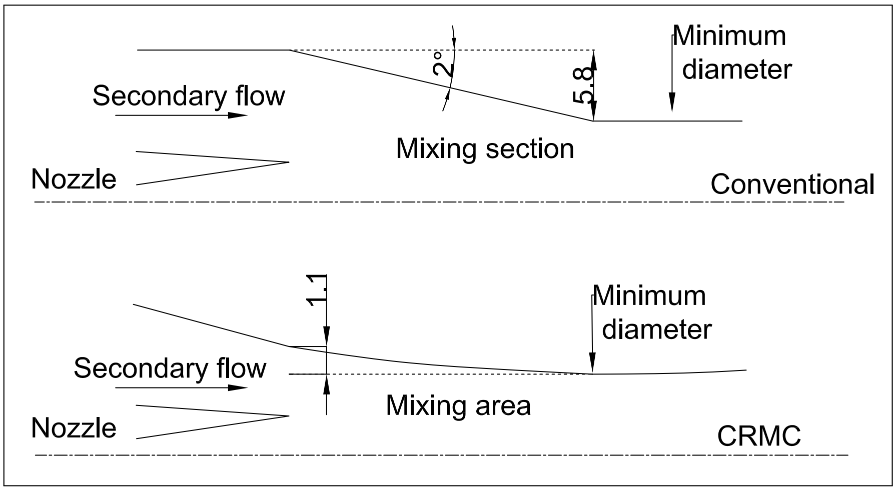

Figure 7.27: Ejector profiles for the conventional and CRMC ejectors (all dimensions in mm).

7.7.3 Critical back pressure comparison

The ratio of critical back pressure to secondary pressure represents another key parameter of the ejector performance as explained in Chapter 6. To evaluate the ability of the CRMC and conventional ejectors to increase the static pressure of the flow through the diffuser, pitot pressure was calculated at the beginning of the subsonic diffuser of the conventional ejector and at the same distance of the CRMC ejector. In the case of subsonic flow, the pitot pressure is equal to the flow total pressure (Anderson 1990).

$$\frac{P_{pitot}}{P} = \left(1 + \frac{\gamma - 1}{2} M^2\right)^{\gamma/\gamma-1} \tag{7.19}$$

However, due to the shock compression process that occurs in supersonic flow, some of the total pressure is lost, and the pitot pressure is expressed (Massey & Ward-Smith 1998)

$$\frac{P_{pitot}}{P} = \left(\frac{\gamma - 1}{2} M^2\right)^{\gamma/\gamma-1} \left(\frac{\gamma + 1}{2\gamma M^2 - \gamma + 1}\right)^{1/\gamma-1} \tag{7.20}$$

where γ is the specific heat ratio for air, taken as 1.4.

At the start of the diffuser, the pitot pressure near the ejector wall in the conventional ejector is slightly higher than that of the CRMC ejector as shown in Figure 7.28. For radius values less than 7.8 mm, the situation is reversed as the centreline is approached and the flow is supersonic. The average pitot pressure at any stream wise location can be calculated using

$$\overline{P_{pitot}} = \frac{\int_0^R 2\pi r P_{pitot} dr}{\pi R^2} = \frac{2}{R^2}\int_0^R r P_{pitot} dr \tag{7.21}$$

where the ejector wall radius at this position is R=12.7 mm for the conventional ejector and 13 mm for the CRMC ejector.

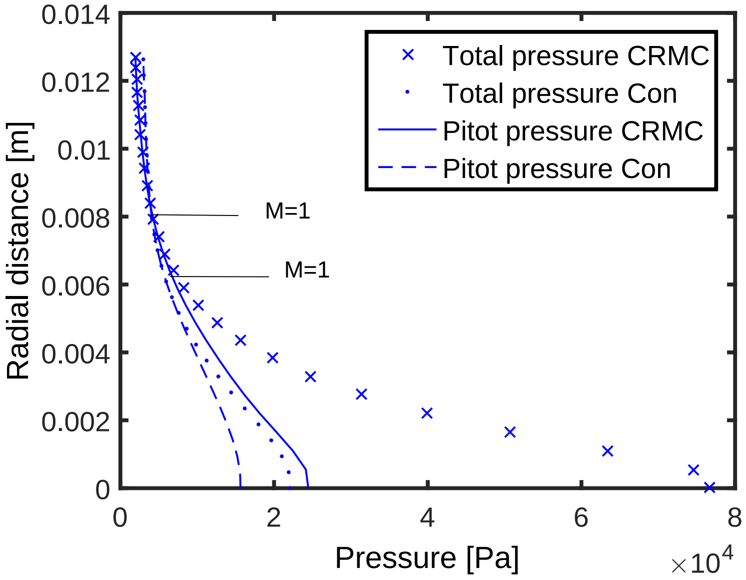

Figure 7.28: Pitot pressure and total pressure distribution in the CRMC and conventional ejectors at distance of 60 mm downstream of the primary nozzle.

Typically, the deceleration process for supersonic flows in conventional ejectors involves total pressure losses associated with shock waves thus, the pitot pressure reflects the achievable stagnation pressure of the supersonic flow better than the total pressure (Ariafar, Buttsworth, Al-Doori & Malpress 2015). It can be seen that the average pitot pressure of the CRMC ejector is higher than that for the conventional one as listed in Table 7.7 and thus, it should be possible to achieve higher critical back pressure in the CRMC ejector at these particular operating conditions. For the present operating conditions, the entrainment ratio for the conventional ejector was 0.33, where as the entrainment ratio of the CRMC ejector was 0.39 as listed in Table 7.7.

Table 7.7: Calculated values for the pitot and total pressure.

Ejector model	Average pitot pressure (kPa)	Average total pressure (kPa)	ER
CRMC	88.3	198	0.39
Conventional	56.2	71.7	0.33

7.8 Chapter Summary

A CFD study has been performed using ANSYS FLUENT v 14.5 to investigate the global and local features and flow behaviour inside the CRMC ejector. Two turbulence models, $sst-\kappa\omega$ and $\kappa-\epsilon$ were selected in this study and air modelled as an ideal gas was used to simulate the CRMC ejector configuration. The following is a summary of the results obtained in this chapter.

- The experimental data of the present work presented in Chapter 6 were taken as a reference. When the ejector model was run at a range of operating conditions, the $sst-\kappa\omega$ simulations showed a reasonable agreement with the experimental work in terms of entrainment ratio and static pressure distribution along the ejector wall. The disagreement between the CFD and experimental results of static pressure along the ejector wall was 6.3 % for $sst-\kappa\omega$ and 6.8 % for $\kappa-\epsilon$ turbulence models in the double choked mode. The disagreement between the CFD and experimental results for entrainment ratio was 3 % for $sst-\kappa\omega$ and 3.4 % for $\kappa-\epsilon$ in the double choked mode when the operating conditions were 200 kPa and 1.6 kPa as the primary and secondary pressures respectively. When the secondary pressure increases to 2.5 kPa the disagreement in the entrainment ratio decreases to 1.54 % for $sst-\kappa\omega$ and 3.1 % $\kappa-\epsilon$ turbulence models in the double choked mode. In the single choked mode, the disagreement in the entrainment ratios were 0.15 for $sst-\kappa\omega$ and 0.313 for $\kappa-\epsilon$.
- The $sst-\kappa\omega$ turbulence model exhibited better capability to predict the ejector performance than the $\kappa-\epsilon$ turbulence model and thus, the latter was excluded from further application in this study. The key parameters such as the entrainment ratio, the static pressure profile along the ejector axis and ejector wall, and

the Mach number were examined. Since the discrepancy between the available experimental results and the CFD results was found to be low, the numerical results were considered to be reliable.

- A comparison between theoretical results taken from Chapter 3 and numerical results was also presented in this chapter for static pressure along the ejector duct. The results from the CFD study showed that the flow within the ejector deviates from the analytical calculations. Consequently, better performance throughout the optimization of the geometry should be possible using a higher fidelity approach than that available from the one-dimensional model.

- The sonic surface maximum diameter, the location of this diameter relative to the nozzle exit position and the length of the sonic line from the nozzle exit to the ejector centreline were defined from the CFD results. As the primary pressure increases, the sonic surface diameter and length also increases.

- Apart from the shocks at the primary nozzle exit, the CRMC ejector includes a gradual and largely shock-free increase in static pressure until the primary pressure reaches value of 230 kPa. However, the pressure gradients are very different from the CRMC design values, and are not very different from those of the conventional design of Al-Doori (2013). Evidence for the elimination of the shock compression in the CRMC ejector as being the cause of enhanced performance of the CRMC duct has not been achieved.

- Numerical results show a difference in total pressure of the primary flow between CRMC and conventional ejector just downstream of the nozzle exit position. Total pressure of the CRMC ejector remains 15 % larger than the conventional one which leads to entrainment of more secondary mass flow rate and higher back pressure. The cause of such difference could be assigned to a different contraction angle of the ejector duct adjacent to the primary nozzle, but it is not directly attributable to the CRMC duct design.

- The CFD simulation allowed the visualization of the flow separation and recirculation inside the ejector duct for a range of operating conditions. Furthermore, when the exit pressure exceeds the ejector failure point, the CFD was able to reveal the reverse flow in the secondary inlet. The ability to successfully model experimental ejector data supports the use of CFD modelling to optimize jet ejectors. The results show that, in spite of some deviation, CFD could generally predict the flow behaviour inside the ejector with an acceptable accuracy and it can be considered as an effective tool to examine both global and local features of the ejector in different operating modes ranging from the single choke mode to the reverse flow mode. CFD results can assist in the design, optimisation, and application of the CRMC ejectors.

Chapter 8

Flow Visualisation

8.1 Introduction

The application of lasers in flow visualisation has made methods like interferometry, Particle Image Velocimetry (PIV), and Laser Induced Fluorescence (LIF) useful and convenient techniques to assist in visualisation of various flow phenomena. This chapter describes a flow visualisation method which uses laser illumination and image processing for visualising the mixing zone between the high-speed primary flow and the low-speed, co-axial secondary flow in the CRMC ejector.

A transparent ejector test section was designed, fabricated, and operated in an ejector system using air as the working fluid. Visualisation was achieved by illuminating particles, delivered to the ejector via the secondary flow. The laser beam was traversed across the flow, generating sufficient light intensity for images to be captures on a high speed camera. Successive frames were combined using image processing in Matlab. The process achieved flow visualisation in a qualitative way, but had sufficient resolution to allow the measurement of the primary jet core flow diameter and length. The technique has the potential to assist in the design of ejectors, and its application in the validation of numerical simulations is demonstrated herein.

8.2 System main components

8.2.1 Transparent duct

To achieve the visualisation, an ejector duct was designed based on the Constant Rate of Momentum Change theory and fabricated in a transparent material. Air was chosen as the primary and secondary working medium as it is well suited for application in an open system. A mould was created to cast the transparent duct. Each of the outer and inner parts of the mould were created using 3D printing and built in several sections because of the printer's limited print-size. The inner and outer moulds each consisted of six 75 mm long sections. Each outer section was made in two parts which were then joined by four 4 mm bolts. Each of the sections making up the inner mould and the outer mould were aligned using male and female spigots as presented in Figure 8.1.

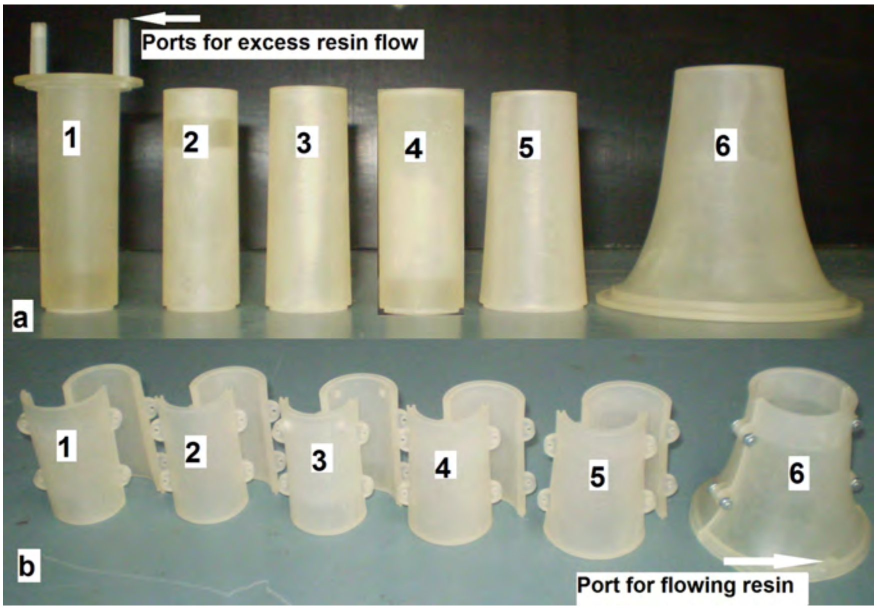

Figure 8.1: Photograph of the parts used to create the mould to cast the transparent duct: a. inner parts b. outer parts.

To ensure that the transparent ejector duct was able to operate at the required conditions and maintain its shape, the wall thickness was chosen to be 8 mm. Creo parametric 3.0 software was used to design these mould parts and produce files compatible with the available 3D printer. Parts were then created from VisiJet Crystal material using the Multi-Jet-Modelling (MJM) Technology, 3D printer Type ProJet^{TM}HD 3500. Figure 8.2 shows the assembled inner and outer moulds.

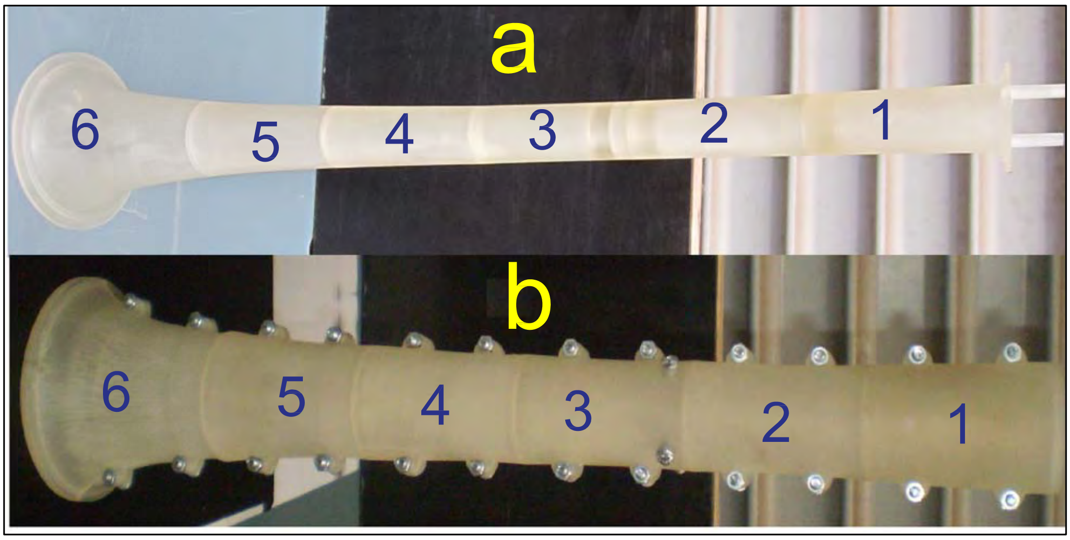

Figure 8.2: Photograph of the assembled parts used to create the mould to cast the transparent duct: a. inner part b. outer part.

To allow disassembly after casting, the inner mould was separated between section 2 and 3 as illustrated in Figure 8.2. The longer portion of the inner mould was inserted into the outer mould, and then the mating sections were re-attached from the opposite end. A draw bolt (Figure 8.3), pulling on a plate at each end, held the assembled mould together. The assembled mould was placed inside an encasing PVC shield as in Figure 8.3. Attention was paid to ensure that the assembled inner mould was centred in the assembled outer mould, and to ensure this was the case, additional centralising bolts were introduced to maintain the designed ejector wall thickness along the axis length.

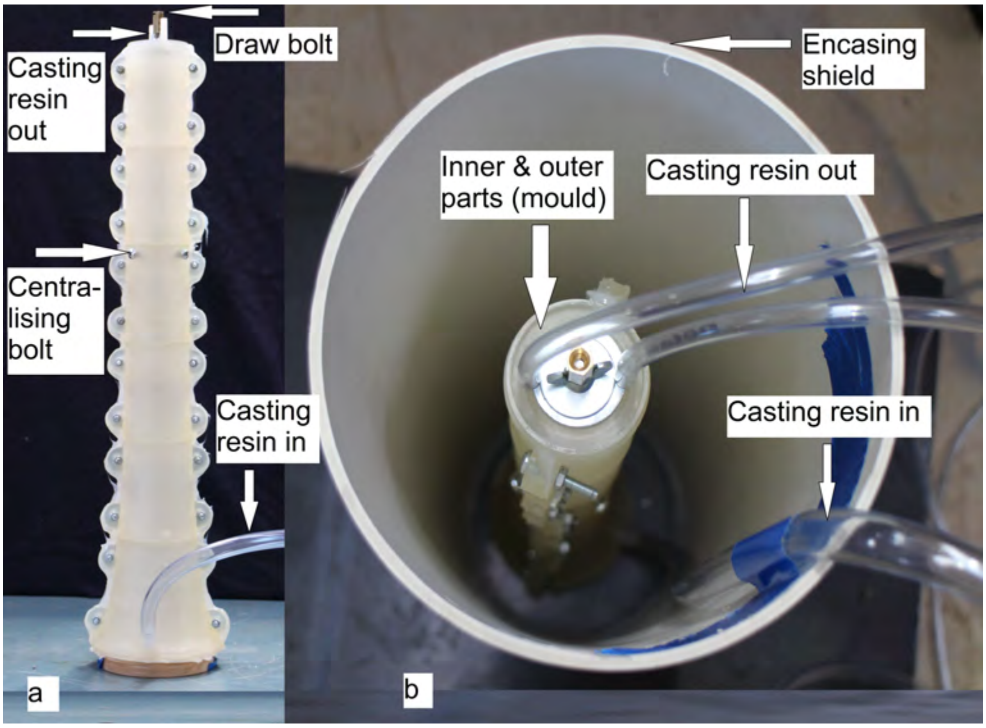

Figure 8.3: Photograph of a. mould b. mould inside encasing shield.

During the casting and curing process, the resin produces an exothermic reaction which has the potential to reduce the stiffness of the 3D printed material used for the mould. To assist the mould to maintain its design shape, the mould assembly was supported by filling the encasing shield with fine dry sand.

Crystal Clear® Resin was used as the transparent material for the ejector duct. It is a water clear rigid urethane resin made specifically for "applications that require absolute clarity". This casting material was selected because of it very low shrinkage during curing and its suitable viscosity for casting.

The resin is mixed from two materials (parts A and B) in the ratio 100:90 respectively by weight. Entrained air from the mixing process must be removed to allow for sufficient clarity in the finished duct. Air was removed from the resin before pouring into the mould by placing the mixture in a vacuum. The curing time of the mixture at room temperature is 40 minutes, but it takes several days to achieve its ultimate stiffness.

The surface finish achieved on the moulds, together with the need for the moulds to have mould release compounds applied, resulted in inner and outer surfaces imperfections which reduced the clarity of the cast duct when removed from the mould. To improve the surface finish, two steps were taken. Firstly, the duct external surface was coated with resin by drawing a resin-impregnated smooth brush over the surface, fed axially while spinning the duct in a lathe. This process was repeated several times, especially in areas of heavy imperfections. The coating process continued until the entire external surface was covered with a very thin layer of resin and letting it meld into a clear finish. Secondly, the internal surface was polished to remove the parting lines created from the join of each mould section.

The outcome of the casting and finishing processes is shown in Figure 8.4. The primary nozzle core flow was expected to end between 60 mm and 150 mm (in either zone 1, 2 or 3) and thus, extra care was taken to improve the clarity of the duct over that length as Figure 8.4 shows.

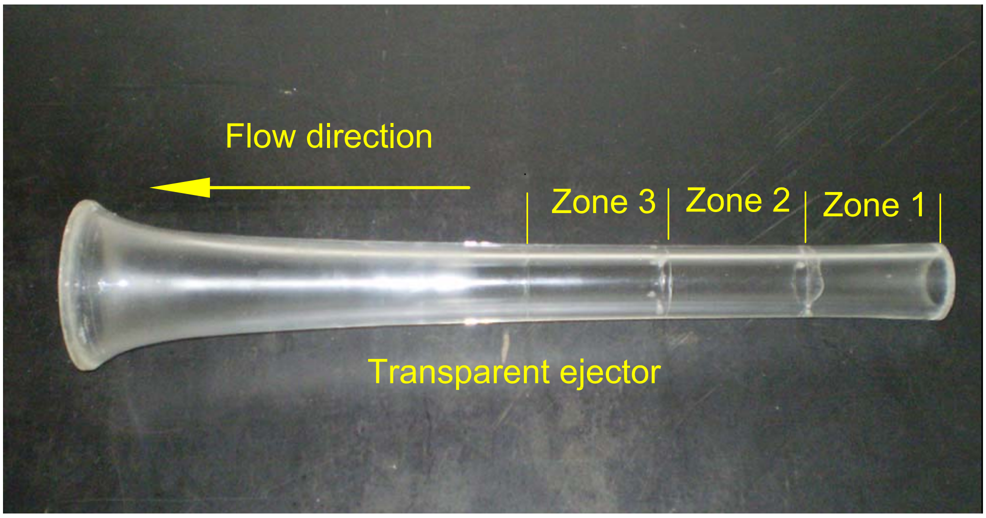

Figure 8.4: Photograph of the transparent ejector duct.

8.2.2 High speed camera

An OLYMPUS® $i - SPEED\,3$ high speed camera was used to record the flow visualisation images. The main specifications of this camera are listed in Table 8.1.

Table 8.1: OLYMPUS® $i - SPEED\,3$ high speed camera specification.

Feature	Definition
Sensor type	Custom CMOS
Resolution	1280 x 1024
Pixel size	21 μm
Aspect ratio	5:4
Shutter type	Global exposure
Specified shutter time	Global 2.16 μs
Bit depth	10 bit
Maximum frame rate	150,000 fps

8.2.3 Seeding system

To achieve a successful flow visualisation, an appropriate type of seeding particle must be selected. The particle size must be large enough to scatter sufficient light for image acquisition and must be small enough for faithful tracking of the flow. The particle seeding density must be high enough for data processing and low enough that it does not disturb the flow field. In the present work, talc powder was used as a seeding material. The general chemical name of talc powder is Hydrated Magnesium Silicate and its chemical composition is $3MgO_4SiO_2H_2O$ with a density of 2.7 - 2.8 g/cm^3 at $20°C$.

Someya (2012) used talc to seed subsonic flow over a flat plate. However, this substance apparently has not been used for flow seeding in an ejector system or in a supersonic flow before. Talc powder appears especially well suited for seeding applications because it is non-toxic, chemically inert, highly reflective, and rather low cost compared with other seed materials. Figure 8.5 shows a micrograph of a sample of the seeding particles used in the present work, as loaded into the seeding system.

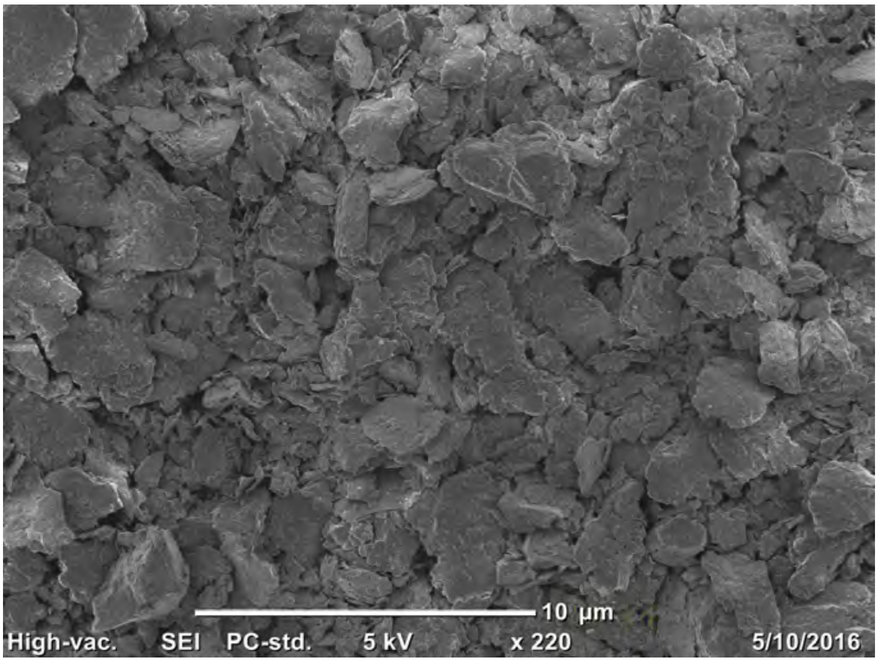

Figure 8.5: Micrograph of talc powder as loaded into the seeding system.

The behaviour of the suspended particles has to be examined in order to confirm the particles will accurately track the fluid motion.

The particle relaxation time τ_s, is a measure for the time scale over which particles will attain velocity equilibrium with the flow and is given by Raffel, Willert, Wereley & Kompenhans (2013):

$$\tau_s = d_p^2 \frac{\rho_p}{18\mu} \tag{8.1}$$

where d_p the particle diameter, ρ_p the particle density, and μ is the flow dynamic viscosity. However, some particles in Figure 8.5 have sizes significantly larger than $1\,\mu$m which, according to Equation 8.1 calculations, would not faithfully follow the flow. To attain smaller size particles, a sieve apparatus was established as part of the particle seeding system. A micrograph of particles delivered from the sieve system is presented in Figure 8.6, showing particle sizes in the vicinity of $1\,\mu$m and smaller.

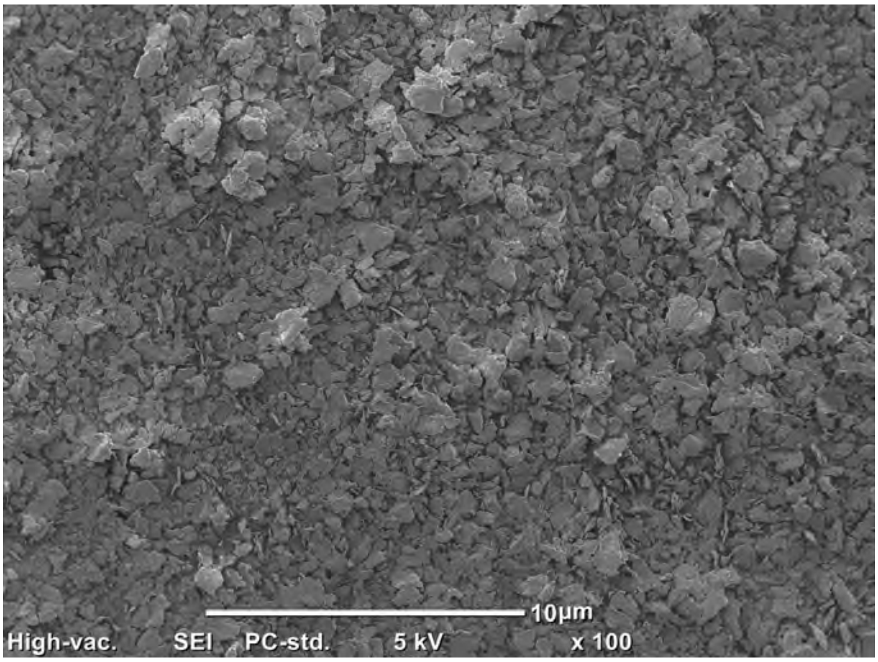

Figure 8.6: Micrograph of talc powder as delivered from the seeding system.

Calculation of the relaxation time τ_s of particles with a diameter of 1 μm (taking the dynamic viscosity of air as 1.8×10^{-5} kg/ms) gives $\tau_s = 8.64\,\mu s$. Taking a representative mixing layer velocity difference as 500 m/s and a representative mixing layer length scale as 5 mm, gives an indicative mixing layer time scale of 10 μm. Hence, for such conditions, the particles with average diameter of 1 μm and smaller, which appear in Figure 8.6, should faithfully follow the flow.

Some drawbacks of using talc were encountered, included the challenge of achieving suitable dispersion of solid particles, as well as achieving a uniform supply for sufficient time to perform the experiments. To address these challenges, a purpose-built seeding technique was created on the secondary flow line as presented in Figure 8.7. Two mesh layers, one connected to the vibrator, delivered the seeding particles to the secondary stream at a relatively constant concentration. The flow rate of particles and their concentration can be governed by varying the vibrator motor speed using a controllable power supply. The concentration of the generated particles increases with increasing the motor input current and vice-versa. The seeding powder was kept dry to minimise moisture in the seeding system. Formation of agglomerates was minimized by shortening the connection line between the seeding system and the secondary line.

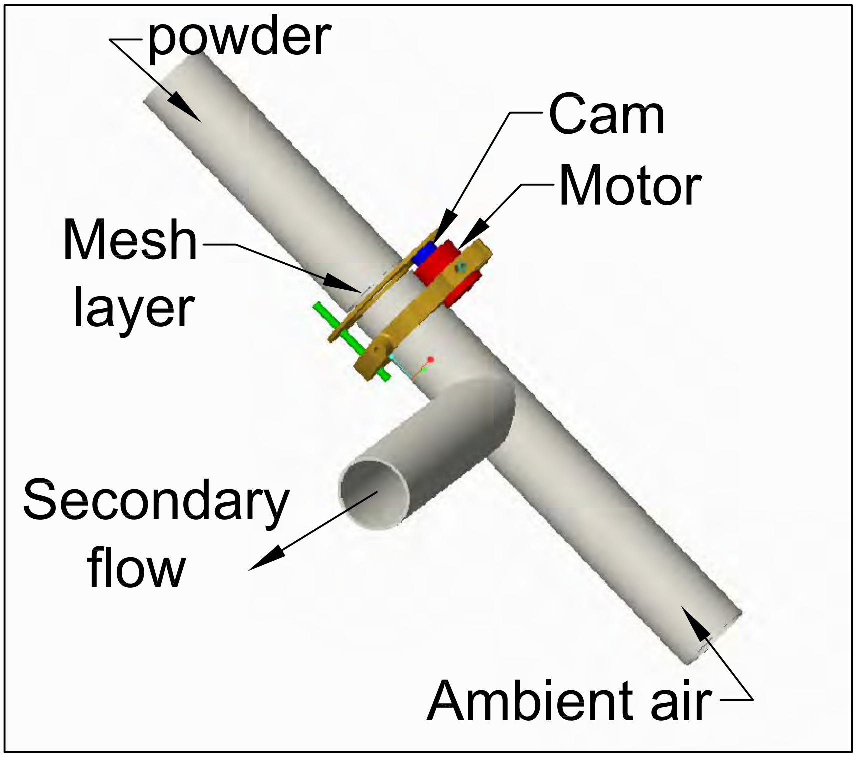

Figure 8.7: 3D solid model of the seeding system.

8.3 Experimental set up

A schematic diagram and pictorial representation of the arrangement are shown in Figures 8.8 and 8.9, while Figure 8.10 shows a photograph of the experiment's set up. The primary nozzle and the ejector duct geometries remain the same as that used in Chapters 4 and 5. The primary flow is controlled by a pressure regulator and ball valve. The secondary flow is sourced from the ambient atmosphere and the flow rate was measured using an orifice plate and pressure transducer, before it enters into the mixing duct. A window was installed downstream of the ejector exit to allow optical access for the laser along the ejector axis. The laser is directed through this glass window, generally co-axial with the flow direction, see Figure 8.9.

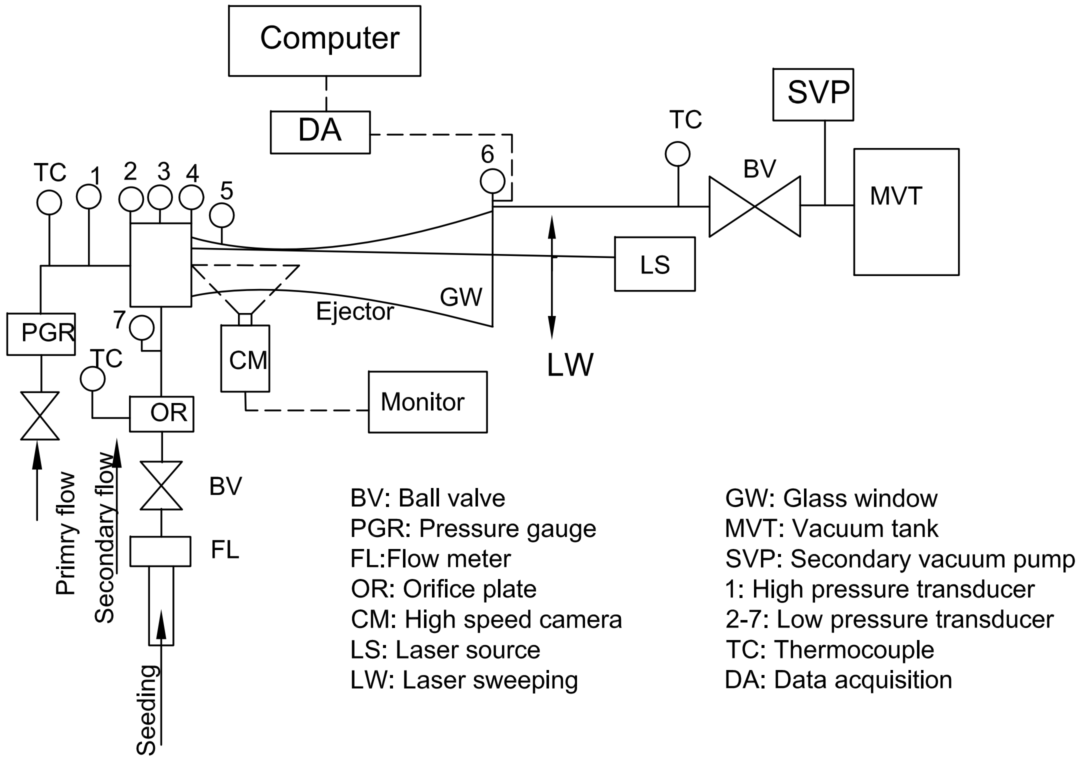

Figure 8.8: Ejector apparatus schematic diagram for flow visualization.

The light source is a continuous diode laser at 532 nm and 500 mW giving a 1 mm beam diameter. The laser direction can be modified by using a motor-driven mechanical device which allows the adjustment of the laser direction between the upper wall and lower wall of the ejector. In the present work, the time to scan the entire flow field inside the ejector duct was 200 s. The laser beam passes into the ejector flow passage through the glass window. The laser direction is able to be controlled to move upward and downward to provide a full scan from top to bottom of the ejector duct. The light scattered by the seeding particles suspended in the flow is captured by the camera viewing perpendicular to the axis of the duct. A photograph of the ejector system and the flow visualization technique is shown in Figure 8.10.

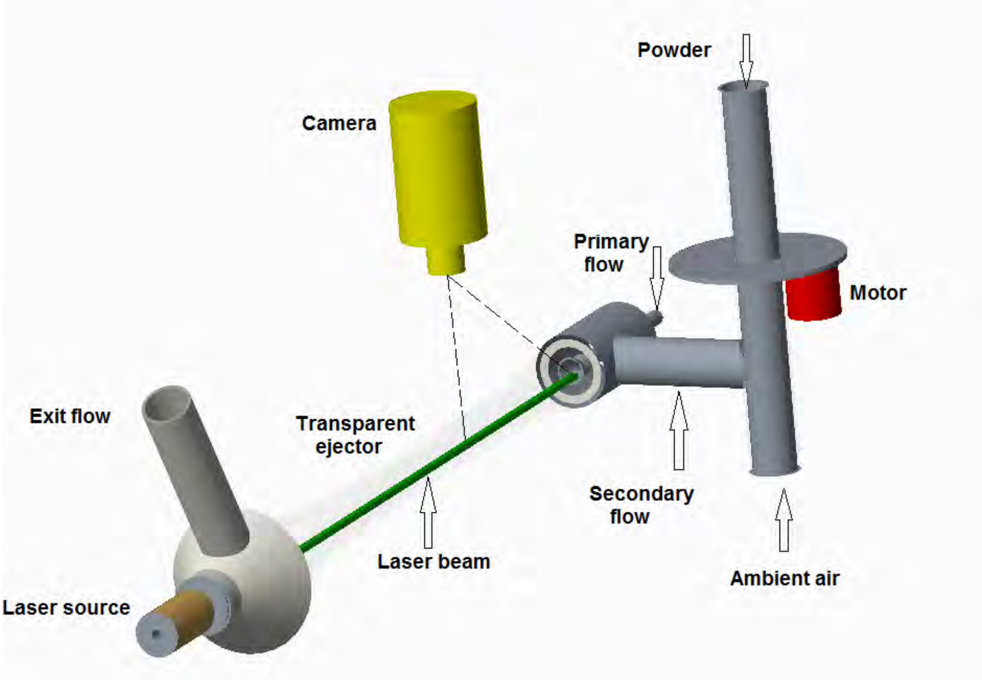

Figure 8.9: 3D sketch of the transparent ejector and flow visualization system.

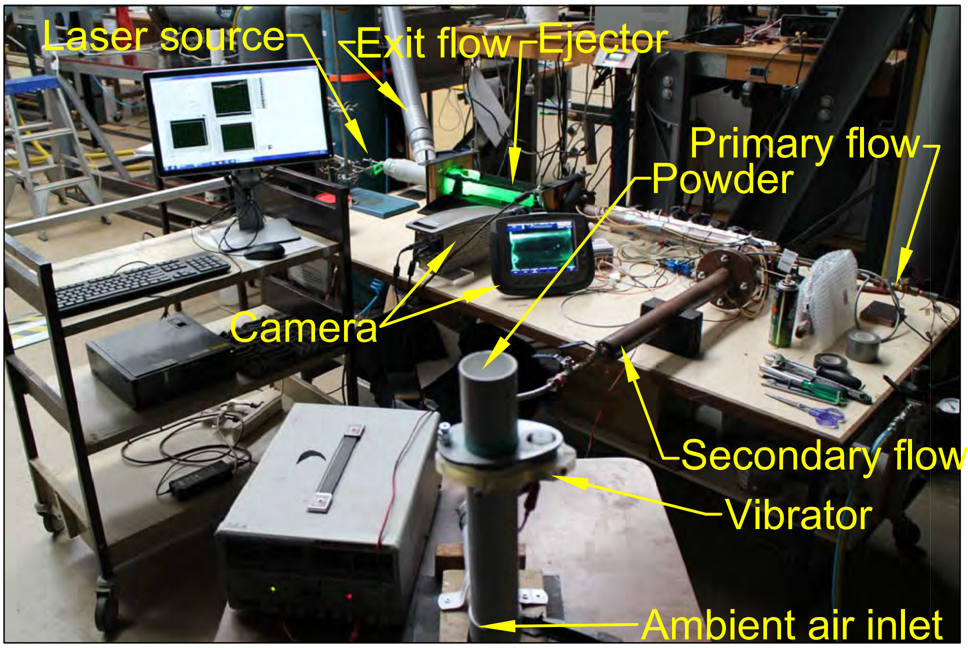

Figure 8.10: Photograph of the transparent ejector and flow visualization system.

The best configuration of light source and camera parameters were reached after a series of trials to optimise the images produced from the process. Figure 8.11 presents a still image from a video sequence acquired during the experiments.

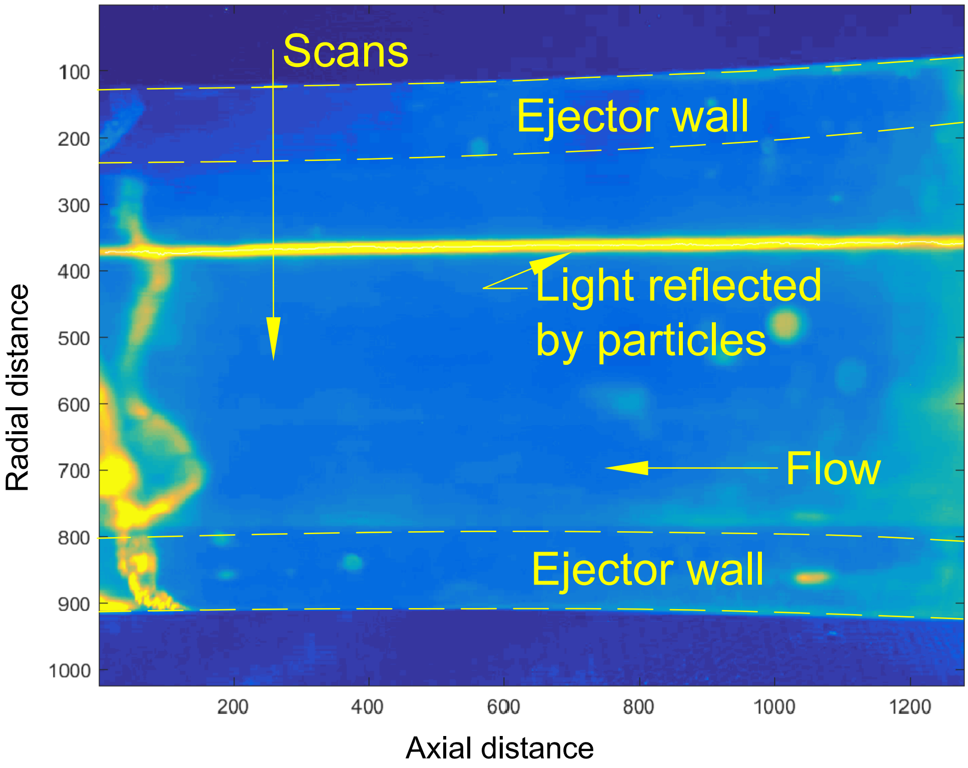

Figure 8.11: Photo of the first section of the ejector during flow (the axial and radial distances are in pixel, 1 mm=17 pixel).

8.4 Operating procedures

In the present experiment, the following procedures were followed

1. Ensure the high speed camera is positioned to capture images of the area of interest.
2. Fill the seeding reservoir with the talc material.
3. Open the valve to the vacuum tank.
4. Turn on the laser source.
5. Turn on the seeding system vibrator and the secondary flow valve to allow the high speed camera to be focused on the laser illuminated seeding particles.

6. Turn on the primary flow valve and data acquisition system to record all flow data.
7. Turn on the laser moving system, traversing the laser vertically from the upper wall to the lower wall to scan the entire flow field.
8. To minimize undesired reflections of the laser beam from the ejector wall, the scanning process starts at point where the laser just contacts the ejector wall.
9. At the end of the start-up sequence, the high speed camera is triggered to acquire the flow field images over the duration of the test.
10. All the acquired data is processed using Matlab image processing software to extract the required parameters.

Repeated tests were performed to ensure the experiments were producing consistent results.

8.5 Experimental results

Particles were introduced into the entrance region of the secondary flow pipe, allowing for good mixing with the secondary flow before entering the mixing chamber. To ensure a minimal change in the flow characteristic in the ejector due to seeding, the talc concentration was kept low as presented in Table 8.2. A range of operating conditions was selected for comparison with experimental work presented in Chapter 6. The wall static pressure of the seeded flow differs by a maximum of 2 % from the unseeded flow as presented in Figure 8.12 which indicates that the seeding has a very small effect on the flow.

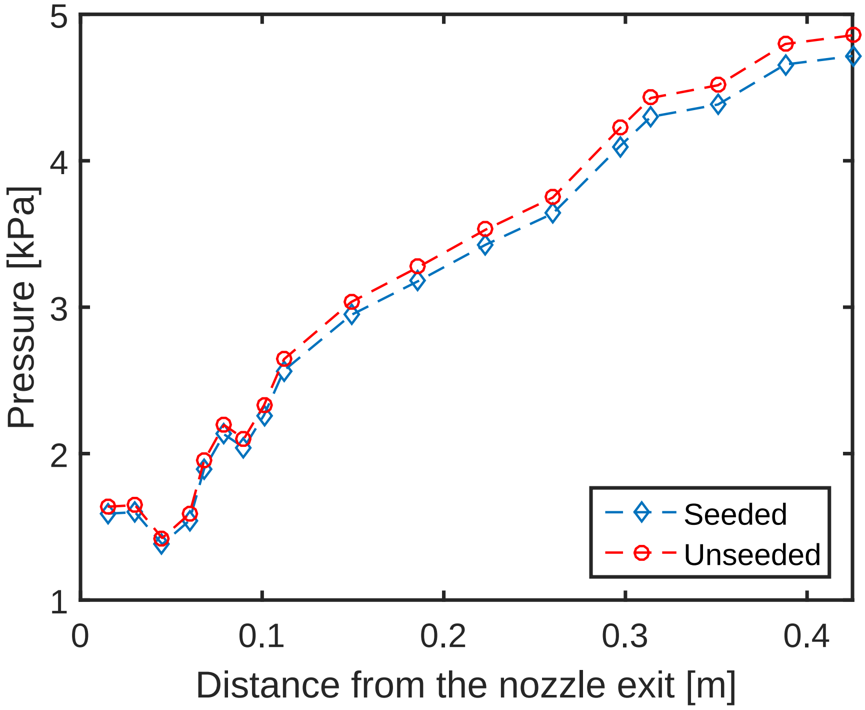

Figure 8.12: Static pressure plots along the ejector for seeded and unseeded flow at 200 kPa, 1.6 kPa and 4.8 kPa as the primary, secondary and back pressures respectively.

Table 8.2: Powder consumption during the experiments for a range of primary pressures and a secondary pressure of 1.6 kPa. P_p, $\dot{m}_s$, t, m, $\dot{m}$ refer to primary pressure, secondary mass flow rate, test time, powder consumption and powder mass flow rate respectively.

P_p (kPa)	$\dot{m}_s$ (g/s)	t (s)	m (g)	$\dot{m}$ (g/s)
190	1.413	200	5.64	0.0282
200	1.45	200	5.8	0.029
210	1.577	200	6.1	0.0305
220	1.62	200	6.3	0.0315

For these visualisation experiments the nozzle was positioned at the entrance of the mixing duct, corresponding to the nozzle exit position of 60 mm in Table 5.2. If the nozzle exit was positioned upstream of this location, the opaque walls of the entrance region would have prevented observation of the region immediately downstream of the nozzle exit. Figure 8.13 is an image of the ejector before the test started. It shows some imperfections in the walls of the duct, which are illuminated by refracted and reflected light from the laser. The internal surface of the duct had a similar surface texture to the internal surface of ejector experiments reported in Chapter 6. However, the intensity of laser light recorded with the camera would have been the combined effect of light reflected from the particles and the parasitic light reflection on the transparent surface of the ejector duct.

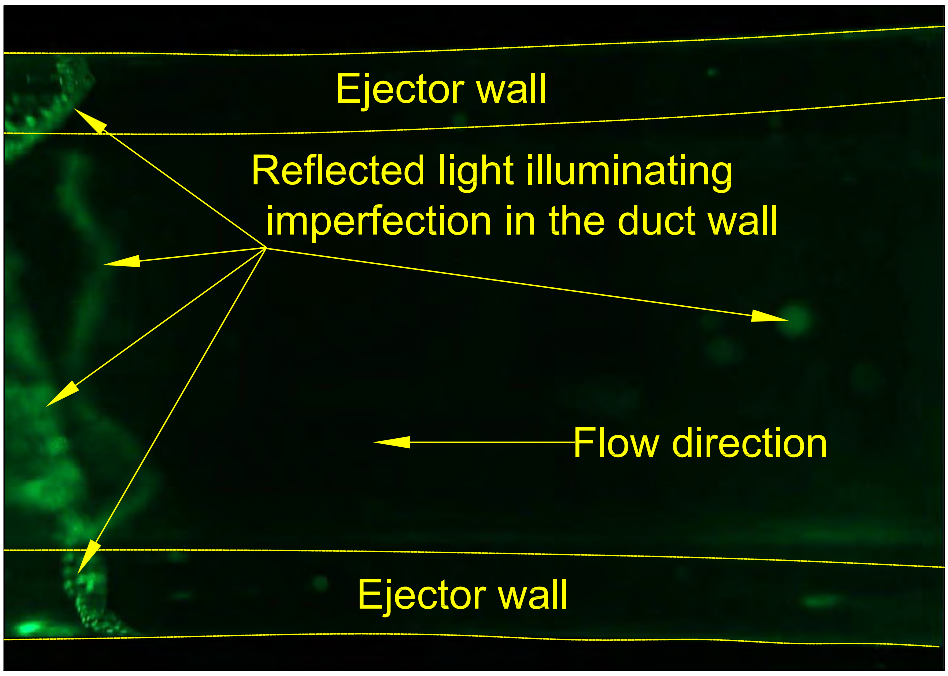

Figure 8.13: Photo of the first section of the ejector prior to testing.

During fabrication of the duct, surface imperfections were generated as the resin changed volume while curing. All internal surface imperfections were repaired to produce a smooth surface, but the interface between the repair material and the material of the cured duct scattered light, producing the image in Figure 8.13. These regions were removed during image processing by subtracting the no-flow image from flow images, so that the only effects of interest caused by the flow were analysed.

Since this technique permits the visualization of the entire ejector duct, in the series of images in Figures 8.14, 8.15, 8.16, 8.17, 8.18, 8.19, 8.20 and 8.21, the visualisations extended to 155 mm from the primary nozzle exit. Figure 8.14 reports results up to 75 mm downstream of the nozzle exit to examine the flow behaviour. Up to approximately 65 mm from the nozzle exit, the primary jet core flow remains. The plots from scans at 65 mm and beyond indicate the seeding particles have been entrained onto the centreline of the primary flow and hence, the core flow has disappeared by these stations.

As the seeded flow inside the ejector was recorded by the high speed camera, the video was converted into a sequence of single frame images. Matlab code was created to read the images from video sequence and then, extract the frames and perform the image processing to quantify the required parameters of the flow.

Interpretation of Figure 8.14 indicates that mixing of the two streams has extended to involve the full diameter of the duct at 65 mm downstream of the nozzle exit position. Upstream of this position, the core flow region of the primary jet can be distinguished by the absence of any reflected intensity near the centreline of the duct. The primary flow jet core starts to decrease as the flow moves downstream then, it disappears at a position of 65 mm downstream of the nozzle exit. Distinction between primary and secondary flows becomes more difficult as the flow moves further downstream as evident in Figure 8.15. It can be seen that by 80 mm from the nozzle exit the two flows become completely indistinguishable.

In Figure 8.15 the intensity of light reflected from the particles appear relatively uniformly distributed across the ejector duct which implies that the two flows have become mixed. It can be seen in this figure that the particle concentration at the station 140 mm downstream of the nozzle exit is less than that in the station upstream of this location. This can be attributed to two effects. First, as the flow becomes mixed, the particles occupy all the ejector section rather than only the annulus area available for secondary flow. Second, the CRMC ejector duct diameter starts to increase and thus the ejector area section also increased. This section is positioned at the end of zone 2 in Figure 8.4.

As the primary pressure increases, the distance to the termination of the primary flow jet core also increases as Figure 8.16 illustrates. When the primary pressure increases to 200 kPa, the core flow is clearly distinguishable at the 65 mm station downstream of the nozzle exit. Figures 8.18, 8.18, 8.20 and 8.21 present the intensity variation within the ejector duct at locations between 2 and 155 mm from the nozzle exit at

210 kPa and 220 kPa respectively and secondary pressure at 1.6 kPa. It can be seen, for all these tests, that beyond the end of the jet flow core the data intensity has a very similar behaviour. This behaviour is due to the homogeneity of the flow which indicates that the flow has become relatively well mixed.

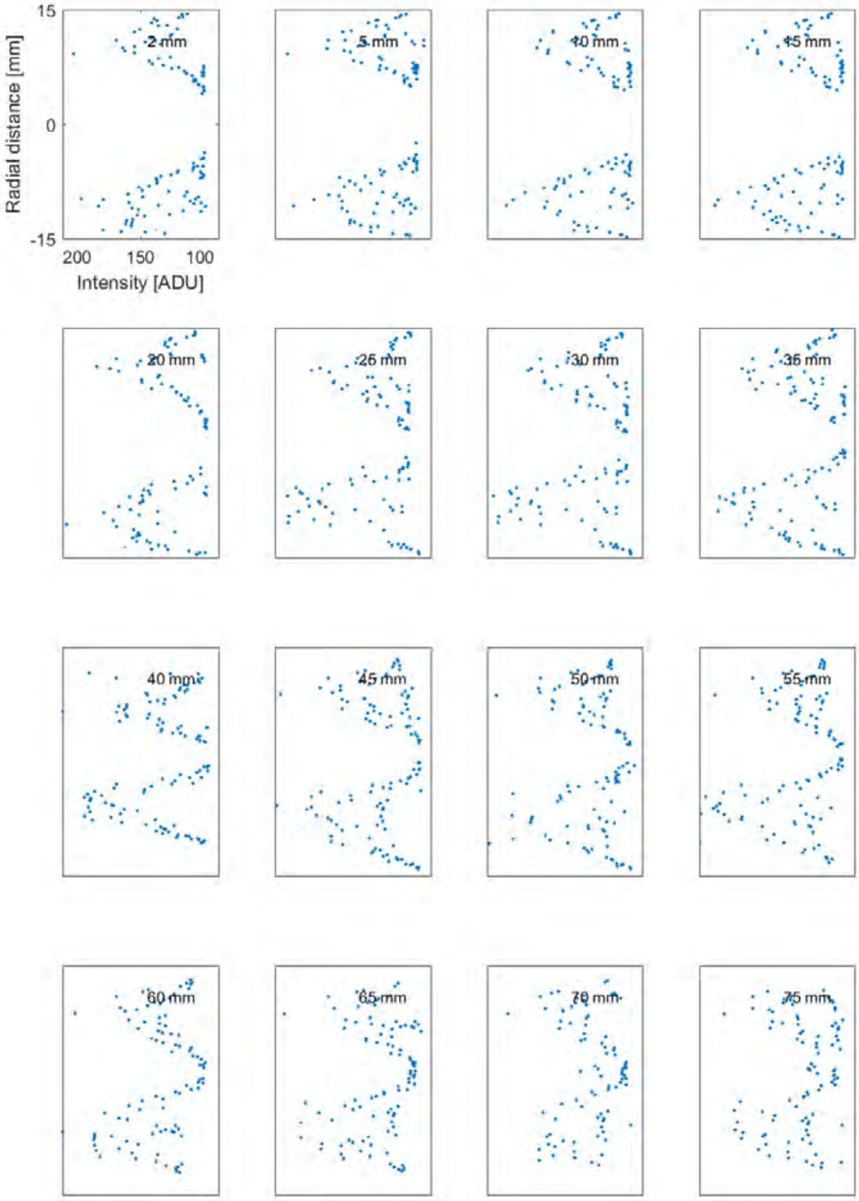

Figure 8.14: Intensity variation within the ejector duct at locations between 2 and 75 mm from the nozzle exit at 190 kPa, 1.6 kPa and 4.5 kPa as a primary pressure, secondary pressure and back pressure respectively.

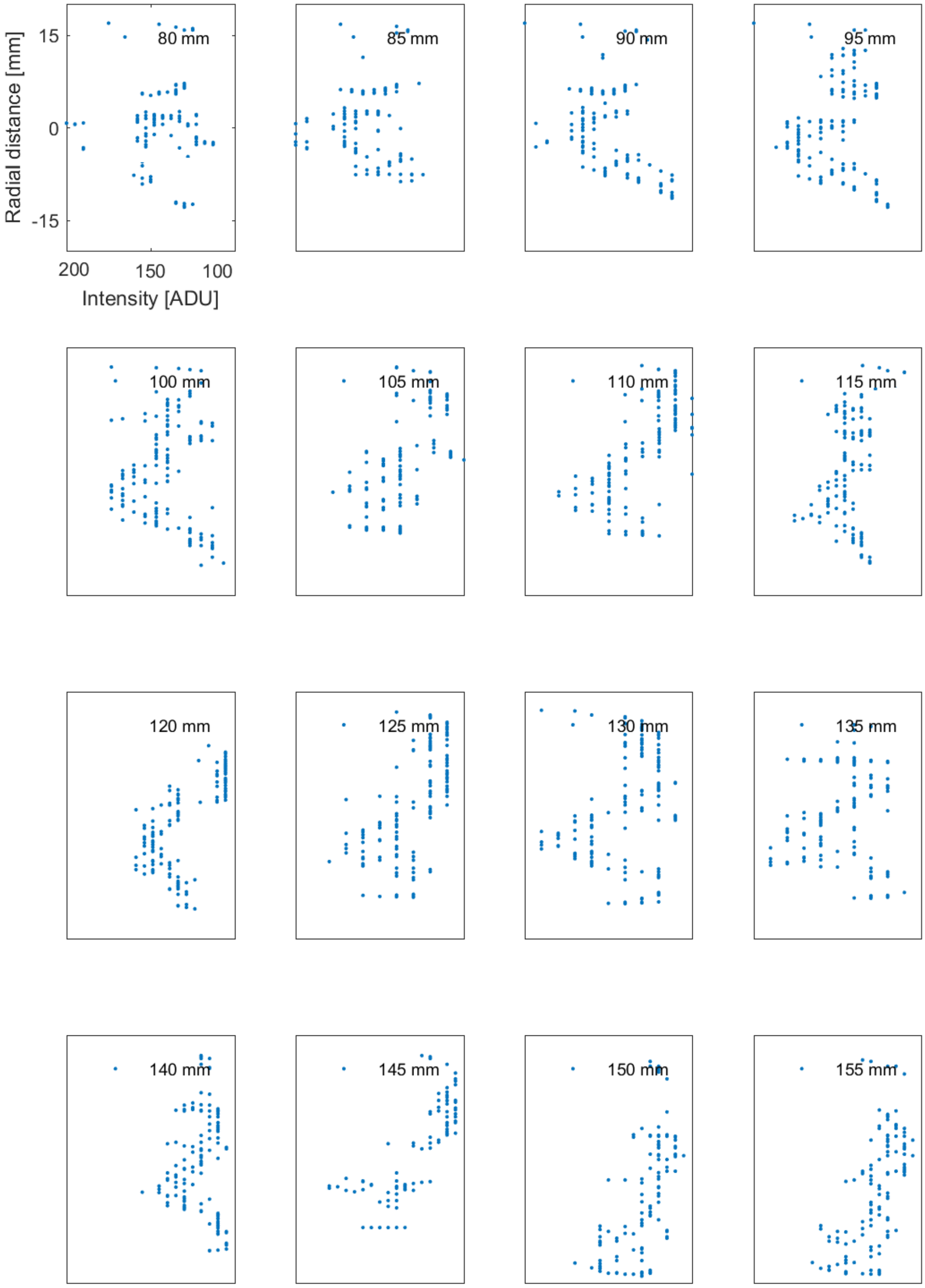

Figure 8.15: Intensity variation within the ejector duct at locations between 80 and 155 mm from the nozzle exit at 190 kPa, 1.6 kPa and 4.5 kPa as a primary pressure, secondary pressure and back pressure respectively.

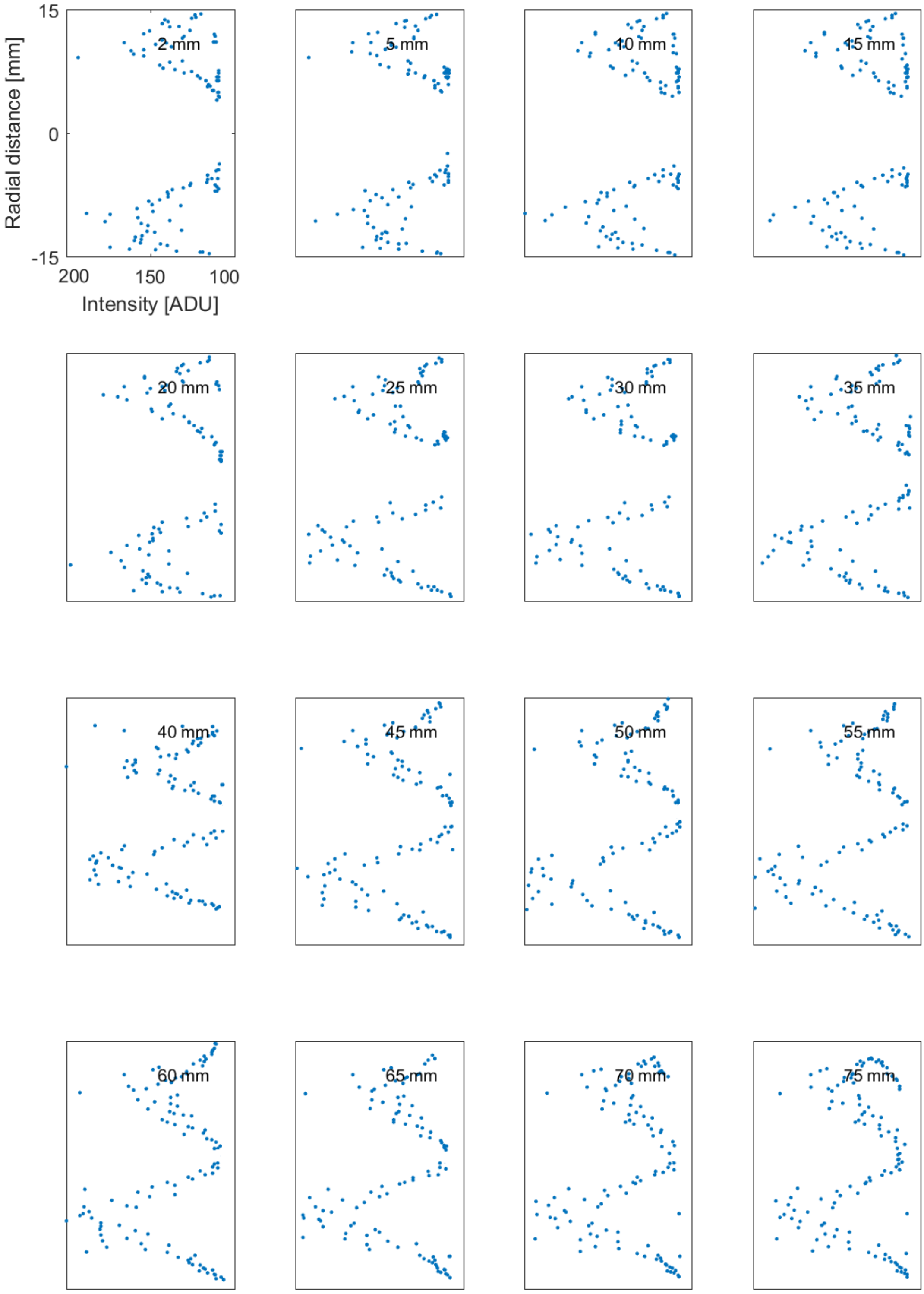

Figure 8.16: Intensity variation within the ejector duct at locations between 2 and 75 mm from the nozzle exit at 200 kPa, 1.6 kPa, 4.8 kPa as a primary, secondary pressure and back pressure respectively.

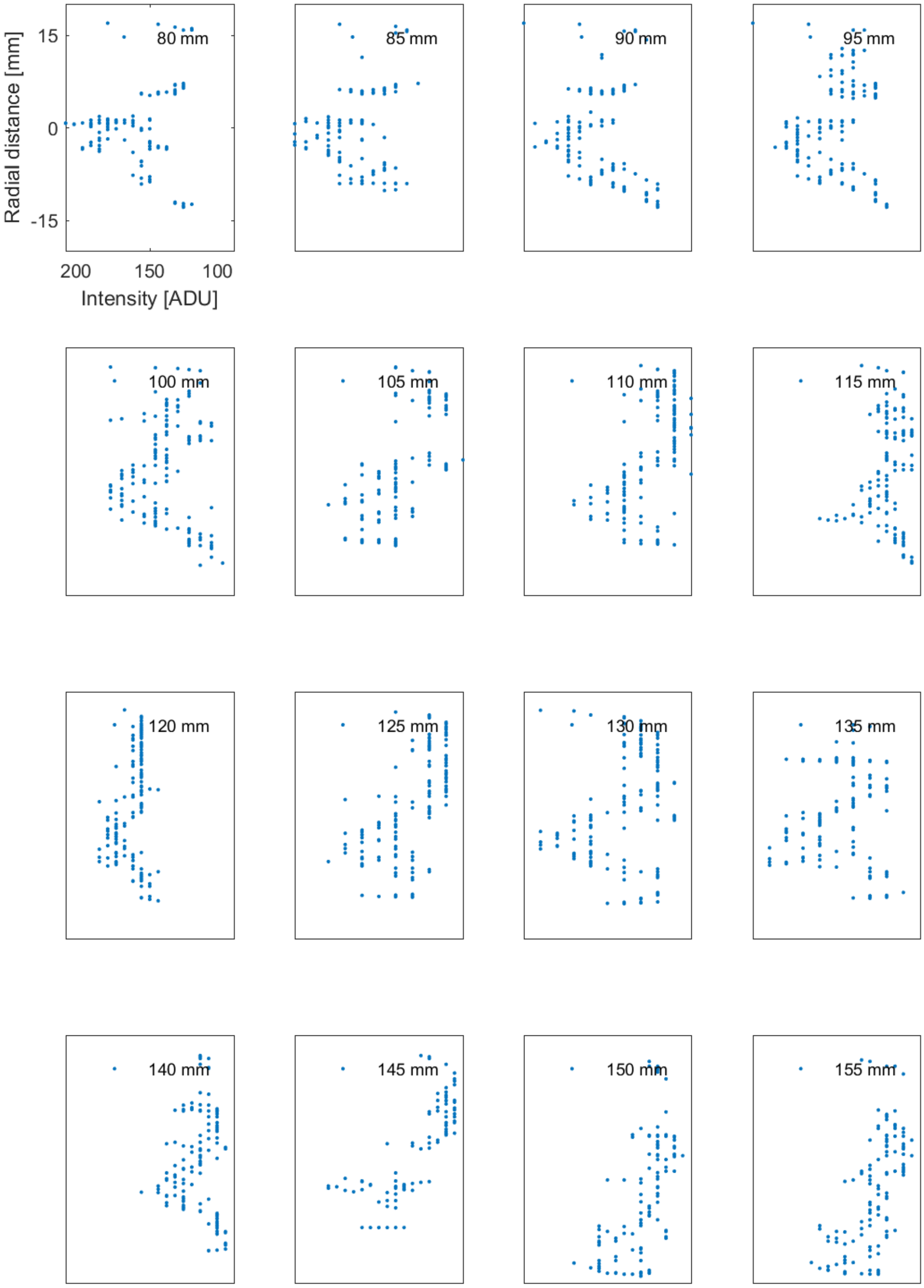

Figure 8.17: Intensity variation within the ejector duct at locations between 80 and 155 mm from the nozzle exit at 200 kPa, 1.6 kPa and 4.8 kPa as a primary, secondary pressure and back pressure respectively.

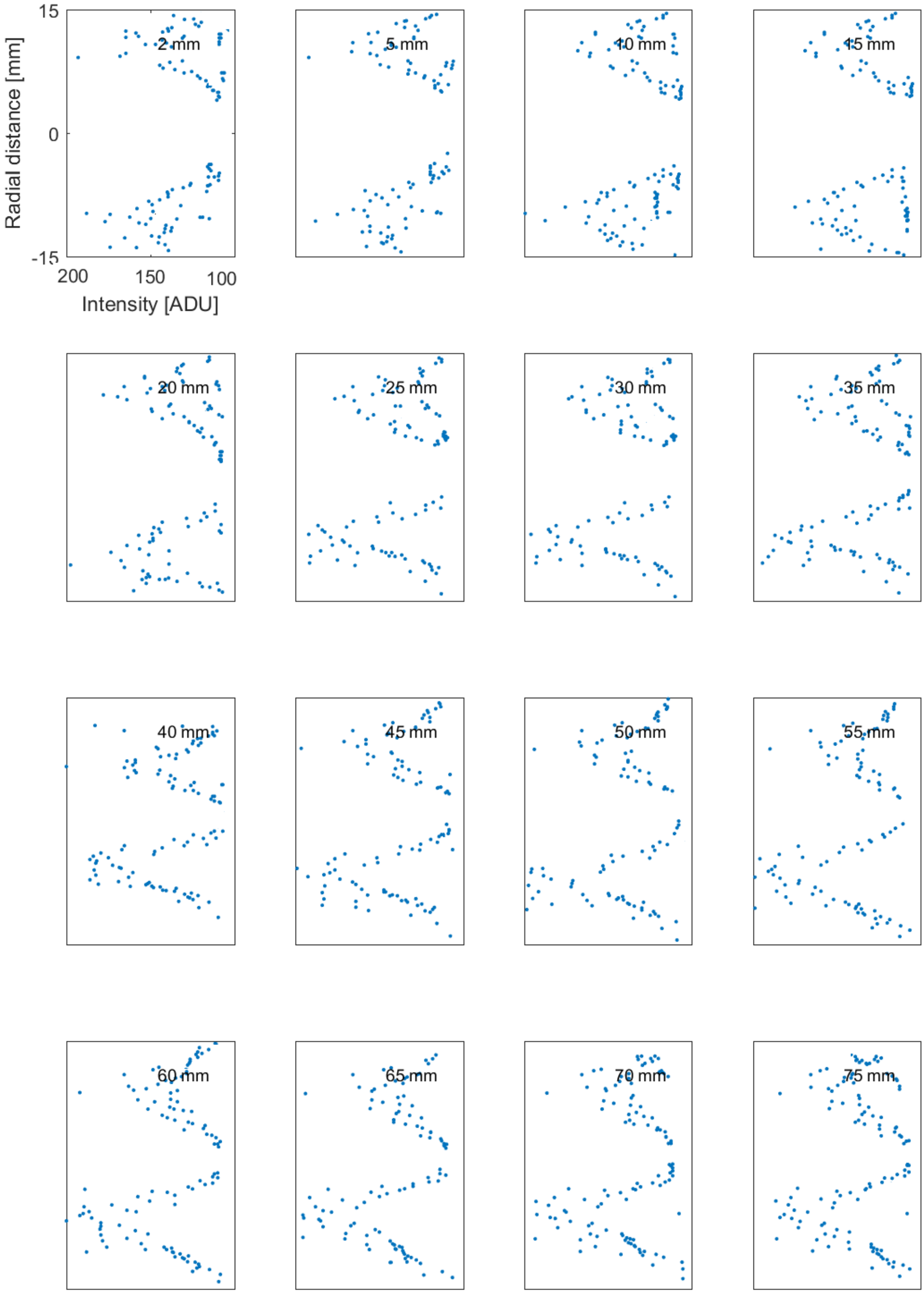

Figure 8.18: Intensity variation within the ejector duct at locations between 2 and 75 mm from the nozzle exit at 210 kPa, 1.6 kPa and 5.2 kPa as a primary pressure, secondary pressure and back pressure respectively.

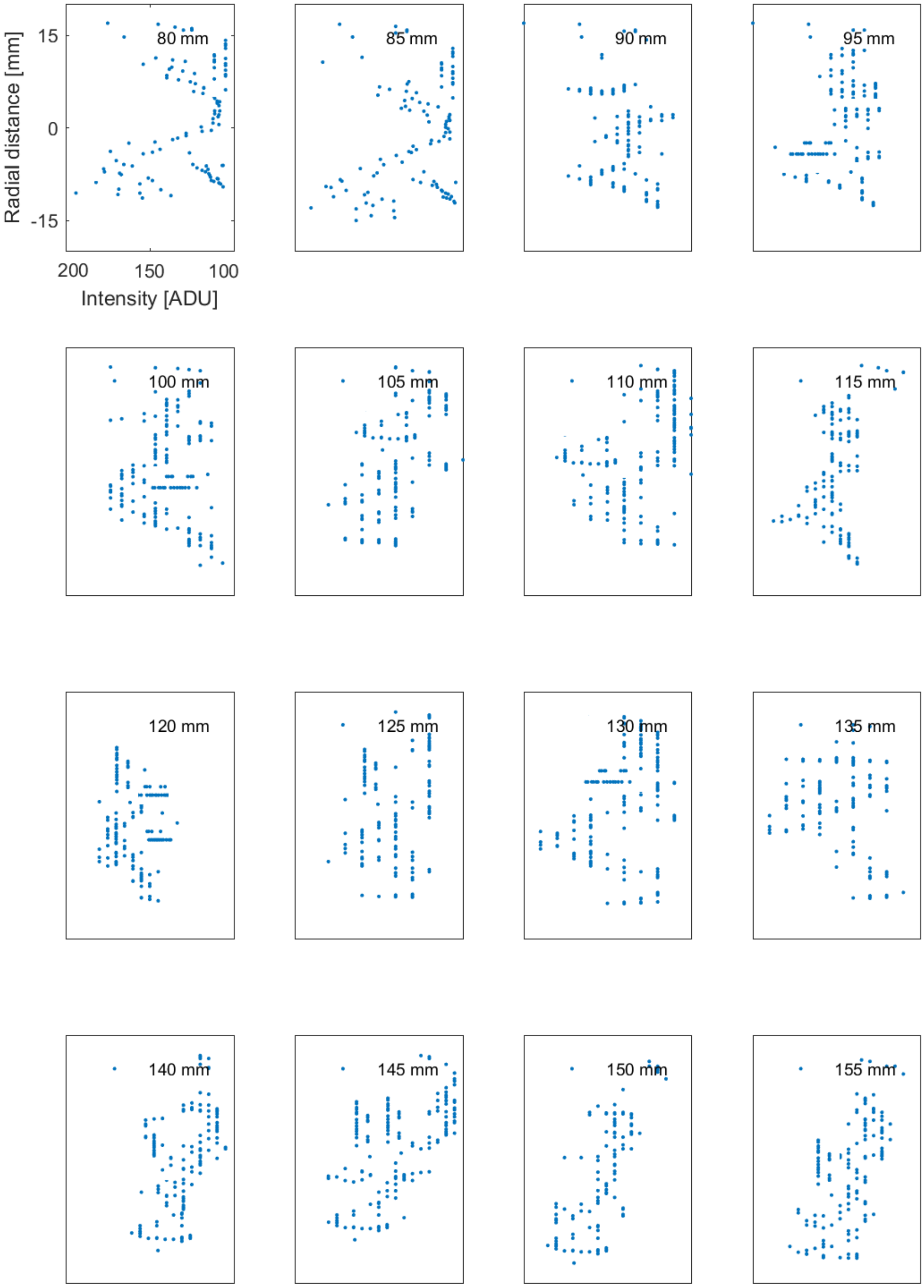

Figure 8.19: Intensity variation within the ejector duct at locations between 80 and 155 mm from the nozzle exit at 210 kPa, 1.6 kPa and 5.2 kPa as a primary pressure, secondary pressure and back pressure respectively.

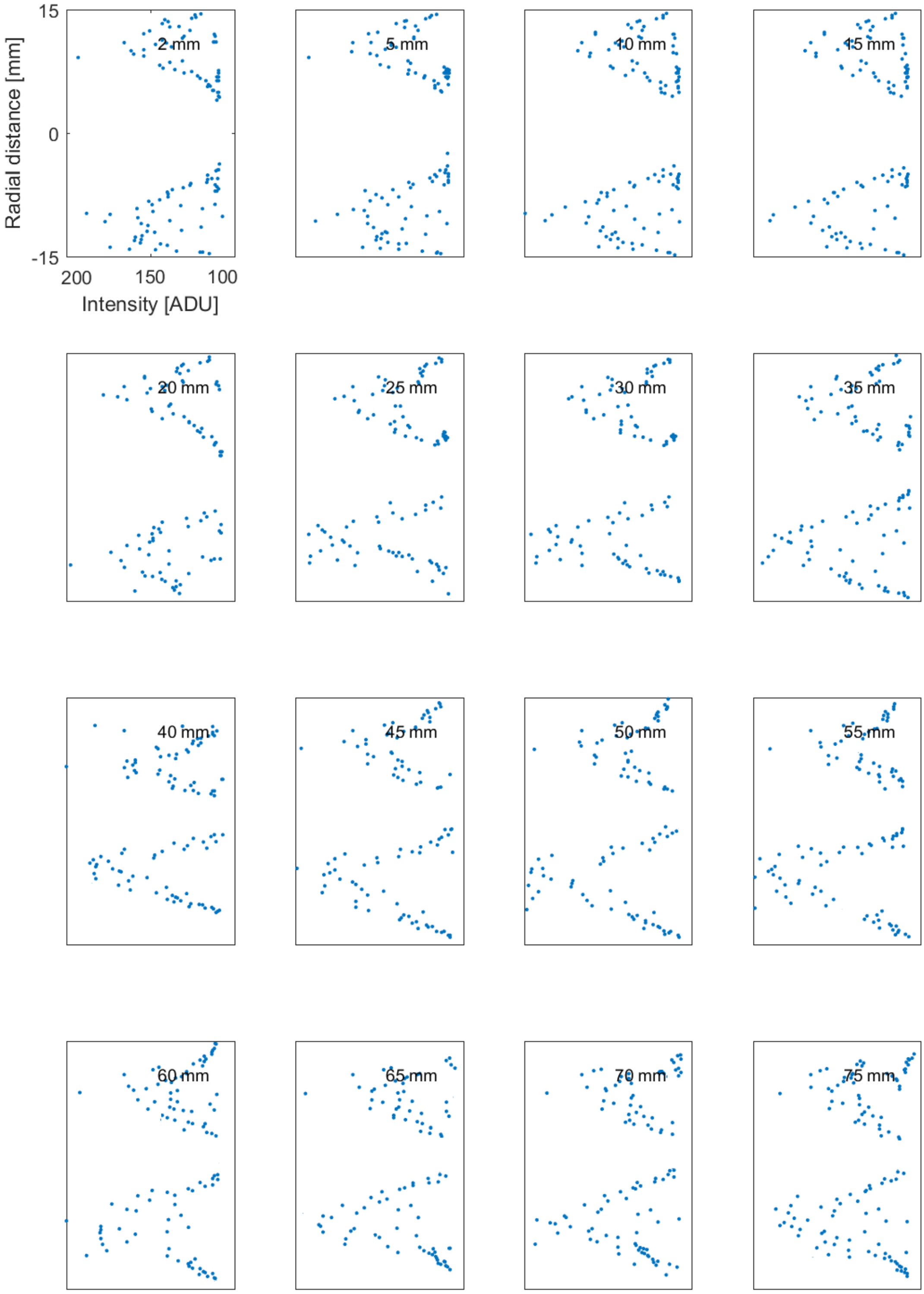

Figure 8.20: Intensity variation within the ejector duct at locations between 2 and 75 mm from the nozzle exit at 220 kPa, 1.6 kPa and 5.7 kPa as a primary pressure, secondary pressure and back pressure respectively.

Figure 8.21: Intensity variation within the ejector duct at locations between 80 and 155 mm from the nozzle exit at 220 kPa, 1.6 kPa and 5.7 kPa as a primary pressure, secondary pressure and back pressure respectively.

8.6 Core flow length

The core flow length is defined as the distance within the ejector duct from the primary flow nozzle exit to the point where the primary flow is no longer distinctly different from the secondary flow. Figure 8.22 shows the core flow length is 75 mm for the specified operating conditions. The duct diameter is used as a reference dimension to convert image pixels to mm. It was found that each 17.5 pixels was the equivalent of 1 mm. This image is an overlay of successive frames as the reflections from the traversing laser beam were added together in Matlab with an average of the resulting intensity to produce a visualisation of the flow in the ejector.

Figure 8.22 shows key details such as the secondary flow, and most importantly, the primary core flow region. The region within the duct where the intensity transitions to the minimum value can be visually interpreted and the boundary marked on the image. The secondary flow with the suspended particles is seen as a bright region around the primary jet which appears as a dark region. The unseeded primary flow potential core is invisible while the seeded secondary flow is illuminated and made visible.

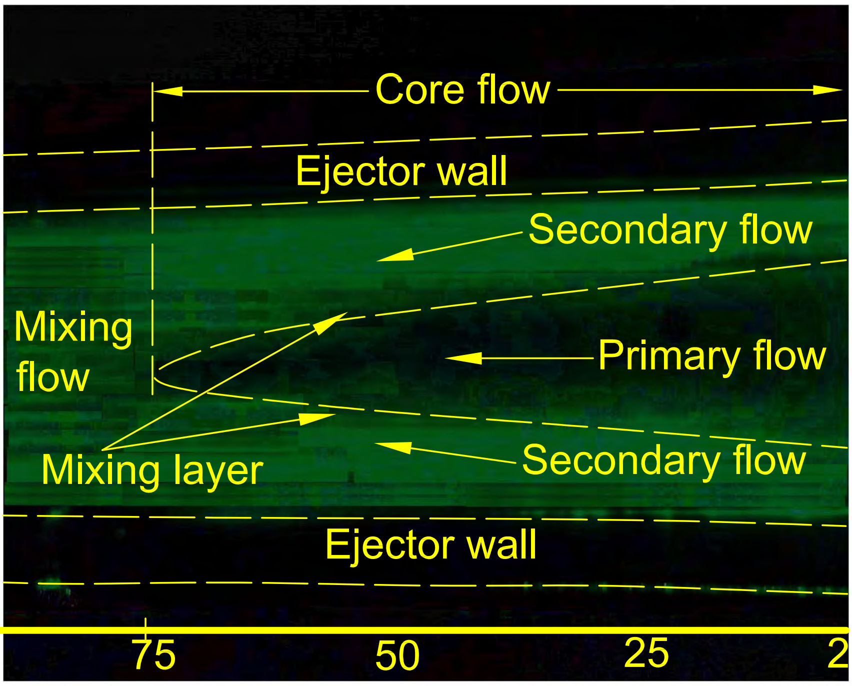

Figure 8.22: Composite image of the flow at 200 kPa and 1.6 kPa as a primary and secondary pressure respectively (dimensions in mm).

The contrast between the two regions in the nozzle exit area allows an analysis of the core flow shape and determination of the core flow length. The edge of the illuminated zone marks the shape of the supersonic mixing layer on the primary stream side and the extent of the unmixed region of the primary flow. Thickness of the shear layer grows as the flow move downstream and ultimately, no unmixed primary flow remains.

Figure 8.23 shows the intensity data and the core flow diameter at the location of 2 mm downstream of the nozzle exit. The operating conditions of the ejector were primary, secondary and back pressures of 200 kPa, 1.6 kPa and 4.8 kPa respectively. An envelope for the visualisation intensity data was fitted to the results at each station. The core flow diameter was defined from the intersection of this envelop and the minimum intensity, as illustrated in Figure 8.23. The core flow diameter at this position is 8.7 mm. At a distance of 75 mm downstream of the nozzle exit, the primary jet core flow disappears.

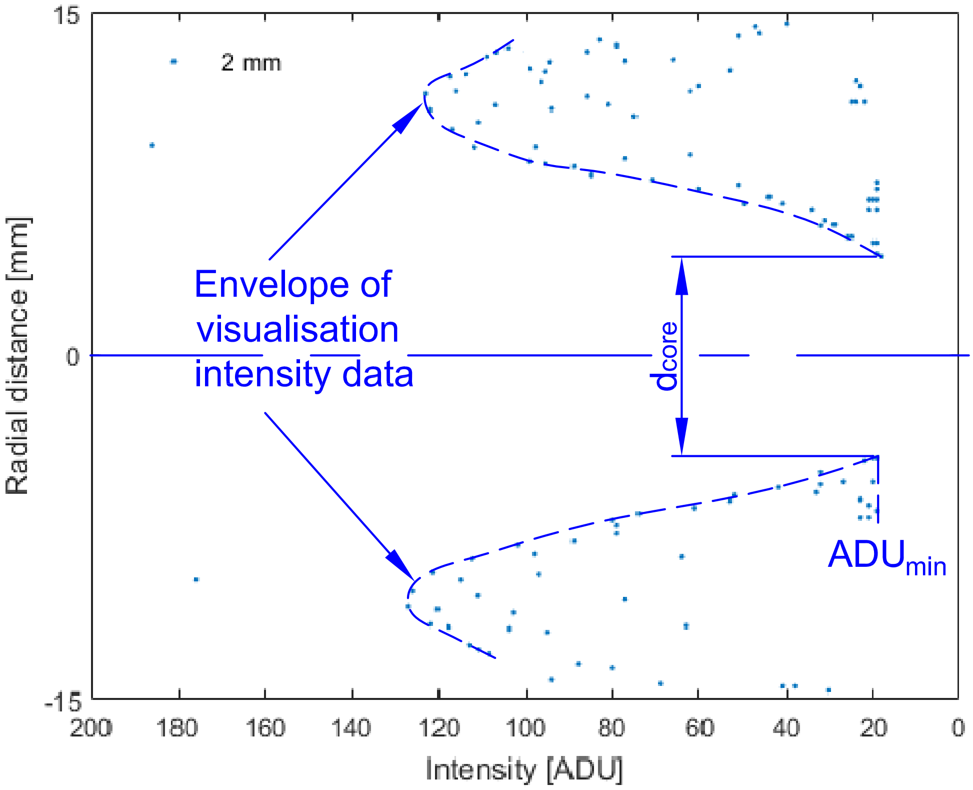

Figure 8.23: Visualisation intensity data of flow for operating conditions of 200 kPa, 1.6 kPa and 4.8 kPa as a primary, secondary and back pressures respectively.

Figure 8.24 present the jet core flow diameters at different locations downstream of the nozzle exit. It can be seen all curves have a same trend. As the flow moves downstream, the jet core flow diameter increases and then reaches its maximum value. As the flow moves further downstream, the jet flow core diameter starts to decrease. The maximum diameter and the length of the jet core flow vary depending on the ejector operating conditions. The maximum diameter and length of the jet core flow were achieved at maximum primary pressure. The jet core flow in this figure has the similar trend of the simulation results for the sonic line as presented in Figure 7.18.

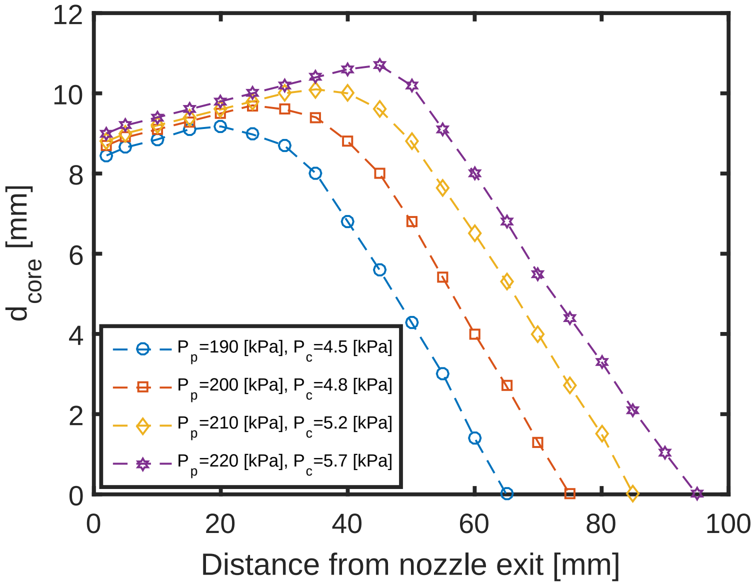

Figure 8.24: Jet flow core diameter at different locations from the nozzle exit for range of primary and back pressures and 1.6 kPa as a secondary pressure.

Figure 8.25 presents the turbulence kinetic energy (TKE) of the flow along the ejector centreline for the operating condition of 190 kPa, 1.6 kPa as a primary and secondary pressures respectively. The TKE values in the core flow are very low up to the distance of 20 mm from the nozzle exit. The increase and oscillation in TKE in the region between 20 mm and 60 mm is associated with wave processes in the primary stream. From 60 mm, the TKE decreases gradually until the mixing layers merge on the jet centreline. The location of the minimum value of TKE is taken as the point at wich the core flow terminated.

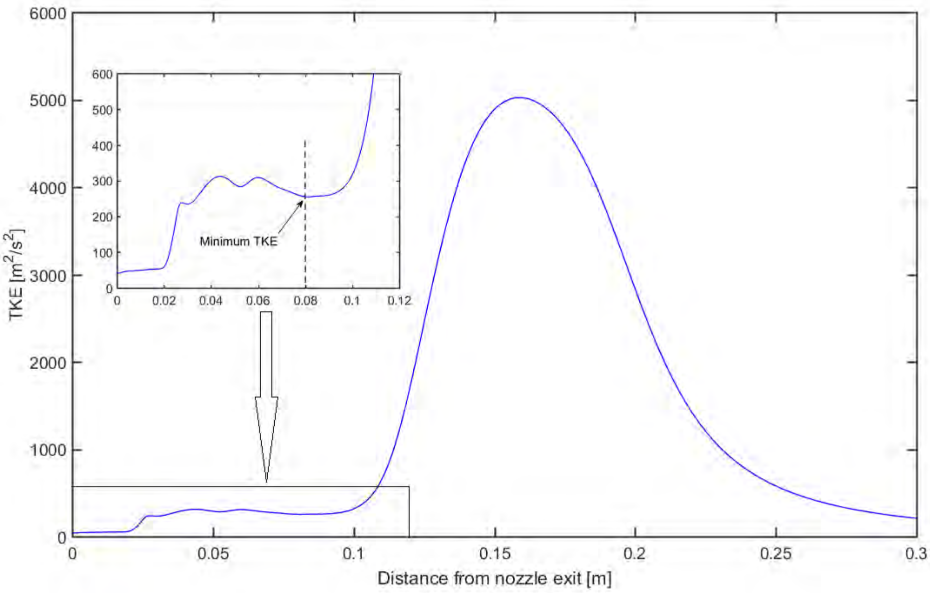

Figure 8.25: Simulation of the turbulent kinetic energy along the ejector centreline for operating condition of 190 kPa, 1.6 kPa as primary and secondary pressures respectively.

Visualised jet core flow lengths for the range of primary pressures are illustrated in Figure 8.26. This figure also includes the results from the CFD simulations based on the minimum TKE values. It can be seen that the core flow lengths from the experiments and simulations have a similar trend but differ in magnitude by a maximum of about 15 mm. As the primary pressure increases, the primary jet core flow length increases. This is because the high pressure primary flow has high momentum which allows it to extend further downstream in the ejector duct. The numerical results show a longer core flow than the visualisation results for all primary pressure values.

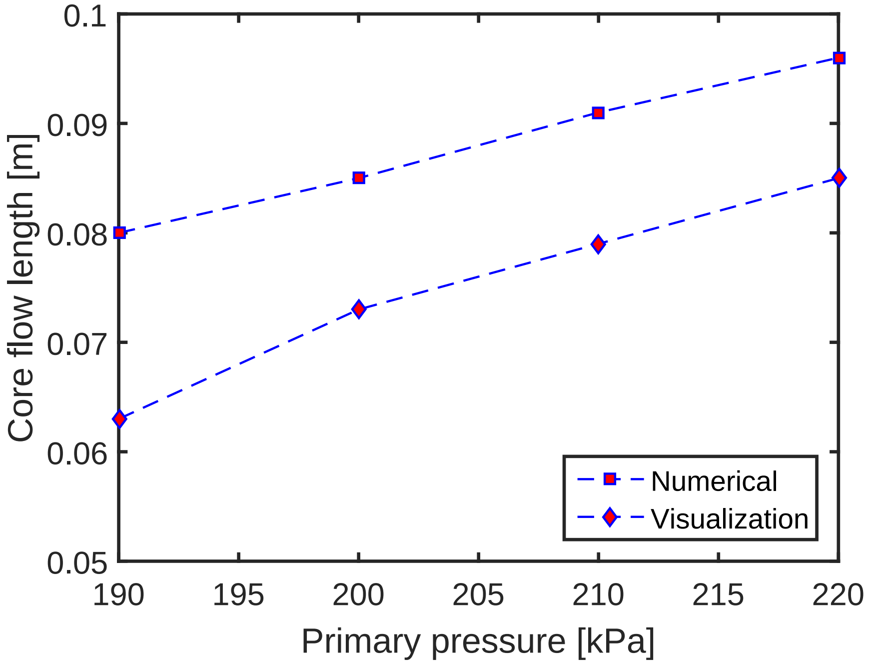

Figure 8.26: Jet core length for a range of primary pressure.

8.7 Chapter Summary

Based on the CRMC theory, a transparent ejector test section was designed, fabricated, and operated in an ejector system using air as the working fluid. A purpose-built, laser-based flow visualisation method has been implemented in which a laser light beam of diameter of 1 mm was used to visualize the seeded flow. The following is a summary of the results obtained in this chapter.

- Experiments were carried out on the ejector for a range of primary pressure from 190 kPa to 220 kPa, and entrainment ratios ranging between 0.34 and 0.39. During this experiment the secondary flow was seeded while the primary flow was kept unseeded. The core flow length, in which the primary and secondary flows are visually distinguishable within the ejector is used to identify the mixing process in the CRMC ejector. The images produced from the experiments provided insight into the complex flow behaviour inside the ejector duct.

- It was demonstrated that the transparent ejector duct could be manufactured locally using a casting technique.

- Despite some drawbacks, talc powder appears especially well suited for seeding applications because it is non-toxic, chemically inert, highly reflective, and rather low cost compared with other seed materials.
- Image processing algorithms were used to analyse a series of images produced from the experiments. The jet core flow diameter at different locations downstream of the nozzle exit were measured. The core flow length has been found to lie between 65 mm and 95 mm from the nozzle exit depending on the ejector operating conditions. As the primary pressure increases, the primary jet core length increases.
- For the ejector operating conditions considered in this work, the core flow length measurements were within about 20 % of those from the CFD simulations.
- Given the relatively long core flow region, the primary and secondary streams cannot be considered as fully mixed at least within the entrance region of the CRMC duct.

Chapter 9

Conclusion and recommendation

9.1 Conclusions

9.1.1 CRMC ejector

Despite the extensive research, ejector design has changed little in recent decades. Several studies have adopted the CRMC ejector design and this configuration appears to have significant potential, but the strengths and weaknesses of the approach have not been clearly defined. The CRMC design was introduced in an effort to minimise losses associated with shock compression in the diffuser and the prescription relies on the primary and secondary streams entering the diffuser duct in a fully mixed state.

A new apparatus for exploring supersonic ejectors based on the CRMC theory has been designed and fabricated. A combination of software and hardware tools were used to model and fabricate the convergent-divergent primary nozzle, the CRMC ejector, primary flow line, secondary flow line, and other parts. The present apparatus was operated extensively with different operating conditions using air as a working fluid to investigate the flow inside the ejector. Analysis of flow in the CRMC ejector included identification of the entrainment ratio, critical back pressure, and static pressure along the ejector duct. The ability of the CRMC ejector to eliminate the shock waves and provide better performance was also examined. A comparison with different ejector profiles and a gas dynamic model was performed.

- The static pressure increases more or less gradually along the ejector wall as expected from the CRMC-designed ejector. However, the rate of rise of the wall static pressure observed in the present work is not especially gradual relative to the pressure rise that can be observed in conventional ejectors. In addition, the CRMC ejector did not provide strong evidence that the shocks associated with the compression process inside a conventional ejector had been eliminated.
- The primary nozzle exit position does not influence significantly the ejector performance and the optimum position is not affected strongly by the operating conditions. This result agrees well with other literature.
- The optimum primary pressure that the ejector worked with was 225 kPa; the achieved entrainment ratio was 0.4, 0.68, 1.11, 1.21 at secondary pressures of 1.6 kPa, 2.5 kPa, 4 kPa, and 5 kPa respectively.
- The maximum isentropic Mach number values at the minimum static pressure value on the CRMC duct wall demonstrates that isentropic-choked conditions are not generated for all secondary pressures and primary pressure of 200 kPa. For the primary pressure of 225 kPa, the isentropic Mach number for all secondary pressures values was higher, but showed isentropic-choked flow conditions were still not generated.
- Geometrical parameters play the same role in the establishing of performance of the CRMC ejector as they do in a conventional ejector.
- A modest level of improvement in terms of entrainment ratio and pressure lift ratio was achieved in the present CRMC ejector relative to a conventional ejector. It is not clear if the additional complexity associated with the manufacturing of the CRMC ejector is warranted given the modest levels of performance improvement.

9.1.2 Computational simulation

A CFD study has been performed using ANSYS FLUENT v 14.5 to investigate the global and local features and flow behaviour inside the CRMC ejector. Two turbulence models, $sst - \kappa\omega$ and $\kappa - \epsilon$ were used in this study, and air was modelled as an ideal gas to simulate the CRMC ejector configuration.

- The $sst - \kappa\omega$ turbulence model exhibited a better simulation of the ejector performance than the $\kappa - \epsilon$. The numerical results were considered to be reliable because the discrepancy between the experimental results and the CFD results was found to be in the vicinity of 5 %.
- The results from the CFD study showed that the flow within the ejector deviates from the analytical design calculations which assume a fully-mixed flow at the entrance of the ejector duct.
- The CRMC ejector showed a gradual and largely shock-free increase in static pressure until the primary pressure reaches a value of 230 kPa but, the pressure gradients are very different from the CRMC design values, and are not very different from those of the conventional design of Al-Doori (2013). Evidence for the elimination of the shock compression in the CRMC ejector as being the cause of enhanced performance of the CRMC duct has not been achieved.
- Total pressure of the CRMC ejector primary flow remains 15 % larger than that in the conventional ejector which leads to more secondary mass entrainment and higher back pressure in the CRMC case. The different contraction angle of the duct adjacent to the primary nozzle is considered as the major cause of such differences, rather than the CRMC duct design.

9.1.3 Flow visualization

To examine the degree of mixing between primary and secondary streams, a transparent CRMC ejector test section was designed, fabricated, and operated in the ejector system, again using air as the working fluid. A purpose-built, laser-based flow visualisation tool has been implemented in which a thin laser light beam of diameter of 1 mm was used to visualize the seeded secondary flow.

- Experiments were carried out on the ejector for a range of operating conditions. During experiments, the secondary flow was seeded while the primary flow was kept unseeded. The mixing process in the CRMC ejector was identified through measurement of the primary stream core flow dimensions.
- Talc powder appears well suited to the present seeding application because it is non-toxic, chemically inert, highly reflective, and rather low cost compared with other seed materials. The wall static pressure of the seeded flow match well with that of the unseeded flow which indicates that the talc powder has a very small effect on the flow.
- Image processing algorithms using Matlab software were developed and these were used to analyse a series of images produced from the experiments. The core flow diameters at different locations downstream of the nozzle exit were defined. The core flow length was found to lie between 65 mm and 95 mm from the nozzle exit, depending on the operating conditions. When the visualisation results of the core flow length were compared with CFD results, differences around 20 % were registered.
- Although there are significant differences between the mixing observed in the experiments and the CFD-simulated mixing, both approaches demonstrate that the primary and secondary streams are not fully mixed at the entrance to the CRMC duct.

9.2 Summary and future work

The flow is not mixed at the entrance to the CRMC duct, so the primary and secondary streams retain aspects of their identity to some distance inside the CRMC duct. Within the designed CRMC duct, the rate of change of the momentum flux for the hypothetical fully-mixed stream may be constant with axial distance, but the exchange of momentum between the primary and secondary flows due to the mixing process will not be constant with axial distance. Consequently, neither the primary nor the secondary streams within the CRMC will actually be undergoing a constant rate of momentum change.

Prescription of the rate of momentum change is derived from empirical knowledge and has not yet been related to a criterion for minimising the strength of compression shocks in the diffuser. In the present work, the length of the CRMC duct was selected to approximately match a conventional ejector of similar throat dimensions and there is some evidence of performance gains relative to conventional ejectors. However, the performance gains do not appear to be directly linked to reduced strength of compression shocks in the diffuser.

Given the CRMC duct is not operating as hypothesised and yet there appears to be performance gains associated with such ejectors ducts having gradually-changing diameters, it is conceivable that further optimisation can be performed if alternative duct profiles are considered, profiles that are not constrained to satisfy the CRMC prescription. Such optimisation might be achieved through CFD simulation and could use a mesh based on a CRMC profile for initiation of the optimisation process.

Improvement of the laser technique introduced in this work is possible by increasing the light source power and using a laser sheet technique to allow instantaneous study of the structures in the flow. In addition, improving the flow seeding technique and minimizing the transparent duct imperfections would enhance the flow visualisation of the ejector. By making such improvements the visualisation technique will become similar to a traditional Particle Image Velocimetry (PIV) which will allow quantitative data on the mixing flow to be obtained.

References

Al-Ansary, H. A. & Jeter, S. M. (2004), 'Numerical and experimental analysis of single-phase and two-phase flow in ejectors', *HVAC&R Research* **10**(4), 521–538.

Al-Doori, G. (2013), Investigation of refrigeration system steam ejector performance through experiments and computational simulations, PhD thesis, University of Southern Queesland.

Anderson, J. D. (1990), *Modern compressible flow: with historical perspective*, McGraw Hill Higher Education.

Aphornratana, S. & Eames, I. W. (1997), 'A small capacity steam-ejector refrigerator: experimental investigation of a system using ejector with movable primary nozzle', *International Journal of Refrigeration* **20**(5), 352–358.

Ariafar, K., Buttsworth, D., Al-Doori, G. & Malpress, R. (2015), 'Effect of mixing on the performance of wet steam ejectors', *Energy* **93**, 2030–2041.

ASHRAE (1986), *ASHRAE Handbook: Refrigeration systems and applications*, American Society of Heating, Refrigerating and Air Conditioning Engineers.

Bartosiewicz, Y., Aidoun, Z., Desevaux, P. & Mercadier, Y. (2005), 'Numerical and experimental investigations on supersonic ejectors', *International Journal of Heat and Fluid Flow* **26**(1), 56–70.

Bartosiewicz, Y., Aidoun, Z. & Mercadier, Y. (2006), 'Numerical assessment of ejector operation for refrigeration applications based on CFD', *Applied Thermal Engineering* **26**(5), 604–612.

Bouhanguel, A., Desevaux, P., Bailly, Y. & Girardot, L. (2012), 'Particle image velocimetry in a supersonic air ejector'.

Buttsworth, D. R. (2017), Calibration of a gas dynamic model for ejector performance, *in* 'Proceeding of the 2nd Thermal and Fluid Engineering Conference, TFEC2017 4th International Workshop on Heat Transfer, IWHT2017 April 2-5, 2017, Las Vegas, NV, USA'.

Chaiwongsa, P. & Wongwises, S. (2008), 'Experimental study on R-134a refrigeration system using a two-phase ejector as an expansion device', *Applied Thermal Engineering* **28**(5), 467–477.

Chandra, V. V. & Ahmed, M. R. (2014), 'Experimental and computational studies on a steam jet refrigeration system with constant area and variable area ejectors', *Energy Conversion and Management* **79**, 377–386.

Chang, Y.-J. & Chen, Y.-M. (2000), 'Enhancement of a steam-jet refrigerator using a novel application of the petal nozzle', *Experimental Thermal and Fluid Science* **22**(3), 203–211.

Chong, D., Hu, M., Chen, W., Wang, J., Liu, J. & Yan, J. (2014), 'Experimental and numerical analysis of supersonic air ejector', *Applied Energy* **130**, 679–684.

Choutapalli, I. M. (2006), An experimental study of a pulsed jet ejector, PhD thesis, Florida State University.

Chunnanond, K. & Aphornratana, S. (2004), 'An experimental investigation of a steam ejector refrigerator: the analysis of the pressure profile along the ejector', *Applied Thermal Engineering* **24**(2), 311–322.

Dennis, M. (2009), 'Solar cooling using variable geometry ejectors', *The Australian National University Canberra, ACT* **200**.

Dennis, M. & Garzoli, K. (2011), 'Use of variable geometry ejector with cold store to achieve high solar fraction for solar cooling', *International Journal of Refrigeration* **34**(7), 1626–1632.

Desevaux, P. (2001), 'A method for visualizing the mixing zone between two co-axial flows in an ejector', *Optics and Lasers in Engineering* **35**(5), 317–323.

Desevaux, P. & Aeschbacher, O. (2002), 'Numerical and experimental flow visualizations of the mixing process inside an induced air ejector', *International Journal of Turbo and Jet Engines* **19**(1-2), 71–78.

Desevaux, P., Marynowski, T. & Khan, M. (2006), 'CFD prediction of supersonic ejectors performance', *International Journal of Turbo and Jet Engines* **23**(3), 173.

Dong, J., Chen, X., Wang, W., Kang, C. & Ma, H. (2017), 'An experimental investigation of steam ejector refrigeration system powered by extra low temperature heat source', *International Communications in Heat and Mass Transfer* **81**, 250–256.

Dong, J., Ma, H. & Guo, L. (2013), Study of optimum nozzle exit position (nxp) in a steam ejector refrigeration system, *in* 'AIP Conference Proceedings', Vol. 1547, AIP, pp. 115–123.

Dutton, J. & Carroll, B. (1988), 'Limitation of ejector performance due to exit choking', *Journal of Fluids Engineering* **110**(1), 91–93.

Eames, I., Aphornratana, S. & Haider, H. (1995), 'A theoretical and experimental study of a small-scale steam jet refrigerator', *International Journal of Refrigeration* **18**(6), 378–386.

Eames, I. W. (2002), 'A new prescription for the design of supersonic jet-pumps: the constant rate of momentum change method', *Applied Thermal Engineering* **22**(2), 121–131.

Eames, I. W., Ablwaifa, A. E. & Petrenko, V. (2007), 'Results of an experimental study of an advanced jet-pump refrigerator operating with r245fa', *Applied Thermal Engineering* **27**(17), 2833–2840.

Eames, I., Wu, S., Worall, M. & Aphornratana, S. (1999), 'An experimental investigation of steam ejectors for applications in jet-pump refrigerators powered by low-grade heat', *Proceedings of the Institution of Mechanical Engineers, Part A: Journal of Power and Energy* **213**(5), 351–361.

ESDU (1986), 'Ejectors and jet pumps: Design for steam driven flow, data item 86030'.

Fabri, J. & Siestrunck, R. (1958), 'Supersonic air ejectors', *Advances in Applied Mechanics* **5**, 1–34.

Fu, W., Li, Y., Liu, Z., Wu, H. & Wu, T. (2016), 'Numerical study for the influences of primary nozzle on steam ejector performance', *Applied Thermal Engineering* **106**, 1148–1156.

Gutiérrez, A. & León, N. (2014), 'Conceptual development and CFD evaluation of a high efficiency–variable geometry ejector for use in refrigeration applications', *Energy Procedia* **57**, 2544–2553.

He, S., Li, Y. & Wang, R. (2009), 'Progress of mathematical modeling on ejectors', *Renewable and Sustainable Energy Reviews* **13**(8), 1760–1780.

Hedges, K. & Hill, P. (1974), 'Compressible flow ejectors: Part idevelopment of a finite-difference flow model', *Journal of Fluids Engineering* **96**(3), 272–281.

Hemidi, A., Henry, F., Leclaire, S., Seynhaeve, J.-M. & Bartosiewicz, Y. (2009), 'CFD analysis of a supersonic air ejector. part i: experimental validation of single-phase and two-phase operation', *Applied Thermal Engineering* **29**(8), 1523–1531.

Huang, B., Chang, J., Wang, C. & Petrenko, V. (1999), 'A 1-d analysis of ejector performance', *International Journal of Refrigeration* **22**(5), 354–364.

ISO (2006), '5167–2', *Measurement of flow by means of pressure differential devices inserted in circular cross-section conduits running full–Part* **2**.

Ji, M., Utomo, T., Woo, J., Lee, Y., Jeong, H. & Chung, H. (2010), 'CFD investigation on the flow structure inside thermo vapor compressor', *Energy* **35**(6), 2694–2702.

Kastner, L. & Spooner, J. (1950), 'An investigation of the performance and design of the air ejector employing low-pressure air as the driving fluid', *Proceedings of the Institution of Mechanical Engineers* **162**(1), 149–166.

Keenan, J. H. (1950), 'An investigation of ejector design by analysis and experiment', *Journal of Applied Mechanics* **17**, 299.

Kim, H., Lee, J., Setoguchi, T. & Matsuo, S. (2006), 'Computational analysis of a variable ejector flow', *Journal of Thermal Science* **15**(2), 140–144.

Kong, F., Jin, Y., Setoguchi, T. & Kim, H. D. (2013), 'Numerical analysis of chevron nozzle effects on performance of the supersonic ejector-diffuser system', *Journal of Thermal Science* **22**(5), 459–466.

Kumar, V., Singhal, G. & Subbarao, P. (2013), 'Study of supersonic flow in a constant rate of momentum change (crmc) ejector with frictional effects', *Applied Thermal Engineering* **60**(1), 61–71.

Little, A. B. & Garimella, S. (2016), 'A critical review linking ejector flow phenomena with component-and system-level performance', *International Journal of Refrigeration* **70**, 243–268.

Ma, X., Zhang, W., Omer, S. & Riffat, S. (2010), 'Experimental investigation of a novel steam ejector refrigerator suitable for solar energy applications', *Applied Thermal Engineering* **30**, 1320–1325.

Manshoor, B. b., Nicolleau, F. & Beck, S. (2011), 'The fractal flow conditioner for orifice plate flow meters', *Flow Measurement and Instrumentation* **22**(3), 208–214.

Massey, B. S. & Ward-Smith, J. (1998), *Mechanics of fluids*, Vol. 1, CRC Press.

Matsuo, K., Sasaguchi, K., Kiyotoki, Y. & Mochizuki, H. (1982), 'Investigation of supersonic air ejectors: Part 2, effects of throat-area-ratio on ejector performance', *Bulletin of JSME* **25**(210), 1898–1905.

Mazzelli, F., Little, A. B., Garimella, S. & Bartosiewicz, Y. (2015), 'Computational and experimental analysis of supersonic air ejector: Turbulence modeling and assessment of 3d effects', *International Journal of Heat and Fluid Flow* **56**, 305–316.

Mazzelli, F. & Milazzo, A. (2015), 'Performance analysis of a supersonic ejector cycle working with r245fa', *International Journal of Refrigeration* **49**, 79–92.

Meakhail, T. A. & Teaima, I. R. (2013), 'A study of the effect of nozzle spacing and driving pressure on the water jet pump performance', *International Journal of Refrigeration* **2**(5).

Meyer, A., Harms, T. & Dobson, R. (2009), 'Steam jet ejector cooling powered by waste or solar heat', *Renewable Energy* **34**(1), 297–306.

Milazzo, A., Rocchetti, A. & Eames, I. W. (2014), 'Theoretical and experimental activity on ejector refrigeration', *Energy Procedia* **45**, 1245–1254.

Munday, J. T. & Bagster, D. F. (1977), 'A new ejector theory applied to steam jet refrigeration', *Industrial & Engineering Chemistry Process Design and Development* **16**(4), 442–449.

Nishijimi, H., Tsuchii, K. & Nakagawa, M. (2016), 'Experimental study on the behavior of the two phase flow shock waves occurring in the ejector refrigeration cycle', *Mechanical Engineering Journal* **3**(6), 16–00255.

Opgenorth, M. J., Sederstrom, D., McDermott, W. & Lengsfeld, C. S. (2012), 'Maximizing pressure recovery using lobed nozzles in a supersonic ejector', *Applied Thermal Engineering* **37**, 396–402.

Park, I. S. (2009), 'Enhancement of entraining performance on thermal vapor compressor for multi-effect desalination plants by swirl effects of motive steam', *An International Journal of Computation and Methodology* **56:5**, 406–421.

Pianthong, K., Seehanam, W., Behnia, M., Sriveerakul, T. & Aphornratana, S. (2007), 'Investigation and improvement of ejector refrigeration system using computational fluid dynamics technique', *Energy Conversion and Management* **48**(9), 2556–2564.

Porcar, R. & Prenel, J. (1976), 'Visualization of shock waves in a supersonic ejector-utilization of the polarization of diffuse light', *Optics Communications* **17**, 346–349.

Pridasawas, W. (2006), Solar-driven refrigeration systems with focus on the ejector cycle, PhD thesis, KTH.

Raffel, M., Willert, C. E., Wereley, S. & Kompenhans, J. (2013), *Particle image velocimetry: a practical guide*, Springer.

Rao, S. M. & Jagadeesh, G. (2014), 'Observations on the non-mixed length and unsteady shock motion in a two dimensional supersonic ejector', *Physics of Fluids* **26**(3), 036103.

Riffat, S. & Everitt, P. (1999), 'Experimental and CFD modelling of an ejector system for vehicle air conditioning', *Journal of the Institute of Energy* **72**(491), 41–47.

Riffat, S. & Omer, S. (2001), 'CFD modelling and experimental investigation of an ejector refrigeration system using methanol as the working fluid', *International Journal of Energy Research* **25**(2), 115–128.

Roy, C. J. & Blottner, F. G. (2003), 'Methodology for turbulence model validation: application to hypersonic flows', *Journal of Spacecraft and Rockets* **40**(3), 313–325.

Ruangtrakoon, N., Thongtip, T., Aphornratana, S. & Sriveerakul, T. (2013), 'CFD simulation on the effect of primary nozzle geometries for a steam ejector in refrigeration cycle', *International Journal of Thermal Sciences* **63**, 133–145.

Ruangtrakoon, Natthawut, T. T. A. S. et al. (2012), 'CFD simulation on the effect of primary nozzle geometries for a steam ejector in refrigeration cycle', *International Journal of Thermal Sciences* **63**(1), 133–145.

Rusly, E. (2004), Ejector cooling with reference to combined ejector-vapour compression system, PhD thesis, The University of Melbourne.

Rusly, E., Aye, L., Charters, W. & Ooi, A. (2005), 'CFD analysis of ejector in a combined ejector cooling system', *International Journal of Refrigeration* **28**(7), 1092–1101.

Scott, D., Aidoun, Z. & Ouzzane, M. (2011), 'An experimental investigation of an ejector for validating numerical simulations', *International Journal of Refrigeration* **34**(7), 1717–1723.

Seehanam, W., Pianthong, K., Behnia, M., Chunnanond, K. & Aphornratana, S. (2007), 'Simulation on performance of cpm and crmc steam ejectors using CFD technique', *Ubon Ratchatany University, Thailand* .

Someya, T. (2012), *Advanced combustion science*, Springer Science & Business Media.

Sriveerakul, T., Aphornratana, S. & Chunnanond, K. (2007), 'Performance prediction of steam ejector using computational fluid dynamics: Part 1. validation of the CFD results', *International Journal of Thermal Sciences* **46**(8), 812–822.

Sun, D.-W. (1996), 'Variable geometry ejectors and their applications in ejector refrigeration systems', *Energy* **21**(10), 919–929.

Sun, D.-W. (1997), 'Experimental investigation of the performance characteristics of a steam jet refrigeration system', *Energy Sources* **19**(4), 349–367.

Sun, D.-W. & Eames, I. W. (1995), 'Recent developments in the design theories and application of ejectors: a review', *Journal of the Institute of Energy* **68**(475), 65–79.

Varga, S., Oliveira, A. C. & Diaconu, B. (2009*a*), 'Influence of geometrical factors on steam ejector performance–a numerical assessment', *International journal of refrigeration* **32**(7), 1694–1701.

Varga, S., Oliveira, A. C. & Diaconu, B. (2009*b*), 'Numerical assessment of steam ejector efficiencies using CFD', *International Journal of Refrigeration* **32**(6), 1203–1211.

Varga, S., Oliveira, A. C. & Ma, X. (2011), 'Experimental and numerical analysis of a variable area ratio steam ejector', *International Journal of Refrigeration* **34**(7), 1668–1675.

Vyas, B. & Kar, S. (1975), Study of entrainment and mixing process for an air to air jet ejector, *in* 'In: Symposium on Jet Pumps and Ejectors and Gas Lift Techniques, 2nd, Cambridge, England, March 24-26, 1975, Proceedings.(A76-38476 19-34) Cranfield, Beds., England, BHRA Fluid Engineering, 1975, p. C2-15 to C2-25.', Vol. 1, p. 2.

Watanabe, I. (1972), 'Experimental investigations concerning pneumatic ejectors, with special reference to the effect of dimensional parameters on performance characteristics', *Jet pumps and ejectors* pp. 97–120.

Wilcox, D. C. (1998), *Turbulence modeling for CFD*, Vol. 2, DCW industries La Canada, CA.

Worall, M. (2001), An investigation of a jet-pump (ice) storage system powered by low-grade heat, PhD thesis, University of Nottingham.

Yadav, R. L. & Patwardhan, A. W. (2008), 'Design aspects of ejectors: Effects of suction chamber geometry', *Chemical Engineering Science* **63**(15), 3886–3897.

Yang, X., Long, X. & Yao, X. (2012), 'Numerical investigation on the mixing process in a steam ejector with different nozzle structures', *International Journal of Thermal Sciences* **56**, 95–106.

Zhu, Y. & Jiang, P. (2014), 'Experimental and numerical investigation of the effect of shock wave characteristics on the ejector performance', *International Journal of Refrigeration* **40**, 31–42.

Appendix A

A.1 Primary nozzle

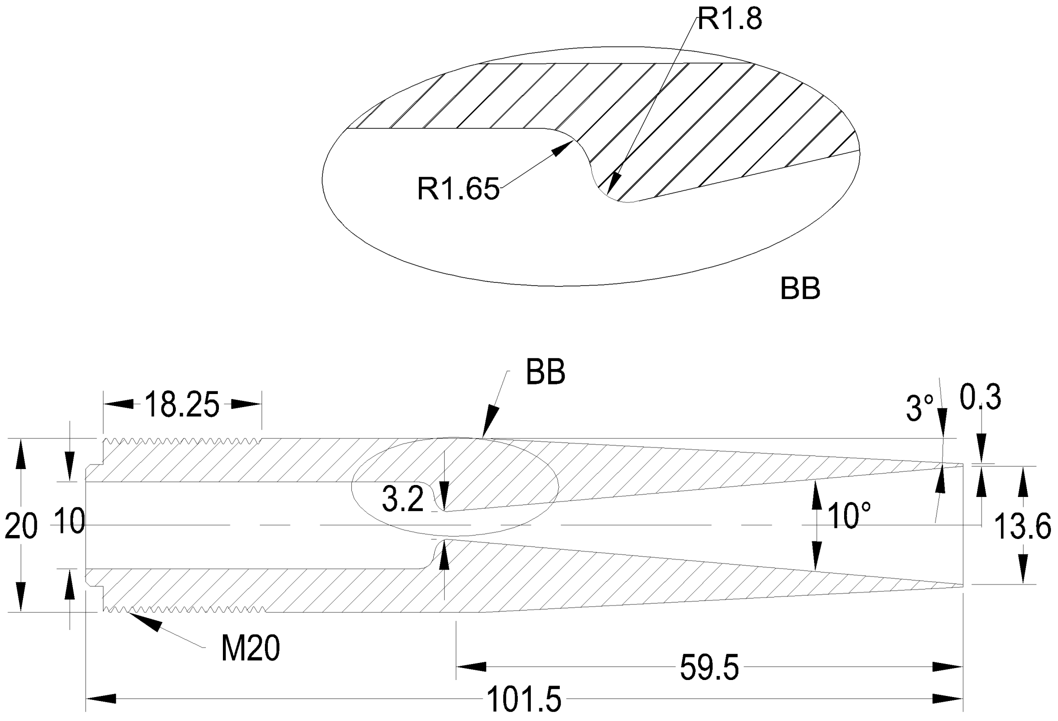

Figure A.1: Profile of the primary nozzle with overall dimensions, all dimensions in mm.

A.2 Primary nozzle holder

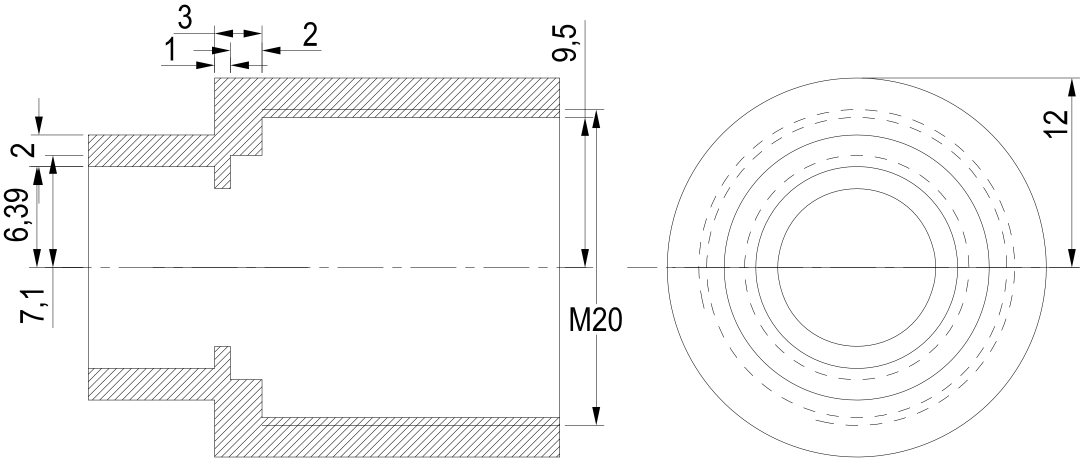

Figure A.2: Profile of the primary nozzle holder with overall dimensions, all dimensions in mm.

A.3 Spider

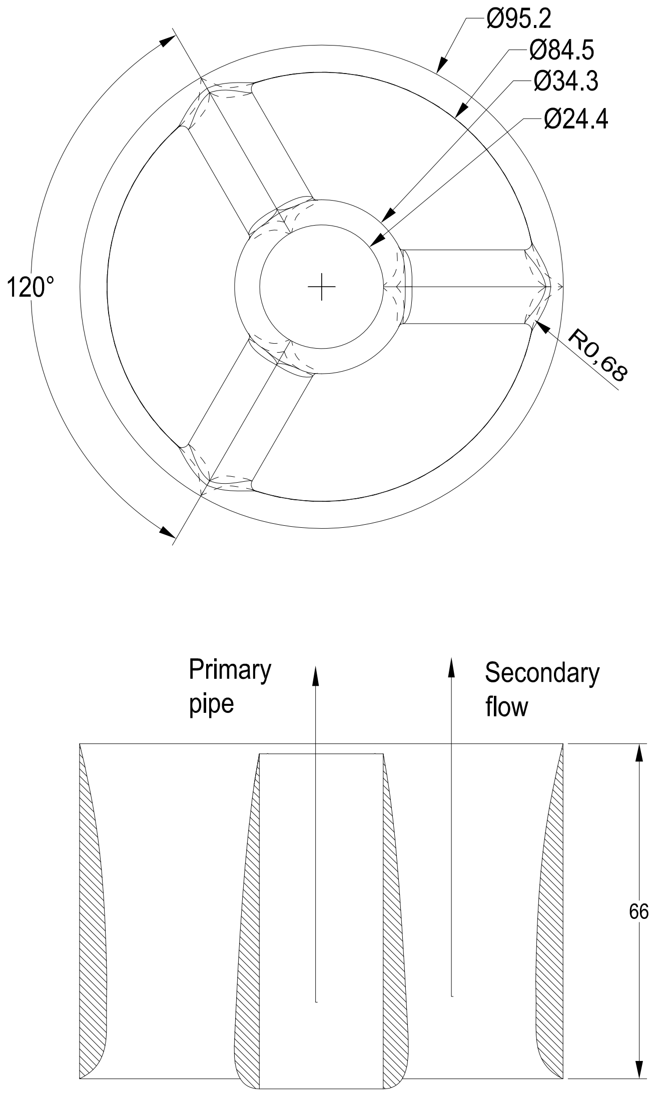

Figure A.3: Profile of the hub with integral spokes with overall dimensions, all dimensions in mm.

A.4 Secondary flow pipe

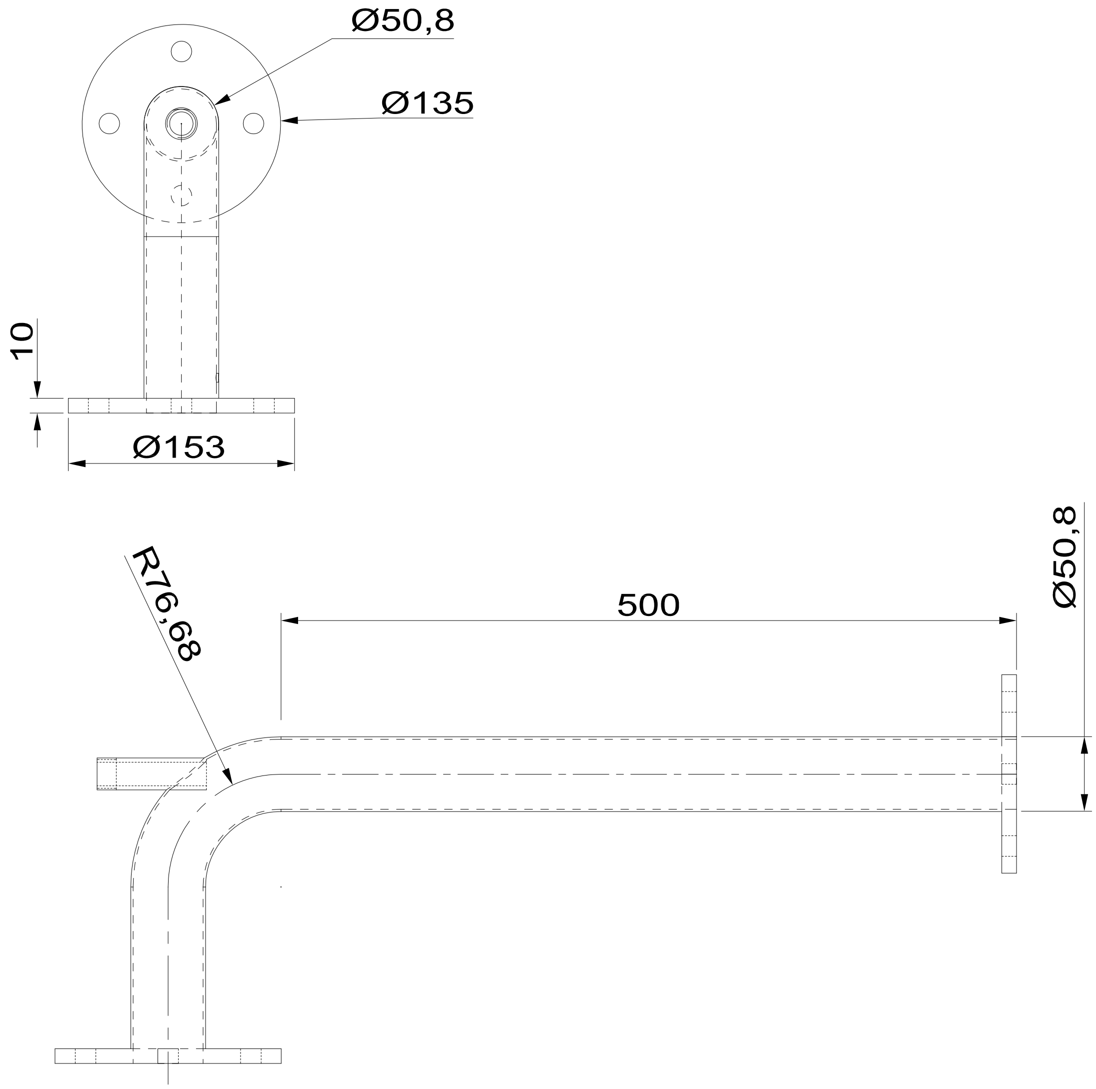

Figure A.4: Profile of the secondary flow pipe part 1 with overall dimensions, all dimensions in mm.

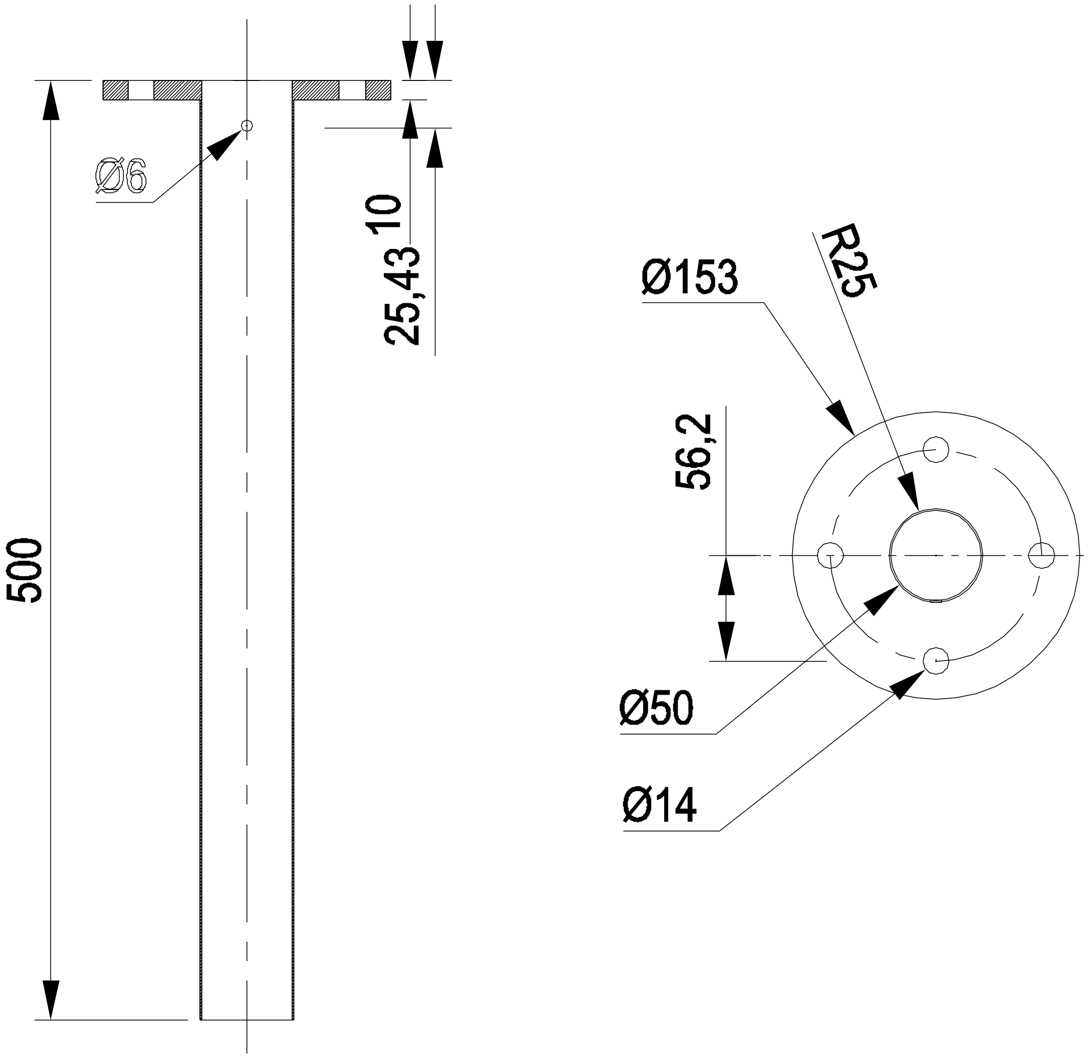

Figure A.5: Profile of the secondary flow pipe part 2 with main dimensions, all dimensions in mm.

A.5 Orifice plate

The orifice plate has a simple construction, low maintenance cost and a wide applicability to different fluids including both liquids and gases (Manshoor, Nicolleau & Beck 2011). In addition, the overall accuracy of the standard orifice plate is 0.5 % (ISO 2006). The axis of the orifice plate is coincident with that of the secondary flow pipe. The position of the orifice plate within the system is shown through part 2 in Figure 4.3 and its geometry is shown in Figure A.6.

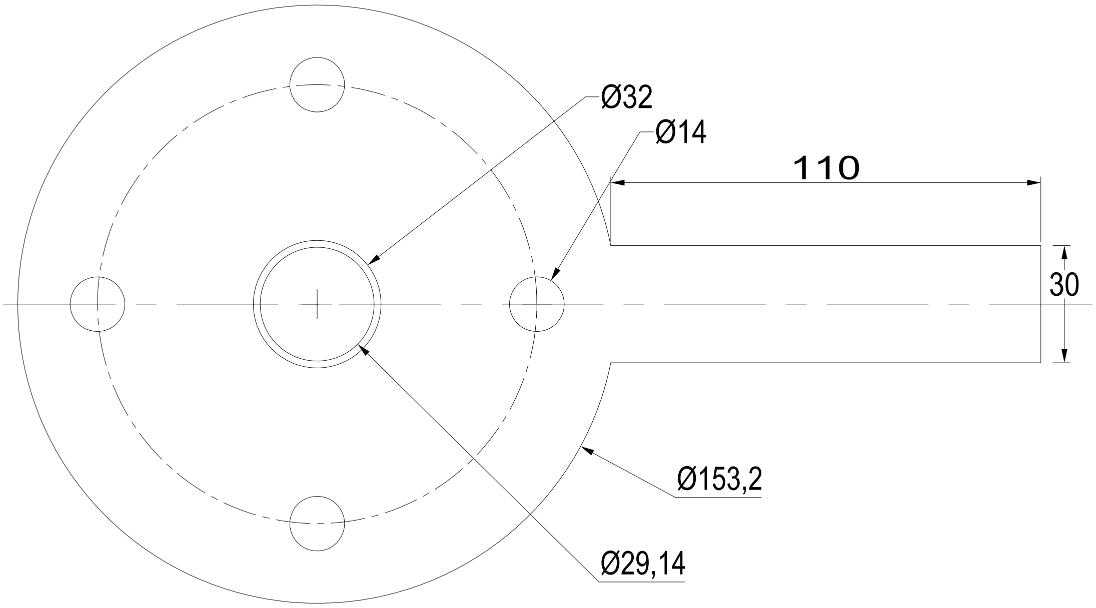

Figure A.6: Profile of the orifice plate with main dimensions, all dimensions in mm.

Mild steel flange orifice plates were manufactured in the USQ workshop. Orifice plates were produced with a range of inner diameters of 10, 14, 18, 23.4, and 30 mm to accommodate various secondary flow rates through the pipe required for the range of ejector entrainment ratios and secondary pressures. Pressure taps were positioned upstream and downstream of the orifice plate and connected to the low pressure transducers. Knowing the pressure drop across the orifice plate, secondary mass flow rate can be calculated using the Equation A.1 below (ISO 2006):

$$\dot{m} = \frac{C_d}{\sqrt{1-\beta^4}}\gamma A_{or}\sqrt{2\rho\Delta p} \tag{A.1}$$

where:

C_d: Coefficient of discharge, taken as 0.6 according to (ISO 2006).

β: Ratio of orifice plate diameter to pipe diameter

γ: Fluid specific heat ratio, taken as 1.4

A_{or}: Orifice plate area (m^2)

Δp: Static pressure losses across the orifice plate (kPa)

ρ: Fluid density (kg/m^3)

A.6 Entrainment section

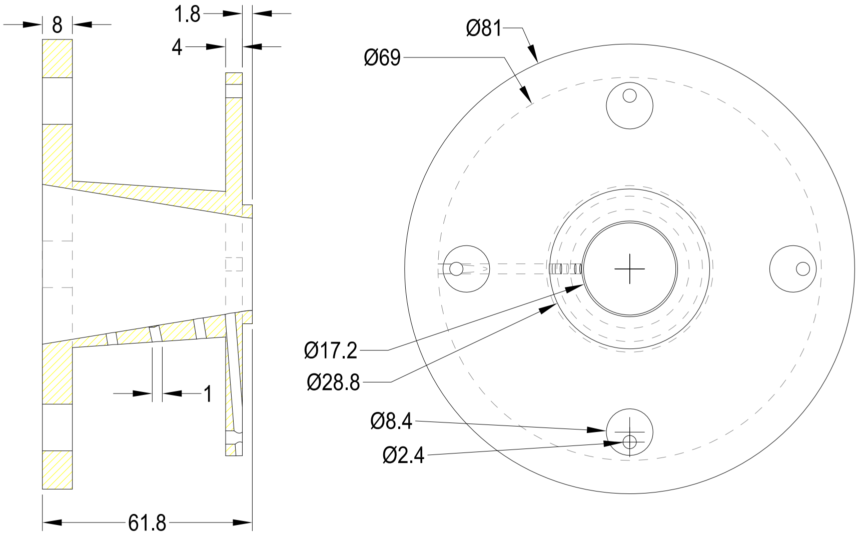

Figure A.7: Profile of the entrainment section with main dimensions, all dimensions in mm.

A.7 Connection section

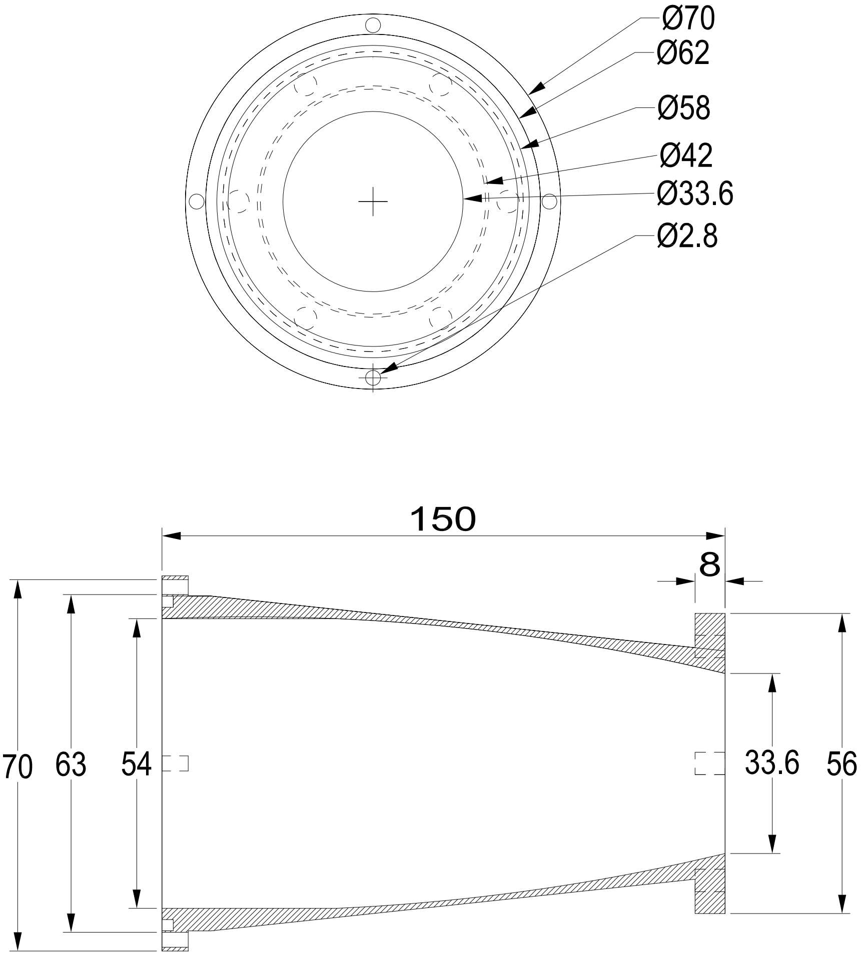

Figure A.8: Profile of the connection section with main dimensions, all dimensions in mm.

A.8 Condenser pipe

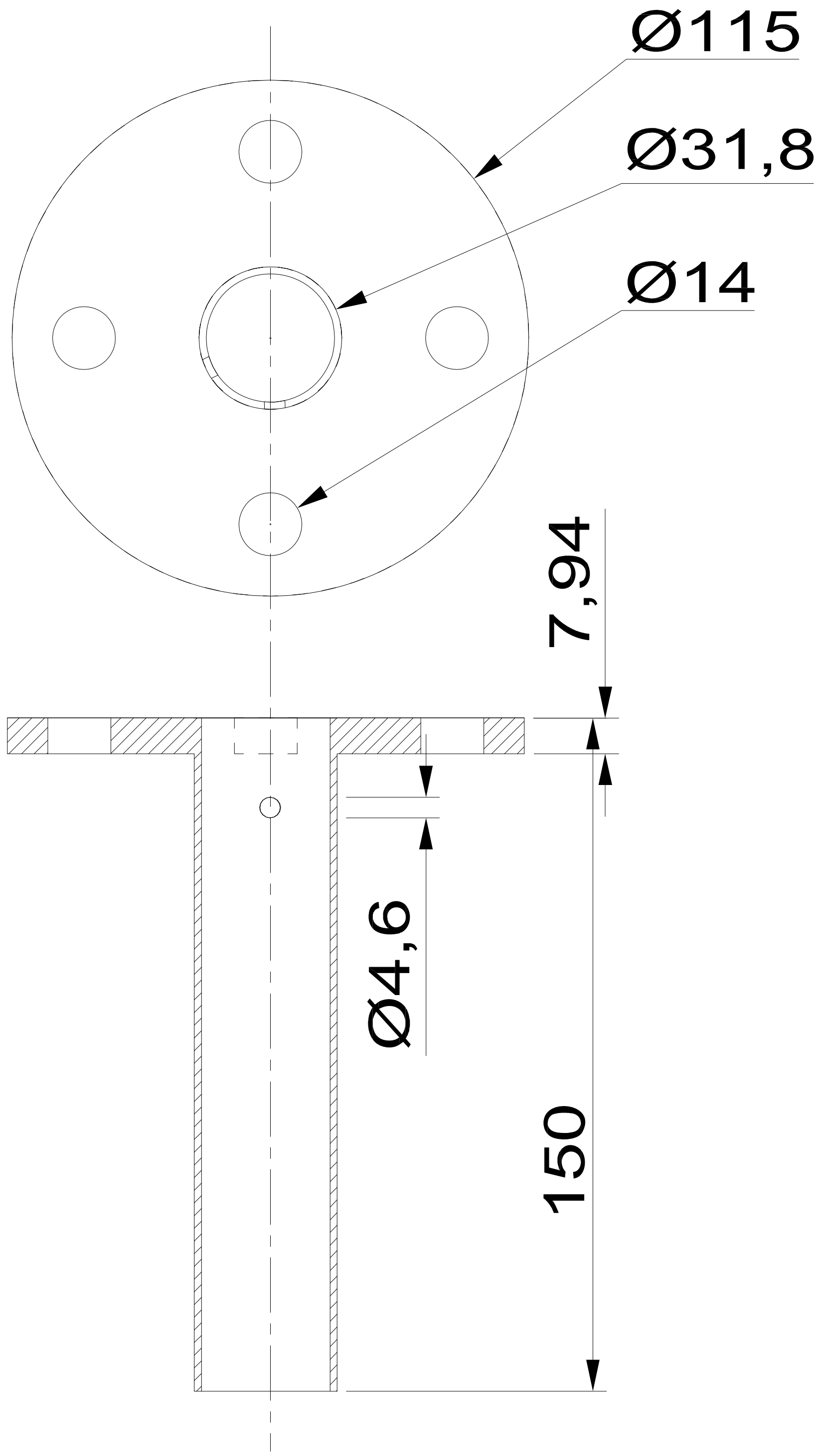

Figure A.9: Profile of the exit section with main dimensions, all dimensions in mm.

A.9 CRMC ejector part 1

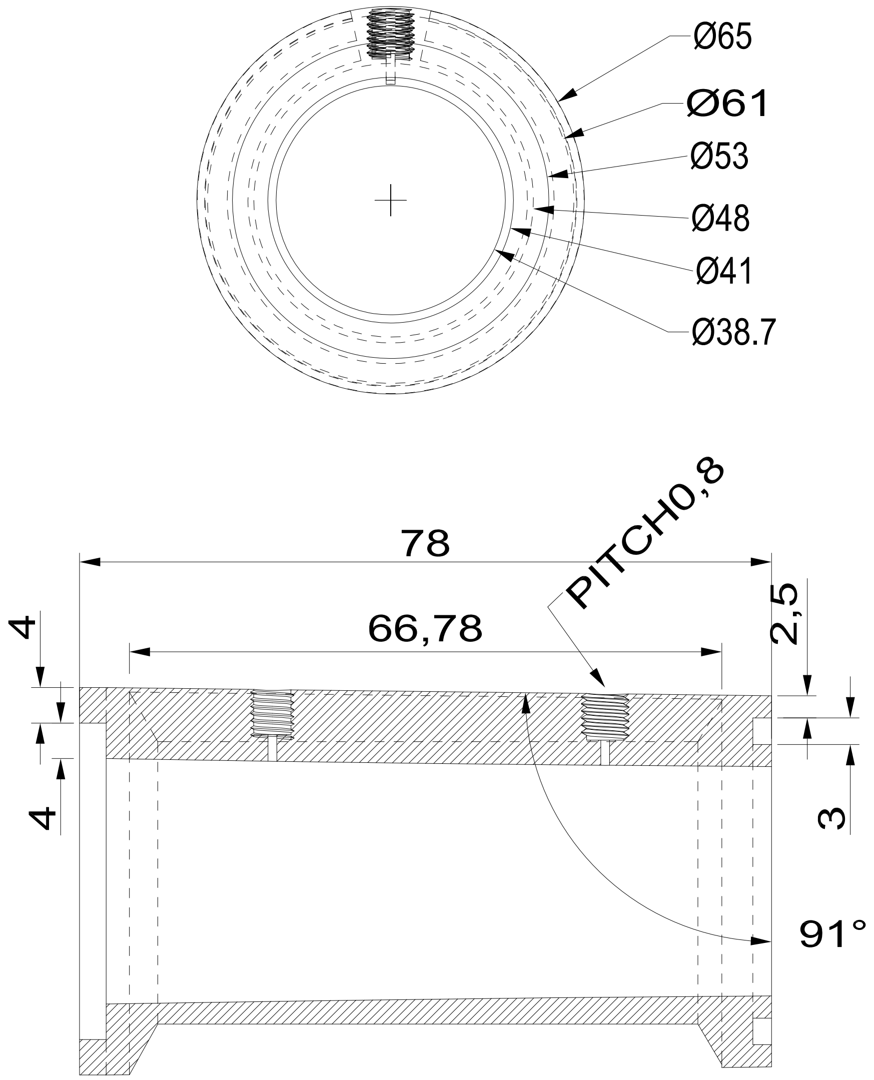

Figure A.10: Profile of the part 1 of CRMC ejector with main dimensions, all dimensions in mm.

A.10 CRMC ejector part 2

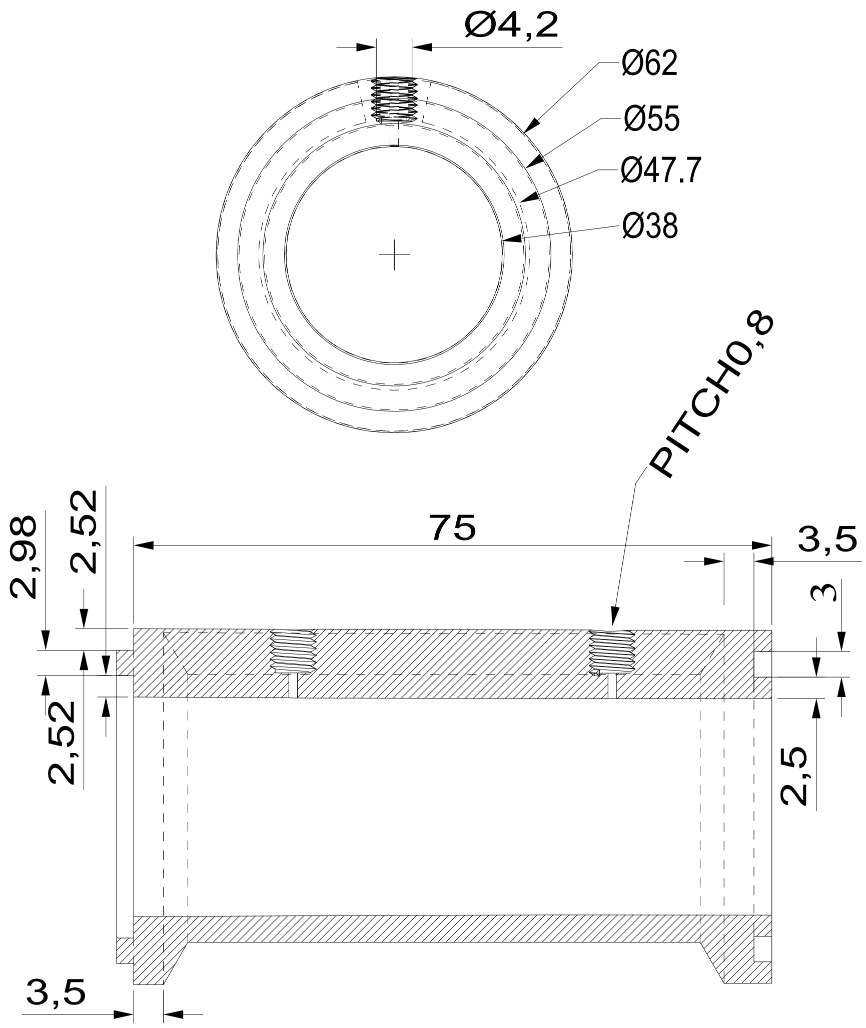

Figure A.11: Profile of the part 2 of CRMC ejector with main dimensions, all dimensions in mm.

A.11 CRMC ejector part 3

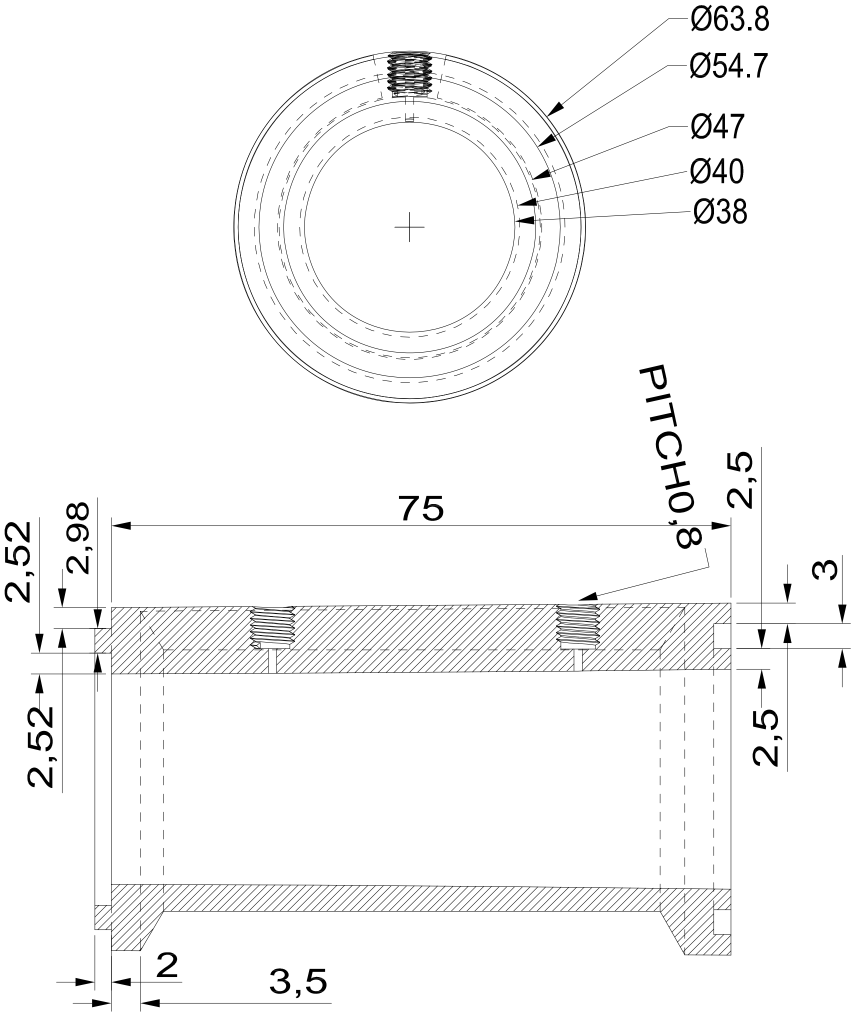

Figure A.12: Profile of the part 3 of CRMC ejector with main dimensions, all dimensions in mm.

A.12 CRMC ejector part 4

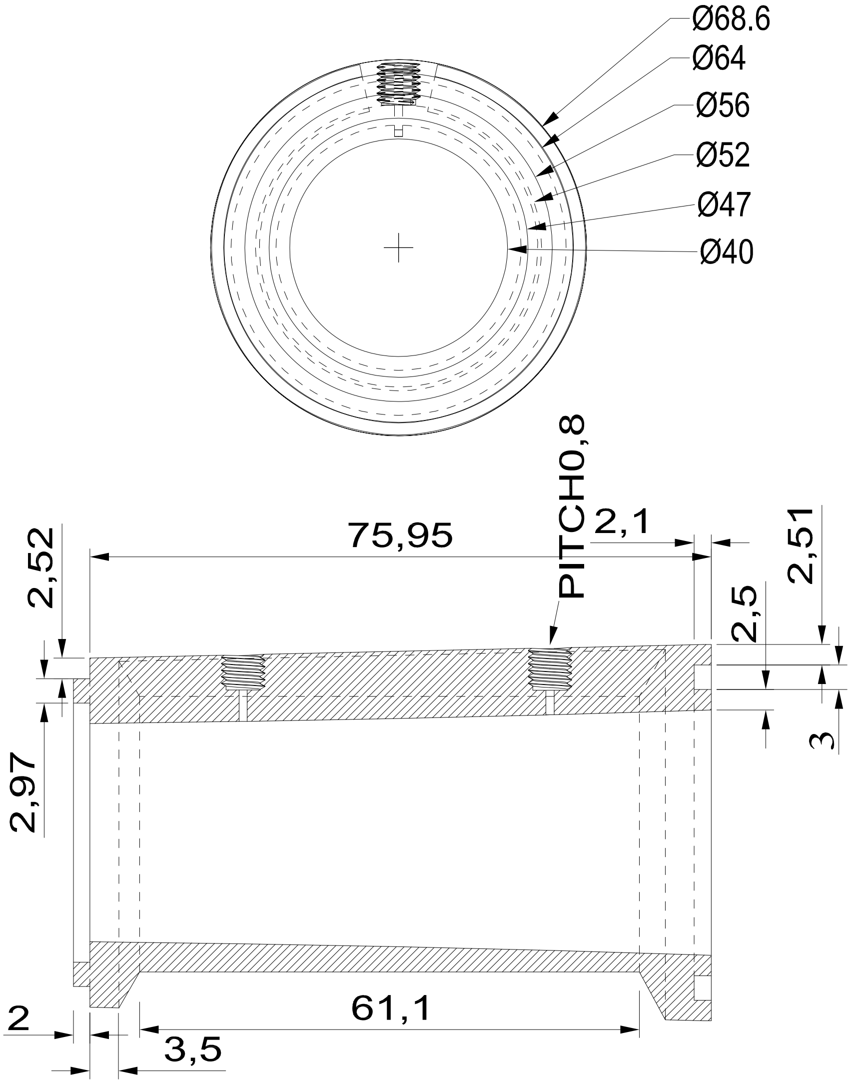

Figure A.13: Profile of the part 4 of CRMC ejector with main dimensions, all dimensions in mm.

A.13 CRMC ejector part 5

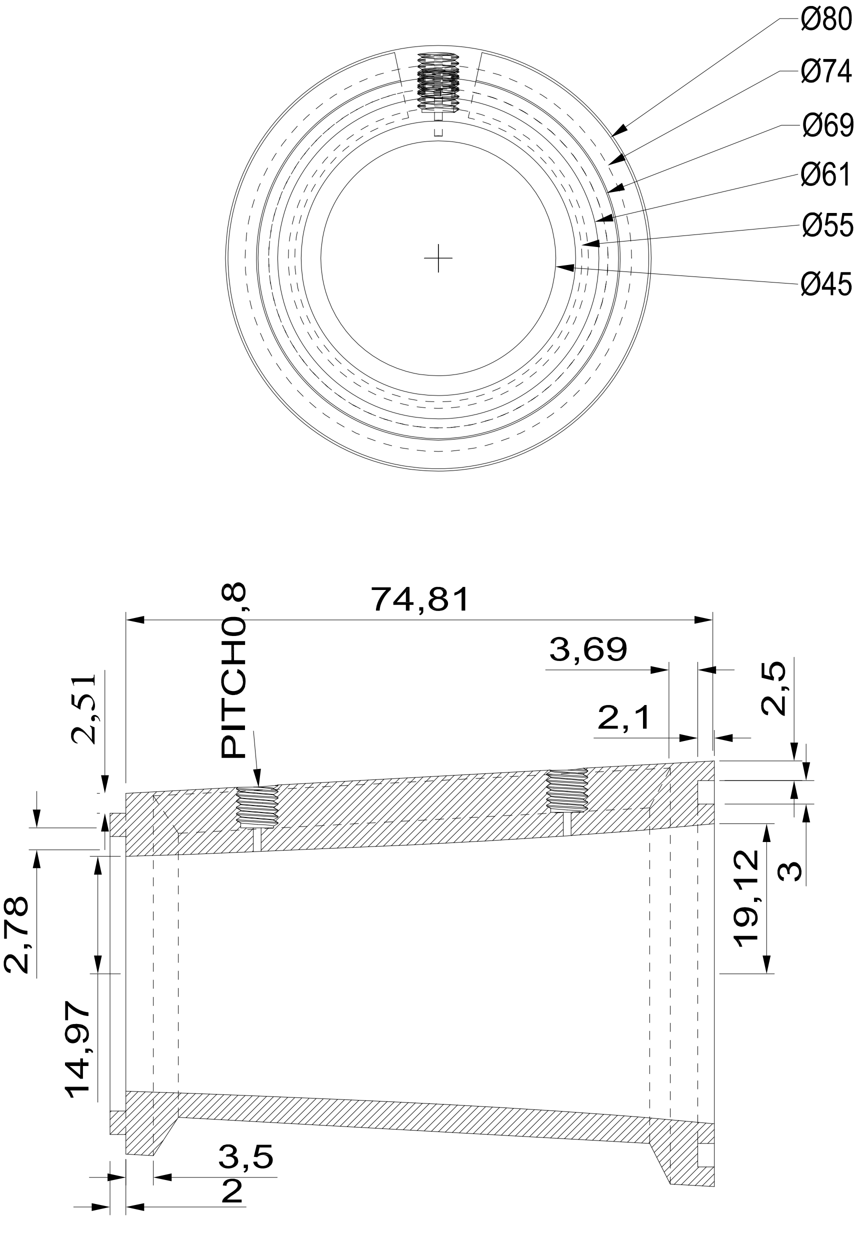

Figure A.14: Profile of the part 5 of CRMC ejector with main dimensions, all dimensions in mm.

A.14 CRMC ejector part 6

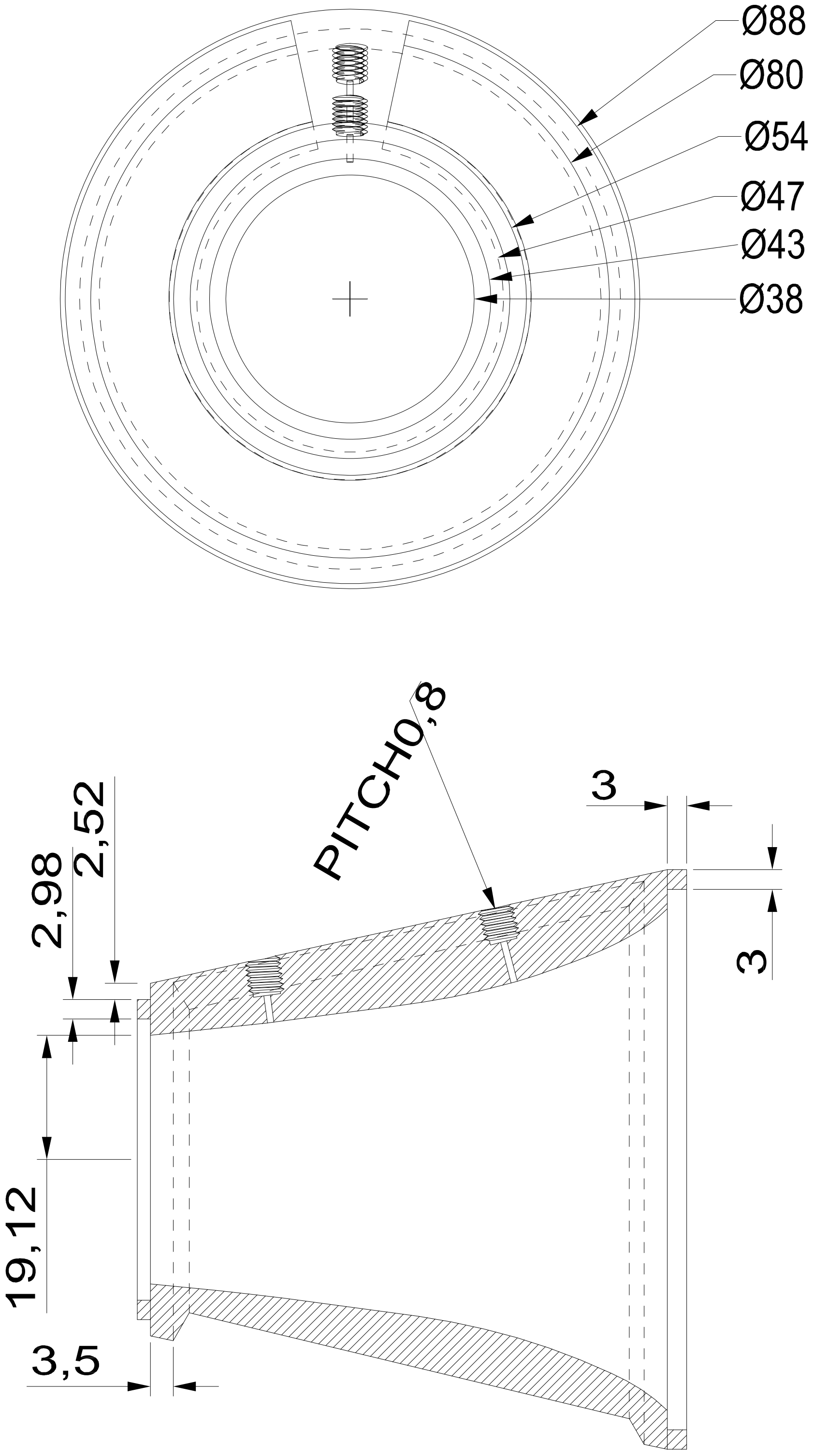

Figure A.15: Profile of the part 6 of CRMC ejector with main dimensions, all dimensions in mm.

Appendix B

Instrument calibration

B.1 Pressure transducer calibration

There are three types of pressure transducers used in the apparatus:

1. High pressure transducer, type Wika model A-10.
2. Low pressure transducer, type Wika model A-10.
3. Low pressure transducer, type BSDX.

A pneumatic dead-weight tester, Budenberg model 550 series, was used to calibrate the above three types of low pressure transducers. This tester worked in conjunction with a special adaptor model 24 vacuum adaptor piston/cylinder unit mounted upside down together with annular weight to produce a sub-atmospheric pressure . FigureB.1 shows the model 24 adaptor which is suitable for the calibration of the two types of low pressure transducers. Figure B.3 illustrates representative results of the calibration of the two types of pressure transducer. Table C.1 represents the results of the calibration.

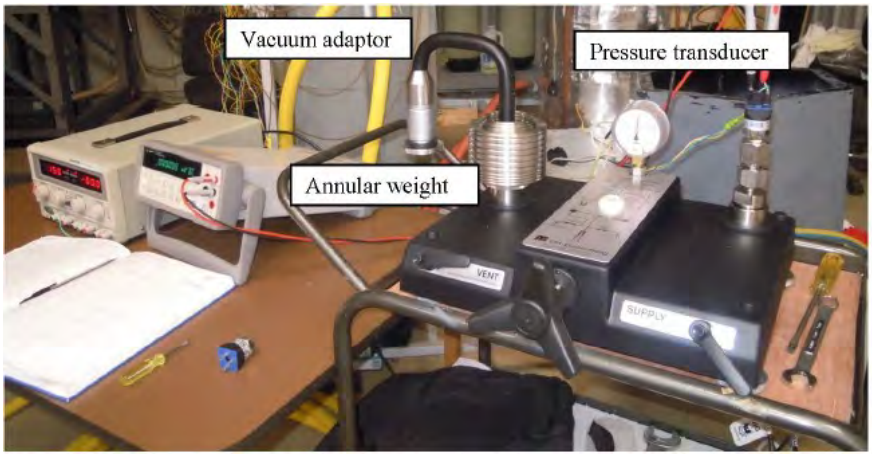

Figure B.1: Photograph of the pneumatic dead-weight tester model 550 series (Budenberg).

Figure B.2: Photograph of the hydraulic dead-weight tester model 580 series (Budenberg).

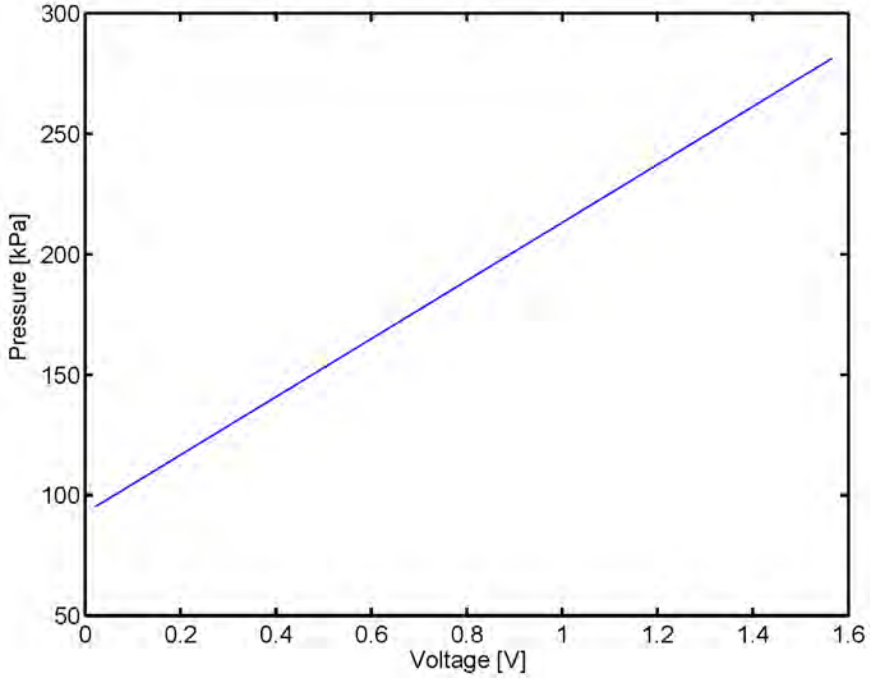

Figure B.3: Calibration of the Wika high pressure transducer-representative results.

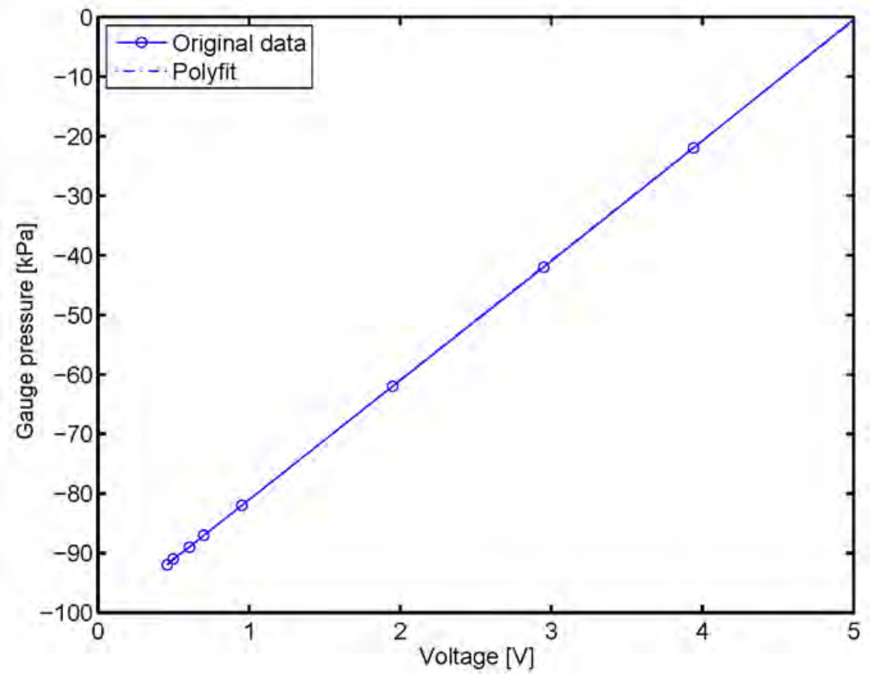

Figure B.4: Calibration of the Wika low pressure transducer-representative results.

Table B.1: Calibration of Wika low pressure transducers. V_{meas}= measured voltage. Voltage in Volt, and pressure in kPa.

	Serial number	Pressure	Equation
1	110263XV	H.P	$Pa=120.59V_{meas}-1.5289+Patm$
2	1102HF3P	L.P	$Pa=20.132V_{meas}-101.15+Patm$
3	1102HF3L	L.P	$Pa=20.113V_{meas}-100.92+Patm$
4	1102HF3B	L.P	$Pa=20.087V_{meas}-100.4+Patm$
5	1102HF3C	L.P	$Pa=20.087V_{meas}-100.91+Patm$
6	1102HF3I	L.P	$Pa=20.092V_{meas}-101.18+Patm$
7	1102HF3M	L.P	$Pa=20.13V_{meas}-101.297+Patm$
8	1102HF3N	L.P	$Pa=20.076V_{meas}-100.67+Patm$
9	1102HF3O	L.P	$Pa=20.07V_{meas}-101.19+Patm$
10	1102GF3E	L.P	$Pa=20.066V_{meas}-100.2+Patm$
11	1102HF3D	L.P	$Pa=20.024V_{meas}-101.3+Patm$
12	1102HF3F	L.P	$Pa=20.038V_{meas}-101.23+Patm$
13	1102HF3J	L.P	$Pa=20.071V_{meas}-101.1+Patm$
14	1102HF3K	L.P	$Pa=20.102V_{meas}-101.1+Patm$
15	1102HF3G	L.P	$Pa=20.089V_{meas}-101.05+Patm$
16	1102HF3H	L.P	$Pa=20.107V_{meas}-101.1+Patm$
17	BSDX1	L.P	$Pa=21V_{meas}-105.2+Patm$
18	BSDX2	L.P	$Pa=21.2V_{meas}-103.3+Patm$
19	BSDX3	L.P	$Pa=21V_{meas}-105.1+Patm$
20	BSDX4	L.P	$Pa=21V_{meas}-105.2+Patm$
21	BSDX5	L.P	$Pa=21V_{meas}-105.1+Patm$
22	BSDX6	L.P	$Pa=21V_{meas}-105.27+Patm$
23	BSDX7	L.P	$Pa=21V_{meas}-103.91+Patm$

B.2 Flow meter calibration

As voltage (V) is the flow meter output signal which received in lab-view , a correlation between the secondary flow rate and the output signal was produced as in Figure B.5.

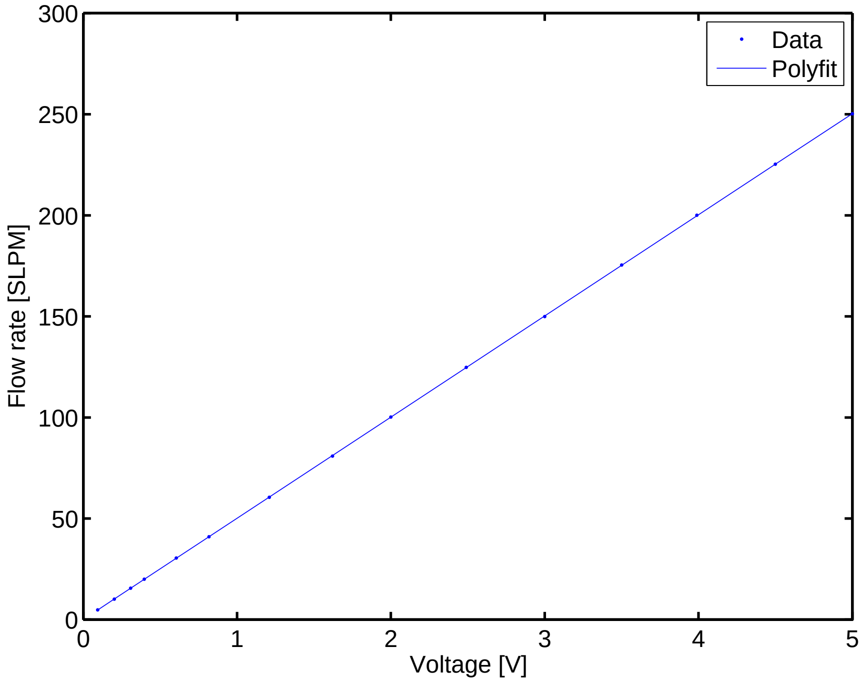

Figure B.5: Calibration of the Omega flow meter-representative results.

To avoid using flow meter in the primary flow line in the experiments, and the primary flow was always choked, a correlation between the primary flow rate and the primary pressure was produced as presented in Figure B.6.

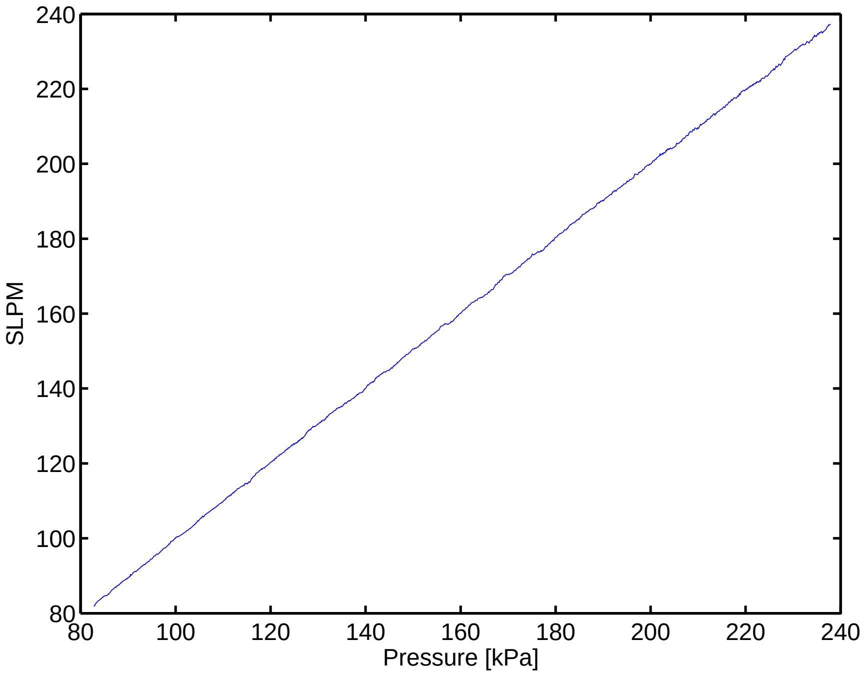

Figure B.6: Correlation of the flow rate and the pressure in the primary stream-representative results.

Appendix C

Tables of experimental data

Table C.1: Data from experiments with different nozzle positions and a nominal primary pressure of 200 kPa for a range of secondary and back pressures conditions. Primary mass flow rate was 3.58 g/s for the nominal primary pressure of 200 kPa.

NXP (mm)	P_{atm} (kPa)	T_s (°C)	T_c (°C)	P_s (kPa)	P_p (kPa)	P_c (kPa)	$\dot{m}_s$ (g/s)	ER
0	94.78	25.5	24.0	1.59	198.67	5.40	1.18	0.33
	94.20	17.1	15.0	2.57	202.00	5.90	2.26	0.48
	93.90	21.1	18.2	4.00	200.00	7.30	3.384	0.84
	94.05	23.5	20.3	5.00	196.50	7.80	3.976	1.08
10	94.00	24.40	22.1	1.65	208.00	5.40	1.258	0.34
	93.93	24.1	21.7	2.44	202.50	5.98	1.866	0.50
	93.90	23.7	20.8	4.00	216.00	7.30	3.38	0.87
	94.00	22.9	19.7	5.00	200.00	7.80	3.97	1.10
20	93.80	23.6	21.5	1.63	201.00	5.40	1.19	0.35
	94.00	24.3	21.8	2.45	200.00	5.90	2.27	0.55
	93.80	25.19	23.2	4.00	201.00	7.30	3.4	0.87
	93.80	25.1	22.0	5.00	202.20	7.77	3.95	1.08
30	94.18	25.6	23.50	1.62	202.60	5.48	1.195	0.36
	94.15	26.6	24.2	2.56	202.50	5.88	2.3	0.57
	94.13	27.3	24.5	4.00	202.85	7.20	3.41	0.92
	94.10	27.3	24.2	5.00	202.33	7.94	3.91	1.15
40	94.13	23.6	21.9	1.6	204.30	5.42	1.181	0.38
	94.13	22.5	20.4	2.50	204.77	5.95	2.25	0.66
	94.18	21.5	19.0	4.00	203.40	7.26	3.4	0.99
	94.20	20.8	18.0	4.87	201.27	8.0	3.99	1.19
50	94.30	22.6	20.4	1.51	200.77	5.45	1.2	0.36
	94.25	24.5	22.2	2.40	205.50	5.92	2.29	0.58
	94.20	25.4	22.6	4.00	206.40	7.22	3.38	0.93
	94.20	25.0	22.2	5.00	200.36	7.90	3.9	1.16
60	94.25	22.5	20.3	1.65	200.75	5.60	1.68	0.34
	94.25	21.5	19.2	2.43	200.77	6.00	2.24	0.55
	94.25	19.8	17.3	4.00	201.32	7.08	3.42	0.88
	94.28	19.0	16.3	4.88	201.18	7.98	4.1	1.15

Table C.2: Data of experimental with different nozzle positions and a nominal primary pressure of 225 kPa for a rage of secondary and back pressures conditions. Primary mass flow rate was 3.89 g/s for the nominal primary pressure of 225 kPa.

NXP (mm)	P_{atm} (kPa)	T_s (°C)	T_c (°C)	P_s (kPa)	P_p (kPa)	P_c (kPa)	$\dot{m}_s$ (g/s)	ER
0	94.1	22.5	19.4	1.58	225.3	5.75	1.3	0.36
	94.0	24.0	21.5	2.5	225.00	6.35	2.3	0.51
	94.4	23.5	21.7	4.00	225.4	7.80	3.52	0.88
	94.1	24.5	22.3	5.00	226.0	8.30	4.1	1.14
10	94.20	24.70	22.7	1.65	225.00	5.77	1.251	0.365
	93.95	24.5	21.5	2.48	225.3	6.48	2.4	0.52
	94.60	23.7	20.5	4.00	225.00	7.65	3.45	0.89
	94.50	23.9	20.7	5.00	225.30	8.4	4.1	1.16
20	93.60	23.5	21.5	1.6	225.40	5.82	1.272	0.38
	94.20	24.5	21.6	2.5	225.00	7.0	2.406.0	0.59
	94.40	25.0	23.0	4.00	225.60	7.75	3.415.0	0.91
	94.50	25.50	22.40	5.00	225.5	8.44	4.11.6	1.18
30	94.4	24.6	23.0	1.6	225.6	5.88	1.24	0.38
	94.2	26.3	24.5	2.51	225.50	7.08	2.45	0.67
	94.3	25.5	23.0	4.00	225.85	7.76	3.46	1.1
	94.3	25.3	23.2	5.00	225.0	8.55	4.1	1.22
40	94.3	23.3	22.5	1.6	225.4	5.97	1.3	0.39
	94.5	23.5	21.4	2.50	226.0	7.2	2.42.6	0.68
	94.2	21.5	20.0	4.00	225.40	7.61	3.35	1.11
	94.20	21.5	19.2	5.0	225.0	8.4	4.02	1.21
50	94.20	22.1	20.2	1.61	226.0	5.8	1.22.1	0.38
	94.6	24.0	22.0	2.50	225.0	6.46	2.472	0.59
	94.4	24.3	22.5	4.00	224.40	7.72	3.42.6	0.96
	94.4	24.4	22.4	5.00	224.36	8.45	4.12	1.19
60	94.0	19.8	17.8	1.58	225.0	5.9	1.25	0.37
	94.5	21.3	19.5	2.5	226.0	6.55	2.36	0.57
	94.2	22.9	20.4	4.00	225.4	7.74	3.48	0.91
	94.4	23.4	21.7	5.0	225.7	8.59	3.995	1.18

Table C.3: Data of experimental with different nozzle positions and a nominal primary pressure of 250 kPa for a range of secondary and back pressures conditions. Primary mass flow rate was 4.25 g/s for the nominal primary pressure of 250 kPa.

NXP (mm)	P_{atm} (kPa)	T_s (°C)	T_c (°C)	P_s (kPa)	P_p (kPa)	P_c (kPa)	$\dot{m}_s$ (g/s)	ER
0	94.2	22.5	19.4	1.58	253	6.1	1.21	0.32
	94.0	23.0	21.0	2.5	254.00	6.80	2.38	0.49
	94.3	23.1	21.2	4.00	254.00	8.30	3.52	0.74
	94.5	23.5	20.3	5.00	254.50	8.80	4.18	0.92
10	94.25	24.40	22.1	1.65	254.00	6.140	1.22	0.33
	93.95	24.0	21.3	2.48	253.00	6.98	2.47	0.49
	94.55	23.7	20.8	4.00	254.00	8.0	3.39	0.75
	94.00	22.9	19.7	5.00	253.00	9.0	3.887	0.93
20	93.80	23.4	21.0	1.6	254.00	6.2	1.21	0.33
	94.2	24.0	21.6	2.5	254.00	8.10	2.38	0.50
	93.9	25.2	23.2	4.00	254.00	8.2	3.415	0.77
	93.95	25.0	22.0	5.00	253.5	9.1	3.98	0.94
30	94.85	24.6	23.50	1.6	253.6	6.28	1.23	0.35
	94.25	26.8	24.8	2.51	253.50	8.28	2.415	0.52
	94.51	25.3	23.5	4.00	253.85	8.32	3.62	0.79
	94.150	27.3	24.2	5.00	254.0	9.15	4.15	0.95
40	94.1	23.7	22.0	1.6	254.0	6.32	1.22	0.36
	94.7	22.5	20.4	2.50	254.0	7.3	2.398	0.52
	94.78	21.5	19.0	4.00	253.40	8.5	3.43	0.79
	94.26	20.5	18.2	5.0	254.0	9.2	4.08	0.94
50	94.20	22.1	20.2	1.61	254.0	6.15	1.211	0.33
	94.55	24.4	22.4	2.50	254.0	7.0	2.42	0.50
	94.25	24.4	22.6	4.00	253.40	8.22	3.45	0.76
	94.5	24.0	22.2	5.00	254.36	9.0	4.055	0.93
60	94.6	19.7	17.8	1.58	254.0	6.2	1.23	0.318
	94.25	21.5	19.4	2.5	253.0	7.10	2.38	0.475
	94.24	22.9	20.4	4.00	253.4	8.4	3.416	0.74
	94.35	23.4	20.7	5.0	253.7	9.2	3.995	0.92

Table C.4: Data of experimental with different nozzle positions and a nominal primary pressure of 270 kPa for a range of secondary and back pressures conditions. Primary mass flow rate was 4.55 g/s for the nominal primary pressure of 270 kPa.

NXP (mm)	P_{atm} (kPa)	T_i (°C)	T_o (°C)	P_s (kPa)	P_p (kPa)	P_c (kPa)	$\dot{m}_s$ (g/s)	ER
0	94.2	22.5	19.4	1.58	272.4	7.1	1.16	0.28
	94.7	23.0	21.0	2.5	273.00	7.80	2.14	0.44
	94.3	23.1	21.2	4.00	272.00	9.30	3.12	0.68
	94.05	23.5	20.3	5.00	270.50	9.80	3.65	0.85
10	94.00	24.40	22.1	1.65	273.00	7.140	1.155.1	0.29
	93.95	24.0	21.3	2.48	273.00	7.98	2.23.6	0.44
	94.2	23.7	20.8	4.00	274.00	9.0	3.22	0.69
	94.6	22.9	19.7	5.00	271.00	9.80	3.66	0.86
20	93.80	23.4	21.0	1.6	274.00	7.2	1.21	0.29
	94.3	24.0	21.6	2.5	274.30	9.10	2.23	0.45
	93.8	25.2	23.2	4.00	272.30	9.2	3.4	0.71
	93.9	25.0	22.0	5.00	271.2	9.81	3.95	0.87
30	94.8	24.6	23.50	1.6	272.6	7.28	1.168	0.31
	94.5	26.8	24.8	2.51	273.30	9.28	2.25	0.47
	94.17	25.3	23.5	4.00	273.55	9.32	3.35	0.73
	94.2	27.3	24.2	5.00	272.30	9.85	3.97	0.88
40	94.1	23.7	22.0	1.6	272.20	7.32	1.185	0.32
	94.16	22.5	20.4	2.50	274.20	8.3	2.241	0.47
	94.18	21.5	19.0	4.00	274.40	9.5	3.25	0.73
	94.26	20.5	18.2	5.0	274.40	9.92	3.96	0.87
50	94.28	22.1	20.2	1.61	272.50	7.15	1.158	0.29
	94.15	24.4	22.4	2.50	273.60	8.0	2.13	0.45
	94.25	24.4	22.6	4.00	273.40	9.22	3.18	0.70
	94.51	24.0	22.2	5.00	272.63	9.80	3.55	0.83
60	94.53	19.7	17.8	1.58	272.20	7.2	1.158	0.28
	94.28	21.5	19.4	2.5	274.40	8.10	2.12	0.42
	94.32	22.9	20.4	4.00	273.50	9.4	3.29	0.68
	94.25	23.4	20.7	5.0	273.30	9.92	3.57	0.85